"Fade Countermeasure Modelling for Ka Band Digital Satellite Links"

Boris Christian Grémont

A thesis submitted in partial fulfilment
of the requirements of
Coventry University
for the degree of
Doctor of Philosophy

November 1997

Coventry University in collaboration with the Rutherford Appleton Laboratory

"Any lone cloud in an otherwise clear sky has got some explaining to do. Very probably it has just got cut off from the main herd or has lost his mother, but occasionally it is a rogue cloud looking for someone to rain on."

***Miles Kington**, 1941- : Nature Made Ridiculously Simple (1983).*

This thesis investigates the modelling of fade countermeasures (FCMs) for the design of geostationary Ka band digital satellite communication systems. The analysis focuses on a typical low-power low-rate very small aperture terminal application using adaptive forward error correction as a way of counteracting the high level of detected dynamic atmospheric fading.

The management and performance of such systems is conditioned greatly by the ability of practical controllers at detecting the actual level of total signal attenuation. At 20 or 30 GHz, rain attenuation and tropospheric scintillation are the two major propagation effects of interest. Part of the solution relies on the consideration and integration of their random and dynamic nature in the design process.

The finite response time of practical countermeasure systems is a source of performance degradation which can be minimised by the implementation of predictive control strategies. This is the focal point of this thesis. A novel on-line short-term predictor matched to the Ka band fading process is proposed.

While the rain attenuation component is efficiently predicted, tropospheric scintillation is the source of the estimation error. To take this into account, a statistical model, based on an extension of the global fading model for rain and scintillation, is then developed so that long term performance of predictive countermeasures can be drawn.

Two possible ways to compensate for scintillation-induced prediction errors, namely the fixed and variable detection margin approaches, are proposed, analysed and then compared. This is achieved by calculating the FCM utilisation factor, as well as the throughput and bit error rate performance of a typical Ka band system in the presence of dynamic fading within the context of predictive fade countermeasure control operations.

In the last part of this thesis, the inclusion of instantaneous frequency scaling in the design of efficient FCM control schemes is investigated. This is applicable to systems using fade detection at a base frequency. In particular, a new statistical model, accounting for the impact of the stochastic temporal variations of rain drop size distribution on rain attenuation, is presented.

This thesis further confirms that countermeasure systems are technologically viable. The consideration of more specific design problems does not change the overall validity of this statement. In this thesis, it is shown that a predictive FCM technique, based on readily available punctured convolutional codes, with their relatively modest coding gain, is sufficient to provide high link availability and user data throughput on a low-power low-rate in-bound VSAT link.

Acknowledgements

I would like to express profound gratitude to my director of studies, Mr Paul Gallois, for giving me the great opportunity of going into research. His patience, experience, help and guidance was invaluable throughout this work.
I am also greatly indebted to my second supervisor, Dr Stephen Bate, whose expertise, guidance and encouragement played a key role in this project.

I am grateful to Coventry University for funding this project. In particular, I gratefully acknowledge the staff of Coventry University for providing a good and enjoyable work environment. A special mention goes to the staff at the Lanchester Library for their professionalism and excellent quality of service.

I would like to thank my family and friends for their continuous and limitless moral and logistic support especially throughout the last three years. Thank you to my best friend here in the UK, Mr Shaun Yeates, for listening and helping when I needed.

Contents

A	Attenuation
ACF	Auto-Correlation Function
ACK	Acknowledgement
AFEC	Adaptive Forward Error Correction
AIC	Akaike's Criterion
ALC	Automatic Level Control
Ant.	Antenna
APSK	Adaptive Phase Shift Keying
AQAM	Adaptive Quadrature Amplitude Modulation
ARMA	Auto Regressive Moving Average
ARQ	Automatic Repeat Request
A_u	Up-link Attenuation
A_u	Down-link Attenuation
AWGN	Additive White Gaussian Noise
B	Bandwidth (Hz)
B-ISDN	Broadband ISDN
BER	Bit Error Rate
BLC	Burst Length Control
bps	Bit per second
BPSK	Binary Phase Shift Keying
c	Velocity of light
C	Frequency band between 4 and 8 GHz
χ	Amplitude Scintillation Random Variable
C/B	Channel Capacity per unit Bandwidth
C/I.	Carrier-to Interference Ratio
C/N, C/N_o	Carrier-to-Noise Ratio
CCIR	International Radio Consultative Committee
CCITT	Consultative Committee on International Telegraphy and Telephony
CD	Compact disk
CDF	Cumulative Distribution Function
CNR	Carrier-to-Noise Ratio
CODE	Co-Operative Data Experiment
codec	Coder/Decoder
COST	Cooperation Europeenne dans le domaine de la recherche Scientifique et Technique
CPA	Co-Polar Attenuation
CRC	Code Rate Change
CSP	Constant Satellite Power sharing
CV	Convolutional
D	Diameter
d	Down-Link
DA	Demand Assignment
dB	Decibel
DBS	Direct Broadcasting
DDS	Direct Digital Synthesis

DS-SS	Direct Sequence Spread-Spectrum
DSP	Digital Signal Processing
e	Residual error made by the predcitor
ε	Excess Low-Fade Margin
E_b/N_o	Energy per bit to noise spectral density ratio
EES	Electrical Electronic and Systems
EIRP	Effective Isotropic Radiated Power
E_s/N_o	Energy per symbol to noise spectral density ratio
ESA	European Space Agency
EU	European Union
ϕ	Pointing loss (degree)
f	Carrier Frequency
FA	Fixed Assignment
FCM	Fade CounterMeasure
FDM	Frequency Division Multiplexing
FDM	Fixed Detection Margin
FDMA	Frequency Division Multiple Access
FDV	Frequency Diversity
FEC	Forward Error Control
FPM	Fixed Power Margin
FSS	Fixed Satellite Services
$f_x(x)$	pdf of the random variable x
Γ	Spectral efficiency in baud /second
γ	Constraint length of a code
G/T	Antenna Gain to Noise Temperature ratio
G_c	Coding gain
GF	Global Fading
GHz	GigaHertz
η	Antenna efficiency
h	Normalised Power Spectrum Density
H	Energy Gain (dB)
HARQ	Hybrid ARQ
HDTV	High Definition TeleVision
HPA	High Power Amplifier
HPF	High Pass Filter
Hz	Hertz
IBO	Input back-off
IDU	Indoor Unit
IFSF	Instantaneous Frequency Scaling Factor
ILL	Inter-Library Loan
IPS	Input Power for Saturation
ISDN	Integrated Service Digital Network
ITU-R	International Telecommunication Union - Recommendations
J	Joule
k	Boltzman's constant
	prediction time of a predictor (k= 1,2,... seconds)
K	Kelvin
Ka	Frequency band between 17.7 and 21.2 GHz
Ku	Frequency band between 12.5 and 18 GHz

Λ	Lognormal pdf
λ	Wavelength
L	Loss (Attenuation), Length
LNA	Low Noise Amplifier
LPF	Low pass Filter
M	M-ary index
m	Meter, Median value for the lognormal model of rain attenuation
M_0	Fixed excess margin
m_2	Second Order Moment
m_4	Fourth Order Moment
MCPC	Multiple Channel Per Carrier
MGF	Modified Global Fading
MHz	Megahertz
M_i	Margin for implementation
MMSE	Minimum Mean Square Error
Modem	Modulator/Demodulator
MPhil	Master of Philosophy
MV	Moulsley-Vilar
N	North
n	AWGN noise component
np	Neper
OBO	Output Back-off
OD	Orbital Diversity
OPEX	Olympus Propagation EXperiment
OSI/ISO	Open System Interconnection
P	Power
p%	Percentage of Time
Pdf	Probability Density Function
PhD	Doctor of Philosophy
P_{out}	Probability of outage
PRBS	Pseudo Random Binary Sequence
Prob{ }	Probability
PSD	Power Spectral Density
θ	Elevation angle
Q( )	Error function
q^{-1}	Backward Shift Operator
QAM	Quadrature Amplitude Modulation
QPSK	Quadrature Phase Shift Keying
R	Slant path length
ρ	FEC code rate
R	Rain rate
r.v.	Random variable
RAL.	Rutherford Appleton Laboratory
R_b	User information bit rate (bps)
RCPC	Rate Compatible Punctured Convolutional Codes
RELS	Recursive Extended Least Squares
RF	Radio Frequency

ROM	read Only Memory
R_p	Chip rate
Rq	Required
R_s	Symbol Rate (baud)
RS	Reed Solomon
R_s	Symbol Rate (baud)
Rx	Receiver
σ	Standard Deviation
S( )	Power Spectrum density
S/N	Signal-to-Noise Ratio
SAT	Satellite
SCPC	Single Channel Per Carrier
SD	Site Diversity
SR	Shared Resource
SS-TDMA	Satellite-Switched TDMA
T, t	Duration, Time
TDM	Time Division Multiplex
TDMA	Time Division Multiple Access
TWTA	Travelling Wave Tube Amplifier
Tx.	Transmitter
u	Up-Link
U	FCM utilisation ratio
ULPC	Up-Link Power Control
VDM	Variable Detection Margin
VSAT	Very Small Aperture Terminal
ω	Angular Frequency (rd/s)
W	West
w.r.t.	With Reference to
y	Rain attenuation random variable
Z	Global fading random variable (i.e. rain and scintillation)_

1. Introduction

This thesis describes a three year full-time MPhil/PhD project, started in October 1994, which is now considered to have reached an appropriate stage to seek the approval of the University's Research Degrees Committee for the award of the degree of PhD.

Prior to embarking on this project, the author gained some experience in the installation, operating and maintenance of microwave terrestrial links, while doing military service for the French forces based in Germany.

During the last eight years, the University's former Department of Electrical, Electronic & Systems Engineering (EES) has accumulated research and student projects in the field of Satellite and Digital Communications. The work presented here seeks to build upon this experience and to exploit the facilities of the Electronics and Communications Group's Satellite Reception Centre. It also strives at strengthening the links previously established with the Rutherford Appleton Laboratory and the former members of the European Space Agency's Olympus Experiment (OPEX).

More particularly, this project has been the object of an inclusion within the research activity of the EU's COST 255 project entitled: "Radiowave propagation modelling for new satcom services at Ku band and above".

1.1 The Ka Band*

Since the first geostationary commercial satellite (INTELSAT I) launched in 1965, satellite communication has reached the status of a mature and accepted technology **[1.1]**. Its greatest achievement is the great reduction in cost and complexity of Earth stations allowing satellite technology to become closer to the end-user.

The increasing demand in traffic capacity and the multiplication of specific communication services is leading to many problems of co-ordination and management of the Radio-Frequency (RF) spectrum **[1.2]**. This is particularly true for the USA and Western Europe where C** and Ku*** bands are approaching saturation and will necessitate the move to the higher Ka band **[1.3]**.

The primary attraction of the 20/30 GHz band is the 2.5 GHz bandwidth available for accommodating the increasing traffic capacity and for supporting new wide-band services such as ISDN (Integrated Service Digital Network) traffic.

The exploitation of a higher and yet empty band allows a very efficient utilisation of the satellite capacity via better frequency reuse capability within a low interference environment.
For spatially separated spot beam coverages, multibeam operation with on-board switching and moderate sized spacecraft antennas allow the generation of high density narrow beams **[1.4]**. As a consequence, ground-based antenna diameters can be reduced:

- on down-links, without loss of quality,
- on up-links, without generating extra interference, when compared to C or Ku band systems.

---

* *17.7-21.2 GHz Down link 27.5-31 GHz Up link*
** *4/8 GHz*
*** *12.5/18 GHz*

The 20/30 GHz band seems therefore very attractive for supporting new innovative services and is likely to create a revolution in the world of telecommunications.

The main future advanced applications will cover **[1.5]**:

- Fixed multimedia communications (for private business networks)
- Mobile/Personal communications
- Digital high definition television (HDTV)
- Sound broadcasting to portable receivers
- Navigation and Air Traffic Management **[1.6]**.

In this thesis, particular emphasis will be placed on Very Small Aperture Terminals (VSATs). Due to their ease of installation, maintenance and reconfiguration, VSAT networks are one of the main potentials for exploiting the 20/30 GHz band. Furthermore the technology already exists and can take full advantage of the smaller antenna size and low interference levels.

Most present commercial VSAT systems operate at C or Ku bands. So far, the Ka band has only been used for experimental purposes **[1.7]**. However there is no doubt that it will be soon exploited commercially since a portion of the Ka* band is strictly allocated to Fixed Satellite Services (FSS) to which VSATs belong.

VSAT systems are finding increasing applications as an alternative to terrestrial networks for servicing areas with no, or poor, infrastructure **[1.8]**. The current trend towards a 'blanket licensing' procedure **[1.9]**, based on type approval of VSATs, will trigger their success in Europe for corporate applications **[1.10]**.

1.2 Fade countermeasures

The major problem for the utilisation of the Ka band for new communication services is the high value of the total atmospheric attenuation. At Ka band it is mainly dominated by rain attenuation and tropospheric scintillation. At such frequencies, it is not appropriate to achieve high link availability by introducing a

* 19.7/20.1 GHz Down-link, 29.5 GHz/29.6 GHz Up-link for Europe and the USA

fixed power margin, as was previously done at C or Ku bands. Instead, adaptive methods known as Fade Countermeasures (FCMs) were proposed as a more efficient means to achieve low link unavailabilities **[1.11]**. This is particularly relevant to VSATs, which are power limited on in-bound links and require advanced mitigation schemes on out-bound links.

The problem of fade countermeasures lies with the fact that, at high frequency, it is difficult to provide the equivalent power range necessary to ensure a specified (possibly high) link availability and/or throughput. As a consequence, designers are faced with the challenge of providing sufficient gains by exploiting efficiently and in combination the (scarce) fundamental satellite resources; namely power, bandwidth, transmission time and geographical diversity.

As in most cases, those resources are shared, and for greater efficiency, they need to be allocated dynamically as and when required. Fade countermeasures are thus low-fade margin adaptive control systems, which need to be deployed according to the detected real-time conditions of a monitored channel.

As a consequence, geostationary earth-space slant path propagation must be seen as a time-varying channel. This has motivated new propagation experiments (**[1.12, 1.13]**), which have produced new results in the characterisation of the dynamics of the atmospheric fading.

These two aspects, FCM techniques and dynamic fading control, form the basis of Fade Countermeasure modelling and design. Due to its commercial potential, it is the source of intensive research.

1.3 Literature Survey

The purpose of the literature survey in the course of this project was to identify more precisely the focal point of the work within the context of fade countermeasures. The survey was carried out using the facilities of the library of Coventry University and the internet. Reference books and CD ROM databases have been consulted, whilst relevant specialised documentation was obtained either at the library premises or through the Inter-Library Loan (ILL) services.

Some effort has also been made to understand the basic requirements of a MPhil/PhD research project **[1.14]**. The "Research methods and Professional Skills module" delivered by Coventry University was attended at the start of this research.

Different subjects were identified as of particular interest to this project. They are:

(i) Very Small Aperture Terminals

(ii) Fade Countermeasure techniques

(iii) Fade control and dynamic Ka band fading

(iv) Radiowave propagation on Earth-Space slant paths

(vi) Time-series analysis and stochastic control

(vii) Digital & Satellite communications

Approximately 200 references have been collected and analysed, however, due to length constraints imposed on this document, a detailed literature survey is not provided here. The references which are of importance to this present work will however be given in the subsequent chapters. The final conclusion that came out of the literature survey is, however, given in the next section.

1.4 Conclusions from Literature Survey

In recent years the utilisation of the Ka band has aroused a great interest in both industrial and scientific fields. This is demonstrated by the efforts for the development and the realisation of operational and cost effective systems in this band. The research is now in the stage of the feasibility study, the outcome of which should be a technical proof to investors of the economical viability of Ka band systems as the support for future communications satellite systems. They will probably be fully integrated within terrestrial networks. VSAT networks, were identified as of particular interest to this project.

The exploitation of these frequency bands requires the implementation of fade countermeasure techniques in order to compensate for the high levels of dynamic fading mainly dominated by hydrometeor attenuation. FCM strategies require the development of control systems based on the dynamic and stochastic nature of the total fading process over the satellite channel. As a consequence, the atmospheric

attenuation must be seen as a time varying process, which has, in turn, motivated extensive propagation experiments for characterising in detail the Ka band fading. Whilst the fading process and each of its constituting components are now well defined statistically on a long term basis, more work is however required for developing further site diversity models such as to dimension appropriately shared common resource FCM systems and distributed satellite systems. On the dynamic aspect, substantial innovative theoretical and experimental work has been produced in recent years. Tartaskii's physical model of tropospheric scintillation **[1.15]**, based on turbulence theory, is found to describe appropriately the power spectral density of amplitude scintillation during stationary intervals. However, scintillation is known to be non-stationary and to have a lognormally distributed variance. No satisfactory equivalent physical model has yet been proposed for explaining temporal variations of rain induced attenuation. Very few studies (statistical or dynamic) on joint rain attenuation and amplitude scintillation are available in the literature. This is due primarily to the difficulty of separating both effects efficiently via filtering techniques. Few results are available on the modelling of the variability of the instantaneous frequency scaling of rain attenuation and tropospheric scintillation.

The real time control of FCM resources must be predictive due to the inherent delays in any adaptive satellite systems. These delays are functions of the system configuration. As a consequence, the real-time deployment of FCM techniques must be closely matched to the Ka band fading. The high frequency component of tropospheric scintillation cannot be neglected because it will induce channel estimation errors. Therefore hydrometeor attenuation and scintillation are the major effects to consider. Other losses such as gaseous absorption or all other processes may still be considered as constant and may be accounted for in basic link budget analysis.

As the conditions change dramatically from rainy to dry situations, only an adaptive model seems capable of tracking in real-time the non-stationary nature of the global fading process. Such a model can be devised using stochastic control theory and time series analysis tools.

1.5 Objectives and scope of the project

As a result of the preceding study, the aim of this project is to produce a novel model of a digital satellite link suffering dynamic fading with a particular emphasis on the real-time deployment of fade countermeasures in the presence of dynamic fading. The significance of such a study would be the accurate evaluation of realistic FCM systems performance in the presence of realistic Ka band fading. This will allow extension of known results and propagation models to include FCM controller limitations. Ultimately, this will offer the possibility to dimension and design appropriately FCM systems so as to meet long-term system specifications.

More particularly, the applicability of predictive control strategies for the regulation of satellite links operating at Ka band frequencies will be assessed. Although in the literature, predictive FCM control has been hinted at and/or proven empirically or by simulation as a more efficient way to counteract atmospheric effects, this has not yet been studied and characterised mathematically. The impact of time delays on overall system performance is therefore the prime focus of this thesis.

A real-time predictive controller will be developed using classical stochastic model identification techniques. The proposed solution is based on a self-tuning approach, which, to the knowledge of the author, is novel. The controller will be derived from and then applied to an experimental CPA time-series collected by the Rutherford Appleton Laboratory during the Olympus experiment. The outcome of this should result in a fully tested real-time algorithm suitable for realistic predictive FCM systems. To draw any long term performance, the predictor is coupled to a statistical model including rain attenuation, tropospheric scintillation and FCM controller-induced effects. The synthesis of typical fade events is also investigated in the light of possible simulations of FCM systems in real-time.

The analysis is applied to a typical star-shaped Ka band VSAT network. More particularly a well tractable low-power low-rate back-to-back VSAT link configuration is considered. In this document, an Adaptive Forward Error Control (AFEC) countermeasure has been studied on an in-bound link with focus on the impact of time delays on availability/throughput performances for digital satellite

systems. The impact of delays on the design of the predictive FCM controller is analysed numerically.

Finally, the inclusion of the instantaneous frequency scaling of rain attenuation and tropospheric scintillation is also considered within the context of predictive control of Ka band fades based on base-frequency fade detection schemes. In particular, a novel stochastic model of the instantaneous scaling factor of rain attenuation is introduced in Chapter 6. It accounts for the temporal random variations of rain drop size distributions and it is found to yield promising results.

The likely contribution of this work is to a greater understanding of the links between propagation effects and FCM design. While rain and scintillation need be considered (using known propagation models), the existence of time delays due to FCM system response time will change the statistical definition of the problem. These changes have to be quantified and they will depend on the prediction ability of particular predictors. To be justifiable, such predictors have to be matched in some way to the dynamics of the Ka band fading process. In this thesis, a minimum mean square error predictor based on an ARMA structure is shown to be well matched to the Ka band fading power spectrum.

Errors made by the predictor are system-based but they are essentially conditioned by the unpredictable nature of the Ka band fading process. Similarly, in the case of base frequency detection schemes, the stochastic variability of the instantaneous frequency scaling of rain and scintillation must be catered for in the design of efficient fade detection schemes.

Another source of estimation error of the actual fades are the measurements errors made by any particular fade detector like a beacon detector. These errors would include, for example, quantisation errors, extra thermal noise introduced by down or up conversion and filtering noise. These types of errors are also system specific but they are deterministic and are well known to design engineers **[1.16, 1.17]**. Therefore they have not been considered in this thesis, where a perfect detection of the fade level is implicitly assumed. Focus is solely placed on the impact

of the dynamics of the Ka band fading on the design of efficient fade detection/prediction schemes.

1.6 Contents of this document

The content of Chapter 2 is essentially a review of fade countermeasure techniques and their control. The description follows the structure and viewpoint of classical review papers (which are referenced where appropriate). Chapter 2 bears therefore little originality.

Chapter 3 is dedicated towards the statistical modelling of rain and scintillation through a back-to-back link using the concept of global fading, originally introduced by M. Filip and E. Vilar (see Chapter 3 for references). This latter was not introduced by the author and therefore the only original work lies in the fact that the global fading model has been applied to a particular satellite link, namely the Chilton-Olympus back-to-back test-case configuration. The format of Chapter 3 is very close to Chapter 2 of the original PhD work of Dr Filip in **[1.18]**.

Chapter 4 and those succeeding are believed to be novel work by the author. The objective is to identify and characterise statistically a suitable dynamic model for predictive countermeasure system. This is achieved in Chapter 4 by application of parametric identification methods and extension of the global fading model introduced in Chapter 3, so that FCM controller imperfections can be included in the modelling and design process.

Chapter 5 builds upon the modified global fading model which is then employed to derive different quantities essential to the design and performance analysis of FCM systems. These include, for example, required scintillation margins, code rate change boundaries, FCM utilisation factor, channel capacity utilisation and required scintillation margin. Two particular methods, namely the fixed and variable detection margin approach are proposed, analysed and then compared. With the fixed or variable margin approaches, the novelty comes from the fact that all these quantities and their time-delay dependence can be obtained analytically.

It is found in Chapter 5 that the variable detection scheme is the best suited for the Chilton-Olympus test-case example, that is a low-power low rate application based on adaptive forward error control as a countermeasure. Furthermore, this scheme allows the natural inclusion of instantaneous frequency scaling of both rain and scintillation. To achieve that, a new model of the instantaneous scaling of rain attenuation is proposed in Chapter 6. This model considers the impact of the variation of drop size distribution on the instantaneous frequency scaling of rain attenuation.

Chapter 7 is a discussion of the results obtained in the previous chapters and give the areas for further research work.

References

[1.1] M. Williamson, "How satcoms took off, the genesis of the communications satellite", *IEE Review*, Nov./Dec. 1991, pp 379-383.

[1.2] K.A. Hughes, R.G. Struzak, "Application of propagation data in system planning and frequency allocation", *Proc. Olympus Utilisation Conf., Vienna, 12-14 April 1989, ESA SP-292,* May 1989, pp 475-476.

[1.3] F. Carassa, "The evolution of satellite communications in the period between SIRIO and ITALSAT", *Rivista Tecnica Selenia*, Vol. 11, No 4, 1990, pp 6-15.

[1.4] A. Startelli, "The multibeam satellite payload", *Rivista Tecnica Selenia*, Vol. 11, No 4, 1990, pp 155-166.

[1.5] ESA, "Europe at the cross-roads: the future of its satellite communications industry", *ESA SP-1166*, Nov. 1993, 58 pages.

[1.6] L. Boying, H. Wenlong, "Air traffic control based on satellite", *Int. Conf. on Systems, Man and Cybernetics*, Vol. 2, 1992, pp 1163-1168.

[1.7] M. Mwanakatwe, M. Willis, B.G. Evans, "CODE: a Ka band Co-Operative Data Experiment for Olympus", *IEE Colloquium on Olympus Experiment,* 1987, pp 5.11, 5.16.

[1.8] A.K. Ghose, "VSAT Networks in India, Specifications and applications", *Int. J. of Satellite Comms*, Vol. 11, 1993, pp 211-216.

[1.9] M.W. Mitchell, R.A. Hedinger, "The development of VSAT performance standards in the USA", *Int. J. of Satellite Comms*, Vol. 11, 1993, pp 195-200.

[1.10] J. Salonen, S. Bull, "VSAT standards, status and applications in Europe", *Int. J. of Satellite Comms*, Vol. 11, 1993, pp 181-194.

[1.11] A.P. Gallois, "Fade countermeasure techniques for satellite communication links", *International Symposium on Communications Theory an Applications"*, July 1993.

[1.12] F. Davarian, "Earth-Space propagation research", *IEEE Comms Magazine*, April 1994, pp 74-79.

[1.13] L.W. Barclay, "The need for propagation studies", *Journal IERE*, Vol. 58, No 6, Sept.-Oct. 1988, pp S135-S139.

[1.14] E.M. Phillips, D.S. Pugh, "How to get a PhD, a handbook for students and supervisors", 2nd edition, Open University Press, 1994.

[1.15] V.I. Tartaskii, "Wave propagation in a turbulent medium", York: Dover, 1961.

[1.16] E.H. Satorius, L.H. Tong, "Analysis of a rain compensation algorithm for K/Ka band communications", *Int. J. of Satellite Comms*, Vol. 14, 1996, pp 297-311,

[1.17] N. Lay, K. Dessouky, "A communication protocol for mobile satellite systems affected by rain attenuation", *IEEE J. on Select. Areas in Comms., Vol. 10, No 6,* Aug. 1992, p 1037-1047.

[1.18] Miodrag Filip, "Adaptive modulation as a fade countermeasure", PhD thesis, University of Portsmouth, May 1992.

2. Fade Countermeasures

2.1 Introduction

Most satellite systems operating at C or Ku bands were designed to operate at an acceptable availability by implementing an adequate fixed power margin for the up and down link segments. Classical ways to achieve this are to increase the size of antennas or to increase the RF power of the transmitters in the communication chain. Such solutions, albeit simple in principle, are however constrained by regulatory, economic and practical limitations. For example, the admissible radiated power flux density is limited on the ground, whilst satellite power is limited by spacecraft size consideration. Increasing receiver antenna size is also directly detrimental to the trend towards small aperture terminals. High power transmitters will be a source of undesirably high levels of interference. As high levels of Ka band fading occur irregularly, a fixed compensation is inadequate. This would be particularly wasteful when it is applied when it is not required, namely during clear-sky (i.e. no rain) conditions.

In the previous chapter, the use of adaptive techniques at Ka band was hinted at as a better approach to cope with the large atmospheric attenuation encountered at Ka band. These methods are known as Fade Countermeasures (FCMs). In this chapter, the FCM strategies proposed in the literature are reviewed. A particular emphasis is initially placed on the equivalent power range achievable by each of the strategies, their possible domain of application and the basic engineering trade-offs they involve. The second part of this chapter describes practical implementation problems. Fade Countermeasures, which are adaptive, require a control algorithm which will allocate efficiently FCM resources according to the detected fades on a satellite link. Detection schemes and basic models for evaluating the performances of such algorithms are then introduced to provide a sufficient background for the next chapters. They will focus on the performance degradations brought by FCM controller imperfections.

If a countermeasure has to be deployed adequately, one must first obtain an accurate estimate of the total attenuation on a particular satellite link. The measurement error made by any device or system employed to evaluate the level of dynamic fading should be compensated for. Although very important to fade countermeasure design, this is not the objective of this thesis. Such considerations are specific to the system being considered and they can only be realistically understood while designing a real countermeasure system.

Once an accurate or corrected measurement of fades has been carried out, different operations need to be performed to evaluate the required level of FCM protection. Any FCM system will have a finite response time. Thus the Ka band fading must be predicted. Due to the randomness of the fades, prediction errors will be made and they need to be catered for. This is the main focus of this thesis. In the case of base-frequency detection schemes, the level of up-link attenuation must be inferred based on down-link attenuation. Thus the variability of the scaling factor of the fading process must be considered in the design of efficient FCM controllers. This is also studied in this thesis.

2.2 Fade countermeasure techniques

The high levels of attenuation encountered in millimetre wave satellite communications and the necessity to provide high link availability has required the development and detailed analysis of new strategies which allow a dynamic compensation of the fades. These techniques, known as Fade Countermeasures (FCMs), are control systems whose role is to compensate in real-time for the detected dynamic fades on a particular satellite link. This allows a more efficient utilisation of the overall system resources. Such an adaptiveness allows an approach of 'compensation only when and as required'. It should be opposed to the fixed power margin approach where compensation is offered even during clear-sky conditions. As a consequence, a saving or reduction in overall control effort can be achieved on a long-term basis, while still offering the desired quality of service. The savings, which designers want to maximise, depend on which adaptive technique is being used and lead to basic trade-offs which are discussed in this section. The FCM strategies may be classified in three different groups, namely, classical FCMs, adaptive transmission FCMs and reserve capacity FCMs **[2.1]**. In the latter, the saving in control effort can be re-invested for the compensation of other links which share a limited common resource within a multiple access environment (FDMA/TDMA). The various schemes to be described present different performance and complexity and their domain of application is dependent on the type of network and the type of service to be supported.

Some restoring techniques for overcoming severe attenuation have been devised and implemented successfully in the past and therefore, they may be referred to as classical methods. They generally are based on either a re-route strategy operating on a per-link basis (Diversity), or, simply accommodation of the fades by increasing adaptively the transmitted power or equivalent (e.g. Link Power Control). Respectively, these two approaches may also be classified in terms of their effects: the methods which improve the outage probability, or, the methods which improve the power margin **[2.2]**. Other more novel methods make use of more robust transmission techniques (adaptive modulation or coding) on a per-link basis or they may be incorporated in multiple access systems leading to common-resource FCM

strategies. We first start by discussing the different performance criteria and design issues which can be used to evaluate and possibly compare FCM systems.

2.2.1 Performance Criteria and Design Issues

Outage and Availability

A critical parameter specified for a VSAT network is the availability of its links, that is, the percentage of time that information can be transmitted and received with acceptable quality. For digital signals, the information quality is objectively described in terms of the bit error rate (BER) and carrier-to-equivalent noise-spectral-density ratio (C/N_o or CNR) at the demodulator/decoder input. The BER-C/N_o relationship is a function of modulation and coding schemes used. It is often supplied by the manufacturers in terms of BER and E_b/N_o which is the energy -per-(uncoded) bit-per-noise-density ratio. E_b/N_o (dB) and C/N_o (dBHz) are directly related using also the (uncoded) bit rate R (bps) using:

$$E_b/N_o = C/N_o - 10 \cdot \log_{10} R \quad \text{dB} \qquad \textbf{(2.1)}$$

An alternative way, which is widely in use in the satellite community, is to evaluate the system performance in terms of carrier-to-noise ratio **[2.3]**. In view of (2.1), this presents no great conceptual difficulty.

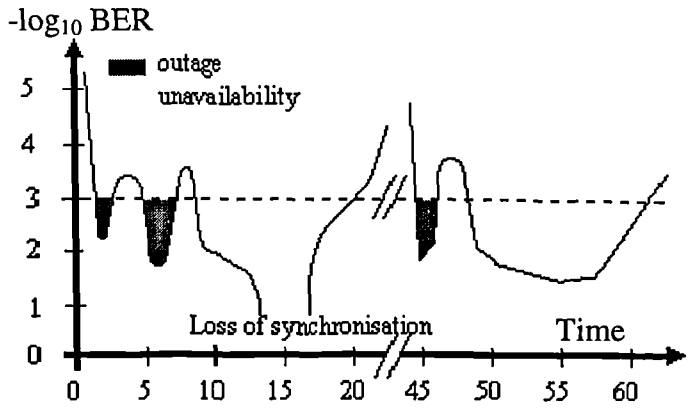

Figure 2. 1: Bit error ratio history for a particular link, showing outage times and unavailability times. The threshold BER is 10^{-3}.

According to CCIR/CCITT recommendations **[2.4]**, an outage event is said to occur in a digital receiver if its BER exceeds a specified threshold (typically 10^{-3}) for not more than 10 consecutive seconds. Outage time is the accumulated seconds for all outage events in a given time period, say a year. If the events lasts more that ten seconds, the link is said to be unavailable. This distinction between outage time and unavailability arises from the fact that digital trunks often lose framing when high BERs persist over a long period of time. The answer to such requirements must be expressed in terms of statistical models. In the real world, however, outage and unavailability are often used interchangeably. In the strict sense, radio unavailability is associated with long lasting events, like rain above 10 GHz, equipment failures and sun transit*. On the other hand, outages are associated with brief events like tropospheric scintillation. However such distinction is still beyond the reach of science. The most commonly used performance criterion is that the short-term bit error rate, typically, the one-second average BER, should not exceed some value depending on the service required.

The most reliable way to assess the performance for a given satellite system on a given slant path is to install the system and measure its outage time. This is also the most expensive one and is very time-consuming. This approach cannot readily be used in the all-important design stages, wherein alternative approaches are evaluated and compared. For this reason, practitioners and researchers must resort to obtaining statistical models for the Ka band fading channel and performing system studies via mathematical analysis, in the laboratory and/or the computer using these models.

Design issues

Designers are forced to design systems with only a low fixed excess margin of the order of a few dB. Fade countermeasure action, which is effectively a time-varying margin, has to be added in real-time on top of this low fixed excess margin, so as to cover for propagation impairment and maintain a certain grade of service.

---

* *Sun transit occurs when the sun is so close to the boresight axis of a directional antenna that the additional noise power generated by the sun causes the link to operate below acceptable quality. Such events may last a few minutes (up to 10) and can occur up to 12 times a year. This also depends on the orbit of the satellite* **[2.5]**.

The low excess margin is a safeguard ensuring good BER performance in clear-sky to very low attenuation conditions.

To be efficient, the FCM controller has to determine accurately when and how much time-varying effort must be provided by the FCM technique based on current measured channel conditions. In selecting the variable countermeasure margin which leads to the operating carrier-to-noise ratio for the system, the steepness of the BER vs. CNR curve must be kept in mind. Typically one dB in CNR produces about an order of magnitude in error probability. In the context of countermeasures, any channel estimation error, especially under-estimation of the real fades, will result in an error in estimating the BER, and the system may well operate below its specified performance. Impairment varies or may be uncertain. In order to ensure that performance does not become worse than the BER threshold, the designer usually insists on adding a few dB of margin to the required varying FCM control effort on top of the detected level of impairment. This is what is called a detection margin in this thesis. Two different schemes will be evaluated: a fixed and variable detection margin, to be added on top of the detected level of atmospheric attenuation. This added new (detection) margin is actually a central specification of any predictive FCM system and it is the focus of this thesis. It is mainly conditioned by the estimability/predictability of the rain attenuation and tropospheric scintillation processes. It will depend on:

- the measurement error in the detection and processing of the FCM control signal,
- the ability of practical systems at predicting the variations of the fades,
- the time delays in the control operations,
- the uncertainty in the prediction models used to scale in frequency the up-link attenuation.

The design of fade countermeasure systems should be seen as an optimisation problem once the link availability requirements have been met. FCMs are adaptive systems whereby the transmission is adapted to the channel fading conditions. It is then interesting to try to maximise the utilisation of the system resources. In the case of adaptive transmission systems like adaptive rate, coding or modulation FCMs, the objective is to maximise the user data throughput while meeting BER requirements.

This criterion can be used to compare and select the most appropriate countermeasure technique for any particular system based on adaptive transmission. Such optimisation has been carried out in **[2.6], [2.7]** under Rayleigh fading. Those two very interesting papers considered the optimum control rule for dual countermeasure systems based on adaptive power control and adaptive transmission rate via the use of Lagrange multipliers. The objective is to minimise the BER while satisfying an average throughput constraint. Although such mathematics can become very involved, such methods could well be applied to the less tractable Ka band systems via the use of computational algorithms for carrying out the optimisation. In the case of multiple access systems like adaptive TDMA, the optimisation consists in having each individual link using the common resource pool as economically as possible so that the overall system can support a maximum number of links at any time. This may be seen as a maximisation of the traffic through the satellite transponder.

2.2.2 Re-route strategies

Site Diversity

The high level of fading at Ka band is due primarily to the passage of convective rainstorms through the satellite link. Meteorological data showed that such events are generally limited in geographical extent and that the smaller the size of the rain cell the greater the storm. Site Diversity (SD) consists in setting up, to serve a certain location, two or more back-up ground terminals and a terrestrial link between them. Provided that the distance between the earth station and its back-up(s) is larger that the expected extent of the raincells ($\approx$ 10 to 15 km), the terminal with best reception is selected at any given time by a diversity processor (Figure 2.2).

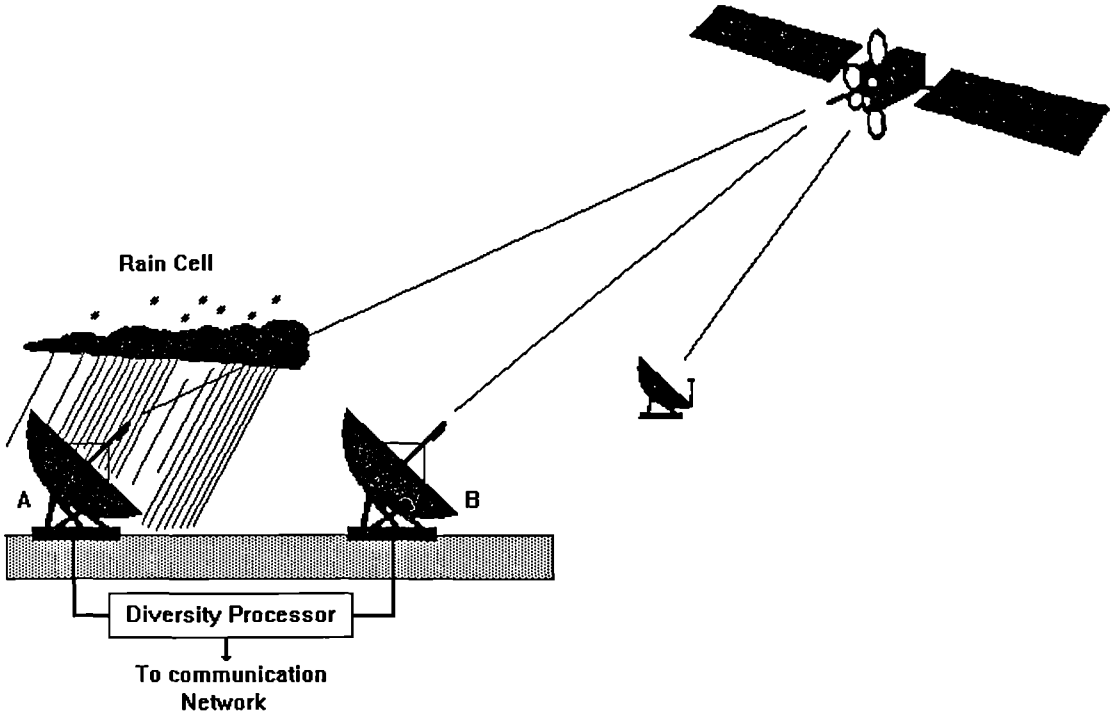

Figure 2. 2: Concept of Site Diversity.

To see the basic principle of SD, we shall investigate the simplified case of a dual site diversity link, where the rain distributions are identical but are statistically independent. In such a case, the probability of outage of the dual SD link with attenuation A_1 on link 1 and A_2 on link 2 is given by :

$$P_{out} = Prob\{A_1 \geq M_o \ , \ A_2 \geq M_o\} = Prob\{ A_1 \geq M_o\}.Prob\{A_1 \geq M_o\} = (Prob\{ A \geq M_o\})^2 \quad \textbf{(2.2)}$$

For large power excess margins, M_o, the probability of outage, $Prob\{A \geq M_o\}$, at one particular site being generally close to zero, the outage probability, P_{out}, of the dual SD link will be smaller than (or equal to) the single link outage probability $Prob\{A \geq M_o\}$ (length BC in Figure 2.3). Alternatively, and this is the most interesting aspect of SD as a countermeasure, for a same outage probability, the SD link will require a smaller power fixed margin than the single link system (length AB in Figure 2.3) therefore each single link can be designed with a smaller fixed excess margin.

Based on this principle, although total statistical independence between the different slant paths cannot be achieved, overall diversity gains of the order of 20 dB may be achieved during deep Ka band fades ([**2.8**]). SD is therefore one of the most powerful fade countermeasures and is particularly suited to high availability communication systems. Its main disadvantage is that a doubling of all the equipment is required* along with the purchase or rent of a second piece of ground. SD is therefore more suitable for systems where quality prevails over price. Clearly SD is not suitable for in-bound SCPC VSAT systems and/or low-rate/low-cost applications.

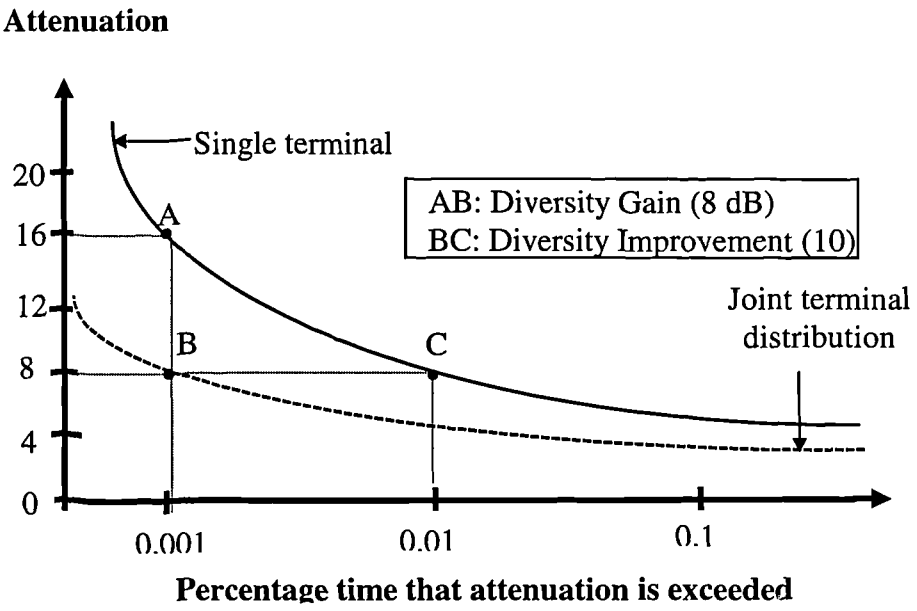

Figure 2. 3: Definition of diversity gain and diversity improvement for SD systems.

The evaluation of the performance of SD requires the knowledge of the joint distribution of attenuation amongst the stations. Some small-scale diversity models, derived from empirical data, have been proposed in the literature and cater for SD arrangements with typical site distances between 5 and 25 km [**2.9**]. They all predict a sharp increase of diversity gain for site distances up to 15 km while the improvement stabilises for greater distances. Some more refined empirical models, outlined in [**2.10**], allow more accurate inclusion of frequency, elevation angles and

* *for a dual site diversity system.*

baseline orientation dependent parameters. An interesting new model, based only on physical consideration was developed in **[2.11]**. It only requires the local rain rate distribution (measured at one of the two sites or using the ITU-R model) with the geometrical configuration and operational frequency of the SD system. It allows the determination of the bivariate distribution of dual diversity links. This model was tested against empirical data obtained from beacon, radiometer and radar data for frequencies up to 30 GHz and yielded results as accurate as the one obtained by the more classical Hodge model (**[2.9]**).

From a control viewpoint, SD is therefore an on-off type of control system. The diversity processor will choose the least attenuated signal from the real-time monitoring of the link performances. For the case of down-link diversity, this can be achieved relatively simply by measuring the power of the incoming signals on each of the SD down-links and the stronger one can be selected for effective communications. For up-link diversity systems, the problem is more complex due to the fade detection problem requiring a model of the instantaneous frequency scaling of rain and scintillation **[2.12]**. This will be extended later in this chapter since this problem is common to all FCMs applied to signal restoration on up-links.

Orbital Diversity

Orbital Diversity (OD) consists in setting up two separated spacecraft so as to provide two separate converging paths to a single ground terminal. Contrary to SD, OD is not based on the cellular properties of rainstorms, but rather exploits the statistical decorrelation between the two converging paths. As a consequence, the achievable gains of OD are only marginal, of the order of 5 dB. Measured data indicate an improvement factor (diversity gain/prime site attenuation) of the order 20 % (**[2.13]**, **[2.14]**) making OD quite unsuitable for Ka band systems. This technique is not a classical one, however it is mentioned here because it is based on the same philosophy as site diversity.

2.2.3 Equivalent Power strategies

In this section, strategies which are based on the direct increase of the carrier-to-noise ratio of an attenuated carrier are considered. This may be achieved directly by increasing for example, the power transmitted by a transmitting station on up-links, or by changing the gains of the spacecraft antennas for satellite down-links. Their analysis only requires radio frequency analysis of the link (i.e. typically link budgets) and is measured in terms of outage probability with the constraint of minimising degradations like interference and intermodulation.

Up-link Power Control

Up-Link Power Control (ULPC) is the most direct FCM technique of all. Its goal is to adapt the transmitted power to the attenuation of the affected link.

The philosophy is to counteract with minimum effort the adverse effect of fades. The basic strategy is justified by the fact that a built-in fixed power margin (very large at Ka band) is quite unsuitable during clear-sky conditions, since the earth-stations will generate a much higher power than what is effectively required. This would result in stations operating in clear-sky under heavy interference. The basic control algorithm used in ULPC is generally Constant Satellite Power-sharing (CSP) **[2.15]**, that is, the up-link fades are alleviated by keeping the input power to the transponder constant. The CSP control scheme does not compensate for down-link fades, so that a fixed down-link fade power margin should also be implemented.

In FDMA (Frequency Division Multiple Access), if the multi-carrier transponder is operated in the linear (i.e. backed-off) mode, an up-link fade results in a direct decrease of the overall CNR on a dB-dB basis, while the impact of down-link fades is much more limited and depends on the link balance **[2.16]**. The up-link fades can be overcome by individual compensation for each carrier by implementing ULPC at each of the transmitting earth stations. In single carrier operation of a saturated transponder, a decoupling of up and down link fades can be achieved with ALC (Automatic Level Control) of the transponder total power, thereby maintaining the satellite EIRP constant. For high link balance, up-link fades within the ALC range

have then little impact on the overall CNR which is only affected by down-link fades on dB-dB basis **[2.16]**.

The main advantages of ULPC are an improved link performance with a same earth station EIRP, a fixed carrier-to-interference ratio (C/I) within the ULPC range*, and no change in bandwidth or data rate, therefore it can be coupled with any other FCM technique. The principal disadvantage is that the earth station will not operate at maximum output power during clear-sky conditions, therefore the overall link is more sensitive to down-link fades. However, depending on the link balance, ULPC remains a very effective FCM, since generally up-link fades are the dominant source of link degradation. Within the context of VSAT operations, ULPC may prove necessary to ensure the required quality of service. However, cost considerations make ULPC a good candidate as an additional technique to be coupled with another FCM.

Spot beams

The signal received by a ground terminal can be increased during fade events by switching to a higher spacecraft antenna gain. This switching results in a narrowing of the antenna beam and a higher EIRP (Effective Isotropic Radiated Power). The reduction in serviced area may be resolved by implementing a multiple spotbeam coverage. This requires a multibeam satellite payload with complex antennas and payload architecture. Beam interconnectivity may be realised using advanced on-board baseband switching matrix technology **[2.17]**. This type of system is still very experimental at Ka band and the integration of spotbeam flexibility as a FCM, along with networking aspects, is still to be done. This type of countermeasure is not very suitable for VSAT systems since it is not really intended to cater for systems on a per link basis.

* *This is precisely why ULPC is advantageous over the fixed power margin approach*

2.2.4 Adaptive Transmission FCMs

While the methods described previously have a direct impact on the radio frequency analysis of the link (either by changing the fading statistics or the CNR), adaptive transmission techniques are more subtle and require the consideration of the modulation and coding schemes employed. They are based on the principle of maintaining the dimensionless ratio E_b/N_o to the value required to meet specified BER (Bit Error Rate) specifications**. This is achieved in an adaptive manner for FCM systems, with fundamental system parameters, like bit rates, code rate or modulation being varied according to the channel conditions. In that sense, this should be paralleled to the link power control strategy as a means to avoid the fixed power margin worst-case design, source of undesirable interference. In the context of adaptive transmission systems, the goal is transferred to maximising the gross data throughput while providing a BER quality of service. This class of FCM strategies is particularly suited to VSAT systems (especially in-bound links which are of interest in this thesis) since these are generally power limited. Also, they are only applicable to services where a variable data rate is acceptable. These techniques may be assessed using **[2.18]** :

$$\frac{E_b}{N_0} = \frac{C}{N_0} - 10 \cdot \log_{10} \frac{R_b}{\rho} - M_i \geq \left.\frac{E_b}{N_0}\right|_{rq@BER,\rho} = \left.\frac{E_b}{N_0}\right|_{BPSK} - G_c$$

Introducing the clear sky carrier-to-noise ratio, $\left.\frac{C}{N_0}\right|_0$ (dB.Hz), and the global attenuation, z (dB), accounting for rain and scintillation effects, we obtain:

$$\left.\frac{C}{N_0}\right|_0 - \left(\left.\frac{E_b}{N_0}\right|_{BPSK} - G_c\right) - 10 \cdot \log_{10} \frac{R_b}{\rho} - M_i \geq z \quad \text{dBHz} \qquad \textbf{(2.3)}$$

where $E_b/N_0|_{BPSK}$ is the energy per bit to noise spectral density ratio (dB) for uncoded BPSK, R_b is the information bit rate (bit/s), G_c is the coding gain of the code with rate ρ employed (dB), M_i (dB) represents the margins for good practical operation (such as margin for modem implementation). The ratio $R_s = R_b/\rho$ (symbol/s) is known as the symbol rate. The required bandwidth is $B = R_s/\Gamma$ (Hz), where Γ is the

** *The relationship between E_b/N_0 and BER depends on the type of modulation and forward error correction schemes used.*

spectral efficiency in bit/sec/Hz and is constant for any particular modulation scheme. In view of equation (2.3), a fade of A dB will increase the required CNR by A dB. Adaptive transmission systems will vary the system parameters on the left hand side in order to compensate for the fade, the clear-sky CNR remaining constant.

Adaptive Bit Rate Modems **[2.19]**

One of the most straight-forward ways to counteract atmospheric effects is to change the transmission rate (symbol and information bit rate) of the modulator/demodulator according to the fades while still maintaining the bit error rate below its minimum specified value. This implies, of course, that the current symbol rate is known to both receiver and transmitter at any one time. During clear-sky conditions, the symbol rate would be very high, and it would be reduced gradually as channel conditions are getting worse. For example, a reduction by 2 of the modulator symbol rate would increase the energy-per-symbol to noise-spectral-density ratio (E_s /N_0) by 3 dB, therefore offering an extra of 3 dB of protection against fades (Table 2.1). This is valid provided that the equivalent noise bandwidth is also reduced by 2 (since bandwidth = symbol rate/spectral efficiency). This is the major disadvantage of this type of countermeasure since such systems require bandpass RF filters with a variable bandwidth matched to the current symbol rate, in addition to a variable bit rate modulator. Although the total transmitted power remains constant, the power per unit bandwidth will also increase with lower data rate. This may lead to problem of interference and high intermodulation products. An equivalent power gain of 10 dB (corresponding to a moderate fade at Ka band) would require a reduction of the data rate by a factor of 10. Such dramatic reduction of the information rate may not be acceptable in most practical cases. Therefore adaptive bit rate FCM may be a candidate as an additional strategy to be associated with another main FCM. The last column corresponds to the minimum required clear-sky carrier-to-noise ratio calculated from (2.3) for z and M_i = 0 dB, uncoded BPSK at a BER of 10^{-7}. This will be used to compare the power requirements of adaptive transmission FCMs.

Data Rate (bps)	Gain w.r.t. uncoded BPSK (dB)	RF filter Bandwidth (Hz)	Min. Required $C/N_0|_0$ (dBHz) (Rq. BER=10^{-7})
9600	0	9600	51.3
4800	3	4800	48.3
2400	6	2400	45.3
1200	9	1200	42.3

Table 2. 1: Protection gain and filter characteristics of an adaptive transmission rate FCM (uncoded BPSK, ρ=1, max. bit rate 9600 bps).

Adaptive forward error control coding (AFEC)

Another digital method to counteract dynamic fades is to use adaptive coding systems, whereby redundancy overheads (i.e. code rate) are varied according to the channel, while the symbol rate of the modem is kept constant. This allows us to add extra correcting power as a fade worsens without needing variable filtering. This is achieved by changing the information bit rate proportionally to the changes in coding rate. Bearing in mind that a reduction in coding rate results in an increase in coding gain*, such AFEC systems can accommodate fades equal to the coding gain. The basic trade-off is thus reduction in throughput against fade compensation capacity.

Adaptive code rate as a FCM may be implemented with a bank of codecs, each with a specified code rate, possibly matched to the channel. However this method may prove very expensive. A more practical approach is to use puncturing techniques to provide adaptive code rate capability. This has been successfully applied to constraint length γ=7, 1/2 rate convolutional encoder/Viterbi decoder. The code has bits removed periodically prior to transmission according to a deleting map known to both transmitter and receiver. The deleted bits are then reinserted with a zero metric at the receiver. The choice of appropriate deleting map allows the generation of codes with rate $\rho=(n-1)/n$,$n \geq 2$ and can be found through computer search. It has been shown that such methods show little coding gain difference (0.2 dB) with convolutional codes with same rate ([**2.20**]). From a practical viewpoint, punctured codes can be implemented at low cost with a complexity

slightly greater than a that of a standard 1/2 rate code ([2.21]). The performance of punctured codes of rate 1/2, 3/4, 2/3, 7/8 are given in Table 2.2.

code rate	coding gain (dB)	Data throughput w.r.t. uncoded BPSK (%)	Min. Required $C/N_0 I_0$ (dB.Hz) (Rq. BER=10^{-7})
1	0	100	51.3
7/8	3.8	87.5	47.5
3/4	4.4	75	46.9
2/3	5.0	66.66	46.3
1/2	5.6	50	45.7

Table 2. 2: Coding gains, data throughputs and power requirements relative to the uncoded case for different punctured codes (BER =10^{-7}, BPSK, Rb/ρ=9600).

They were estimated assuming a total degradation of 0.4 dB accounting for 8-level soft quantisation and punctured coding effects relative to original γ=7 convolutional codes of the same rate with infinite quantisation. One can notice that the coding gain is limited to about 5.5 dB. This may be substantially improved by using convolutional codes with lower code rates or with greater constraint lengths. The latter would be at the cost of an increased decoder complexity.

Relatively simpler decoders, with greater coding gains, may also be achieved using concatenated codes (while still keeping the symbol rate constant). They are based on the principle of applying two levels of coding/decoding in succession. The inner code is usually chosen to be low rate while the outer code is generally a Reed-Solomon code tuned to the inner code in order to yield good overall coding gains. Such coding schemes have been analysed and compared in [2.22] and [2.23]. A high gain code with K=7 1/2 rate convolutional codes as inner code, and a (127,111) Reed-Solomon code as outer code, was identified in [2.22]. It can provide a total gain of 10.5 dB at a BER of 10^{-5} for a throughput of 43.7% w.r.t. to the uncoded case. A simple adaptive system would thus operate only with the inner codec for moderate fades (5 dB, throughput 50% w.r.t. uncoded) while the outer codec would be

* *Roughly $G_c \approx 10.\log_{10}(d_{free}.\rho)$ for convolutional codes (d_{free} is the free distance of the code).*

activated for higher fades providing protection up to 10 dB. Throughput can be optimised by introducing further 'code rate' adaptiveness with a variable punctured convolutional code (as the one described previously). Concatenated codes may thus provide the high coding gains required for Ka band fading at the expense of a double codec system.

Adaptive fade spreading

Adaptive fade spreading refers to systems making use of spread-spectrum techniques with a variable information bit rate according to the fades **[2.24]**. In such systems, the user data is multiplied by a pseudo random binary sequence (PRBS) with fixed chip rate matched to the available spread-spectrum bandwidth. This has the effect of spreading the power spectrum of the information data over the spread-spectrum bandwidth (the total power being the same). This signal is transmitted over the channel after modulation, frequency up-conversion and fixed* bandwidth RF filtering. The signal is then de-spread at the receiver by multiplication with a coherent replica of the original PRBS sequence. The signal is finally low-pass filtered at baseband frequency to recover the original user information. The information data rate being variable, this operation must be carried out using variable bandwidth filters, tuned to the information data rate. A main difference with the adaptive bit rate modem approach, is that the variable bandwidth function must be provided here at baseband and not at RF frequencies, therefore substantial cost savings can be made knowing also that a fixed rate modulator is required. The spectral density characteristic makes spread-spectrum ideally suited for Frequency Division Multiple Access (FDMA) systems. Low levels of power per unit bandwidth allow to operate satellite transponder near saturation in a frequency plan where intermodulation is minimised. The gains that can be made using fade spreading result from the noise power rejected by the low-pass filter and can be shown to be equal to the processing gain of a classical Direct-Sequence Spread Spectrum (DS-SS) system given by:

$$G_c = 10 \cdot \log_{10} \frac{Rp}{R} \text{ dB} \qquad \textbf{(2.4)}$$

*since the chip rate of the PRBS sequence is constant.

Rp and R (in bit/sec.) are respectively the chip rate and data rate. Thus in a fade spreading system, the variable gain is achieved by changing the data rate or equivalently the spreading ratio. Typical gain performance are shown in Table 2.3. Note that a spreading ratio of 1 corresponds to the situation where the information data is merely scrambled and no spreading is made.

Apart from the trade-off of coding gain versus throughput, inherent to all adaptive rate FCMs, a major disadvantage is that the E_b/N_0 ratio is fairly small at the input of the demodulator, due to the spread-spectrum operation. This may have drastic effects on symbol timing recovery and phase recovery ([**2.24**]). As a consequence, spread spectrum techniques are less attractive than adaptive coding or adaptive modulation countermeasures to be described in the following section.

Data Rate (kb/s)	**Chip Rate (kb/s)**	**Spreading ratio**	**LPF Bandwidth (kHz)**	**Fade Tolerance (dB)**	**Throughput w.r.t. uncoded (%)**
2048	2048	1	1434	0	100.00
1024	2048	2	717	3	50.00
512	2048	4	358	6	25.00
256	2048	8	179	9	12.50
128	2048	16	90	12	6.25
64	2048	32	45	15	3.12

Table 2. 3: Coding gains, and data throughputs relative to the uncoded case for a typical fade spreading system

(The low-pass filter bandwidth was calculated using 1.4.*R/2).

Adaptive modulation

Adaptive modulation schemes, like adaptive PSK (APSK) or adaptive QAM (AQAM) allow design of the link so as to maximise the transmitted information rate over a bandlimited channel while maintaining a specified value of BER. This is achieved at the expense of E_b/N_0 and therefore assumes that sufficient resources (i.e. power) are provided during clear-sky conditions. For the same BER, the adaptive modulation strategy is therefore appropriate for medium to high power applications,

while AFEC countermeasure is more appropriate for more power-limited links. For the same power characteristic, AFEC would have a better availability than adaptive modulation, but the latter would have a greater throughput. These two approaches are in contention, and the basic selection can be made by asking which constraint, may it be throughput or availability, is paramount to the system design and thus should be maximised.

If the required BER availability is met under fading with the more robust modulation (e.g. BPSK in APSK), then substantial improvement in data throughput can be made by using adaptive modulation **[2.25]**. The basic principle of adaptive PSK modulation is to use high-order PSK schemes during low-fade conditions and decreasing the modulation complexity with increasing fades. Of course the reverse operation must also be provided. This is made assuming a constant RF bandwidth. For M-PSK, the spectral efficiency is $\Gamma = \log_2 M$ (b/s/Hz) where M denotes the M-arity* of the PSK modulator. The bandwidth** is $B = R_s/\Gamma = R_s/\log_2 M$ yielding $R_b/\rho = B.\log_2 M$. Thus for increasing M, the information bit rate can be increased by factors 1,2,3... for M=2,4,8. This shows how throughput may be improved by using more complex M-arity. As higher M-arity require higher E_b/N_o, this is only feasible whenever atmospheric conditions improve and depends on the clear-sky carrier-to-noise ratio. The estimated performance of M-PSK are given in Table 3.3 for a BER of 10^{-7}. If 32-PSK *is capable* of ensuring a BER of 10^{-7} for clear-sky conditions, then the achievable equivalent power gains are given in the fifth column.

---

* *where M is the number of phases used.*

** *where the bandwidth is null-to-null.*

Modulation	Bits per symbol	Min. Required $C/N_0\|_0$ (dBHz) (Rq. BER=10^{-7})	Throughput (%) w.r.t. uncoded BPSK	Fade Protection Margin (dB) of a APSK*
BPSK	1	51.3	100	19.7
QPSK	2	54.1	200	16.9
8-PSK	3	59.4	300	11.6
16-PSK	4	65.1	400	5.9
32-PSK	5	71.0	500	0

Table 2. 4: Equivalent power gains and data throughput relative to the uncoded case for an uncoded APSK system(BER=10^{-7}, R_b =9600 bps max.).

The implementation of adaptive modulation relies on the possibility of designing an adaptive modulator/demodulator to support all the provided modulation schemes. This is demonstrated in **[2.26]** using direct digital synthesis techniques (DDS) where the authors describe a system capable of handling both M-PSK and QAM constellations. They show more particularly that the implementation of a modulator does not present great conceptual difficulty. The concept of an adaptive demodulator is also introduced and they discuss the problem of a universal carrier recovery loop for both PSK and QAM signals using digital signal processing.

2.2.5 Shared-Resource FCMs

Another important approach is to counteract atmospheric effects without reducing the information throughput as was the case for adaptive transmission systems. This can be done using a shared-common resource within a multiple access environment. This reserve capacity is dedicated to the compensation of affected transmissions while the data rate, as seen from the user, remains constant. Since generally the fades on different links are not totally correlated, this reserve capacity can be shared amongst the stations of a distributed network. It can be allocated 'on demand' according to the adverse conditions whenever the small link power margin of each individual link is exceeded. A major issue for such systems is the dimensioning of the shared-resource and the choice of a fixed power margin such as to ensure specified availability and maximum throughput. This is dependent on the

* *supporting 32-PSK during clear-sky conditions i.e. $C/N\|_0 \geq 10log(9600)+11.3+1$ 9.7 = 71 dB.*

joint fade statistics at the various sites, the number of earth-stations and the traffic distribution within the network **[2.27]**.

Adaptive TDMA (A-TDMA)

Adaptive Time Division Multiple Access, also known as Burst-Length Control (BLC), is a shared-resource technique based on variable transmission rate methods. The back-up capacity consists of a fraction of the frame interval. Whenever the attenuation exceeds the small fixed power margin (M_0) on one particular link, this link is assigned on demand a number of back-up time slots for additional protection. These spare time slots are used as additional burst time intervals during which extra coding information and/or reduced transmission rate data can be transmitted. The achievable total fade protection margin is given by **[2.27]**:

$$M = M_0 + 10\log_{10}H + G_c \quad \text{dB} \qquad (2.5)$$

where H is the energy gain and G_c is the coding gain.

For example, a 1/2 rate convolutional code and BPSK, Viterbi decoded, provides a gain of 5.6 dB at a BER of 10^{-7} w.r.t. uncoded BPSK. If the code rate is 1/2, then the symbol rate $R_s = R_b/\rho$ is increased by two. To operate at fixed bandwidth ($B\Gamma = R_s$) and fixed transmission time, the symbol rate must also be slowed down *at least* by 2 by increasing the symbol duration by a factor H=2. Thus the achievable extra fade protection would be 8.6 dB for H=2, 11.6 dB for H=4 etc.

A major impairment is that A-TDMA is particularly inefficient if it is to compensate for both up and down link fades in the network at low unavailabilities. This comes from the fact that up-link fades are usually very large, thereby requiring a large portion of the total frame interval. Also, the proportion of the shared-resource used for down-link compensation would be comparatively very small. An accepted approach to avoid this, is to use up-link power control to compensate at least partially for up-link fades. This has the effect of reducing the required size of the shared resource and leads to greater throughput efficiency. The performance of such a system, ULPC/A-TDMA, has been evaluated in **[2.28]**. It is based on a simple model for predicting the joint statistics of a distributed system over different zonal regions of diameter between 250 and 4000 km. It was found that, for 100 stations, the back-

up resource should represent 30 to 60 % of the overall frame, depending on the area considered. Another model for application to an ULPC/A-TDMA is presented in **[2.29]**. It is based on a large scale quadruple site diversity model and gives a good description of the FCM control algorithm.

Dual-band frequency diversity **[2.30-2-31]**

Dual-band or cross-band or Frequency Diversity (FDV) is an adaptive fade countermeasure applicable to the case where the links can operate in two frequency bands, typically a high frequency band like the Ka band and a low frequency band like the C or Ku band. Most of the traffic is carried in the high frequency band under low-fading conditions. When the small fixed margin on one particular link is exceeded, the traffic on that link is switched to the lower frequency band, which serves as a back-up resource. The attenuation at the lower frequency being smaller than at the higher, a substantial equivalent power gain can be achieved. Similarly to A-TDMA, the back-up resource can be shared since on the average, the probability of simultaneous back-up demands is low for spatially separated sites. In **[2.32],** a system using the Ka band for main traffic and the Ku band as back-up. The author found that FDV can provide gains of the order of 15 to 20 dB with a back-up band equal to 10% of the total Ka band bandwidth. Obviously this strategy is reserved to FDMA systems, and its main disadvantage is the need to duplicate the RF equipment, adding substantial cost overheads.

Common resource Site Diversity

As mentioned earlier, the main disadvantage of site diversity systems is the need for the duplication of the earth stations. The larger the ratio of back-up stations relative to the total number of station the higher is the cost The duplication cost can be reduced by implementing a shared resource site diversity system where the back-up station(s) is shared amongst all the stations belonging to a same network **[2.32]**.

2.3 Adaptive transmission as a fade countermeasure

In this section, we discuss a typical VSAT application where adaptive transmission techniques, like adaptive forward error control coding and adaptive modulation as fade countermeasures, are particularly suitable. This will allow us to understand better the implications and requirements of FCM systems, which need to be integrated with existing system architecture. Let us keep in mind that such FCM systems are applicable to variable user data rate applications and therefore they must be very low cost and standard compatible to be attractive. The system to be described matches this constraint by offering cheap VSAT stations, while the complexity is translated to the Hub station. Although a single network will be described, the Hub may be shared amongst networks thereby allowing to share this extra cost.

2.3.1 General System Architecture [2.33]

A simple and cheap VSAT network configuration is shown in Figure 2.4. It is based on a star-shaped architecture and is similar to the architecture of the CODE experiment **[2.34]**. This type of two-way network is particularly suited to small to medium corporate networks with central offices. Information from the remote sites can be gathered at the central site (Hub) via the in-bound link, while information can be distributed to the VSAT terminals via the out-bound link. Also, the Hub may be used as a relay, if communication between two VSATs is required.

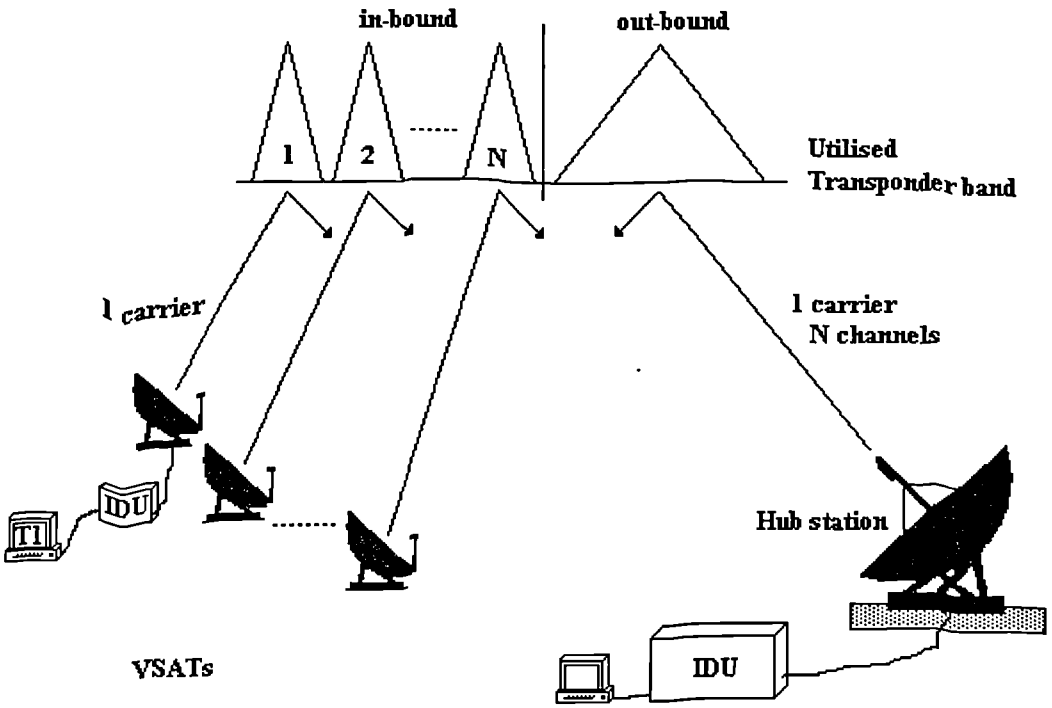

Figure 2. 4: FDM-SCPC in-bound/ TDMA outbound star-shaped VSAT network.

The network comprises N VSATs, a Hub and an FDM* access to the satellite transponder. Each VSAT can support 1 terminal via 1 carrier and access the satellite transponder on the corresponding VSAT channel at up-link frequency (30 GHz). As only one remote terminal per VSAT is supported, only one modulator is needed making this configuration particularly cheap. N down-link carriers (20 GHz) being received at the Hub, N demodulators need to be provided.

The central Hub ensures full interconnectivity between each of the VSATs terminals via a Time Division Multiplex (TDM) scheme, which is then transmitted on one MCPC outbound carrier at up-link frequency (30 GHz). Thus only one modulator and one demodulator are needed at the Hub and each VSAT respectively.

In the context of the CODE experiment, the system can support ULPC/Adaptive TDMA on the outbound link and Adaptive FEC (and possibly Adaptive Modulation) as countermeasures. Link condition is assessed by beacon monitoring at a rate of 1 Hz **[2.34]**.

* *FDMA if frequency agility is provided.*

2.3.2 Adaptive transmission FCM system

For economical and practical reasons, adaptive coding or modulation systems as countermeasures are well applicable to SCPC in-bound links. Both strategies assume that the symbol rate is constant, therefore they are introduced at the expense of a reduced information rate. Such a system should comply to the OSI/ISO (open system interconnection) reference for compatibility purposes and thus data should be organised in packets or frames. This is shown in Figure 2.5.

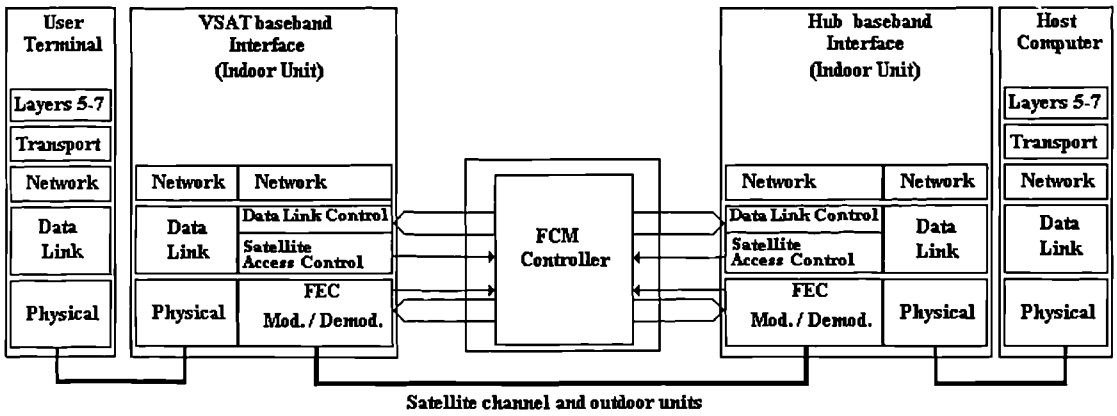

Figure 2. 5: OSI model for a VSAT network with adaptive transmission fade countermeasure.

For satellite links having longer time delays and larger bit error rates, protocols designed for terrestrial links may prove unsuitable. The VSAT and Hub baseband interfaces allow protocol conversion (emulation) to cater for the different needs of terrestrial and satellite links **[2.33]**.

If the conversion is adequate, end-to-end transparency will be maintained and the end user will have the impression of being directly connected.

In this example, only the three lower layers of the OSI/ISO model are emulated. The network layer conversion can perform address mapping enabling network addresses to be different from terminals addresses while still routing packets from the source to the desired destination.

The emulated data link layer allows 'data link control' ensuring reliable transfer of framed data across the physical satellite link, with a decoupling with the data layer of the terminals. This involves essentially addition of header/trailer bit

sequences used for frame identification, synchronisation, error control and flow control. Due to long round trip times over satellite links, detection of damaged, lost or duplicated frames can be achieved efficiently by a sliding window ARQ protocol **[2.33]**. 'Satellite access control' deals with the access to the satellite transponder resources via multiplex/multiple access techniques. This will depend on whether Demand Assignment (DA) or Fixed Assignment (FA) is employed and should be matched to the expected traffic demand **[2.35]**. Within the context of the CODE configuration, the received out-bound information is based on adaptive TDMA as a FCM, so that information+back-up TDMA sub-bursts should be demultiplexed appropriately from the bit stream out of the VSAT FEC decoder. If frequency agility is provided on the in-bound link then extra satellite access protocol must be added.

The adaptive modem or adaptive codec* form the basis of the adaptive user transmission system at the physical link layer. Also, channel specific measures may be implemented for appropriate formatting of the data stream prior to transmission on the satellite link. This may include, for example, data interleaving for burst error cancellation at the output of the FEC codec.

The FCM controller is the heart of the FCM management unit. It must operate closely with Hub and VSAT baseband interfaces. More precisely it must interact between 'peer' physical and data link layer levels of both Rx and Tx. A centralised FCM management at the Hub should be preferred since it is easier to perform for star-shaped network and it shifts the complexity from VSATs to Hub, thus reducing the terminal costs **[2.35]**. The main functions to be supported are:

- link conditions monitoring and detection of current system settings,
- signalling of service communication between Rx and Tx baseband interface within the OSI framework,
- allocation of FCM resources/Satellite resource access assignment,
- synchronisation and switching of FCM and satellite access resources,
- alarm and error control management.

* *In practice, they would be mutually exclusive, i.e. only one of them may be adaptive, the other being fixed.*

2.3.3 FCM control protocol

The objective of the FCM controller is to ensure that good quality data can be passed between host computer (Hub) and user terminal (VSAT) over the satellite channel. Due to the structure of the OSI model, reliable data with specified BER must be provided at the data link level. A suitable data link protocol must be defined so that the frames are successfully transmitted via the use of the sliding window ARQ protocol (due to round trip delays) in conjunction with the FCM (AFEC or A-modulation). Such an algorithm is described below.

In normal mode of operations, the bit error rate at the output of the Rx FEC decoder will be small (typically below 10^{-7}) and thus correct unpacking of data frames can be performed. The Rx then tests the integrity of the frame by testing checksum bits in the trailer of the frame.
If the frame is error-free, an acknowledgement (ACK) is sent to Tx via the feedback channel. If there is a frame error, then no acknowledgement is transmitted. The absence of ACK signal in a given time limit will be detected at the Tx side on its return link and then will initiate a re-transmission of the faulty frame. The process is repeated for a specified number of times until successful reception of the frame. If still not successful, the FCM controller will initiate (if applicable) a 'FCM switching' procedure to a more robust level of FCM protection. This is repeated until successful reception or total communication failure.

Every second, based on the detected propagation sounding and the current system settings, the FCM controller evaluates whether an 'FCM switching' to a more or less robust level of FCM protection is feasible. If 'yes', an appropriate 'FCM switching' procedure is launched otherwise the FCM protection level is kept the same.

The 'FCM switching' routine must ensure that a transmitted frame is properly demodulated/decoded at the receive end. As a consequence, Hub and VSAT must not only know the current levels of FCM protection used for the in-going frames, but also they need to 'prepare' (since FCM level switching is not instantaneous) to switch to a new level of protection by being notified *in advance* of the level to be

used in the *nth* frame after the current one (e.g. n=1 if the FCM switching lasts less than one frame duration).

The FCM switching must equivalently be initiated based on information on the predicted channel conditions obtained from channel sounding at both Hub and VSAT. The prediction horizons must be matched (rounded up) to the estimated round trip delay including subsystem response times, hop delays and response time penalty introduced by the FCM control protocol. This would allow to cover for the possible change in propagation effects during the total round trip delays of the FCM system.

In a centralised FCM control system, where the controller is at the Hub, the 'in advance' notification for the outbound link can be transmitted as soon as the FCM controller has made a decision, along with the predicted FCM assignment made to the in-bound transmitter.

For the inbound link, VSAT needs to notify in advance the effective level of FCM protection currently to be used (this should be the same as the one dictated by the controller) as well as a predicted FCM protection level request based on detected channel conditions, so that the FCM controller can make appropriate decision.

In some instances, during severe level of fades and/or wrong estimation/prediction of the channel conditions, the BER out of the Rx FEC decoder will not be small enough, and all the frames will be received in errors. This repetition of successive faulty frames (and possibly the total absence of frame) must be detected at the Rx after a specified duration, so that the FCM controller can switch into an outage recovery mode. In such a situation, there is partial or total service communication failure between Rx and Tx of both Hub and VSAT, which thus may well become out-of-step and de-synchronised **[2.34]**. The FCM controller has to make out what is the best decision so as to restore as soon as possible the service communication in both direction of the VSAT/Hub link. This decision must be based on the partial information available at Hub and VSAT.

As seen from the Hub, a high BER (or equivalent) may be detected on the received inbound data link. The atmospheric fade for the satellite to Hub (denoted hereafter SAT/Hub) link is accessible via beacon monitoring/frequency scaling, thus Hub will know whether the fade is on the SAT/Hub link or not. Appropriate ULPC

will thus always be possible on the Hub/SAT outbound link (in the limit of the ULPC range). The Hub will not know the exact depth of the fade on the VSAT/SAT link. The FCM controller will thus have to allocate 'arbitrarily' a suitable FCM level of protection for the SAT/VSAT outbound down-link. For the CODE system, this involves for example the allocation of extra time slots for extra coding for protection on the outbound link. As the common resource is shared, this A-TDMA FCM allocation should only be provided for a certain duration. This duration should correspond to the one expected from fade duration statistics at the last correctly received attenuation level transmitted from VSAT to Hub. During that time, the Hub would try to transmit a service command to VSAT transmitter for selection of its most robust of FCM protection for the inbound link. If by the end of this period, the inbound link is still in failure, the outbound downlink FCM would be resetted back to a default level until good communication is restored on the inbound link. The inbound receiver of the Hub would then enter a re-acquisition mode.

Similarly the VSAT has access to its own beacon estimation/prediction for the VSAT/SAT link. If the received outbound BER (or equivalent) at the VSAT is high, the FCM assignment for the inbound transmitter will not be received and thus the VSAT transmitter should switch to its most robust level of protection so as to ensure good service communication to the Hub. This would be used to notify the controller that a bad estimation of the channel fade was made previously ant that more effort from Hub is necessary on the outbound link. If after a certain time, the outbound link is not restored, VSAT inbound transmitter should enter a re-acquisition mode.

The re-acquisition mode would consist in regaining bit/symbol/carrier synchronisation on inbound and/or outbound links.

2.3.4 Combination of ARQ and FCM strategies

The main aim of fade countermeasure systems is to deliver safely data at the physical link layer. In order to lower down even further the error rate over the satellite channel, as it would be required for data communications, it will probably prove essential to couple any particular FCM with an Automatic Repeat Request, or ARQ, strategy. In such a case, the problem translates to the safe delivery of data packets or frames over the satellite link , without lowering excessively the

throughput. This implies that a suitable co-ordination between the ARQ and FCM techniques is achieved. As a consequence, the design of efficient fade control algorithm should also consider the protocol issue for agencing efficiently both ARQ and FCM strategies **[2.36]**.

The development of predictive fade control, as described so far in this chapter, assumes that the channel conditions are being monitored by measuring the strength of a pilot tone. In most cases, like ULPC, SD, FDV or adaptive transmission rate FCMs, this causes no problem at all and therefore, these countermeasures permit the implementation of predictive fade control, as described later in this chapter. However for some other techniques, like AFEC or APSK, the implementation of predictive FCMs may prove unnecessary, depending on which and how ARQ and FCM are interlinked together. This essentially depends on whether the ARQ and FCM are operated in a decoupled mode or not.

For example, in a decoupled mode, an AFEC technique based on punctured convolutional codes would be operated based on the predicted channel conditions, while the ARQ strategy would be operated independently based on the detected errors of the linear block code used for CRC testing. In such a case, the satellite faded channel with the AFEC countermeasure would be seen by the ARQ as a Super Binary Symmetric Channel, or SBSC, (interleaving would be most certainly required for removing burst errors). A similar reasoning could apply to APSK.

The combination of ARQ and AFEC techniques has been the subject of much research in recent years, and some very efficient Hybrid ARQ (HARQ), have been proposed in the literature. One such ARQ/AFEC scheme was proposed, for example, by Hagenauer in **[2.37]**. However, for these systems, the changes in code rate of the punctured convolutional code are conditioned by the decision made by the ARQ strategy, and therefore, they make more difficult the implementation of predictive fade control.

A related issue is that the operation of FCM may require the transmission of FCM service information on both forward and backward link, so that accurate

synchronisation, call set-up and relinquishment and fade detection can be performed in real-time. As a consequence, the organisation of the packets, i.e. the inclusion of FCM specific service information and associated protocolling issues may be seen as integral part of the FCM control algorithm **[2.38-2.39]**.

2.4 FCM control

FCM control refers hereafter to the necessary operations that need to be undertaken so as to deploy efficiently the fade countermeasure system based on detected attenuation (see Figure 2.6). This control scheme should be designed to meet long-term design specifications. In the case of adaptive transmissions systems, this would be defined in terms of availability and data throughput. Therefore FCM control should result in a practical real-time algorithm, with fully characterised long term performance in the presence of Ka band fading, i.e. including both rain and scintillation processes.

The main functions that need to be supported by any FCM controller are outlined in Figure 2.6 along with their dependencies on propagation and system parameters. In this thesis, focus will be placed on the three shaded boxes, namely short-term prediction, fade detection rule and fade control rule for an AFEC countermeasure. More particularly, the impact of time delays and the variations of instantaneous frequency scaling, on each of the mentioned three operations, will be analysed.

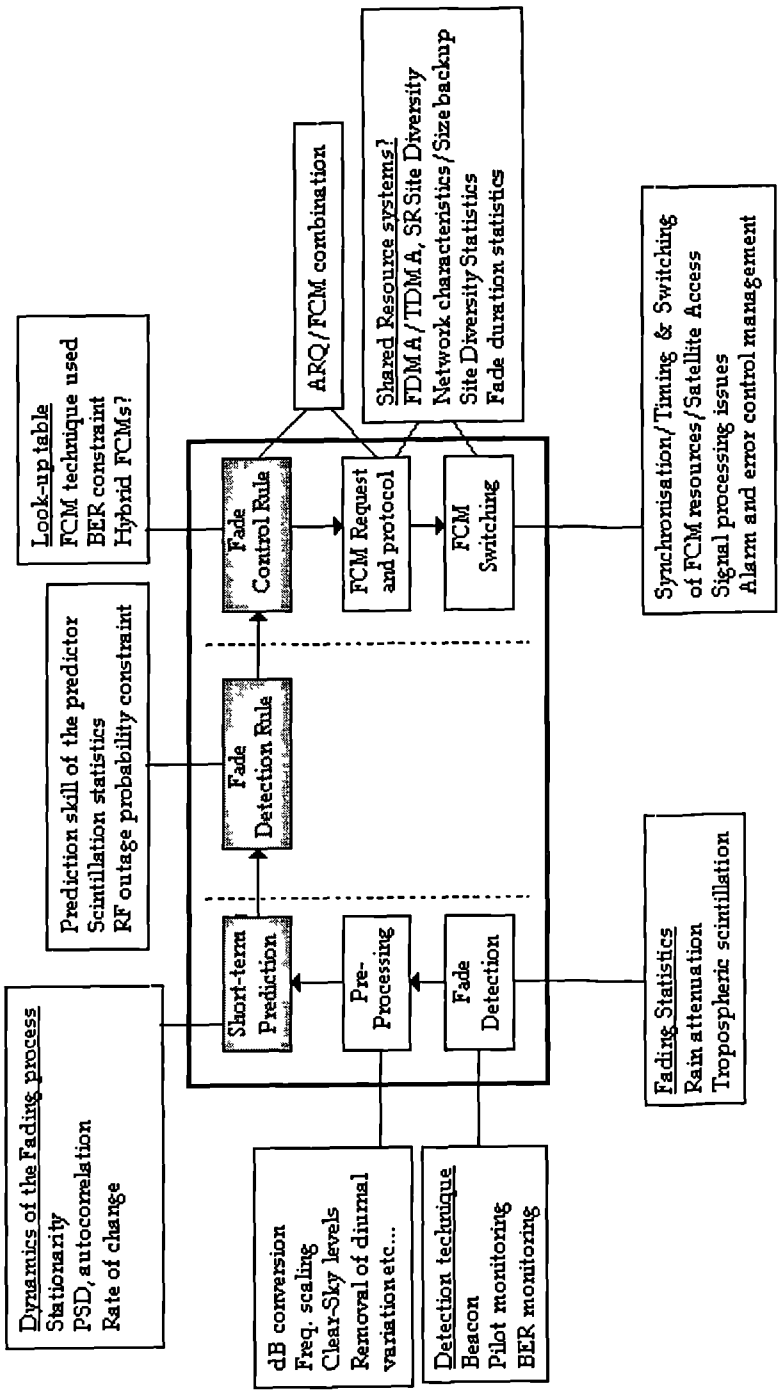

Figure 2. 6: Basic operations required for control of FCM resources.

2.4.1 Fade detection systems

The real-time deployment of fade countermeasures requires monitoring the time-varying link so that the appropriate counter-action can be taken. This is the fade detection problem. Depending on the detection method, FCM systems, which are basically control systems, may operate either in open loop or closed loop **[2.12]**. The different detection configurations may result in different complexity, and therefore different cost. As this thesis is concerned with VSAT systems, the cheaper or more interesting options will be pointed out in the context of a 30/20 GHz system for up and down links respectively.

Total link attenuation can be measured by monitoring a beacon at the earth-station. Hence a (cheap) beacon receiver must be used for this purpose. As the attenuation is inferred on a close but independent slant path as the one carrying the information, this method is an open loop one.

Down-link beacon monitoring [2.12]

A commonly accepted approach is to monitor a beacon at a frequency close to the down link frequency (i.e. 20 GHz). This has the advantage that a single LNA/down converter can be used for communication and fade detection purposes. However, in order to infer the attenuation on the up-link, it is necessary to solve two problems. The first problem is to determine the clear-sky level of the received beacon (if not known) so that the absolute total attenuation level can be evaluated accurately by straight difference.

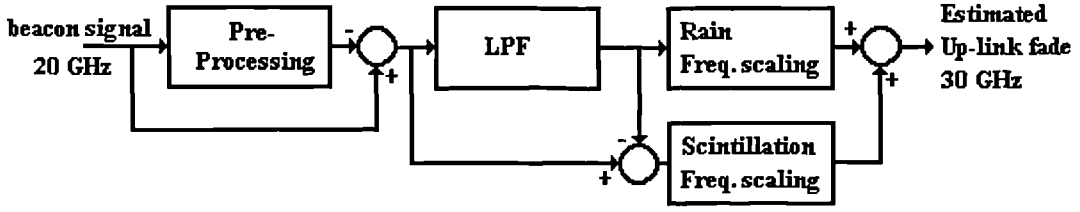

Figure 2. 7: Fade detector for down-link beacon monitoring system in the presence of rain and scintillation.

The evaluation of the up-link fade requires the frequency scaling of the total attenuation. The second problem is that the different components of the total fading process, essentially rain and tropospheric scintillation, do not scale in the same way. Therefore an efficient scaling can only be performed if both components are first separated, then scaled individually according to their particular scaling rule, and then recombined together. Also related is the fact that hydrometeor attenuation (rain+clouds) is a slow-varying non-stationary random process, while scintillation is a fast-varying quasi-stationary process. As a consequence the instantaneous frequency scaling for both components will be time-varying and stochastic. A typical fade detector applicable to down link beacon monitoring is depicted in Figure 2.7.

Up-link beacon monitoring

A simpler method is to monitor a beacon at a frequency close to the up-link frequency (i.e. 30 GHz), thereby avoiding the need for scaling in frequency the components of the Ka band fading. The fade detector still needs however to estimate the clear-sky beacon level for evaluating the absolute fade level. This method is probably more accurate than the previous one, however it is more expensive since a second LNA/down converter is needed at the receiving end **[2.12]**.

Carrier-to-noise ratio and signal strength measurements

The strength of the received information signal may be monitored in real-time to give a closed-loop estimate of the degradations caused by atmospheric effects. This can be done by monitoring the sample mean and variance at the output signal of a correlation receiver (or matched filter). Such a system cannot differentiate between up and down-link fades and can only give estimates of the total attenuation. This is unsuitable for FCMs like ULPC, however would be interesting for countermeasures based on adaptive error coding **[2.40]**. Similar to beacon based methods, there is still a need to know the clear-sky level.

BER monitoring

For digital links, monitoring the bit error rate may be a closed loop detection method applicable to fade countermeasures. However, for low data rates, which would be typically the case for inbound VSAT applications, this would be an extremely slow process. For example, if for a BER threshold of 10^{-5}, it is necessary to detect 100 errors, then $100 \cdot 10^5$ bits have to be processed. At a bit rate of say 2 Mbit/sec, the detection would take 5 seconds. This is unsuitable for FCM systems and would get worse for slower data rates. It is however possible to reduce this processing delay by using pseudo error methods **[2.41]**. This is however at the expense of a lower accuracy of the measured BER.

Radiometer

A further method is based on the estimation of the up-link fade by using a radiometer pointing to the same slant path as the one used for the communication link. As a consequence, the FCM system will be in open loop. The attenuation can be inferred from the monitored sky noise temperature. This type of detector is usually limited to systems where no other alternative (as exposed above) is possible and it is not suitable for VSAT systems. Generally radiometer measurements offer good accuracy in the low range of attenuation and they are insensitive to satellite borne signal fluctuations. The major disadvantages are: the cost, insensitivity to non-absorptive effects (like amplitude scintillations) **[2.32]**. This could however be used to extract rain from scintillation in a very efficient way wich otherwise is a difficult task.

2.4.2 Response time of practical fade countermeasures

A major issue is the finite time delay inherent to the set-up of the FCM system whenever FCM action is required. The consequence is that FCM controllers must be predictive in order to account for the stochastic variations of the total attenuation on the CNR during this time delay **[2.1]**, **[2.40]**. This will be the major

aspect treated in chapter 4 of this thesis. An indicative delay diagram of an open loop FCM controller is given in Figure 2.8 (see also **[2.32]**).

Acquire t_A	*Pre-process* t_{PP}	*Prediction* t_{PR}	*Fade Detection Rule* t_{FD}	*FCM decision* t_D	*FCM activation* t_{ACT}	*Propagation* $n \cdot t_P$
Evaluate BER CNR/SNR	*Evaluate UL Attenuation*	*Short-term Prediction*	*Calculate required FCM RF equivalent power*	*Choose action*	*Resource Switching*	*Hop Delays n (protocol) t_P= 125 ms*

Figure 2. 8: Delay diagram of a FCM control system.

A first factor is due to the time to acquire the raw attenuation data, may it be in terms of BER, carrier-to-noise ratio etc. The second factor is the time taken for extracting the attenuation data. This involves the evaluation of the clear-sky attenuation level and possibly frequency scaling of the total attenuation (see Figure 2.6). The short-term prediction of the global fading should be based on a prediction interval equal to the total time delay including its own computation time i.e.

$$T_{pred} = t_A + t_{PP} + t_{PR} + t_{FD} + t_D + t_{ACT} + n \cdot t_P \qquad (2.6)$$

The fourth factor accounts for the time needed to compute the required FCM power knowing the predictor imperfections. This may simply consist of simply adding a constant offset to the predicted value and will be discussed later in detail. Also, the FCM controller will have to decide what action is necessary to achieve good performance in the next sample. This may involve, for example, choosing the next code rate in an adaptive FEC system. The sixth factor is the time to effectively carry out the appropriate switching of the FCM actuator. Finally, there is the propagation delay(s) from earth station to spacecraft. The number of hops will depend on the application and FCM service protocol, and will be function of whether or not on demand allocation of FCM resources is employed. This delay will be the predominant one in the whole chain. A total delay of the order 1 to 10 seconds may be expected.

Attenuation data measured during propagation experiments (e.g. Olympus) is sampled at a frequency of 1 Hz. This implies that the update of the FCM controller will occur at this rate and therefore that the controller should accommodate fades of durations greater than or equal to 1 second. If the total time delay is not a multiple of one second, then it should be at least rounded up to the next integer delay. Note that this may prove however quite impractical due to the fast scintillation process which may cause frequent and undesirable switchings of the FCM resources and this would need to be checked upon. Due to the complexity of the operation outlined above, fade controller systems must be computer-based.

2.4.3 Principle of a FCM predictive controller

Based on the discussion in sections 2.3 and 2.4, we will now restrict the problem of modelling an adaptive transmission FCM system by only considering a simplified block diagram depicted in Figure 2.9. Binary digits enter the codec/modem system at a variable rate, R_b bps. They are encoded yielding a rate R_b/ρ, where ρ is the code rate of the codec.

The modulator converts $N=\log_2 M$ consecutive bits into one of M possible symbols with rate $R_s= 1/T=(R_b/\rho)/ \log_2 M= R_b/(\rho \log_2 M)$.

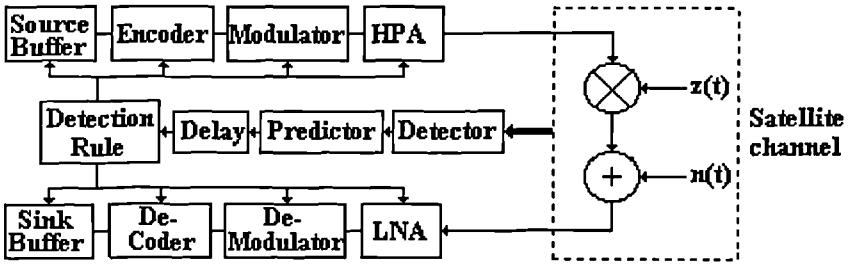

Figure 2. 9: Simplified model of a FCM system.

The fading z(t) (rain and scintillation) is assumed to be slow compared to the symbol duration T sec. and the noise n(t) is assumed Gaussian. Thus the received signal will be of the form $r_i(t)=(2z^2PT)^{1/2}\, \mathrm{Re}\{ u_i(t) \exp(jw_c t)\}+ n(t)$ where $u_i(t)$ is the complex normalised envelope of $s_i(t)$, the transmitted signal.

Based on the detected/predicted channel attenuation, the FCM controller then chooses, via an appropriate detection rule h(z), the optimal new settings in the transmission chain. Of course, transmitter and receiver are notified of those changes so that correct operations are ensured. The total round trip delay can be attributed to the feedback channel.
In the case of link power strategy, the detection rule, h(z)=P(z), will consist in choosing the appropriate signal power as a function of the global attenuation z.

For the case of adaptive user data rate system, based on an adaptive FEC scheme, the data rate $R_b(z)$ and code rate $\rho(z)$ are varied as functions of z, subject to the constraint that $R_s \log_2 M = R_b(z)/\rho(z)$= constant for one modulator. For the case of an adaptive user rate system based on adaptive modulation, the data rate, $R_b(z)$, and the M-ary index, M(z), are varied as functions of z. This is performed subject to the constraint that $R_s\rho = R_b(z)/\log_2 M(z)$=constant for a particular codec.

The model of Figure 2.9 indicates that the satellite fading channel can be modelled via a single random variable, z, denoting the global fading. It accounts for the impact of rain attenuation and tropospheric scintillation on up/down links and satellite transponder effects. Such a model will be derived in chapter 3 using known statistical models. Also, it is necessary to investigate the predictability of the global fading so as to determine the likely degradations caused by time delays in the return channel. Once this known, it should be possible to derive suitable detection rules for specific strategies like ULPC, Adaptive FEC or Adaptive modulation as FCMs.

2.4.4 Short-term prediction of Ka band global fading

They are two possible approaches to implement a short-term predictor of the Ka band fading:

- the two processes of interest , i.e. rain and scintillation are treated separately,
- the Ka band fading is treated as a whole.

The first possibility involves the efficient separation of the two processes which is a difficult task to perform in an automatic manner due to the different non-

stationarity of each individual effect. However in the case of detection schemes based on down-link beacon monitoring, the separation has to be performed anyway. The main drawback is that the design of two predictors is involved.

The second approach, although more coarse, would result in one predictor without the need of separating the effects. This may be a great advantage for quick analysis of beacon time-series and this may also be applicable to real systems based on fade detection schemes like up-link beacon or signal-to-noise ratio monitoring.

In any case, the construction of efficient predictors must be based on a dynamic model, capable of capturing the essential dynamics of the global fading. This implies that a suitable discrete stochastic model has to be identified. Furthermore, the model should be time-varying in order to track the known statistical variability of the Ka band fading. From this model, a short-term predictor can then be implemented.

2.4.5 Impact of instantaneous frequency scaling

In the case of down-link beacon monitoring systems, the random variations of instantaneous frequency scaling factor (IFSF) of rain attenuation will cause, like time delays, an uncertainty in the estimation of the current level of hydrometeor attenuation **[2.1]**. If the FCM is to operate satisfactorily, the variability of the IFSF of rain must also be included in the choice of the fade detection rule. This requires the definition of a new statistical model. One of them will be introduced in chapter 6. Similarly, inclusion of tropospheric scintillation scaling effects should be considered. Note that in this case, the scaling relates to the *variance* of the scintillation process and not scintillation itself **[2.43]**.

2.5 Simulation of FCM systems

Event-based analysis (system testing)

Short-term analysis is useful in order to evaluate the behaviour of an overall FCM system in real-time, so that the efficiency of the FCM controller may be determined in different situations (like no rain conditions). Such a program would allow us to evaluate of the behaviour of system parameters that are not yet accessible theoretically. For example, in the case of a multi-rate AFEC system, it would be interesting to find out whether or not the system would switch quickly from one code rate to another due to the high frequency fluctuations of the Ka band fading. Also, if time allows, the simulation may be run over a long period to determine long-term characteristics. This may be done using measured beacon time-series as primary input, or by using a synthesised signal having the same characteristics. The latter would allow extrapolation of the system performance to places where CPA beacon data has not been collected.

Long-term modelling (perfomance evaluation)

The ultimate objective is to design efficient systems and thus the long term modelling of FCM systems should be formulated on a statistical basis. Such a model, including rain and scintillation, is already available for the ideal control case, that is without delays; it will be discussed in detail in the next chapter. It just needs to be extended to include the practical limitations caused by time delays and realistic short-term predictors. This is the main subject of this research project. The final solution should be given in a format suitable for a maximum of FCM techniques. The results should therefore be given either in the RF domain (i.e. in terms of carrier-to-noise/ signal-to-noise ratio) or in terms of bit error rate (BER) availability and throughput for digital communication systems. Such a long term model will allow determination of essential FCM control parameters such as the required scintillation margin for good FCM operation in the presence of time delays.

2.6 Conclusions

The performance and design issues of fade countermeasure techniques have been reviewed in some detail. The techniques were divided into three different broad

classes. They were characterised in terms of achievable fade protection margin and in terms of the basic engineering trade-offs that are involved.

An emphasis was placed on adaptive transmissions techniques, which will be analysed in more detail in the context of a star-shaped VSAT network of the CODE type. The general concept of the FCM control system has been introduced. More particularly, the fade detection process and the FCM controller have been outlined. The predictive aspect of FCM operations requires further work. There is first the need to evaluate qualitatively the short-term predictability of the Ka band fading process, including rain attenuation and scintillation. This is done in Chapter 4. This will then be used in Chapter 5 for defining efficient fade detection rule and assess the outage probability versus FCM over-utilisation trade-off of particular FCM systems. Chapter 6 will consider the inclusion of instantaneous frequency scaling in a predictive fade controller. The following chapter will first show how the effect of both rain attenuation and tropospheric scintillation can be modelled statistically on a test-case back-to-back link .

References

[2.1] G. Tartara, "Fade Countermeasures in millimetre-wave satellite communications: a survey of methods and problems", *Proc. Olympus Utilisation Conf., Vienna, 12-14 April 1989*, ESA SP-292, May 1989, pp 103-107.

[2.2] F. Carassa, G. Tartara, E. Matricciani, "Frequency Diversity and its applications", *Int. J. of Satellite Comms*, vol. 6, 1986, pp 313-322.

[2.3] C.C. Bantin, R.G. Lyons, "The evaluation of satellite link availability", *IEEE Trans. on Comms,* Vol. COM-26, No 6, 1978, pp 847-853.

[2.4] L.J Greenstein, M. Shafi, "Outage calculation methods for microwave digital Radio", *IEEE Comms Magazine,* Vol. 25, No 2, Feb. 1978, pp 30-39.

[2.5] G. Maral, M. Bousquet, *Satellite Communications Systems*, 2nd edition, John Wiley and Sons, 1994.

[2.6] J.K Cavers, "Variable Transmission for Rayleigh fading channels", *IEEE Trans. on Comms*, Vol. COM-20, No 1, Feb. 1972, pp 15-22.

[2.7] V.O. Hentinen, "Performance for adaptive transmission on fading channels", *IEEE Trans. on Comms*, Vol. COM-22, No 9, Sept. 1974, pp 1331-1336.

[2.8] D. Di Zenobio, P. Lombardi, P. Migliorini, E. Russo, "Site Diversity: a powerful antifading technique for satellite communications in the 20/30 GHz bands", *Proc. Olympus Utilisation Conf., Vienna, 12-14 April 1989* , ESA SP-292, May 1989, pp 135-142.

[2.9] D.B Hodge, "An improved model for diversity gain on earth-space propagation paths", *Radio Science*, Vol. 17, 1393-1399.

[2.10] B. Arbesser-Rastburg, "Large and small scale Diversity", *Proc. Olympus Utilisation Conf., Vienna, 12-14 April 1989* , ESA SP-292, May 1989, pp 235-238.

[2.11] E. Matricciani, "Prediction of Site Diversity performance in communications systems affected by rain attenuation: Extension of the two layer rain model", *Euro. Trans. on Telecomms and Related Technologies*, May-June 1994, Vol. 5 Pt 3, pp 327-336.

[2.12] L.J. Ippolito, *Radiowave propagation in satellite communications*, Van Nostrand Reinhold, 1986.

[2.13] E. Matricciani, M. Mauri, "Italsat-Olympus Orbital Diversity experiment at Spino d'Adda", *IEEE Trans. on Ant. and Prop.*, Vol. AP-43, No 1, January 1995, pp 105-108.

[2.14] C. Capsoni, E. Matricciani, M. Mauri, "Sirio-OTS orbital diversity experiment at Fucino", *IEEE Trans. on Ant. and Prop.*, Vol. AP-38, No 6, June 1990, pp 777-782.

[2.15] A.N Ince, D.W Brown, J.A. Midgley, "Power control Algorithms for Satellite Communications", *IEEE Trans. on Comms*, Vol. COM-24,1976, pp 267-275.

[2.16] J. Hörle, "Up-link Power control of satellite Earth-Stations as a Fade Countermeasure of 20/30 GHz Communication systems", *Fade Countermeasures for Satellite Communications*, ESA STM-235, May 1986, pp 19-28.

[2.17] J.S. Doshi, "Matrix amplifiers for satellite communications applications", *Electronics and Comunication Engineering J.*, December 1991, pp 259-266.

[2.18] V.K Bhargava, D. Haccoun, R. Matyas, P.P. Nuspl, *Digital Communications by satellite, Modulation, Multiple access and coding*, John Wiley & Sons, 1991, 569 pages.

[2.19] O. Kouldeka, "Adaptive transmission rate and variable redundancy systems as a fade countermeasure", *Fade Countermeasures for Satellite Communications,* ESA STM-235, May 1986, pp 11-13.

[2.20] Y. Yasuda, Y. Hirata, K. Nakamura, S. Otani, "Development of variable-rate Viterbi decoder and its performance characteristics", *Proc. 6th int. Conf. on Digital Satellite Communications, Phoenix Arizona*, Sept. 1983, pp XII 24-31.

[2.21] L.J.M. Smith, G.D Burton, "Punctured coding for forward error correction in satellite communications", *J. of the IERE, Vol. 58, No 3*, May 1988, pp 125-131.

[2.22] M.H. Khan, T. Le-Ngoc, V.K. Bhargava, "Efficient adaptive forward error control schemes for Ka band satellite systems", *Int. J. of Satellite Comms*, Vol. 4,1986, pp 139-146.

[2.23] M. Tomlinson, F. Cercas, C.D. Hughes, "Aspects of coding for power-efficient satellite VSAT systems", *ESA J.*, Vol. 15, 1991, pp 165-184.

[2.24] C.D. Hughes, M. Tomlinson, "The use of spread-spectrum coding as a fading countermeasure at 20/30 GHz", *ESA J.*, Vol. 11, 1988, pp 73-81.

[2.25] M. Filip, E. Vilar, "Adaptive modulation as a fade countermeasure. An Olympus experiment", *Int. J. of Satellite Comms*, Vol. 8, 1990, pp 33-41.

[2.26] M. Filip, E. Vilar, "Implementation of adaptive modulation as a fade countermeasure", *Int. J. of Satellite Comms*, Vol. 12, 1994, pp 181-191.

[2.27] F. Carassa, "Adaptive methods to counteract rain attenuation effects in the 20/30 GHz band", *Space Communication and Broadcasting*, Vol. 2, 1984, pp 253-269.

[2.28] D.J. Emerson, R.M. Nelhams, B.L. Clark, "Adaptive TDMA for Fade Countermeasures", *Proc. Olympus Utilisation Conf., Vienna, 12-14 April 1989* , ESA SP-292, May 1989, pp 125- 131.

[2.29] D. Von Hugo, A. Wilde, "An adaptive resource sharing strategy for TDMA", *Int. J. of Satellite Comms*, Vol. 12, 1994, pp 249-256.

[2.30] F. Carassa, G. Tartara, E. Matricciani, "Frequency Diversity and its applications", *Int. J. of Satellite Comms*, Vol. 6, 1988, pp 313-322.

[2.31] F. Carassa, "Methods to improve satellite systems performances in the presence of rain", *Alta Frequenza*, Vol. LVI, No 1-2,1987, pp. 173-185.

[2.32] M. Luglio, *"Satellite systems in Ka band for new services"*, University of Rome "Tor Vergato", PhD thesis, English version, 1994.

[2.33] G. Maral, *VSAT networks*, John Wiley and sons, 1995.

[2.34] M.J. Willis, B.G. Evans, "An adaptive coding/up-path power control fade countermeasure experiment via Olympus", *Proc. Olympus Utilisation Conf., Vienna, 12-14 April 1989* , ESA SP-292, May 1989, pp 151- 155.

[2.35] P.O. Svensk, C. Nycander, "Swedish telecom radio experiment plans for Olympus", *Proc. Olympus Utilisation Conf., Vienna, 12-14 April 1989* , ESA SP-292, May 1989, pp 399- 403.

[2.36] D. Von Hugo, "Fade Countermeasures for satellite-based networks at 20/30 GHz", *Proc. of 2nd Ka band utilization Conf. and International Workshop on SCGII*, Sept. 24-26 1996, Florence (Italy), Sept. 1996, pp 393-400.

[2.37] J. Hagenauer, "Rate Compatible punctured convolutional codes (RCPC codes) and their applications", *IEEE Trans. on Comms*, Vol. COM-36, No 4, Apr. 1988, pp 389-400.

[2.38] N. Lay, K. Dessouky, "A communication protocol for mobile satellite systems affected by rain attenuation", *IEEE J. on Select. Areas in Comms.*, Vol. SAC-10 No 6, Aug. 1992, pp 1037-1047.

[2.39] T-Y Yan, V.O.K. Li, "A reliable pipeline protocol for the message service of a land mobile satellite experiment", *IEEE J. on Select. Areas in Comms.*, Vol. SAC-5 No 4, May 1987, pp 637-647.

[2.40] M.J. Willis, B.G. Evans, "Fade countermeasures at Ka band for Olympus", *Int. J. of Satellite Comm*, Vol. 6, 1988, pp 301-311.

[2.41] E. Newcombe, S. Pasupathy, "Error rate monitoring for digital communications", *Proc. IEEE*, Vol. 70, No 8, pp 805, August 1982.

[2.42] F. Rücker, "The impact of instantaneous frequency scaling factors on up-link power control", *AEÜ*, Vol. 48, No 2, 1994, pp 119-121.

[2.43] G. Ortgies, "Frequency Dependence of slant-path amplitude scintillations", *Electronics Letters*, Vol. 29, No 5, Dec. 1993, pp 2219-2220.

3. Impact of Propagation Effects on Satellite Communications

3.1 Introduction

A radiowave propagating through a noisy channel like the atmosphere will experience a stochastic reduction in signal level due to different physical phenomena caused for example by hydrometeor or gases attenuation. Also in the context of fade countermeasures, scintillation cannot be neglected.

Shannon showed that it is possible to achieve, over noisy channels, arbitrarily low probability of error at rates near channel capacity at the expense of coding or modulation complexity. However in practical systems, the equipment must simply be designed to operate at a specified grade of quality (BER), grade of service (availability) and throughput.

To assess such important engineering issues in the context of fade countermeasures, the calculations, basic results, models and definitions that will be used in this document are laid down in this chapter. The long-term statistical impact of atmospheric effects on a Ka band back-to-back satellite link will be evaluated. This configuration corresponds effectively to a worst-case analysis since generally the correlation coefficient of atmospheric attenuation is less than unity for separated ground sites.

The analysis is carried out using known classical tools, such as link power budget and semi-empirical models i.e. the ITU-R model for quantifying the attenuation caused by hydrometeors (rain + clouds) and gases (water vapour and oxygen).

More recent techniques allowing inclusion of amplitude scintillations in the modelling process will also be used. More particularly the concept of 'global fading' introduced by Filip and Vilar **[3.1]** will be used for describing analytically the impact of joint hydrometeor and scintillation on a realistic back-to-back link. From this, the advantage of adaptive systems over the fixed power margin strategy will be evidenced for Ka band operations.

This chapter reviews and applies the global fading model to a *particular* problem, namely the Chilton-Olympus back-to-back link. This necessary study will serve as a basis to the following chapter and thus bears little novelty.

3.2 Chilton-Olympus Link Budget

3.2.1 The CODE experiment on the Olympus Satellite

Olympus was an experimental 3-axes stabilised satellite system designed to meet the requirements of future European telecommunications satellites. Its mission lifetime was originally 5 years. The spacecraft was placed on the geostationary orbit at a longitude of 19° West and was maintained during its operational lifetime* in a station-keeping window of ± 0.07°. The satellite attitude control was such as to

* *Station-keeping was lost for 76 days during which Olympus drifted along the GEO orbit. A significant technical prowess was achieved by a joint effort of American, European Space agencies which managed to save successfully the spacecraft and re-positioned it back to its allocated slot. This extraordinary experience is described in [3.2].*

ensure spacecraft beam pointing errors below 0.2°. Tracking and Telemetry was carried out by an omni-directional 2 GHz control facility.

Olympus carried four different payloads:

- the 12/20/30 GHz Propagation Package to update and complement propagation models in the higher frequency range,
- the Direct Broadcasting (DBS) Payload composed of two 11 GHz channels use for broadcasting and distance-learning experiments and demonstrations **[3.3]**,
- the multi-beam 12/14 GHz Specialised Services Payload for advanced communication services such as SS-TDMA (Satellite Switched TDMA) **[3.4]**,
- the 20/30 GHz Communications Payload in which the CODE experiment was integrated.

The 20/30 GHz Communications Payload offered a unique opportunity for researchers across Europe to implement and test new innovative experimental communications services and technologies in this frequency band. The payload comprised two independently-steerable transmit/receive spot-beam antennas having a 0.6° nominal coverage. Within the context of the CODE experiment, transmit and receive spotbeams boresights were pointed at a point located at 52° N, 2° W.
Additional parameters of the 20/30 GHz Olympus Communication Payload are presented in Table 3.1.

We shall consider a hypothetical *back-to-back* in-bound VSAT experiment between Chilton (UK) and Olympus-1. That is, the transmit system would be part of a VSAT whilst the receive system would belong to the Hub station. This configuration means that the two Earth stations are then co-located at latitude of 51.6667° N, longitude of 1.2833° W and altitude of 100 m above mean sea level. This implies that the elevation angle is 28.56° and the slant path distance is R=38792.32 km **[3.7]**.

Bandwidth	40 MHz
Rx Polarisation	Linear horizontal
Rx Frequency	28.622255 GHz
Rx Gain at beam centre	42.6 dBmin.
Rx Gain over 0.6° Coverage	40.1 dBmin.
Transponder noise floor (40 MHz)	-120.4 dBW
System noise temperature	32.2 dBK
Noise figure	7.6 dBmax (for narrow band channel)
G/T at beam centre	10.2 dB/K min.
G/T over coverage	7.7 dB/K min.
Input power for saturation (IPS): VSAT to Hub	-104 dBW
Input power for saturation: Hub to VSAT	-101 dBW
Tx Polarisation	Linear vertical
Tx frequency	19.475 GHz
EIRP (Effective Isotropic Radiated Power)	53.3 dBW max. (at beam centre)
EIRP	51.7 dBW min. (over coverage)
Tx Gain at beam centre	42.6 dB min.
Tx Gain over coverage	40.1 dB min.
Station Keeping Window	± 0.07°

Table 3. 1: Parameters of 20/30 GHz Olympus Communications Payload [3.5, 3.6].

The main parameters of the TDS-6 Hub station used during the CODE experiment are given in Table 3.2. We shall now calculate different power link budgets for a set of VSAT antenna diameters and High Power Amplifiers (HPA) assuming a SCPC (Single Channel Per Carrier) access mode.

3.2.2 Advantages of the back-to-back link hypothesis

The overall transmission quality over the in-bound link is directly related to the overall clear-sky to noise ratio and the global fading for up and down links.

The FCM controller should ideally cater for the end effect of up and down link attenuations through the satellite transponder as detected at the receive end (that is the Hub in the in-bound VSAT scenario). The overall carrier-to-noise ratio for a non-regenerative satellite and fading repeater is given by (see equation **(3.8)**):

$$\left.\frac{C}{N_0}\right|_t \equiv \left.\frac{C}{N_0}\right|_{t,0} - z = 10\log_{10}\left(10^{-0.1\left(\left.\frac{C}{N_0}\right|_{u,0} - A_u\right)} + 10^{-0.1\left(\left.\frac{C}{N_0}\right|_{d,0} - Ad\right)}\right)^{-1} \quad \text{dB}\cdot\text{Hz} \qquad \textbf{(3.0)}$$

where z denote the global fading on the in-bound link and A_u, A_d denote the up and down link attenuation (in dB). The FCM controller will have to base its decision on the *estimated* global fading $\hat{z}$, bearing in mind that there will be detection/prediction errors. Furthermore, if one wishes to estimate long term statistical estimates of the performance of the FCM system, the pdf of z must be known. In view of (5.14), z is a random variable given by the non-linear transformation **(3.0)** of two other r.v.s. Recalling that A_u and A_d refer to both rain and scintillation effects, one can realise that the statistical modelling of z becomes a major mathematical problem especially if one considers that in general the rain components of A_u and A_d are not statistically independent and should also include site diversity modelling (scintillation effects on up and down links can be considered as independent). Although such an analysis would be of interest for a general formulation and solution of this 'global fading problem', only the *worst-case* design analysis will be of practical use for determining long term performances. Instead it would be more suitable to find approximations which still yield indicative results. The back-to-back link is such a model. While scintillation will always be present, rain attenuation on up and down links may well be decorrelated due to site diversity. The global fading attenuation will always be greater if some up and down link rain fades are simultaneously present. While in real time and real life, the joint impact of up and down link rain fades on the global fading may well exceed that obtained on a back-to-back link, the latter can be considered as a *long-term* worst-case configuration since it assumes that both links are affected simultaneously over a *very long* period. This has the main advantage of by-passing site diversity modelling thereby simplifying greatly the statistical analysis since total correlation between up and down link is assumed.

3.2.3 Back-to-back Link Power budget

Link budget calculation deals with information transfer at the physical level which involves Forward Error Correction (FEC), modulation, and the evaluation of digital signal quality in terms of Bit Error Rate (BER) over realistic channels.

The BER depends on the type of (de-)modulation and (de-)coding performed, and on the carrier-to-noise spectral density ratio C/N_o at the input of the end-receiver. This ratio, C/N_o, can thus be considered as a quality measure of the radio frequency (RF) link. For the sake of clarity, we shall only consider in this section a simplified link budget.

Antenna diameter	2.5 m	Ambient temperature	270 K
Antenna efficiency	0.7	Rain temperature	275 K
Ant. Tx Gain	55.8 dB	Tx frequency	28.1 GHz
Ant. Rx gain	52.6 dB	Rx frequency	19.5 GHz
Amplifier output (P_{hpa})	300 W	Channel symbol rate	2048 kbits/sec
Rx LNA noise figure	2.7 dB	Modulation (Tx)	QPSK
Elevation angle	28.56°	Tx pointing loss	1.9 dB
Sky temperature	60 K	Rx pointing loss	1.3 dB

Table 3. 2: Main parameters of the TDS-6 Hub station used in the CODE experiment [3.8].

The Effective Isotropic Radiated Power (EIRP) at the transmitting end is

$$EIRP = P_{hpa} + 20 \cdot \log_{10} \frac{\pi D \eta}{\lambda} \quad dBW \tag{3.1}$$

where P_{hpa} [dBW] is the High Power Amplifier (HPA) power output and the second term is the antenna gain. For parabolic antennas ([**3.7**]). D (m) is the antenna diameter, $\lambda = c/f$ m is the wavelength ($c = 3.10^8$ m/s, f in Hz), and η is the antenna efficiency ($\eta = 0.5$ will be assumed). On application to the Chilton back-to-back link, for different HPA power and dish size, one obtains,:

$$EIRP|_u = P_{hpa} + 20 \log D + 46.52 \quad \text{dBW} \tag{3.2}$$

The free-space loss ([**3.7**]) is $L_{free} = 20 \log_{10}\left(\frac{4\pi \cdot R}{\lambda}\right)$ dB ,where R (km) the slant path distance. This yields for up and down links respectively, $L_{free,u}$ = 213.35 dB, $L_{free,d}$ = 210.01 dB.

The total gaseous attenuation caused by both water vapour and oxygen, calculated according to the ITU-R recommendations [**3.9**], with an elevation angle of

28.56° and a water vapour content of 7.5g/m^3 can be found to be $L_{gas,u}$ = 0.523 dB on the up-link and $L_{gas,d}$ = 0.476 dB on down-link.

The pointing losses can be estimated **[3.7]** using $L_{point} = 12\left(\frac{\phi}{\phi_{3\,dB}}\right)^2$ dB ,where ϕ_3 $_{dB}$ =70/ (f*D) (deg) is the half power beamwidth on an antenna of D(m) at frequency f (Hz). For a VSAT antenna of D = 1.2 m with pointing error ϕ = 0.2° and assuming a pointing error of ϕ= 0.1° for the Hub, the pointing losses are respectively $L_{point,u}$ = 1.30 dB on up-link and $L_{point,\,d}$ = 0.65 dB on down-link.

The carrier-to-noise spectral density of the up-link is **[3.7]**

$$\left.\frac{C}{N_o}\right|_u = EIRP|_u - L_{free,u} - L_{gas,u} - L_{point,u} + \left.\frac{G}{T}\right|_s - 10\log_{10}\,\mathrm{k} - z_u \qquad \text{dB.Hz} \qquad \textbf{(3.3)}$$

where $k = 1.38\times10^{-23}$ J / K $\Leftrightarrow$ $10\log k = -228.6$ $dBW/K\cdot Hz$ is Boltzmann's constant, and, z_u (dB) is the atmospheric attenuation due to hydrometeors and scintillations. On application to the Chilton/Olympus link this gives:

$$\left.\frac{C}{N_o}\right|_u = P_{hpa} + 20\cdot\log\,\mathrm{D} + 67.647 - z_u \qquad \text{dB·.Hz} \qquad \textbf{(3.4)}$$

On the down-link, the carrier-to-noise spectral density ratio is **[3.7]**

$$\left.\frac{C}{N_o}\right|_d = EIRP|_{s,sat} - L_{free,d} - L_{gas,d} - L_{point,d} + \left.\frac{G}{T}\right|_{hub} - OBO_1 - 10\cdot\log k - z_d \qquad \text{dB.Hz}$$

(3.5)

where OBO_1 (dB)* is the satellite HPA output back off in dB and $EIRP|_{s,sat}$ is the effective radiated isotropic radiated output power of the satellite at saturation, and, z_d [dB] is the attenuation caused by hydrometeors and scintillation on the down-link.

For non-saturated operation, the output back-off for 1 carrier, OBO_1 , for the Olympus TWTA can be approximately linearised as:

$$OBO_1 \approx 0.94\cdot IBO_1 - 3.99 \qquad \text{dB} \qquad \textbf{(3.6)}$$

* *subscript 1 stands for single carrier.*

where IBO_I is the input back-off (for 1 carrier), provided it is greater than 11 dB **[3.10]**. The input back-off equals to the difference between the Input Power for Saturation (IPS) of the TWTA and the total collected signal power at its input. Using this expression it is thus possible to calculate numerically the down-link carrier-to-noise spectral density for the Chilton/Olympus link,

$$\left.\frac{C}{N_o}\right|_d = 76.86 + 0.94 \cdot P_{hpa} + 18.8 \cdot \log D - 0.94 \cdot z_u - z_d \quad \text{dBHz} \qquad \textbf{(3.7)}$$

Note how the EIRP (depending on P_{hpa} and D) and the up-link fade translate on the down-link carrier-to-noise ratio.

A study of intermodulation products applied to the Olympus TWTA revealed that intermodulation had a very limited effect on the overall carrier-to-noise ratio, even for a large number of SCPC carriers **[3.10]**. As a consequence, intermodulation shall be neglected. Similarly, for the sake of clarity, co-channel and adjacent channel interference will be discarded. Based on these simplifying assumptions, the overall carrier-to-noise spectral density can be shown to be equal to **[3.7]**:

$$\left.\frac{C}{N_0}\right|_t = 10 \cdot \log_{10}\left(10^{-0.1\left.\frac{C}{N_o}\right|_u} + 10^{-0.1\left.\frac{C}{N_o}\right|_d}\right)^{-1} \quad \text{dB} \cdot \text{Hz} \qquad \textbf{(3.8)}$$

Using **(3.4)**, **(3.7)** and **(3.8)** different overall clear-sky carrier-to-noise density ratios can now be computed for clear-sky conditions by letting up and down link attenuations, z_u and z_d respectively, equal zero dB. The values are summarised in Table 3.3 given below. For a particular set (P_{hpa} , D) of VSAT parameters, the clear-sky carrier-to-noise spectral density of the in-bound VSAT back-to-back link can readily be extracted and used numerically for further modelling purposes.

D (m)	Clear sky $C/N_o\|_{t,0}$ Ratio (dBHz)				
0.6	52.80	55.79	57.55	59.75	64.95
0.8	55.28	58.28	60.03	62.24	63.02
1.0	57.21	60.21	61.96	64.16	64.95
1.2	58.79	61.78	63.53	65.74	66.52
1.4	60.12	63.11	64.86	67.07	70.05
Phpa (W)	0.1	0.2	0.3	0.5	1.0

Table 3. 3: Clear-sky overall carrier-to-noise spectral density ratio on the in-bound VSAT back-to-back link.

3.3 Atmospheric effects on radiowave propagation

3.3.1 Hydrometeor Attenuation on satellite slant paths

The impact of hydrometeor attenuation on Earth-space slant paths is of major concern to satellite communications systems especially for frequencies above 10 GHz. The term hydrometeor refers principally to rain, clouds, hail, ice or snow. Their effect on radiowave propagation involves both absorption (thermal dissipation) and scattering (dispersion caused by inhonomogeneities in the propagation medium) of the wave energy **[3.10]**. At Ka band, rain and clouds attenuation are the major sources of fading in terms of amplitudes. Most prediction methods for quantifying hydrometeor attenuation are semi-empirical and are based on the general power law formula given by :

$$y = aR^b \cdot L(R,\theta) \qquad \text{dB} \tag{3.9}$$

where R is the rain rate (mm/h)

$\gamma = aR^b$ [dB/km] is the specific attenuation,

L(R,θ) [km] is the effective path length, itself depending on rain rate and elevation angle.

Although this definition refers specifically to the rain rate, R, these models, like the ITU-R, generally refer more loosely to rain and clouds type of attenuation.

The parameters a and b are frequency, elevation and polarisation dependent. Following the ITU-R recommendations **[3.9]**, their values for the Chilton/Olympus link can be found to be

a = 0.18996, b = 0.99070 at the up-link frequency,

a = 0.06979, b = 1.06911 at the down-link frequency.

The effective path length, L(R, θ) can be obtained from an empirical equation ([**3.11**]) given by:

$$L(R,\theta) = \left[7.413 \cdot 10^{-3} \cdot R^{0.766} + (0.2323 - 1.803 \cdot 10^{-4} \cdot R) \cdot \sin\theta\right]^{-1} \quad \text{km} \qquad \textbf{(3.10)}$$

Noting that Chilton is located in ITU-R rain zone F, the rain rate distribution for this climatic zone can be extracted from the CCIR prediction model **[3.9]**:

% time	0.001	0.003	0.01	0.03	0.1	0.3	1.0
R[mm/h]	78	54	28	15	8	4.5	1.7

Table 3. 4: Rain rate exceeded for p% of the time, ITU-R model, rain zone F.

Similarly Chilton is located in rainzone C of the 1980 Crane global model yielding the rain rate values given in Table 3.5 **[3.10]**.

% time	.001	.002	.005	0.01	0.02	0.05	0.1	0.2	0.5	1.0	2.0
R[mm/h]	80	62	41	28	18	11	7.2	4.8	2.7	1.8	1.2

Table 3. 5: Rain rate exceeded for p% of the time, 1980 Crane Global model, rain zone C.

Both rain rate data given in these two Tables can be combined statistically in order to obtain a better estimate of the rain rate exceeded for p% of the time of an average year and to extend the number of available points. This is shown in the second column of Table 3.6. Also, the up and down link specific attenuations, effective path length and hydrometeor attenuation were calculated using **(3.9)** and **(3.10)**.

Now, the combined effect of hydrometeor attenuation on both up and down links can be evaluated for the Chilton/Olympus back-to-back link. This is achieved by simply inputting equi-probable values of up and down-link rain attenuation found

in *Table 6* into the link budget equations **(3.4)**, **(3.7)** and **(3.8)** for each particular VSAT parameter set (P_{hpa}, D). As was previously seen, up-link fades and VSAT EIRP are translated by the satellite transponder TWTA onto the down-link carrier-to-noise ratio, therefore, the total impact of rain attenuation on the back-to-back link is *not* simply the sum of the individual fades. Instead the total equivalent rain fade of the back-to-back link is defined as **[3.1]**:

$$y = \left.\frac{C}{N_0}\right|_{t,0} - 10 \cdot \log\left(10^{-0.1\left.\frac{C}{N_0}\right|_u} + 10^{-0.1\left.\frac{C}{N_0}\right|_d}\right)^{-1} \quad \text{dB} \qquad \textbf{(3.11)}$$

where the values of the clear sky carrier-to-noise density $C/N_0|_{t,0}$ (dBW.Hz) can be found in Table 3.3.

% time	R[mm/h]	γ_R [dB/km]		L_R [km]	y [dB]	
		up-link	down-link		y_u	y_d
0.001	79	14.41	7.46	3.18	45.75	23.68
0.002	62	11.33	5.76	3.56	40.38	20.50
0.003	54	9.88	4.96	3.76	37.46	18.82
0.005	41	7.52	3.70	4.25	32.02	15.74
0.01	28	5.16	2.46	4.91	25.30	12.07
0.02	18	3.33	1.53	5.64	18.76	8.65
0.03	15	2.78	1.26	5.92	16.46	7.48
0.05	11	2.04	0.91	6.38	13.04	5.78
0.1	7.6	1.42	0.61	6.87	9.74	4.19
0.2	4.8	0.90	0.37	7.39	6.64	2.76
0.3	4.5	0.84	0.35	7.45	6.28	2.60
0.5	2.8	0.53	0.21	7.86	4.14	1.65
1.0	1.8	0.34	0.13	8.16	2.77	1.07
2.0	1.2	0.23	0.08	8.37	1.90	0.71

Table 3. 6:Cumulative distribution of rain attenuation on up and down links.

The total equivalent rain attenuation is thus defined as the difference between overall clear-sky and rainy carrier-to-noise densities. This is illustrated in Table 3.7

for one particular set of VSAT parameters (P_{hpa}, D) = (0.2 W, 0.8 m) for which the total equivalent rain attenuation has been tabulated.

We can now verify that the total equivalent rain attenuation conforms approximately to the lognormal model. This model has a probability density function (pdf) given by:

$$\Lambda_y(m,\sigma) = f_y(y) = \frac{1}{y\sigma\cdot\sqrt{2\pi}}\cdot\exp\left[-\frac{(\ln\ y\ -\ m)^2}{2\sigma^2}\right] \quad , y \geq 0 \qquad \textbf{(3.12)}$$

$$f_y(y) = 0 \ , \text{ elsewhere,}$$

which after integration yields the lognormal cumulative distribution function (CDF):

$$P_y = \text{Prob}\{y \geq a\} = \int_a^{\infty} \frac{1}{y\sigma\sqrt{2\pi}}\cdot\exp\left[-\frac{(\ln\ y\ -\ m)^2}{2\sigma^2}\right]\cdot dy \quad , y \geq 0\,. \qquad \textbf{(3.13)}$$

$$P_y = \text{Prob}\{y \geq a\} = 0 \ , \text{ elsewhere}$$

where m and σ are the median and standard deviation of the distribution.

This can easily be checked graphically once the two parameters of the lognormal model, m and σ, are known. This is shown in Figure 3.1 for the (P_{hpa}, D)= (0.2 W,0.8 m) for which the parameters were estimated using a polynomial curve fitting method described in detail in **[3.1]**.

% time	y_u [dB]	y_d [dB]	y [dB]
0.001	45.75	23.68	56.82
0.002	40.38	20.50	48.86
0.003	37.46	18.82	44.67
0.005	32.02	15.74	37.08
0.01	25.30	12.07	28.29
0.02	18.76	8.65	20.36
0.03	16.46	7.48	17.70
0.05	13.04	5.78	13.85
0.1	9.74	4.19	10.24
0.2	6.64	2.76	6.93
0.3	6.28	2.60	6.55
0.5	4.14	1.65	4.30
1.0	2.77	1.07	2.87
2.0	1.90	0.71	1.96

Table 3. 7: Total equivalent rain attenuation for P_{hpa} = 0.2 W, D = 0.8 m.

A similar methodology was used to calculate the two parameters of the log-normal model of the total equivalent hydrometeor attenuation on the back-to-back link for different sets of VSAT parameters. They are shown in Table 3.8. These allow a representation of the atmospheric channel (including transponder's conversion and Earth station specific parameters) as an unified additive process which can be subtracted directly to the corresponding clear-sky carrier-to-noise density ratio given in Table 3.3.

P_{hpa} [W]	D[m]	$C/No|_{t,0}$ [dB.Hz]	m	σ
0.1	0.6	52.80	-2.5555	1.5731
0.2	0.8	58.28	-2.5583	1.5751
0.3	1.0	61.96	-2.5625	1.5771
0.5	1.2	65.74	-2.5614	1.5777
1.0	1.4	70.06	-2.5614	1.5777

Table 3. 8: Overall carrier-to-noise density ratios and parameters of the fitted log-normal model for different VSAT combinations.

Note that the overall carrier-to-noise ratio density loss loses its dependence on VSAT EIRP for high values of P_{hpa} and D.

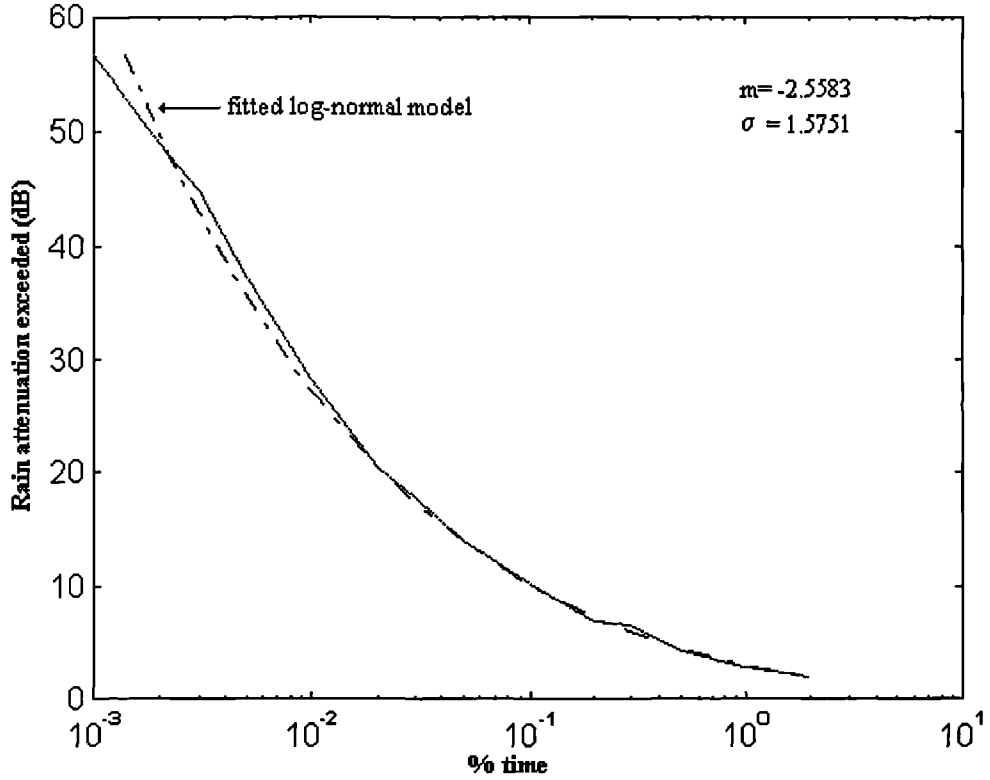

Figure 3. 1: CDF of the total equivalent rain attenuation exceeded for the back-to back link with (P_{hpa} , D)=(0.2 W, 0.8 m) and fitted lognormal model.

3.3.2 Amplitude scintillations

Amplitude scintillations can equally be described stastitically using a two parameter model which is now known as the Moulsley-Vilar model. Amplitude scintillations are the results of small scale variations of the refractive index caused by tropospheric turbulence. They result in random fades and enhancements of the received signal as well as fluctuations of phase and angle. Scintillation shows large temporal and seasonal variations which are catered for by the Moulsley-Vilar model, whose validity has been proven on a long term basis **[3.12]**.

At frequencies above 10 GHz, it has been shown that the effect of scintillation has a definite impact on overall communication system performance ([**3.13**]), especially at low elevation angle. In our application this is not however the case, but, as shall be seen, scintillation will be important within the context of low-fade margin systems and predictive Fade Countermeasures, the dynamic characteristics of this random process forcing designers to increase the fade power margin.

Following the work of Moulsley and Vilar **[3.14]**, the scintillation process can be described through a random variable, χ, (nepers) defined by the log ratio of the effectively received signal A to the unfaded signal, A_0, i.e.

$$c = \ln (A/A_0) \qquad \text{np} \tag{3.14}$$

The Moulsley-Vilar model considers the variable χ (np) to be conditionally Gaussian distributed, that is

$$f_{\chi_{np}}(\chi_{np}|\sigma_{\chi_{np}}) = \frac{1}{\sigma_{\chi_{np}} \cdot \sqrt{2\pi}} \cdot \exp\left(-\frac{\chi_{np}^2}{2\sigma_{\chi_{np}}^2}\right) \tag{3.15}$$

where the intensity of scintillation, $\sigma_\chi{}^2$[nepers^2], is itself log-normally distributed therefore

$$f_{\sigma^2_{\chi_{np}}}(\sigma^2_{\chi_{np}}) = \frac{1}{\sigma^2_{\chi_{np}}\,\sigma_{\sigma_{np}}\sqrt{2\pi}} \cdot \exp\left(-\left(\ln\sigma^2_{\chi_{np}} - \ln\,\sigma^2_{m_{np}}\right)^2 \Big/ 2\sigma^2_{\sigma_{np}}\right) \tag{3.16}$$

where $\ln\,\sigma^2_{m_{np}}$ is the mean of $\ln\sigma^2_{\chi_{np}}$ (i.e. $\sigma^2_{m_{np}}$ is the median of the scintillation intensity) and $\ln\,\sigma^2_{\sigma_{np}}$ is the standard deviation of $\ln\sigma^2_{\chi_{np}}$.

After conventional transformation of probability **[3.15]**, the probability density function of the scintillation expressed in dB* can be written as:

$$MV_{\chi}(\sigma_m,\sigma_\sigma) \equiv f_{\chi_{dB}}(\chi_{dB}) = \frac{1}{\pi\sigma_{\sigma_{np}}} \cdot \int_0^{\infty} \frac{1}{\sigma^2_{\chi_{dB}}} \cdot \exp\left[-\frac{\chi^2_{dB}}{2\sigma^2_{\chi_{dB}}} - \frac{\ln\left(\sigma^2_{\chi_{dB}} / \sigma^2_{m_{dB}}\right)}{2\sigma^2_{\sigma_{np}}} \right] \cdot d\sigma_{\chi_{dB}}$$

(3.17)

Moulsley and Vilar showed that the second order moment of the scintillation process $\overline{\sigma^2_{\chi_{dB}}}$ relates to the Moulsley-Vilar model parameters σ_σ [np] and σ_m [dB] as follows **([3.14])**:

$$\overline{\chi^2_{dB} \cdot f_{\chi_{dB}}(\chi_{dB})} = \overline{\sigma^2_{\chi_{dB}}} \approx \sigma^2_{m_{dB}} \cdot \exp\left(\frac{\sigma^2_\sigma}{2}\right) \equiv m_2 \qquad \textbf{(3.18)}$$

Similarly the fourth order moment of the random process can be found to be given by:

$$\overline{\chi^4_{dB} \cdot f_{\chi_{dB}}(\chi_{dB})} = 3 \cdot \left(\overline{\sigma^2_{\chi_{dB}}}\right)^2 \cdot \exp\left(\sigma^2_{\sigma_{np}}\right) \equiv m_4 \qquad \textbf{(3.19)}$$

The two parameters σ_σ (np) and σ_m (dB) of this model can be determined from semi-empirical equations derived from experiments in **[3.16]**. σ_σ(np) is therefore given by:

$$\sigma_\sigma = 0.515 \cdot (\sin\theta)^{-0.2424} \qquad \text{np} \qquad \textbf{(3.20)}$$

The rms. (root mean square) scintillation intensity, σ_χ(dB) is given by :

$$\sqrt{\overline{\sigma^2_\chi}} = \sqrt{m_2} = 0.0165 \cdot \frac{f^{7/12}}{(\sin\theta)^{11/12}} \quad \text{dB}, \quad \text{if } f \cdot \sin\theta > 2.25 \qquad \textbf{(3.21)}$$

$$\sqrt{\overline{\sigma^2_\chi}} = \sqrt{m_2} = 0.0141 \cdot \frac{f}{(\sin\theta)^{1/2}} \quad \text{dB}, \quad \text{if } f \cdot \sin\theta \le 2.25 \qquad \textbf{(3.22)}$$

f being the frequency in GHz and θ is the elevation angle.

Applying these equations to the Chilton-Olympus link, one can get the standard deviation $\sigma_\sigma = 0.61588$ for up and down-link (elevation angle is 28.56°).

---

* *with two changes of variable given by $\chi_{dB} = 10/\ln(10).\chi_{np}$ and $\sigma_{\chi dB} = 10/\ln(10).\ \sigma_{\chi np}$ to transform χ into dB.*

From **(3.21)**, $\overline{\sigma_{\chi,d}} = 0.183\ dB$, $\overline{\sigma_{\chi,u}} = 0.230\ dB$. Neglecting aperture averaging effects, assuming a (worst-case) dB per dB repeater conversion and that scintillation never drives the Olympus TWT into saturation the overall mean scintillation intensity for both up and down links can be estimated using $\sqrt{\overline{\sigma^2_{\chi,t}}} = \sqrt{\overline{\sigma^2_{\chi,u}} + \overline{\sigma^2_{\chi,d}}} = 0.294$ dB ([**3.1**]). So that the median value σ_m is, from **(3.18)**, $\sigma_m = 0.2674$ dB. Figure 3.2 shows the pdf of the scintillation process computed numerically with these parameter values.

3.3.3 The global fading process

In the context of fade countermeasures, it is now widely accepted that the major atmospheric effects above 10 GHz which need to be accounted for are hydrometeor attenuation and amplitude scintillation. In order to investigate accurately their joint statistical impact on satellite link performance, and, using the concepts previously defined of equivalent fading, one can now evaluate the total equivalent impact of joint hydrometeor and scintillation processes by writing the following equation :

$$\left.\frac{C}{N_o}\right|_{t,t} = \left.\frac{C}{N_o}\right|_{t,0} - y + \chi \quad \text{dBHz} \qquad \textbf{(3.23)}$$

This simply states that the overall carrier-to-noise spectral density ratio (CNR) under joint rain and scintillation equals the difference between clear-sky CNR and the sum of the equivalent losses due to hydrometeor and scintillation respectively. The last two terms of **(3.23)** may logically be defined as the global fading process ([**3.1**]), z [dB], for the back-to-back Chilton-Olympus link i.e.

$$z \equiv y - \chi \quad \text{dB} \qquad \textbf{(3.24)}$$

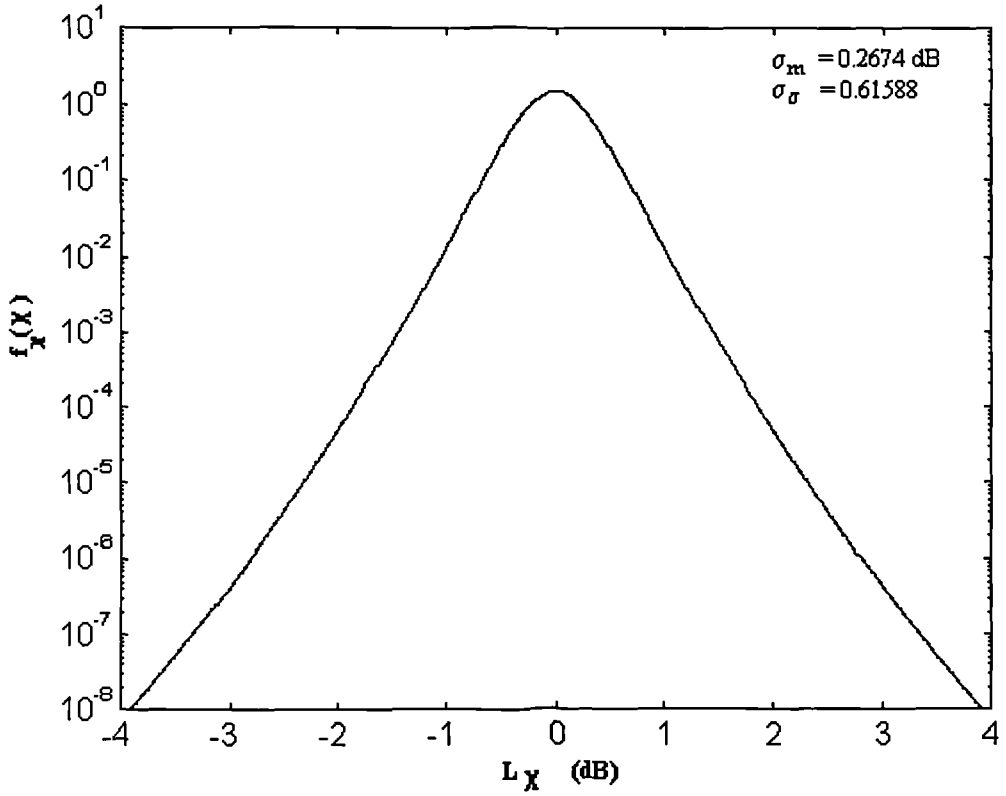

Figure 3. 2: Probability density function of total equivalent amplitude scintillation on the Chilton-Olympus back-to-back link.

Assuming that hydrometeor attenuation and scintillation are independent processes* , then the pdf of the global fading process can be obtained by calculating the convolution of the functions $f_y(y)$ and $f_{\chi_{dB}}(\chi_{dB})$ i.e.

$$GF_z(m,s,\sigma_m,\sigma_\sigma) \equiv f_z(z) = \int_{-\infty}^{\infty} f_y(z-\chi_{dB}) f_{\chi_{dB}}(\chi_{dB}) d\chi = \int_{-\infty}^{\infty} f_y(y)\ f_{\chi_{dB}}(z-y) dy \qquad (3.25)$$

Using **(3.23)**, **(3.24)** and the first equality in the above equation one readily obtains :

$$GF(m,\sigma,\sigma_m,\sigma_\sigma) = f_z(z) = \frac{1}{\sigma_{\sigma_{np}}\cdot\pi}\int_{-\infty}^{\infty}\int_{0}^{\infty}\frac{1}{\sigma^2_{\chi dB}}\cdot\frac{1}{(z-\chi_{dB})\sigma\cdot\sqrt{2\pi}}\cdot\exp\left[-\frac{(\ln(z-\chi_{dB})-m)^2}{2\sigma^2}\right]$$

$$\cdot\exp\left[-\frac{\chi^2_{dB}}{2\sigma^2_{\chi_{dB}}}-\frac{\ln\left(\sigma^2_{\chi_{dB}}/\sigma^2_{m_{dB}}\right)}{2\cdot\sigma^2_{\sigma_{np}}}\right]\cdot d\sigma_{\chi_{dB}}\cdot d\chi_{dB} \qquad \textbf{(3.26)}$$

Figure 3.3 shows the results obtained after computation of **(3.26)** which is a four parameter function of the global fading variable z (dB). It was obtained by convolving the pdfs of the equivalent hydrometeors and scintillation processes with (P_{hpa}, D)=(0.2 W, 0.8 m). It can be noticed, that, as scintillation results in both enhancements and fades of the overall carrier-to-noise ratio, the global fading process naturally inherits also this particular feature justifying the final shape of $f_z(z)$ for $z \leq 0$ dB.

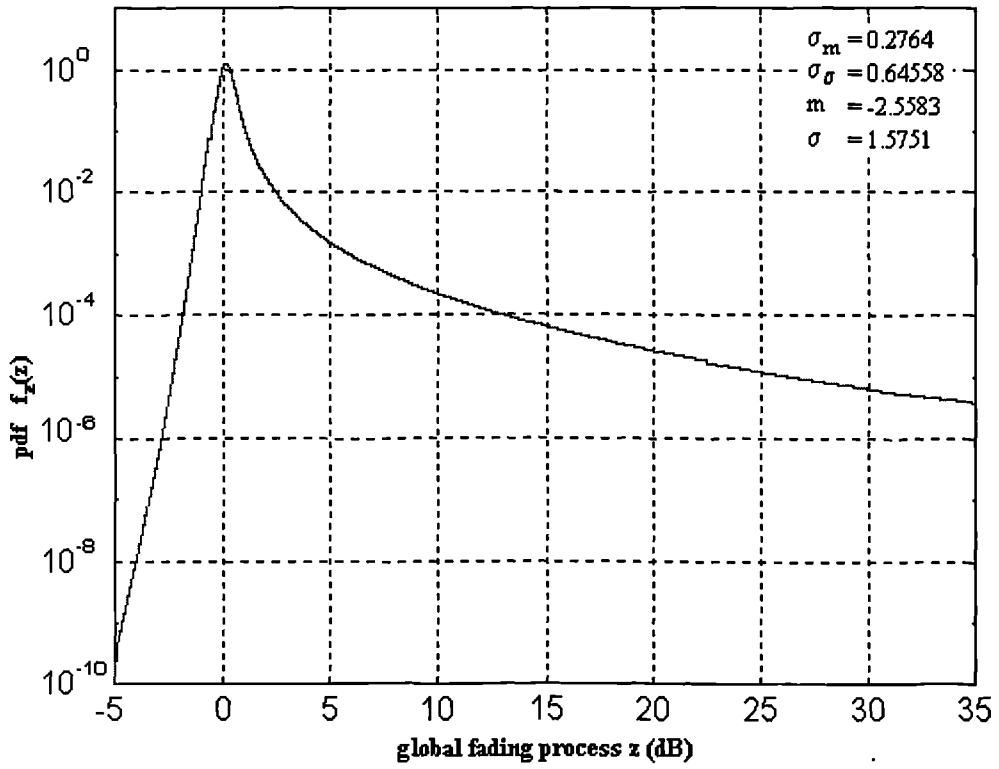

Figure 3. 3: pdf of the global fading process for the Olympus back-to-back link with (P_{hpa} ,D)=(0.2 W, 0.8 m).

* As mentioned in chapter 1, this is currently source of controversy and active research

Now it is possible to evaluate what would be the margin requirements of a satellite system with no fade countermeasure. This can be done by integrating the pdf of the global fading process. This was performed for the Chilton/Olympus system with (P_{hpa} ,D)=(0.2 W, 0.8 m). The required fade protection margins are tabulated below.

% outage	outage time (min)	Required Fade Margin (dB)
1	5260	2.99
0.5	2630	4.33
0.1	526.0	8.64
0.05	263.0	10.67
0.01	52.6	14.02

Table 3. 9: Required Fade protection margin for a typical Ka band in-bound VSAT systems.

Clearly in view of these results, the fixed power margin approach is not applicable to realistic Ka band systems. This is particularly true for VSAT systems which are highly power limited. Also, such high fade protection margins would generate high levels of interference during clear-sky conditions.

3.4 Dynamic impact of fading

3.4.1 Instantaneous frequency scaling

Variations of the rain drop size distribution during events is the source of the time varying instantaneous frequency scaling factor of the rain attenuation process. This has been evidenced both practically and theoretically during the Olympus experiment **[3.17]**. It was found that the instantaneous frequency scaling factor showed a hysteresis characteristic for high level of rain rates. Also, long term study revealed that the scaling factor varies with rain rate. The frequency scaling was found

to agree to a Gaussian distribution centred around the long term scaling factors of the ITU-R model **[3.18]**. The main consequence, for down-link beacon monitoring detection system, is that the extrapolation of the up-link fades based on detected down-link fades, will generate estimation errors which may be of the order of a few dB for high rain rates. As a consequence a fixed margin may need to be introduced to cater for estimation errors in the detection process.

Wet and dry scintillation long-term frequency scaling factors* were found to be identical **[3.19]**. Since the cross correlation factors of scintillations are low in general, especially when derived from data measured with different antennas, it is unreasonable to derive or analyse instantaneous frequency scaling factors. This would result in large short-term variations of the scaling factor.

3.4.2 Rate of change

The rate of change of rain attenuation has received much attention in recent propagation research. This implies that a suitable separation of rain and scintillation processes is performed using filtering techniques. Different methods for doing so are described and compared in **[3.17]**. Results obtained from beacon time-series show that the rate of change increases with attenuation and frequency and the fade slope can reach 1.2 dB/s at 30 GHz **[3.18]**. Although attenuation dependence of fade slope has been identified, no relationship relating those quantities has yet been proposed.

The use of such analysis is that knowledge of the rate of change may be used for short-term prediction of rain attenuation. Also, as any FCM must respond to the real-time variations of the fading process, the FCM control system must be capable of following the stochastic changes of the fading by changing to the appropriate fade protection level. For systems where the levels of fade protection are discrete, there may be outage situations whenever the change in attenuation is greater than the increment to the next fade protection level. The problem would then be to select the appropriate step sizes or required increments so as to minimise those outages due to 'quantisation' effects.

---

* *of the signal standard deviation σ. This is usually based on 1-min variance time-series and equi-probability analysis.*

3.4.3 Fade duration

Short fade durations (<10 sec) are dominated by turbulence effects, rain drop multiple scattering and variation in drop size distribution. They were found to agree to a power law distribution. Long fade durations are mainly rain-induced and were found to conform to a lognormal model.

Fade duration statistics are particularly important for the design of high frequency satellite systems. The obvious utility is to dimension accurately the common pool for shared resource fade countermeasures. Such systems will allocate on demand the back-up resource such as to counteract the deep fades encountered on any particular link. To accommodate any particular network, it is necessary to know the expected duration the resource is likely to be engaged. Also, the analysis of short fades will indicate whether the FCM will suffer frequent switchings in levels of protection, which may be undesirable. Finally, the availability of B-ISDN networks (including a space segment) is specified in terms of cumulative exceedence time composed of intervals greater than 10 seconds and therefore requires the analysis and possible separation of short-fade duration statistics from long-fade duration events **[3.21, 3.22]**.

3.5 Conclusions and further work

Current statistical models for rain attenuation and amplitude scintillations have been reviewed and applied in detail. Their joint impact has been evaluated for different typical Ka band back-to-back link. The system considered is based on a realistic low rate in-bound link VSAT link between the site of Chilton (UK) and ESA's Olympus satellite. This study was based on the concept of global fading, which was introduced by Moulsley and Vilar, through a linearised satellite transponder. The choice of a back-to-back application make this analysis a worst-case one. A less conservative but more truthful approach would be to consider a non back-to-back link using small-scale diversity models.

The dynamic impact of the Ka band fading on realistic FCM satellite systems has been described in terms of instantaneous frequency scaling and rate of change. A particular emphasis was placed on the applicability of such data to the design of practical FCM systems.

The basic results obtained in this chapter will serve as a basis for the long-term statistical modelling of FCM systems. The next chapters will focus on the impact of predictive FCM control operations on overall system performance.

Note that the global fading model introduced by Filip and Vilar does not include the increase in thermal noise generated by absoption by rain and gases (insted a fixed noise temperature is assumed). The global fading model has been extended in **[3.23]** to include this non-negligible effect (up to 2.7 dB in extra carrier-to-noise drop for high attenuation). This was however also neglected for simplicity in this thesis.

References

[3.1] M. Filip, E. Vilar, "Optimum utilization of the channel capacity of a satellite link in the presence of amplitude scintillations and rain attenuation", *IEEE Trans. on Comms.*, Vol. COM-38 No 11, Nov. 1990, pp 1958-1965.

[3.2] M. Williamson, "Salvaging satellites: Mission impossible?", *IEE review*, 1992, pp 179-182.

[3.3] J. Chaplin, "A summary of broadcast activities", *Proc. Olympus Utilisation Conf., Vienna, 12-14 April 1989, ESA SP-292,* May 1989, pp 475-476.

[3.4] D.W. Prouse, "Why SS-TDMA- An introductory tutorial", *Proc. Olympus Utilisation Conf., Vienna, 12-14 April 1989, ESA SP-292,* May 1989, pp 295-299.

[3.5] University of Surrey, Satellite Research Group, *CODE application notes*, ESA contract 7097/87/DG, University of Surrey, Guildford, Nov. 1987.

[3.6] M..J. Willis, B.G. Evans, "An adaptive coding/up-path power control fade countermeasure experiment via Olympus", *Proc. Olympus Utilisation Conf., Vienna, 12-14 April 1989,* ESA SP-292, May 1989, pp 151-155.

[3.7] G. Maral, *VSAT networks*, John Wiley and sons, 1995.

[3.8] ESA, *"Co-operative Olympus demonstration experiment, CODE, Outline system description"*, CCE/45870/CS/ap, Issue 1, December 1987.

[3.9] ITU-R, 1994 PN Series Volume, Propagation in non-ionized media, *"Aspect relative to space telecommunication systems"*, Rec. ITU-R PN.618.3, 1994, pp 329-343.

[3.10] L.J. Ippolito, *Radiowave propagation in satellite communications*, Van Nostrand Reinhold, New York, 1986.

[3.11] V.K. Bhargava, D. Haccoun, R. Matyas, P.P. Nuspl, *Digital Communications by Satellite*, John Wiley & Sons, 1981.

[3.12] ESA, *Second workshop of the Olympus experimenters, Volume 1, Reference book on attenuation measurement and prediction, Noordwijk, 8-10 Nov. 1994,* "Chapter 5: Atmospheric scintillation", ESA ESTEC WPP-083, Noordwijk, The Netherlands, pp 49-64.

[3.13] D. Vanhoenacker-Janvier, H. Vasseur, "Prediction of scintillation effects on satellite communications above 10 GHz", *IEE Proc. Microw. Antennas Prop.*, Vol. 142, No 2, April 1995, pp 102- 108.

[3.14] T.J. Moulsley, E. Vilar, "Experimental and theoretical statistics of microwave amplitude scintillations on satellite down-links", *IEEE Trans. on Ant. and Prop.*, Vol. AP-30, No 6, Nov. 1982, pp 1099-1106.

[3.15] A. Papoulis, Probability, *Random variables and stochastic processes,* McGraw-Hill International ed., 1991.

[3.16] E. Vilar, J.R. Larsen, "Elevation dependence of amplitude scintillations on low elevation Earth-Space paths", *Proc. Sixth Int. Conf. on Antennas and Propagation, ICAP'89*, University of Warwick (UK), April 1989.

[3.17] ESA, *Second workshop of the Olympus experimenters, Volume 1, Reference book on attenuation measurement and prediction, Noordwijk, 8-10 Nov. 1994,* Chapter 7: Characteristics of events, ESA ESTEC WPP-083, Noordwijk, The Netherlands, pp 87-123.

[3.18] F. Rücker, "The impact of instantaneous frequency scaling factors on up-link power control", *AEÜ*, Vol. 48, No. 2, 1994, pp 119-121.

[3.19] G. Ortgies, "Slant-path frequency scaling of amplitude scintillations during clear-sky conditions and rain", *AEÜ*, Vol. 47, No. 4, 1993, pp 203-208.

[3.20] F. Rücker, "Frequency and attenuation dependent fade slope statistics", *Electronics Letters,* Vol. 29, No 9, April 1993, pp 744-746.

[3.21] A. Paraboni, C. Riva, "A new method for the prediction of fade duration statistics in satellite links above 10 GHz", *Int. J. of Satellite Comms.*, Vol. 12, 1994, pp 387-394.

[3.22] T.K.P. Chung, "A study of the dynamic aspects of rain fades on earth-satellite communication links with application to fade countermeasures", MPhil thesis, Coventry University, Sept. 1996.

[3.23] M-S. Alouini, S.A. Borsgmiller, P.G. Steffes, "Channel characterization and modeling for Ka band very small aperture terminals", *Proc. IEEE*, Vol. 85, No 6, June 1997, pp 981-997.

4. Short-term Prediction of the Ka band Fading Process

4.1 Introduction

The total time delay in FCM operation implies the detailed investigation of the predictability of the Ka band fading as a whole. The objective of this chapter is to implement a *novel* short-term predictor based on the dynamic characteristics of the Ka band fading. It is to be included in a predictive FCM control system.

A major concern is the well known non-stationarity of both rain and scintillation processes. As a consequence, a good predictor should take into account the statistical variability of the Ka band fading and should therefore be time-varying. Furthermore, one may desire a predictive controller that can adapt itself to any link configuration without the need for tuning to a particular case. Both operations can be made using the concept of self-tuning systems. One such system will be presented here.

A short-term predictor is obtained by application of classical model identification techniques and stochastic control theory to an experimental beacon time-series at 30 GHz measured by the Rutherford Appleton Laboratory at their site of Chilton (UK). This model is then compared with other predictor proposed in the literature. The proposed predictor is then characterised in terms of rain and

attenuation processes, so that a long-term statistical model including the predictor's performance can be developed. This yields the concept of modified global fading which is then generalised in the last part of this chapter.

4.2 Dynamic characterisation of the Ka band fading

In order to consider the possible impact of time delays on FCM systems in the presence of global fading, a short-term predictor of the Ka band fading is required. Its prediction ability will depend on how this model can capture the essential dynamics of joint hydrometeor and scintillation processes.

4.2.1 Model identification

The following parametric model identification is based on an event analysis of an experimental beacon time series. It was measured by the Rutherford Appleton Laboratory (RAL) at their site at Chilton (UK) during ESA's Olympus experiment. The database spans a period between Sept. 91 and Sept. 92. The sampling frequency was 1 Hz. From this data, 17 rain events at 30 GHz of different amplitude and duration were selected for study. They were fitted into fixed observation windows of 4000 seconds for easy comparison and averaging of autocorrelation functions and power spectrum densities (PSD). The total propagation data used for model identification was thus approximately 19 hours. The raw attenuation was extracted by removing the clear-sky levels manually from the raw Olympus data. The objective was to derive the best discrete linear model of the ARMA (na,nc)* class defined by **[4.1]**:

$$z(t) \approx y(t) = -\sum_{n=1}^{na} a_n \cdot y(t-n) + e(t) + \sum_{n=1}^{nc} c_n \cdot e(t-n) \Leftrightarrow y(t) = \frac{C(q^{-1})}{A(q^{-1})} \cdot e(t) \qquad (4.1)$$

rain component — scintillation component

1 step-ahead predicted rain component

Auto-Regressive Moving Average

with $C(q^{-1}) = 1 + \sum_{n=1}^{nc} c_n \cdot q^{-n}$, $A(q^{-1}) = 1 + \sum_{n=1}^{na} a_n \cdot q^{-n}$.

y(t) and e(t) are respectively the fading variable (dB) and the residual or error variable (dB) at time t. q^{-1} is the backward shift operator defined by q^{-1} y(t)= y(t -1). The other symbols are defined below.

This simple dynamic model is an attempt to consider that rain and scintillation processes are additive according to the global fading hypothesis (see chapter 3). It assumes that the global fading at time t is $z(t) \approx y(t)$* which is equal to a term corresponding to a linear combination of previous detected samples of the rain component, y, as well as a linear combination of previous samples up to and including time (t-1), of the scintillation component, e, at time step, t. The residual sample, e(t), will not be accessible at time t and thus it will result in a prediction error.

Model order Selection

The optimum orders na and nc of the ARMA model were determined using Akaike's criterion (denoted by AIC) coupled with a Gauss-Newton algorithm for iterative MMSE** estimation of the corresponding parameters a_n and c_n **[4.1]**. That is, for each individual event, the parameters, a_n and c_n , were algorithmically computed with the sole constraint of minimising the variance of the resulting residual sequence, {e(t)}.

All the possible combinations (na, nc) for na and nc = 0 to 5 were evaluated. This represents 35 models per selected event. The best model was then identified by studying the average AIC results for the 17 selected events of duration N=4000 seconds.

The AIC defined by **[4.1]**:

$$AIC = \log\left(\frac{1}{N}\sum_{t=1}^{N} e^2(t)\right) + 2\frac{d_m}{N}, \quad d_m = n_a + n_c \qquad \textbf{(4.2)}$$

was used for model order selection.

---

* *This is only an approximation which is valid whenever the fade is dominated by rain.*

** *Minimum Mean square Error*

It considers the sum of a measure accounting for the model fitting errors to which is added a penalty term accounting for model complexity. The first minimum AIC was found to be obtained for a ARMA model of order (3,3). This is shown on Figure 4.1. Note that the purely moving average terms (na, nc)=(0, i), i = 0, 1, 2, 3, 4, 5 are not shown here because they lead very high values of AIC. The AIC curve indicates generally that at least two or three auto-regressive terms are needed for good identification of the Ka band fading. This fits with known previous results obtained by test-out procedure **[4.2]**.

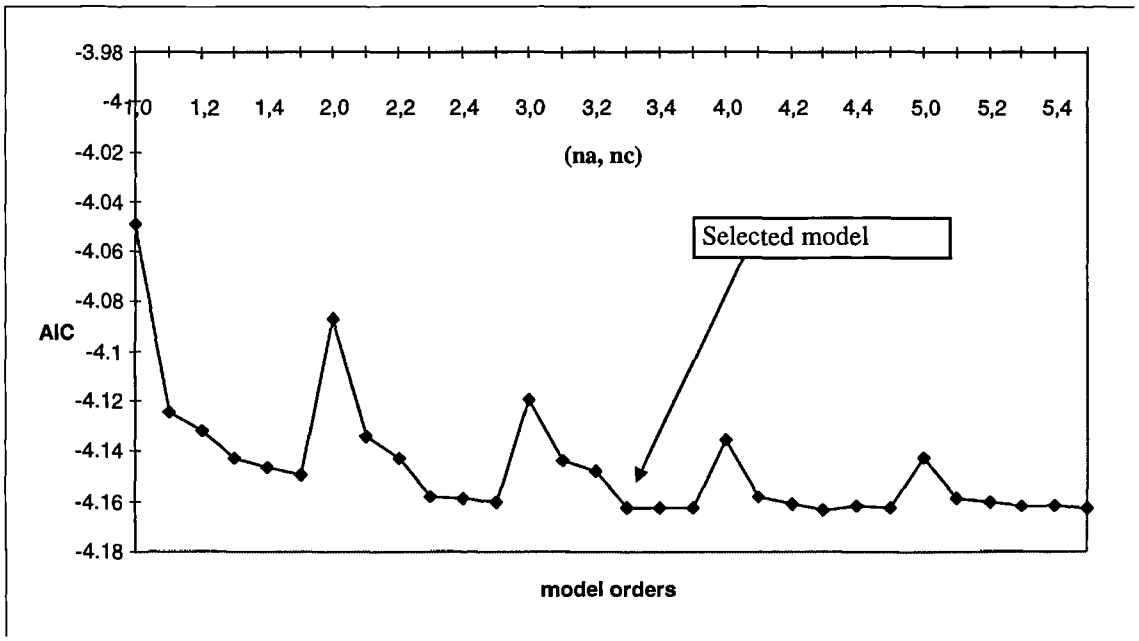

Figure 4. 1: Average AIC criterion for ARMA model order selection.

Model Validation **[4.1]**

Model validation was performed by testing the whiteness of the residual sequence {e(t)} of the candidate models with autocorrelation methods. The autocorrelation function (ACF) of the residual sequences was evaluated for each of the fitted ARMA (3,3) models. The ARMA (3,3) residuals were found to be white with a 99 % level of confidence, thereby validating the ARMA (3,3) model as a suitable model for modelling the Ka band fading.

Modelled power spectrum density (PSD)

It can be shown that the theoretical PSD of the ARMA (3,3) model is given by **[4.3]**:

$$S_{yy}(e^{iw}) = \frac{\sigma_e^2}{2\pi}\left|\left(1+\sum_{n=1}^{nc=3} c_n.e^{-niw}\right)\Big/\left(1+\sum_{n=1}^{na=3} a_n.e^{-niw}\right)\right|^2 \qquad (4.3)$$

where • $_e^2$ is the variance of the residuals.

A typical PSD fitted off-line to one 30 GHz event is shown in Figure 4.2 showing the appropriateness of the ARMA(3,3) model rational spectral density function in the frequency domain. More particularly, the model seems capable of capturing the essential dynamics of the global fading process across the whole frequency range. We shall now characterise the ARMA model in terms of rain and amplitude scintillation processes.

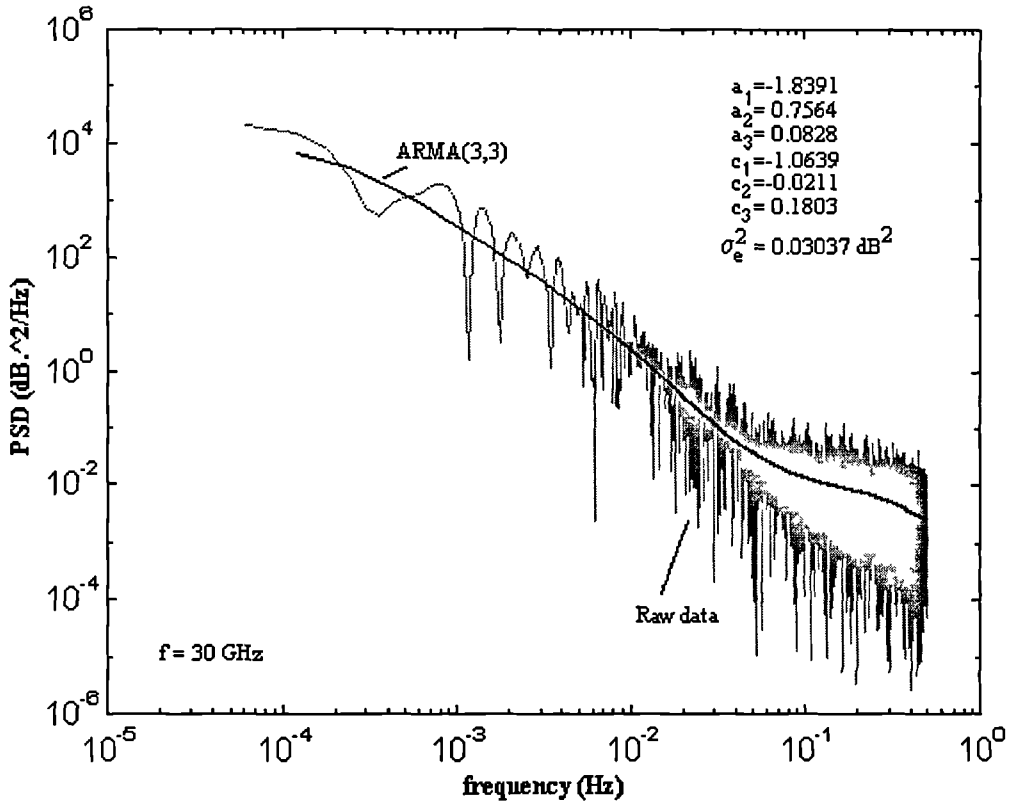

Figure 4. 2: Experimental and modelled PSD for one event at 30 GHz.

4.2.2 Model characterisation in terms of rain and scintillation processes.

On inspection of equation **(4.1)**, one can see that the ARMA(3,3) model is already predictive, with the fading process $z(t) \approx y(t)$, inferred from three previous samples of y and of the error e. Similar results are quoted in **[4.2]** where it is indicated that two or three autoregressive terms are required for good prediction of the rain component of the Ka band fading. However the ARMA model has also Moving Average terms which model a part of the high frequency component, the other part being white and contained in $\{e(t)\}$.

We shall compare the predicted fading sequence $\{y(t)\}$ with the expected rain sequence obtained using classical filtering techniques. In the following, the ARMA model output z(t) has been compared with a low-pass version of the raw Olympus data. The low-pass filter (LPF) was a fourth order zero-phase Butterworth filter and had a cut-off frequency located at 0.07 Hz. The scintillation component was extracted by subtraction between the raw Olympus data and its low-pass version* . The one-step ahead predicted sequence of the ARMA model, $\{z(t)\}$, was then also low-pass filtered and plotted against the estimated Olympus rain sequence for all 17 events. Similarly, the extracted scintillation sequence estimated from the raw data was compared to *the sum* of the high pass sequence of $\{z(t)\}$ with the residuals $\{e(t)\}$.

Mathematically, the output of the ARMA model is

$$z_{Olympus}(t) = z_{ARMA}(t) + e(t) = z_{ARMA|LPF}(t) + (z_{ARMA|HPF}(t) + e(t)).$$

This was compared to the filtered rain and scintillation components given by :

$$z_{Olympus}(t) = z_{Olympus}(t)|_{LPF} + z_{Olympus}(t)|_{HPF} \equiv y(t) + \chi(t).$$

In Figure 4.3 is shown a scatter plot of $z_{ARMA|LPF}(t)$ against $z_{Olympus}(t)|_{LPF}$, which corresponds to the estimated rain component. y(t). Similarly, Figure 4.4 shows the scatter plot of $(z_{ARMA|HPF}(t) + e(t))$ versus $z_{Oympus}(t)|_{HPF}$ which corresponds to the estimated scintillation component $\chi(t)$.

---

* *As the filter used is zero phase, there is no time-delay between the raw data and its LPF version, therefore ensuring efficient separation of effects.*

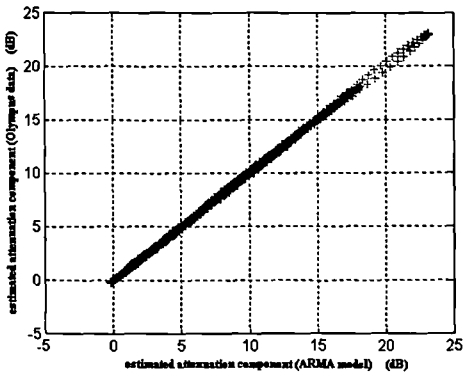

Figure 4. 3: Estimated rain component for 19 hours of data.

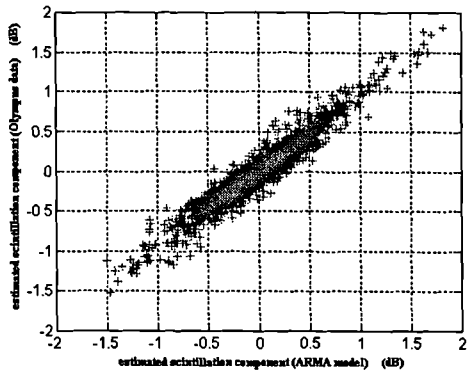

Figure 4. 4: Estimated scintillation component for 19 hours of data.

The match is quite remarkable, showing the equivalence of the two methods for separating rain and scintillation from the raw Olympus data in the time domain. The main difference can be seen in the frequency domain for scintillation. This is shown in Figures 4.5 and 4.6. Figure 4.5 shows the estimated PSD obtained after high pass filtering of the raw Olympus data.

Figure 4.6 shows the estimated PSD of scintillation based on the combination ($z_{ARMA|HPF}$ (t)+e(t)). Clearly both PSDs show the typical $f^{-8/3}$ roll-off of amplitude scintillations ([**4.4**]), however the latter is clearly the best estimate due to the flat low frequency characteristics. This increases substantially the scintillation variance.

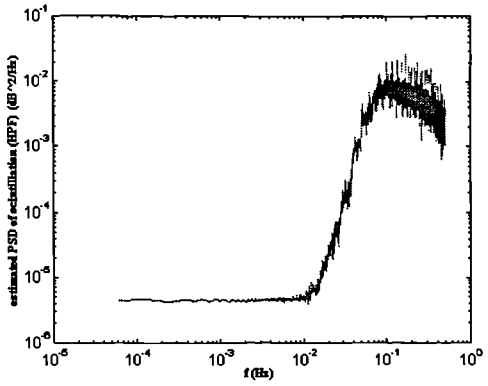

Figure 4. 5: Average PSD of estimated scintillation over a 19 hour period (Based on high pass filtering of the Olympus data).

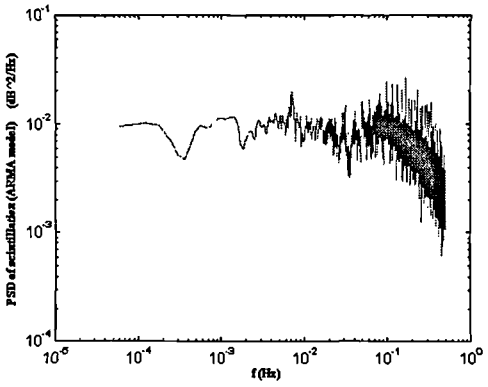

Figure 4. 6: Average PSD of estimated scintillation over a 19 hour period (Based on ARMA model).

The spectrum in 4.6 has such low frequency characteristics due to the white spectrum property of the residuals sequences {e(t)}. In other words, the scintillation component is made of two components, one displaying the $f^{8/3}$ slope and another one being uncorrelated. Thus the ARMA (3,3) model partially captures the scintillation process, the residuals being that part of scintillation that is white and that cannot be predicted. In any case, the residual sequence is the major contributor to the scintillation variance (area under the spectrum) and therefore one may write:

$$\chi(t) \approx y_{ARMA|HPF}(t) + e(t) \Rightarrow \sigma_\chi^2 \approx \sigma_e^2 \text{ because } \sigma^2_{ARMA|HPF} << \sigma_e^2 \qquad (4.4)$$

The sequences of residuals {e(t)} can be expected to have the characteristics of scintillation and thus agree with the Moulsley-Vilar model. Similarly, the ARMA model output sequence {y(t)} is expected to have the characteristics of rain attenuation and it should conform to a lognormal density function.

The discussion in this section should be considered with great care. This comes from the fact that the separation of rain and scintillation from raw data is a difficult operation (see Chapter 6). This section corresponds to an attempt to characterise the ARMA model prediction ability in terms of the physical rain and scintillation processes. This is carried out using an ad-hoc method but this does not infer greatly on the analysis following this section, since, as we shall see, the error has the main statistical characteristics of scintillation. It may therefore be assumed that the error {e(t)} is essentially consistent with scintillation and that as an approximation one can assume that it is reasonably well modelled as scintillation.

4.2.3 Probability density function (pdf) of the residuals

The sample pdf of the residual sequence was evaluated over the 19 hour period and was found to agree to the Moulsley-Vilar distribution, defined in section 3.3.2. More particularly, the two parameters of the Moulsley-Vilar distribution $\sigma^2_{m_{dB}}$ and σ^2_{σ} were evaluated using **(3.18)** and **(3.19)** from the second and fourth order moments $\overline{e^2_{dB} \cdot f_{e_{dB}}(e_{dB})} = m_2$ and $\overline{e^4_{dB} \cdot f_{e_{dB}}(e_{dB})} = m_4$, of the 19 hour empirical residual sequence. This is shown in Figure 4.7. Clearly the agreement is very good.

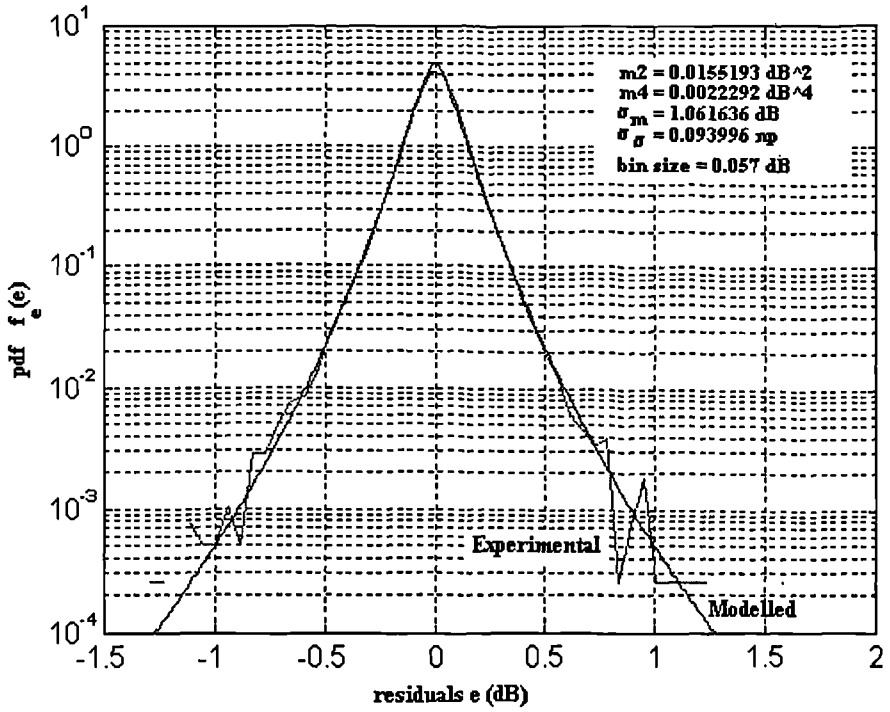

Figure 4. 7: Sample pdf of the residual sequence (19 hour of data).

4.3 Prediction of the Ka Band fading

Both scintillation and rain attenuation are known to be non-stationary. While scintillation appears to reach statistical equilibrium after a few hours ([4.4]) rain is clearly non-stationary and stabilises statistically after period of around 7 to 12 years ([4.5]). As a consequence, the ARMA model must be time-varying. This can be achieved using adaptive or self-tuning systems. Finally, using well-known results of stochastic control theory, the ARMA model will be modified to become predictive using the minimum variance approach. The ARMA-based predictor will then be compared to other predictors proposed in the literature. A block diagram of the self-tuning RELS*/minimum variance predictor is shown in Figure 4.8, where DM denotes a detection margin to be discussed later.

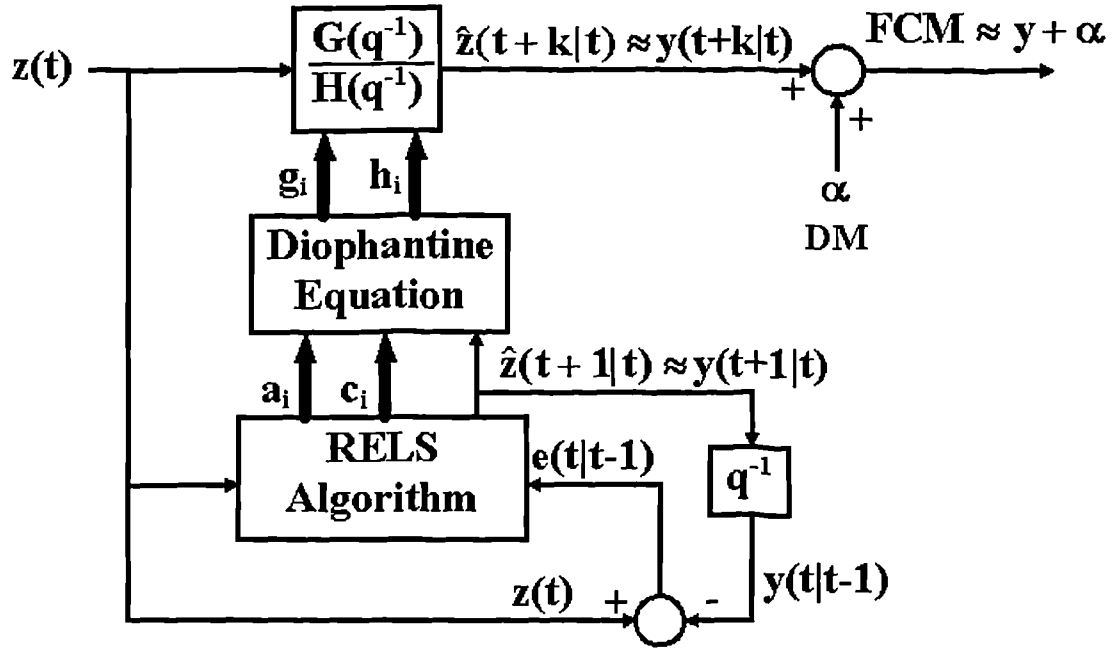

Figure 4. 8: RELS/minimum variance predictor.

4.3.1 Self-Tuning Identification (RELS algorithm)

As mentioned earlier, the residual sequence of the ARMA model has the statistical characteristics of scintillation. The estimation of the model coefficients and residuals was obtained off-line using a Gauss-Newton algorithm for iterative parameter estimation. Within the context of fade countermeasure, the algorithm can be easily transformed into an on-line algorithm in which the 6 parameters of the

* *Recursive Extended Least Squares.*

ARMA model are evaluated every second at time t based on information up to and including (t-1). These methods are based on the minimisation of the on-line residual variance σ_e^2. The MMSE criterion is thus equivalent to finding the mean path of the Ka band fading which minimises the scintillation intensity around that path. This makes sense in the context of Ka band fading since scintillation is usually described in terms of its variance. The MMSE approach can therefore be seen as a means of not overestimating the scintillation intensity ensuring efficient unbiased estimation of the actual real-time fades. Another important aspect is that on-line estimators, due to their self-tuning property, can be applied to any geographical link configuration. This is because they can track on their own the time-varying nature of the atmospheric channel. This may be important whenever FCM controllers are expected to be applicable irrespective of ground location and satellite position. Such an algorithm based on the recursive extended least squares is outlined in Appendix A4.I or **[4.6]**. It has been used to simulate the on-line estimation/prediction of the Ka band fading.

4.3.2 Minimum variance prediction

The ARMA model can easily be extended to a k-step ahead predictor by using the minimum variance approach (see Appendix A4.I or **[4.6, 4.7]**) based on the minimisation of the predicted error variance given samples up to time t i.e.

$$m_2(k) = E\{[y(t+k) - y(t+k|t)]^2\} = E\{e^2(t+k|t)\} \quad dB^2 \qquad (4.5)$$

where E{ } denotes statistical expectation and $k \geq 1$ is the prediction time (in seconds).

For k=1, the ARMA model simply gives a MMSE estimate of the rain fading component. The error is essentially a white scintillation process. In order to identify the two parameters of the Moulsley-Vilar model, the error must first be defined in terms of its second and fourth moments. We shall now express the prediction error as a function of the prediction time k.

4.3.3 Event-based simulation

Figure 4.9 shows the raw Olympus data along with the one obtained after application of the self-tuning predictor for a lead time of 10 seconds. The model parameters were determined on-line using the RELS algorithm, while the prediction was performed using the minimum variance approach. The curves are very similar and a more crucial test is to display the prediction error as a function of time (see Figure 4.10). When the prediction time is only 1 second, the peak error amplitude is limited to approximately 0.8 dB. This figure increases to 4.5 dB when the lead time is 10 seconds. The peak error usually occurs around the maximum level of Ka band fading, which corresponds to the location where large changes in fade slope occur. The error is essentially consistent with scintillation and is almost unpredictable. This would then be compensated using a fixed or variable detection margin (FDM or VDM, see Chapter 5). It is then important to minimise this margin. The MMSE approach to short-term prediction is therefore particularly justified, since the objective is equivalent to minimising the spread of the error around its zero mean, implicitly allowing the sought minimisation (in a mean square sense).

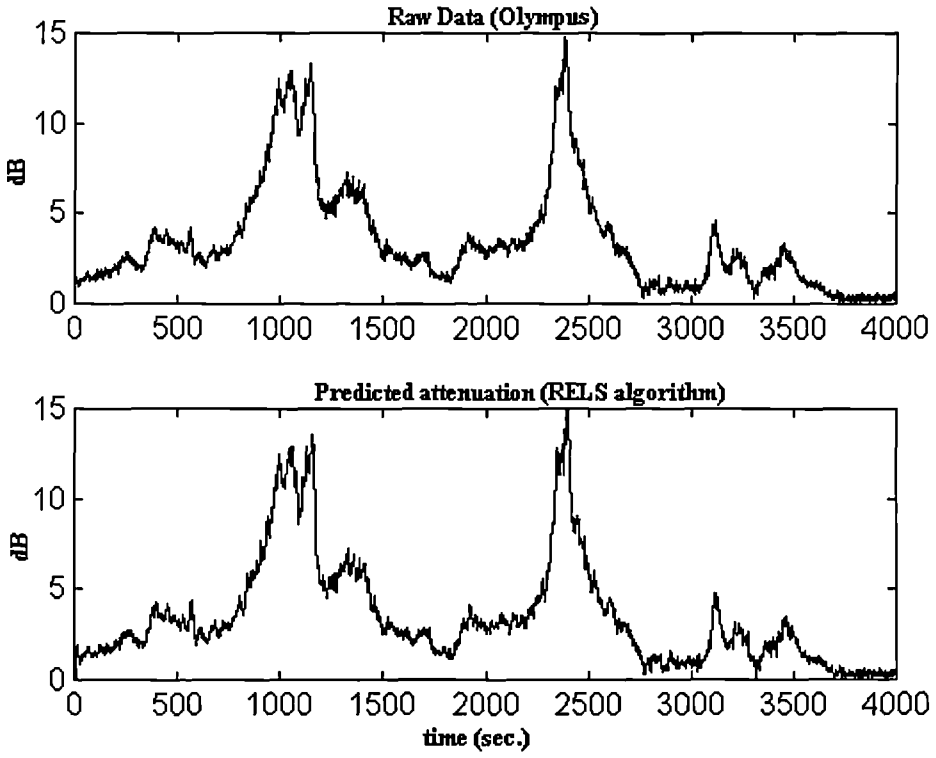

Figure 4. 9: Raw event and short-term predicted total attenuation using the RELS algorithm (frequency = 30 GHz)

Figure 4.11 shows the 6 parameters of the ARMA(3,3) model as determined on-line by the RELS algorithm. The relatively wide variations of each of the parameters tend to confirm the non-stationary nature of the Ka band fading process. The trace of the covariance matrix (Figure 4.12) converges rapidly. This indicates a good certainty in estimating on-line the 6 parameters of the ARMA model. Thus the dynamics of the Ka band fades are captured appropriately by the self-tuning predictor. As long as the rain component is dominant (e.g. around t= 1000 seconds in Figure 4.9), the error variance is relatively small, however in static conditions (e.g. around t = 2000 or t = 3000 s. in Figure 4.9), the error variance increases substantially, emphasising that the ARMA model cannot capture well the scintillation process, which is the prediction error.

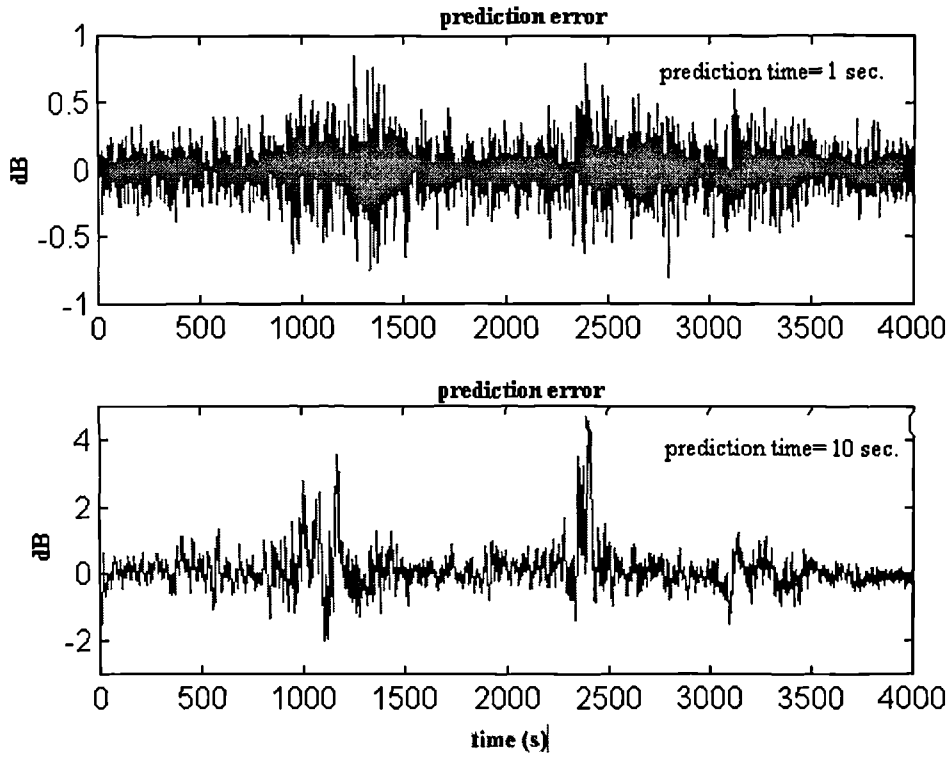

Figure 4. 10: Prediction error for the RELS based predictor for 2 different lead times of 1 and 10 seconds for the event shown in Figure 4.9.

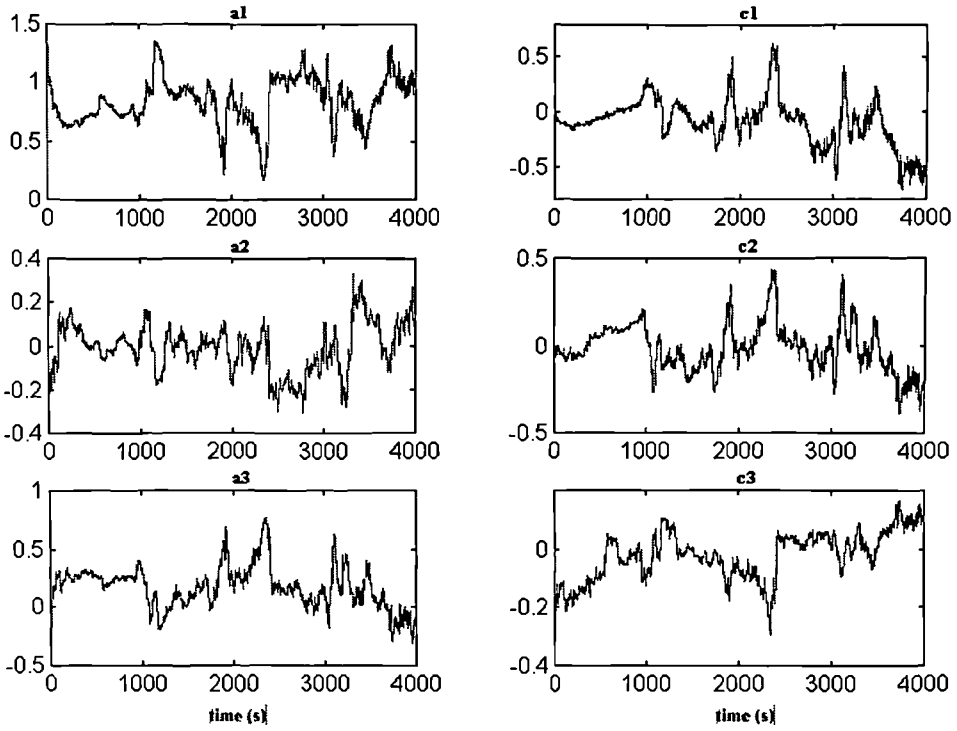

Figure 4. 11: Plots showing the time-varying nature of the 6 parameters of the ARMA model as determined on-line by the RELS algorithm

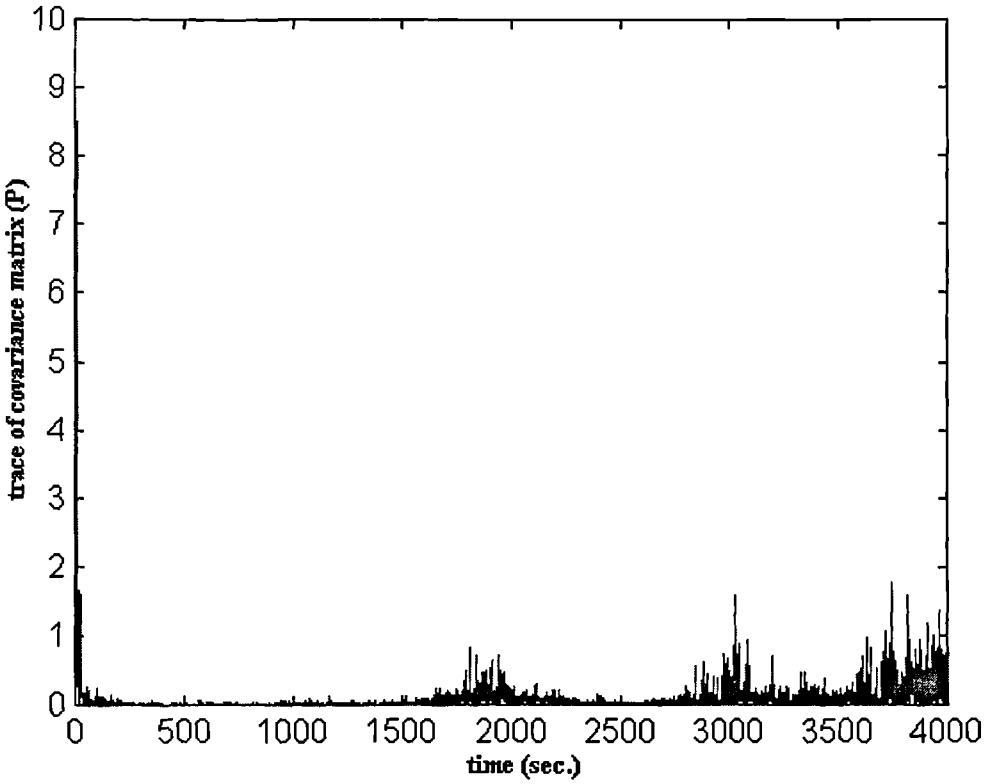

Figure 4. 12: Trace of the covariance matrix as determined by the RELS algorithm.

4.3.4 Comparison with other predictors

Four models were investigated in terms of their prediction errors for a lead time of 1 to 20 seconds using the test Olympus data. They were compared in terms of the prediction error variance as a function of the lead time. The results were averaged for each particular model over the 17 hours Olympus data.

Model (a) is taken from reference **[4.8]**. It assumes that good prediction of the fading is achieved by computing $y(t+T) = y_{lp}(t) + T.\ S(t)$, where T is the prediction time, S(t) is the slope of the rain signal and y_{lp} is a low pass version of the raw time-series. The on-line filter used for this simulation was a moving average low-pass filter given by $y_{lp}(t) = 0.1 \cdot \sum_{i=1}^{10} y(t-i)$.

Model (b) assumes that the attenuation does not change within the prediction time T, that is, $y(t+T) = y_{lp}(t)$ **[4.8]**.

Model (c) results from the application of the parametric identification procedure of the ARMA (3,3) model coupled with the minimum variance approach.

Model (d) is a discrete version of the first order non-linear Markov process. It was inspired from **[4.9]**. It was obtained by fitting the best ARMA (1,0) model to the transformed Olympus time-series u=(ln(y)-m)/• where y is the raw beacon signal m and • • are the estimated parameters of the lognormal model for rain attenuation at 30 GHz* . The best ARMA (1,0) model was then fitted using parametric identification methods to the Gaussian sequences {u (t)}, then the data was transformed back into a lognormal model using exp(• • u_{pred}+m). This allows inclusion of the well-known log-normality of rain attenuation into the model and may be useful for rain event synthesis.

The comparative results are shown in Figure 4.13. They show the superiority of the ARMA (3,3) model especially for long lead times. Also note that the error variance increases approximately linearly for prediction times longer than 10 seconds except for the slope-based predictor. These linear trends for long lead time fit with results found in **[4.8]**. Due to its good prediction ability, the ARMA(3,3) model will

m=-2.3858, σ=1.4943 at 30 GHz for the Chilton Olympus link. This was evaluated using the method and data described in section 3.3.1 and Table 3.6 respectively.

now be retained for more detailed analysis of the impact of time delays on the prediction error pdf.

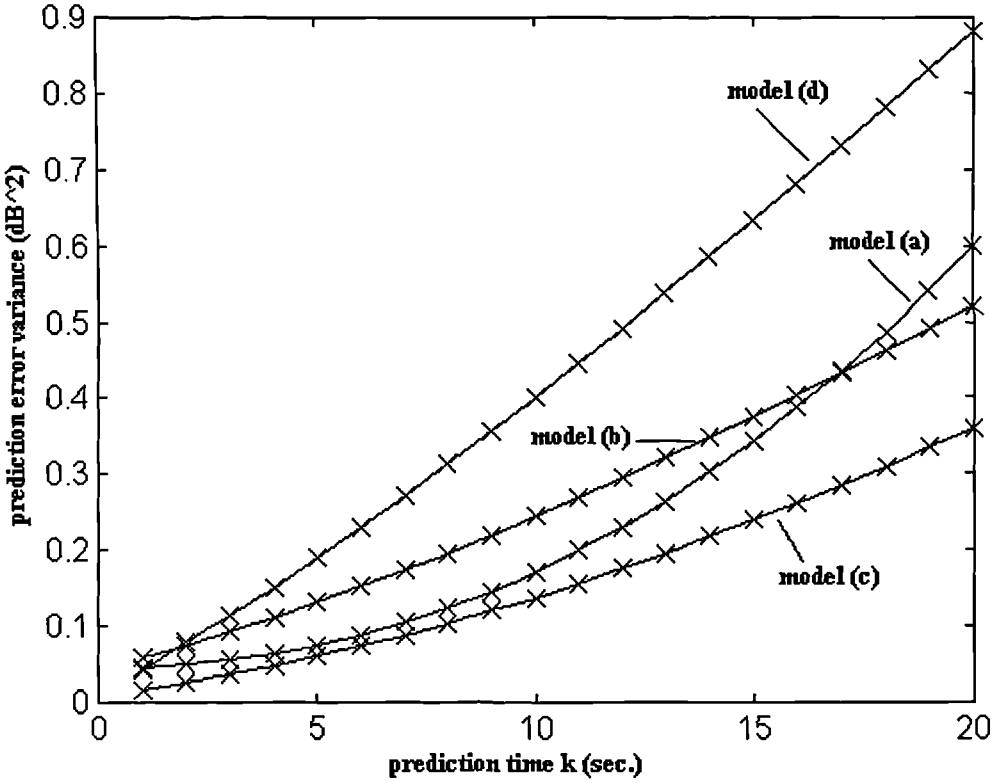

Figure 4. 13: Comparison of four predictive models of the Ka band fading (19 hours of data).

4.4 Impact of time delays on the probability density function of the prediction error

The data revealed that the residuals conformed to a MV pdf. Furthermore, in view of equation (**4.4**), we may assume that $e(t+1|t) \approx \chi(t)$. Full statistical characterisation of $\{e\}$ therefore requires only the study of its second and fourth moments as a function of the lead time, $m_2(k)$ and $m_4(k)$. For k=1 s (no prediction), we can already state that $m_2(1)=m_2$ and $m_4(1)=m_4$, i.e., they are approximately the long term MV parameters (see section 3.3.2).

Although the solution of **(4.5)** can be related directly to the ARMA model parameters and therefore to the dynamics of the Ka band fading, (see section 4.6), we shall use here a more empirical solution for determining the impact of time delays. Using the predictor outlined in Appendix A4.I, the average sample second and fourth moments were computed for the 17 Ka band events as a function of the prediction time k. Least square fitting to the empirical data yielded:

$$\begin{cases} m_2(k) = m_2 \cdot f_2(k) \\ m_4(k) = m_4 \cdot f_4(k) \end{cases} \qquad \textbf{(4.6a)}$$

where

$$\begin{cases} f_2(k) = 0.0337 + 0.487 \cdot k + 0.525 \cdot k^2 \\ f_4(k) = 0.046 + 0.368 \cdot k + 0.319 \cdot k^2 + 0.3499 \cdot k^3 - 0.0312 \cdot k^4 + 0.0022 \cdot k^5 \end{cases} \qquad \textbf{(4.6b)}$$

Figure 4.14 shows the experimental and fitted normalised increase of the second order error moment, $f_2(k)$, and fourth order error moment, $f_4(k)$, error moments. These curves are indicative of the limitations of the ARMA-based predictor. Realistically, an efficient predictor would be expected to have $m_2(k)=m_2$ and $m_4(k) = m_4$ for all k. This would mean that time delays do not change the characteristics of scintillation and that the second and fourth moments are equal to the ones determined by the Moulsley-Vilar model (see section 3.3.2). In practice, different predictors would have different increases in normalised moments. Thus equation **(4.6b)** is indicative of the *particular* performance of the ARMA based predictor. Other predictors would have different characteristic functions $f_2(k)$ and $f_4(k)$.

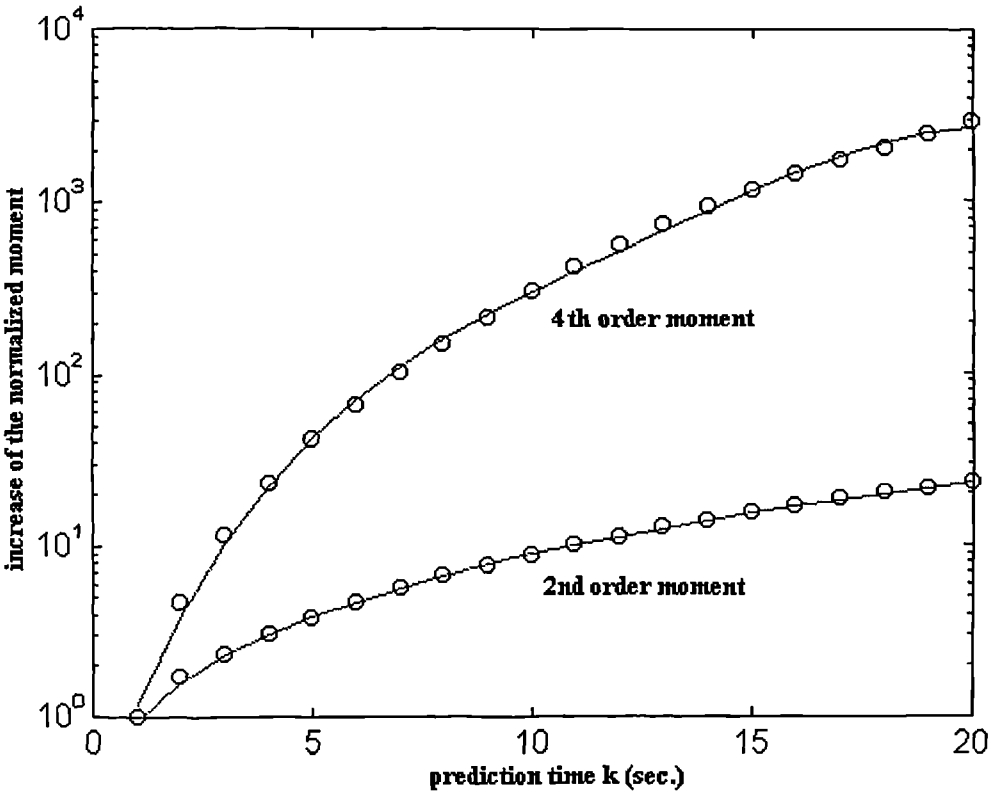

Figure 4. 14: Relative experimental and fitted (solid lines) average increase of the second and fourth moments of the prediction error against lead time (19 hours of data).

Using **(4.6)**, the sample pdf of the error signal e(t+k|t) can now be evaluated for different k. The theoretical pdf shown by dashed lines in Figure 4.15 was obtained by computing (see equation **(3.15)**):

$f_e(e) = \mathrm{MV}_e(\sigma_m(k), \sigma_\sigma(k))$, which on expansion gives:

$$f_{e_{dB}}(e_{dB}) = \frac{1}{\sigma_{\sigma_{np}}(k)\cdot\pi}\cdot\int_0^\infty \frac{1}{\sigma^2_{\chi_{dB}}}\cdot\exp\left[-\frac{e^2_{dB}}{2\sigma^2_{\chi_{dB}}} - \frac{\ln\left(\sigma^2_{\chi_{dB}}/\sigma^2_{m_{dB}}(k)\right)}{2\cdot\sigma^2_{\sigma_{np}}(k)}\right]\cdot d\sigma_{\chi_{dB}} \qquad \textbf{(4.7)}$$

The two parameters of this pdf have been evaluated from inverted forms of **(3.18)** and **(3.19)** giving:

$$\sigma^2_\sigma(k) = \ln\left(\frac{m_4(k)}{3.[m_2(k)]^2}\right) \qquad \textbf{(4.8a)}$$

$$\sigma^2_m(k) = \sqrt{3}[m_2(k)]^2/\sqrt{m_4(k)} \qquad \textbf{(4.8b)}$$

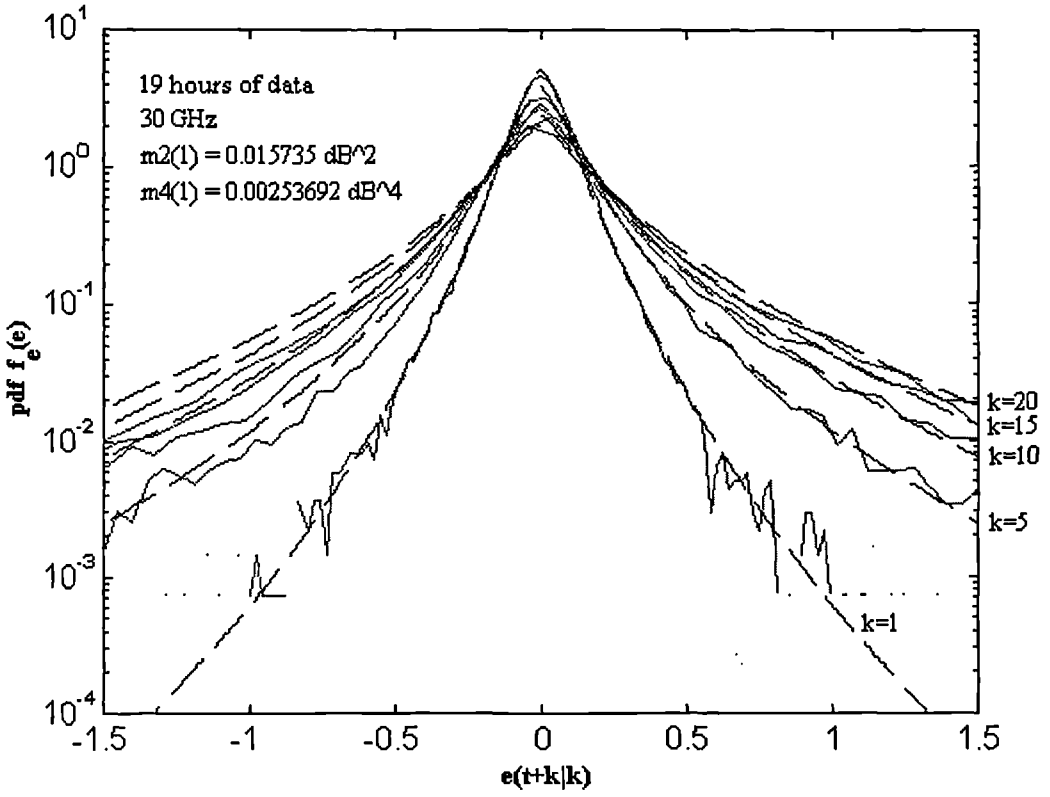

Figure 4. 15: Modelled and measured pdf of the prediction error for different prediction times.

The average pdf of the error has been computed for the 19 hour test data for different lead times. This is shown in Figure 4.15. The fit between theoretical and experimental error pdfs is particularly good for positive amplitudes of the error. For negative errors, the theoretical model seems to over-estimate. The model can however be accepted as very reliable for short time delays ($k \leq 5$ sec.). One can notice the strong impact of time delays on the pdf of the prediction error. For k = 1, the ARMA (3,3) model exhibits a prediction error which has a MV pdf consistent with scintillation i.e. $MV_e(\sigma_m(1),\sigma_\sigma(1)) \approx MV_\chi(\sigma_m,\sigma_\sigma)$. When the model attempts to predict, the error pdf kurtosis diminishes with increasing lead times according to (**4.8a**). This shows the greater spread of errors around the zero mean. This also proves that the predictor is unbiased. The ARMA (3,3) based predictor is therefore capable of capturing the dynamics of the hydrometeor process, while its error corresponds to a 'statistically scaled' scintillation process. This can be justified in terms of the autocorrelation function of scintillation, known to decay rapidly to zero for lag times of 1 or 2 seconds ([**4.8**]), hence scintillation is almost unpredictable. The

ARMA predictor may therefore be assumed as quasi-optimal since its scintillation error has been reduced to a white process. However, further improvement may be achieved by considering possible functional relationships between rain and scintillation processes (see chapter 6).

4.5 Modified Global Fading (MGF)

Once a short-term predictor has been implemented and characterised statistically, one would like to determine the performance of a FCM, not only in the presence of Ka band fading, but also, including the practical limitations of the predictor. This can be done using the modified global fading (MGF) defined by:

$$z'(t+k) \equiv y(t+k|t) - e(t+k|t) \qquad \textbf{(4.9)}$$

This is simply stating that the resultant fading needing compensation, within the context of predictive FCM, must be equal to the predicted hydrometeor fade, including the prediction error e(t+k|t). The pdf associated with the second term in (**4.9**) can be found to be:

$$f_e(-e) = f_e(e) = MV_e(\sigma_\sigma(k),\sigma_m(k)) \qquad \textbf{(4.10)}$$

Assuming that the errors, {e}, sequence and the predicted fading sequence, {y}, are not just merely uncorrelated (this was the experimental case), but are statistically independent, the pdf of the modified global fading z' (dB) can be shown to be:

$$MGF_{z'}(\sigma,m,\sigma_\sigma(k),\ \sigma_m(k)) = f_{z'}(z') = \Lambda_y(m,\sigma) * MV_e(\sigma_\sigma(k),\sigma_m(k))$$

$$= \frac{1}{\sigma_{\sigma_{np}}(k)\cdot\pi}\int_{-\infty}^{\infty}\int_{0}^{\infty}\frac{1}{\sigma^2_{\chi_{dB}}}\cdot\frac{1}{(z-e_{dB})\sigma\cdot\sqrt{2\pi}}\cdot\exp\left[-\frac{\left(\ln\left(z'-e_{dB}\right)-m\right)^2}{2\sigma^2}\right]$$

$$\cdot\exp\left[-\frac{e^2_{dB}}{2\sigma^2_{\chi_{dB}}}-\frac{\ln\left(\sigma^2_{\chi_{dB}}/\sigma^2_{m_{dB}}(k)\right)}{2\cdot\sigma^2_{\sigma_{np}}(k)}\right]\cdot d\sigma_{\chi_{dB}}\cdot de_{dB} \qquad \textbf{(4.11)}$$

This function is plotted in Figure 4.16 for our Chilton-Olympus link and different values of time delays k. Note that for k=1, this reduces to the global fading

process described in chapter 3. Note that the impact of time delays on the global fading is more pronounced for the negative fades (scintillation enhancements) than for the positive fades, dominated by rain.

This suggests that a FCM predictor capable of forecasting these enhancements could achieve an even more efficient channel fading compensation.

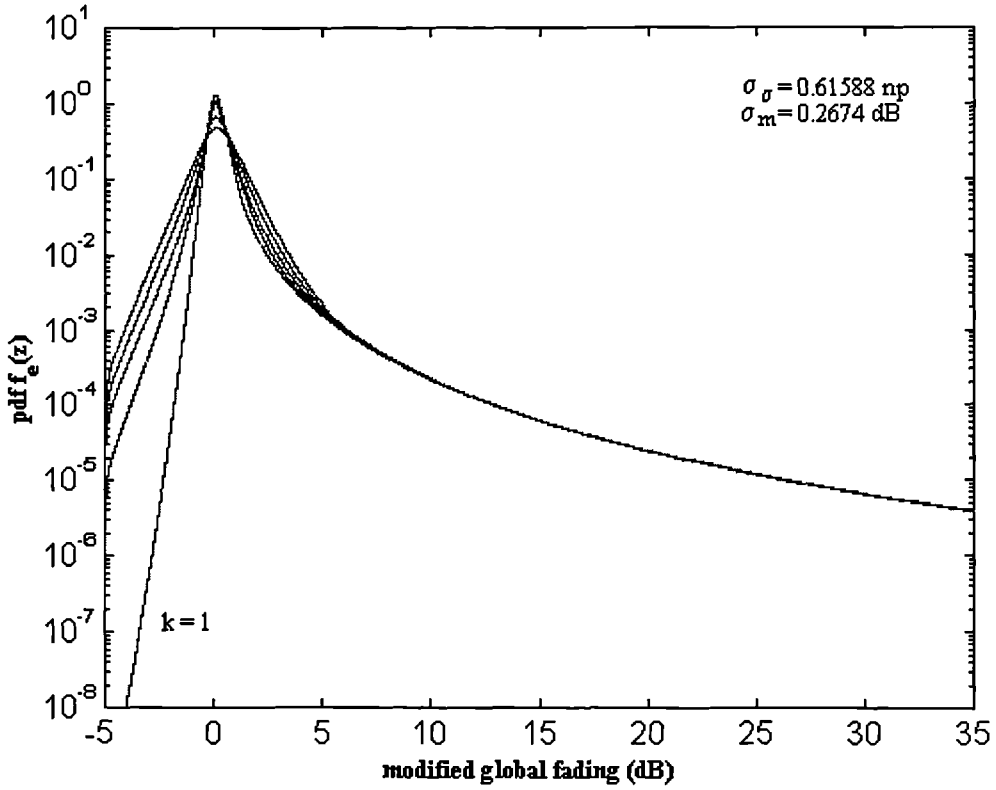

Figure 4.16: Theoretical long-term pdf of the global fading for time delays for k=1 to 5 sec.

4.6 Model Generalisation

So far, the results described in this chapter are only applicable to a carrier frequency of 30 GHz. In this section, an attempt is made to generalise the applicability of the ARMA/minimum variance predictor to other frequencies like 20

GHz. This is achieved via a heuristic discussion based on the invariance properties of the PSD of the Ka band fading process.

a) It is first demonstrated that the performance of the ARMA predictor is invariant at one particular carrier frequency (i.e. it does not vary with time). This is based on the fact that normalised increase in moments (Figure 4.7) and the normalised PSD of the Ka band fading process are directly related. As the latter is invariant in shape and in time, so is the increase in normalised moments of our predictor. Therefore the MGF model is valid on a long-term basis, although it is only based on a short-term analysis of the Ka band fading process.

b) As a first approximation, it is then shown that the increase in moments at 20 and 30 GHz can be assumed as identical. This is based on the properties of the normalised (asymptotic) properties PSD of the global fading process.

4.6.1 Invariance of the normalised increase in moments with time

An important work on the power spectrum density (PSD) of rain was published in **[4.5]**. The authors showed that the normalised PSD of the rain process is, on a long term basis, *invariant in shape* on a loglog scale. They showed that the PSD of rain is merely shifted up or down depending on the intensity of rain activity. Figure 4.17 shows the experimental normalised spectrum of the Ka band fading process (i.e. rain+scintillation) computed from a small event database spanning four different months. Clearly the normalised PSD of the global Ka band fading, i.e. not only that of rain attenuation, also displays this invariance in shape.

Relating this fact to the theory of the ARMA model, the normalised PSD in equation **(4.3)** must also display this feature i.e.

$$h_{yy}\left(e^{i\omega}\right) = S_{yy}\left(e^{i\omega}\right)/S_{yy}\left(e^{i0}\right),\ \omega = 2\pi \cdot f \qquad \textbf{(4.12)}$$

is also invariant in shape.

It can easily be seen from equation **(4.3)** that the normalised spectrum is only a function of the 6 parameters a_i, c_i , i =1,2,3. Thus on a long-term basis, these 6 coefficients are constant.

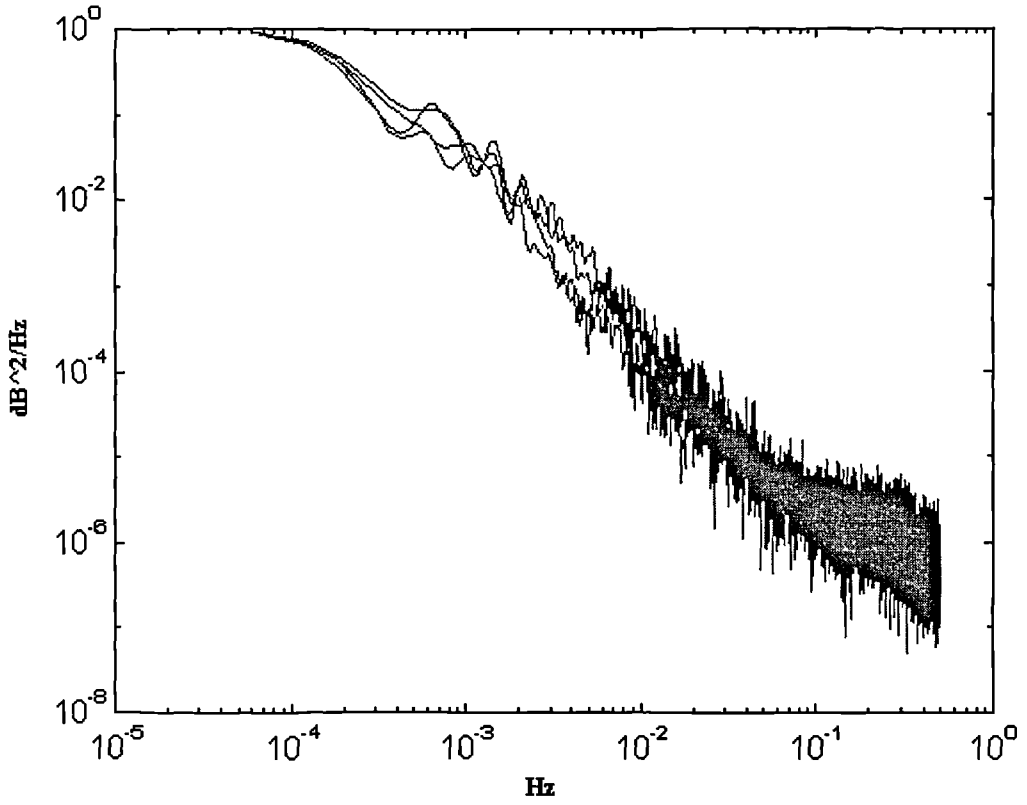

Figure 4.17: Monthly Average normalised spectra for a small selection of rain events at 30 GHz during 4 different months 91/09,91/10,91/11,91/12 (Olympus data).

Furthermore, it is shown in Appendix A4.I that the normalised increase in error variance (equation (A4.I.12)) is given by:

$$f_2(k) = 1 + \sum_{i=1}^{k-1} f_i^2 \qquad \textbf{(4.12)}$$

where the coefficients f_i are also a function of the 6 parameters a_i, c_i of the ARMA model.

As the 6 parameters of the ARMA model are constant on a long-term basis, $f_2(k)$ will also be invariant at one particular carrier frequency. Therefore the MGF model is valid on a long-term basis, although it is only based on a short-term analysis of the Ka band fading process.

4.6.2 Increase in normalised moments at different carrier frequencies

In order to see the applicability of the Modified Global Fading (MGF) model at different frequencies, one first needs to consider the normalised PSD of the global fading process at 20 and 30 GHz. The asymptotic PSD has been evaluated for our test case Chilton-Olympus link, using the simple model described in Appendix A.4.II.

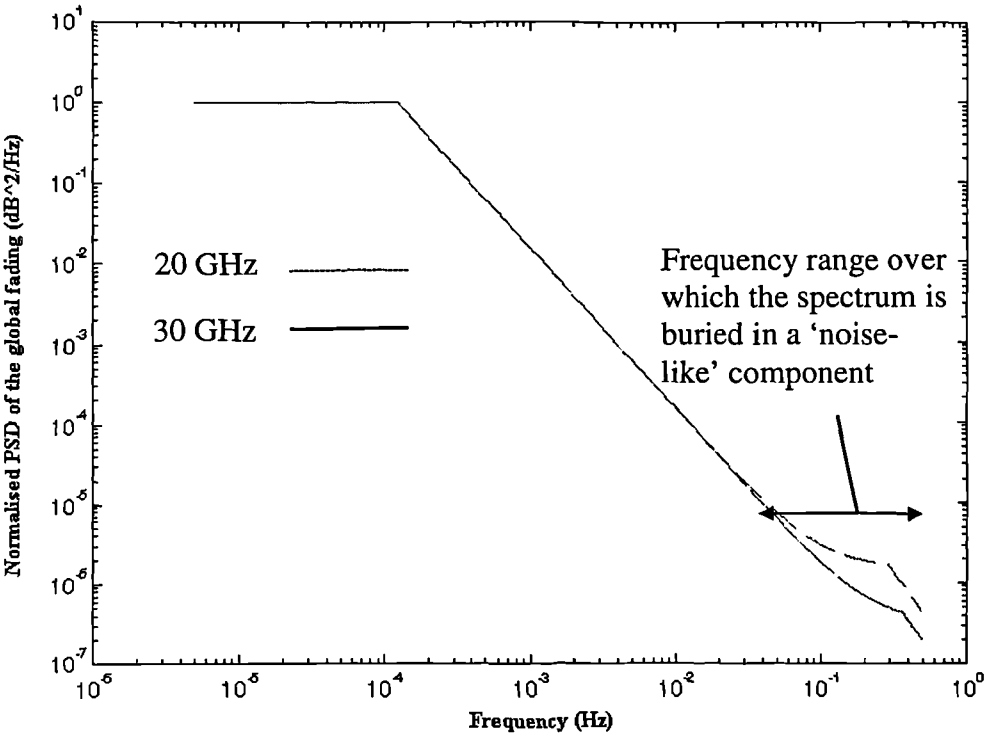

Figure 4.18: Theoretical normalised PSD of the global fading process at 20 and 30 GHz.

The low frequency part of the normalised spectrum, dominated by rain, is the same at 20 and 30 GHz, while the high frequency part is only marginally affected by a change in carrier frequency. In view of these results, one can assume that the two normalised PSDs, and thus the normalised increases in moments are virtually invariant with carrier frequency. This is a very plausible assumption, bearing in mind that the mean high frequency part of the spectrum in Figure 4.18 is buried in a noise like component as shown in the raw spectrum in Figure 4.2. Based on this approximation, the MGF model can be generalised to both 20 and 30 GHz. This is described in section 4.6.3.

4.6.3 Model generalisation

Based on the discussion in sections 4.6.1 and 4.6.2, the modified global fading (MGF) model can now be generalised. The performance of predictive fade countermeasures can be evaluated at a particular frequency by using the following procedure.

1) Determine, via a curve fitting method, the parameters (m,σ) of the lognormal pdf $\Lambda_y(m,\sigma)$ of rain attenuation at a particular carrier frequency. This can be based on experimental copolar data or the ITU-R model (see section 3.3.1).
2) Evaluate the parameters (σ_m,σ_σ) pdf of the Moulsley-Vilar model $MV_\chi(\sigma_m,\sigma_\sigma)$ at a *particular* carrier frequency using equations **(3.20)**, **(3.21)**, and **(3.22)**.

$$\sigma_\sigma = 0.515\cdot(\sin\theta)^{-0.2424} \quad \text{np} \qquad \textbf{(3.20)}$$

$$\sqrt{\overline{\sigma_\chi^2}} = \sqrt{m_2} = 0.0165\cdot\frac{f^{7/12}}{(\sin\theta)^{11/12}} \quad \text{dB}, \quad \text{if } f\cdot\sin\theta > 2.25 \qquad \textbf{(3.21)}$$

$$\sqrt{\overline{\sigma_\chi^2}} = \sqrt{m_2} = 0.0141\cdot\frac{f}{(\sin\theta)^{1/2}} \quad \text{dB}, \quad \text{if } f\cdot\sin\theta \le 2.25 \qquad \textbf{(3.22)}$$

f being the frequency in GHz and θ is the elevation angle.

3) Evaluate the second order moments of scintillation, m_2 (it is just the square of **(3.21)** or **(3.22)**). Using m_2 and σ_σ (equation **(3.20)**) evaluate the fourth order moment of scintillation using equation **(3.19)**. These 2 parameters are frequency dependent.

$$m_4 = 3\cdot(m_2)^2\cdot\exp\left(\sigma_{\sigma_{np}}^2\right) \qquad \textbf{(3.19)}$$

4) The impact of time delays, k (sec.) on m_2 and m_4, in the context of predictive countermeasure, is modelled by equation **(4.6a)** and **(4.6b)*** which yields $m_2(k)$ and $m_4(k)$.

$$\begin{cases} m_2(k) = m_2\cdot f_2(k) \\ m_4(k) = m_4\cdot f_4(k) \end{cases} \qquad \textbf{(4.6a)}$$

where

$$\begin{cases} f_2(k) = 0.0337 + 0.487\cdot k + 0.525\cdot k^2 \\ f_4(k) = 0.046 + 0.368\cdot k + 0.319\cdot k^2 + 0.3499\cdot k^3 - 0.0312\cdot k^4 + 0.0022\cdot k^5 \end{cases} \qquad \textbf{(4.6b)}$$

f_2(k) and f_4(k) are the normalised increase in moments of the ARMA based predictor. These functions may be assumed as independent of the carrier frequency. Different predictors would have however different increase in normalised moments. Alternative predictors may thus be considered provided that its associated increase in normalised moments, f_2(k) and f_4(k), are determined empirically via simulation (as performed in this chapter).

5) Using equations **(4.8a)** and then **(4.8b)**, determine the two parameters $(\sigma_m(k), \sigma_\sigma(k))$ of the pdf of the scaled error signal (scaling introduced by the predictor imperfections).

$$\sigma_\sigma^2(k) = \ln\left(\frac{m_4(k)}{3.[m_2(k)]^2}\right) \ (\mathrm{np}^2) \qquad \textbf{(4.8a)}$$

$$\sigma_m^2(k) = \sqrt{3}[m_2(k)]^2 / \sqrt{m_4(k)} \quad (\mathrm{dB}^2) \qquad \textbf{(4.8b)}$$

6) The MGF model has pdf given by :

$$MGF_z = \Lambda_y(m,\sigma) * MV(\sigma_m(k), \sigma_\sigma(k)) \qquad \textbf{(4.11)}$$

Using this statistical model, the expected long-term performance of practical predictive fade countermeasures can now be inferred. This implies that a particular system and FCM strategy be considered. This will be done in the next chapter.

4.7 Conclusions

The impact of time delays on the pdf of the prediction error has been evaluated both theoretically and numerically. This was based on a dynamic model identified using classical time series analysis. This model was found to agree well in the frequency domain with the raw spectral density function of the global fading process. The model was then characterised in terms of rain and scintillation processes. It was found that the error made by the model was essentially consistent with the scintillation process which has a Moulsley-Vilar statistical characteristic.

The model was then extended using the minimum variance approach to allow the short-term prediction of the global fading. The ARMA model was compared with other predictors and was found to yield a smaller error variance. The impact of time-delays was analysed by considering the increase of the second and fourth order moments of the prediction error, since those are sufficient to define fully the

Moulsley-Vilar distribution. Recombining rain attenuation and prediction error has yielded a modified global fading, which, in the delayless case, reduces to the global fading as proposed initially by Filip and Vilar.

Although the results obtained were found to fit extremely well with the experimental ones, they were based on a limited data set. The crucial stage in the modelling process described here relies heavily on the accurate determination of the normalised increase of the second and fourth order moments of the prediction error. In section 4.6, it is shown heuristically how this normalised increase relates to the power spectral density of the global fading. The latter is invariant in shape and is merely shifted up or down on a logarithmic scale depending on the rain activity. This suggests that the normalised increase in moments can also be considered invariant in time at any particular carrier frequency. Furthermore, changing the carrier frequency from 20 to 30 GHz does not affect greatly the shape of the normalised PSD. As a consequence, the increase in normalised moments can be assumed as intrinsic to the ARMA/minimum variance predictor and not the carrier frequency. This was used in section 4.6.3 to generalise the modified global fading to any desired carrier frequency.

Once a predictor, like the one described in this chapter, has been characterised statistically, it is possible to evaluate the realistic performance of predictive FCM controlled satellite links. This is the objective of the next chapter.

Appendix A4.I : Recursive Extended Least Squares and Minimum Variance

A. RELS algorithm [4.6]

The algorithm used for on-line estimation of the 6 ARMA model parameters was the Recursive Extended Least Squares (RELS) algorithm. It can accommodate in a simple manner the coloured noise corresponding to the moving average terms in the ARMA model definition:

$$y(t) = -\sum_{n=1}^{na} a_n \cdot y(t-n) + e(t) + \sum_{n=1}^{nc} c_n \cdot e(t-n) \Leftrightarrow y(t) = \frac{C(q^{-1})}{A(q^{-1})} \cdot e(t) \qquad \textbf{(A4.1.1)}$$

A directional forgetting factor was also implemented in order to avoid covariance wind-up and also add extra parameter tracking capabilities to the algorithm.

Defining

$$\hat{\theta}(t) = [-a_1 \quad -a_2 \quad -a_3 \quad c_1 \quad c_2 \quad c_3]$$

$$\phi^T(t) = [y(t-1) \quad y(t-2) \quad y(t-3) \quad \varepsilon(t-1) \quad \varepsilon(t-2) \quad \varepsilon(t-3)] \qquad \textbf{(A4.1.2)}$$

where $\varepsilon(t) = y(t) - \phi^T(t)\theta(t-1)$

is the prediction error using output prediction based on information up to (t-1).

The RELS algorithm is then at time t:

(i) Form $\phi^T(t)$ using y(t) and $\varepsilon(t) = y(t) - \phi^T(t)\theta(t-1)$ **(A4.1.3)**

(ii) Evaluate the directional forgetting factor

$$r(t-1) = \lambda' - \frac{1-\lambda'}{1+\phi^T(t)\mathbf{P}(t-1)\phi(t)} \qquad \textbf{(A4.1.4)}$$

(iii) Compute the covariance matrix using :

$$\mathbf{P}(t) = \mathbf{P}(t-1)\left[\mathbf{I}_6 - \frac{\phi(t)\phi^T(t)\mathbf{P}(t-1)}{r^{-1}(t-1) + \phi^T(t)\mathbf{P}(t-1)\phi(t)}\right] \qquad \textbf{(A4.1.5)}$$

(iii) Evaluate the updated model parameters at time t

$$\hat{q}(t) = \hat{\theta}(t-1) + \mathbf{P}(t)\phi(t)\left[y(t) - \phi^T(t)\hat{\theta}(t-1)\right] \qquad \textbf{(A4.1.6)}$$

The initial covariance matrix was set to $\mathbf{P}(t) = 100\mathbf{I}_6$ and the forgetting factor parameter was set to $\lambda' = 0.97$.

B. Minimum Variance Prediction

The ARMA model defined in **(A4.1)** can be rewritten in polynomial form using the delay operator q^{-1}. y(t) = y(t -1). This yields two polynomials, $C(q^{-1})$ and $A(q^{-1})$, of order (na,nc)=(3,3). This is written:

$$y(t)= C(q^{-1})/A(q^{-1}).e(t) \Rightarrow y(t+k)= C(q^{-1})/A(q^{-1}).e(t+k) \qquad \textbf{(A4.1.7)}$$

k being the prediction interval ($k \geq 1$) where the implication is true if y is ergodic. Åström ([**4.7**]) introduced two polynomials $F(q^{-1})$ and $G(q^{-1})$ such as to satisfy the Diophantine equation:

$$C(q^{-1})= A(q^{-1})F(q^{-1})+ q^{-k}G(q^{-1}) \qquad \textbf{(A4.1.8)}$$

where F and G and are polynomials of order (k-1) and max.(na-1,nc-1) respectively. Feeding **(A4.1.7)** into **(A4.1.6)** yields:

$$y(t+k)= F(q^{-1})e(t+k)+G(q^{-1})/C(q^{-1})y(t) \qquad \textbf{(A4.1.9)}$$

In order to find the MMSE estimate, we wish to minimise

$$V_k = E\{ (y(t+k)- \hat{y})^2\} \qquad \textbf{(A4.1.10)}$$

where $\hat{y}$ denotes the best estimate of y at time (t+k) given data up to and including t. Feeding **(A4.1.8)** in **(A4.1.9)** gives:

$$V_k = E\{F^2(q^{-1})e^2(t+k)\}+E\{(\hat{y} -G(q^{-1})/C(q^{-1})y(t))^2\} \qquad \textbf{(A4.1.11)}$$

This is minimised by letting the MMSE predicted value be $\hat{y}= G(q^{-1})/C(q^{-1})y(t)$ and provided that the sequence {e(t)} (with variance σ_e^2) is uncorrelated the predicted error variance can be shown to be:

$$V_k = \left(1+\sum_{i=1}^{k-1} f_i^2\right)\sigma_e^2 \qquad \textbf{(A4.1.12)}$$

The solution of the MMSE prediction problem involves solving the Diophantine equation **(A4.1.7)** for $F(q^{-1})$ and $G(q^{-1})$ given $A(q^{-1})$ and $C(q^{-1})$. Note the latter are estimated on-line by the RELS algorithm. In his original work, Åström derived a set of general recursive equations for doing so. Two other possible algorithms based on the band matrix approach or Kucera's algorithm are described in [**4.6**]. Aström's recursive solution applied to the ARMA(3,3) model is:

$V_1 = \sigma_e^2$

$f_1 = c_1 - a_1$ $\quad f_3 = c_3 - a_1 f_2 - a_2 f_1$

$f_2 = c_2 - a_1 f_1 - a_2$ $\quad f_i = - a_1 f_{i-1} - a_2 f_{i-2} - a_3 f_{i-3}$, $i > 3$ up to $i=k-1$ the prediction time,

and

$g_0 = -a_1 f_{k-1} - a_2 f_{k-2} - a_3 f_{k-3}$

$g_1 = -a_2 f_{k-1} - a_3 f_{k-2}$

$g_2 = -a_3 f_{k-1}$

C. Matlab routine "RELS.m" implementing the RELS/minimum variance algorithm

```
function [tra,thm,yp,ypred,alpha]=rels(y,ff)

% [tra,thm,yp,ypred,alpha]=rels(y,ff)
% RELS/MV algorithm
% y: input vector containing the raw beacon time-series to which the predictor will be
applied
% ff: desired forgetting factor
% tra: trace of the covariance matrix
% thm: vectors containing the 6 on-line estimates of the RELS algorithm
% yp: 1-step ahead predicted attenuation ( 1 second)
% ypred: 10-step ahead predicted attenuation ( 10 seconds)

%-------------------------------------------------------%
% initialisation
%-------------------------------------------------------%
P=eye(6)*10;                % covariance matrix init
thm=zeros(6,length(y));
theta=[1.53 0 0 0 0 0]';  % parameter vector [a1 a2 a3 c1 c2 c3]
X=[y(1) y(2) y(3) 0 0 0 ]';
e=zeros(size(y));
ypred=zeros(size(y));
% -------------------------------------------------------%
for t=4:(length(y))      % Simulates on-line detection/measurement of Ka band fades
  X=[y(t-1) y(t-2) y(t-3) e(t-1) e(t-2) e(t-3)]';
  e(t)=y(t)-X'*theta;
  r= ff-(1-ff)./(X'*P*X);    % directional ff pp157
  gain=X'*P/(1./r+X'*P*X);
  tra(t)=(X'*P)*(P*X)/(1+X'*P*X);
  P=(P*(eye(6)-X*gain));

  theta=theta+(P*X)*e(t);            %gain*( y(t)- X'*theta) ;
  thm(1:6,t)=theta;
```

```
 yp(t)=X'*theta;                    % 1 step ahead prediction
% ------------------------------------------------------%
% Mimimum variance algorithm ( lead time= 10 sec.)
% ------------------------------------------------------%
 a1=-theta(1);a2=-theta(2);a3=-theta(3);
 c1=theta(4);c2=theta(5);c3=theta(6);
 f1=-a1+c1;
 f2=c2-a1*f1-a2;
 f3=c3-a1*f2-a2*f1-a3;
 f4=-a1*f3-a2*f2-a3*f1;
 f5=-a1*f4-a2*f2-a3*f1;
 f6=-a1*f5-a2*f4-a3*f3;
 f7=-a1*f6-a2*f5-a3*f4;
 f8=-a1*f7-a2*f6-a3*f5;
 f9=-a1*f8-a2*f7-a3*f6;
 g0=-a1*f9-a2*f8-a3*f7;
 g1=-a2*f9-a3*f8;
 g2=-a3*f9;
ypred(1:13)=zeros(1,13);
ypred(t+10)=g0*y(t)+g1*y(t-1)+g2*y(t-2)-c1*ypred(t+9);
ypred(t+10)=ypred(t+10)-c2*ypred(t+8)-c3*ypred(t+7);
end
yp=yp';
thm=thm';   % thm contains the varying parameters
```

Appendix A4.II :Engineering model of the PSD of the Ka Band Fading Process

A. Modelling the Power Spectrum of rain attenuation

In this section, we briefly review the model introduced by Matricciani in **[4.11]**. The author proposed a simple model based on the synthetic storm concept and is used to determine the expected power spectrum of rain attenuation. It is described by the following convolution integral* :

$$A(z) = \int_{-\infty}^{\infty} kR^{\alpha}(z-\varepsilon)\cdot \mathrm{Re}ct\left(\frac{\varepsilon}{L}\right)\cdot d\varepsilon \;= kR^{\alpha}(\varepsilon) * \mathrm{Re}ct\left(\frac{\varepsilon}{L}\right) \quad \mathrm{dB} \qquad \textbf{(A4.2.1)}$$

This model considers that the attenuation A(z) depends on the relative position of a rain cell relative to the slant path L (km) of the satellite link. L can be evaluated from the rain height, H_R (km), altitude, H_S (km), of the station and the elevation angle, θ (deg.) using:

$$L = \frac{H_R - H_S}{\sin\theta} \ \mathrm{km} \qquad \textbf{(A4.2.2)}$$

The passing rain cell has a specific attenuation profile $Y(\varepsilon) = kR^{\alpha}(\varepsilon)$ dB / km which is only a function of the distance z (km) and is assumed to be time invariant.

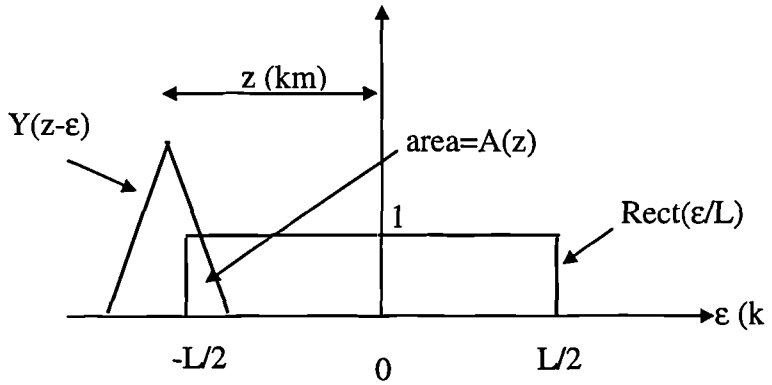

Figure A4. 1: Graphic interpretation of the passage of a fixed rain rate profile on a satellite slant path of length L (km).

* *Rect(ε/L) is the rectangular function of unit amplitude, width (km) centred around the origin.*

Taking the spatial Fourier transform of **(A4.2.2)**, we get:

$$S_A(f_s) = S_y(f_s) \cdot L \cdot \text{sinc}(\pi \cdot f_s \cdot L), \text{ where sinc(x)} = \sin(x)/x \qquad \textbf{(A4.2.3)}$$

f_s denotes the space frequency (in km^{-1}).

Assuming that the cell moves horizontally at a average speed $\bar{v} = z/t$ km/s, the space spectrum can be scaled to obtain a temporal transform using $f(Hz) = \bar{v}\,(km/s)/f_s(km^{-1})$ giving:

$$S_A(f) = S_y(f/\bar{v}) \cdot L \cdot \text{sinc}(\pi \cdot f/\bar{v} \cdot L) \qquad \textbf{(A4.2.4)}$$

Based on a simple meteorological model for the horizontal wind velocity, Matricciani evaluated $\bar{v}$ using:

$$\bar{v} = \frac{0.0015 \cdot \left(H_R^{\,2} - H_S^{\,2}\right)}{2 \cdot \left(H_R - H_S\right)} \text{ m/s} \qquad \textbf{(A4.2.5)}$$

Neglecting the influence of α in **(A4.2.1)**, because it is close to unity at 20 or 30 GHz, the low frequency of the PSD $|S_Y(f)|^2$ of the rain fading process is flat, with value:

$$W_Y^0(f) = \left|S_Y(f)\right|^2 = k^2 \cdot 138 \times 10^3 \quad (\text{mm/h})^2/\text{Hz} \qquad \textbf{(A4.2.6)}$$

This spectrum has an envelope with a first-order low pass characteristics. The cut-off frequency is located at

$$f_R = \bar{v}/(\pi \cdot \text{L}) \text{ Hz} \qquad \textbf{(A4.2.7)}$$

The high frequency part falls off at -20 dB/decade (i.e. proportional to f^{-2}) and is given by:

$$W_Y^{\infty}(f) = W_Y^0(f) \cdot \left(\frac{f}{f_R}\right)^{-2} \qquad \textbf{(A4.2.8)}$$

B. Engineering model of the PSD of tropospheric scintillation [4.20]

Non- smoothed case (i.e. zero diameter antenna)

In this section, we derive an asymptotic model of the PSD of scintillation. It is based on the three well known equations derived from weak scattering theory **[4.17]**, **[4.18]**.

$$\sigma_{\chi}^2 = 0.307 \cdot C_n^2 \cdot k^{7/6} \cdot L^{11/6} \quad \text{np}^2 \tag{A4.2.9}$$

$$W_{\chi}^0(f) = \frac{0.8506 \cdot 1.43}{2\pi \cdot f_{\chi}} \cdot C_n^2 \cdot k^{7/6} \cdot L^{11/6} \quad \text{dB}^2 / Hz, f \le f_{\chi} \tag{A4.2.10}$$

$$W_{\chi}^{\infty}(f) = \frac{2.189 \cdot 1.43}{2\pi \cdot f_{\chi}} \cdot C_n^2 \cdot k^{7/6} \cdot L^{11/6} \cdot \left(\frac{f \cdot 1.43}{f_c}\right)^{-8/3} \quad \text{dB}^2 / Hz, f \ge f_{\chi} \tag{A4.2.11}$$

σ_{χ}^2 : Variance of the scintillation process.

C_n^2 ($m^{-2/3}$): Structure constant of the atmosphere with value of the order of 10^{-9} for weak turbulence.

$k = \frac{2\pi}{\lambda}$ (m^{-1}): Wavenumber

$L = \frac{H}{\sin\theta}$ (m): length of the path through turbulence of height H (m) slanted at an elevation angle θ.

$W_{\chi}^0(f)$: denotes the low frequency asymptote of the PSD of scintillation.

$W_{\chi}^{\infty}(f)$: denotes the high frequency asymptote of the PSD of scintillation.

These two asymptotes meet at f_{χ} (Hz) given by:

$$f_{\chi} = 1.43/2\pi \cdot v\sqrt{k/L} \quad \text{Hz}$$

$$= 1.43/2\pi \cdot v\sqrt{\frac{2\pi}{\lambda L}} \quad \text{Hz}$$

$$f_{\chi} = \frac{1.43}{2\pi} \cdot v\sqrt{\frac{2\pi \cdot f \cdot \sin\theta}{0.3 \cdot H}} \quad \text{Hz} = 1.04156 \cdot v\sqrt{\frac{f \cdot \sin\theta}{H}} \tag{A4.2.12}$$

where f is the carrier frequency and v is the cross path wind velocity (m/s).

Substituting **(A4.2.9)** and **(A4.2.12)** in **(A4.2.10)** and **(A4.2.11)**, we obtain easily:

$$W_{\chi}^0(f) = \frac{0.630}{f_{\chi}} \cdot \sigma_{\chi}^2 \quad (\text{dB}^2 / Hz) \tag{A4.2.13}$$

$$W_{\chi}^{\infty}(f) = W_{\chi}^0(f) \cdot \left(\frac{f}{f_{\chi}}\right)^{-8/3} \quad (\text{dB}^2 / Hz) \tag{A4.2.14}$$

Here for consistency (see equation (3.21)), we will use :

$$\sigma_{\chi} = 0.0165 \cdot \frac{f}{(\sin\theta)^{11/12}} \quad \text{dB} \tag{A4.2.15}$$

to evaluate the magnitude of the scintillation variance.

Aperture Smoothing (see [4.18] for details)

Aperture smoothing requires the inclusion of three parameters accounting for the effects of a effective finite aperture (D in m) on the variance and spectrum of scintillation.

The variance in the smoothed case is given by:

$$\begin{cases} \sigma_\chi^2(D) = \eta_{\sigma^2} \cdot \sigma_\chi^2 \\ \eta_{\sigma^2} = 3.8637\left(x^2+1\right)^{11/12} \cdot \sin\left(\frac{11}{6}\tan^{-1}\left(\frac{1}{x}\right)\right) - 7.0835x^{5/6} \end{cases} \quad \textbf{(A4.2.16)}$$

$$x = 0.0584\frac{2\pi \cdot D^2}{\lambda L} = 12.2313 \cdot \frac{D^2 f \cdot \sin\theta}{H} \quad \textbf{(A4.2.17)}$$

The low and high frequency parts of the spectrum become respectively:

$$\begin{cases} W_\chi^0(D,f) = \eta_{W^0} \cdot W_\chi^0(f) \\ \eta_{W^0} = \frac{14}{3}x^{4/3} - 2(1+x^2)^{7/6} \cdot \sin\left(\frac{7}{3}\tan^{-1}\left(\frac{1}{x}\right)\right) \end{cases} \quad \textbf{(A4.2.18)}$$

$$\begin{cases} W_\chi^\infty(D,f) = \eta_{W^\infty} \cdot W_\chi^\infty(f) \\ \eta_{W^\infty} = 1.053\left(\frac{f_s}{f}\right)\exp\left(\frac{f_s^2}{f^2}\right) \\ f_s = \frac{4.1391}{2\pi}\frac{\nu}{D} \end{cases} \quad \textbf{(A4.2.19)}$$

B. Model of the PSD of global fading process

Assuming that rain and scintillation effects are additive the PSD of the global fading process is:

$$W_{GF}(f,D) = W_Y(f) + W_\chi(f,D) \quad \textbf{(A4.2.20)}$$

and the normalised PSD of the global fading is $W_{GF}(f,D) / W_{GF}(0,D)$.

For the particular case of the Chilton-Olympus 20/30 GHz link, the following numerical values were used (see also chapter 2):

- Specific attenuation parameter: k=0.167 (vertical polarisation) at 30 GHz
  k=0.0751 (horizontal polarisation) at 20 GHz
  (from ITU-R model **[4.19]**)

- Effective rain height: $H_R = 2.65$ km (from ITU-R model **[4.19]**)
- Effective height of the turbulent layer: H= 3000 m
- Elevation angle: $\theta = 28.56^{\circ}$
- Horizontal wind speed for scintillation: v=5 m/s (18 km/h)
- Effective antenna diameter: D= 1.2 m

Using these numerical values, the cut-off frequencies of the Ka band fading PSD are:

$f_R = 1.15 \cdot 10^{-4}$ Hz

$f_\chi = 0.36$ Hz at 30 GHz

$f_\chi = 0.29$ Hz at 20 GHz

The low frequency asymptotes are:

$$\begin{cases} W_y^0 = 3649 \ \ (\text{mm/h})^2 / Hz \ \text{ at 30 GHz} \\ W_y^0 = 778 \ \ (\text{mm/h})^2 / Hz \ \text{ at 20 GHz} \end{cases}$$

$$\begin{cases} W_\chi^0 = 1.66 \ \ \text{dB}^2 / Hz \ \text{at 30 GHz} \\ W_\chi^0 = 0.90 \ \ \text{dB}^2 / Hz \ \text{at 20 GHz} \end{cases}$$

Appendix A4.III : Synthesis of typical Ka band fading events

Some Matlab routines have been developed for the synthesis of typical rain and scintillation events at Ka band frequencies. The goal is not to develop a computational model based on the physics of either processes. Rather, the objective is to generate typical time-series having the main statistical and dynamic characteristics of both rain and scintillation components, so that the performance of practical FCM controller may be tested without the need to recourse to experimental beacon data. This is to avoid the problem of outliers often encountered in experimental data. It is also more flexible while avoiding the need for pre-processing (e.g. removal of diurnal variations). This allows for more control of the simulation and it should result in a substantial saving of processing time. These routines (translated into an appropriate computer language) can also be integrated in a digital signal processing (DSP) environment for synthesis of typical Ka band fading used for laboratory-based hardware simulation of practical FCM systems.

A. Synthesis of scintillation time-series

Scintillation has been modelled so that it can display the following features:

- the probability density function of scintillation events can either display Gaussian or Moulsley-Vilar characteristics. While the former is supposed to be applicable to short-term simulation of scintillation time-series (as assumed by turbulence theory), the latter allows the simulation of the long term behaviour of amplitude scintillation. It assumes that the variance, σ_χ, of the random variable, χ (in nepers), is lognormally distributed with parameters σ_σ and σ_m (see Chapter 3). However the synthesised sequences of scintillation variance are totally uncorrelated (this does not match with the experimental properties where the scintillation variance forms a well structured non-white sequence which has dynamic characteristics very close to that of rain attenuation);
- the low-pass power spectral density of the scintillation process is designed so that an arbitrary cut-off frequency may be chosen by the operator (e.g. typically 0.3 Hz

at 30 GHz). The roll-off of the scintillation spectrum can also be chosen arbitrarily (typically it could be set to -8/3 as derived from turbulence theory). This is achieved by finding the filter which fits best, in a least square sense, with the expected normalised spectrum of the scintillation process (fully specified by the cut-off and the roll-off). This is then scaled by a multiplicative time-series so that the synthesised data has the desired variance (fixed for Gaussian model and lognormally distributed for MV model).

The Matlab routine is given below. A typical scintillation time-series and its corresponding PSD are given in Figure 4.18. This example assumes a Moulsley-Vilar distribution and a cut-off at 0.3 Hz and a -8/3 slope.

Matlab routine "synth_sci.m" synthesising typical scintillation time-series

```
function [sci,sx2]=synth_sci(fc,slope,VARI,No)

% [sci,sx2]= synth _sci(fc,slope,VARI,No)
%
% routine that synthesises
% typical scintillation time-series
% spectral domain fitting approach
% short-term model i.e. Gaussian pdf
% long term model has MV characteristics
%
% fc (Hz):  desired cut-off of the scintillation spectrum
% slope (e.g. -8/3) : desired slope of the PSD of sci.
% VARI: desired variance of the particular event
% if VARI>0 then a lognormal model of sci variance is assumed
% if VARI<0 then a normal model of sci variance is assumed
% where the variance is -VARI>0
% No : number of samples to be generated ( 1 per second i.e. Nyquist freq. is 0.5 Hz)
% i.e. duration in seconds of the synthesised time-series


% EXAMPLES
% fc=.3;  %cut-off of scintillation (Hz)
% slope=-8/3;  %desired slope of the PSD above fc

f=0:0.01:0.5; % generates the frequency vector up to Nyquist freq.
% construction of the normalised asymptotic PSD of scintillation
c1=fc.^(-slope/2);      % calculates constant c1 such that
                        % c1.*f.^(-8/3) intercepts ordinate 1 at fc (Hz)
m=c1.*f.^(slope/2); % m is psd of sci
I=find(m<1);
m(1:I(1)-1)=ones(1,I(1)-1); % below fc the PSD equals unity
```

```
% Evaluate the transfer function which matches best the theoretical normalised PSD
[b,a]=yulewalk(4,f./0.5,m);
[h,w]=freqz(b,a,512);
% synthesise a normal sequence with zero mean and unit variance
randn('seed',sum(100*clock));
n=randn(1,No);
n=(n-mean(n))./std(n); % normalise to unit variance an zero mean
% generate a Gaussian sequence having the normalised PSD calculated above
sci=filter(b,a,n);
sci=(sci-mean(sci))./std(sci);  % normalise to unit variance and zero mean
% scale to appropriate variance
if VARI>0,    sx2=lognrnd(ln(0.2674./4.3429448),0.61588,1,No); ,end
% MV model: Constants were evaluated in Chapter 3
% Alternatively the MV model equations could also be included in this routine to
evaluate the
% constants
if VARI<=0,  sx2= -VARI; ,end % fixed variance i.e. Gaussian model
sci=sci.*sqrt(sx2); % scale time-series to appropriate variance
```

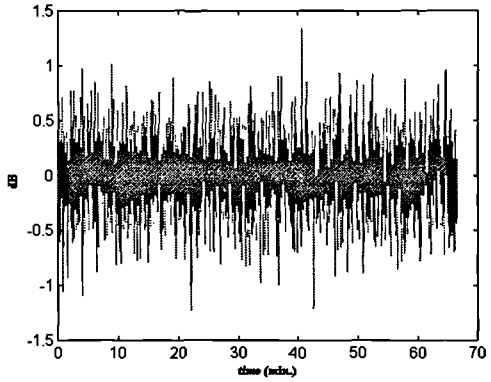

Figure A4. 2: Typical synthesised scintillation time-series.

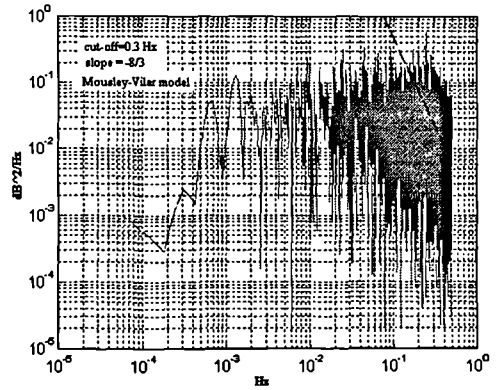

Figure A4. 3: PSD corresponding to the scintillation event shown in Figure 4.2.

B. Synthesis of typical rain events

Rain attenuation has been modelled using a non-linear device. Firstly, the spectral characteristics of the rain process has been modelled by low-pass filtering a white Gaussian random sequence. This random sequence is the normalised to unit variance and zero mean. The first order low-pass Butterworth filter has a selectable cut-off (typically around 0.0001 Hz at 30 GHz). The filtered signal is then fed into a non-linear device which transforms the normal sequence into a lognormal one with arbitrary (m,σ) parameters (see Chapter 3). Figure 4.20 shows a typical synthesised rain event and its corresponding PSD.

Matlab routine "rain.m" synthesising typical rain events time-series

```
function [y,sci,sx]=rain(m_rain,sig_rain,No,fc)

%       Y_rain=rain(m_rain,sig_rain,duration,No,fc)
%       as a first order process
%       m_rain, sig_rain: parameters of the lognormal pdf of rain
%       No : Number of samples to be generated (1/sec.)
%       fc: desired cut-off freq.

%---------------------------------------%
% Synthesise Rain                       %
% --------------------------------------%
randn('seed',sum(100*clock));
n1=randn(1,No);
n1=(n1-mean(n1))./std(n1); % Norrmalise to unit variance and zero mean
[b,a]=butter(1,fc./0.5); % 0.5 is the Nyquist freq.
Y=filter(b,a,n1);
Y=(Y-mean(Y))./std(Y);          % Normalise to zero mean and unit variance
y=exp(m_rain+sig_rain.*Y);  % transform into a lognormal process
```

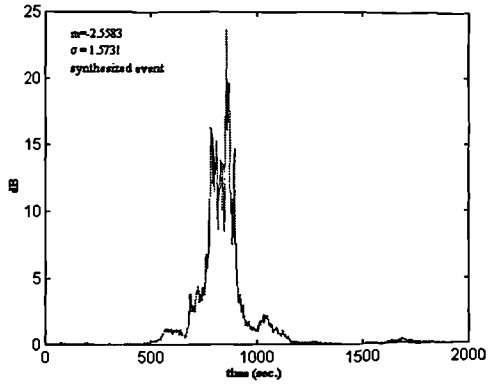

Figure A4. 4: Typical synthesised rain event and its corresponding PSD.

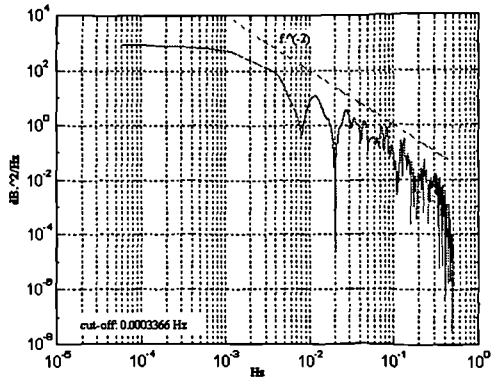

Figure A4. 5: PSD corresponding to the rain event shown in Figure A4.4.

The long-term sample probability density function of synthesised rain and scintillation events have been simulated over a period 145 hours. Practical and expected theoretical pdfs are shown with solid and dashed lines respectively. They show a good agreement.

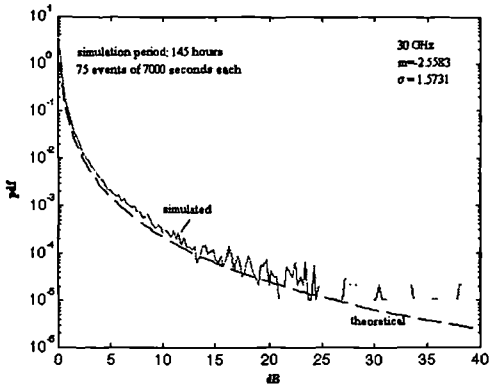

Figure A4. 6: pdf of the synthesised rain time-series.

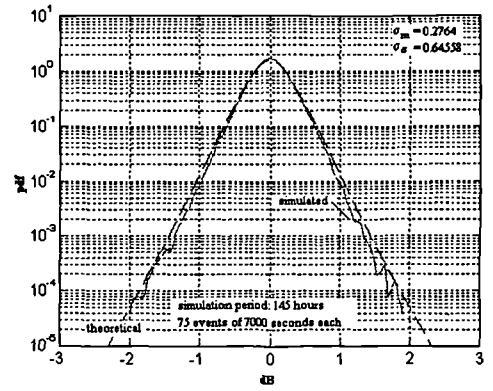

Figure A4. 7: pdf of the synthesised scintillation time-series

(Non-Stationary case)

References

[4.1] L. Ljung, *System Identification, Theory for the user*, Prentice-Hall, Information and systems sciences series, Thomas Keilath, editor, 1987.

[4.2] L. Dossi, "Real-time prediction of attenuation for applications to fade countermeasures", *Electronics Letters,* Vol. 26, No. 4, 1990, pp 250-251.

[4.3] M.B. Priestley, *Spectral analysis and time series,* Probability and mathematical statistics, Academic Press, 1981.

[4.4] T.J. Moulsley, E. Vilar, "Experimental and theoretical statistics of microwave amplitude scintillations on satellite down-links", *IEEE Trans. on Ant. and Prop.*, Vol. AP-30, No 6, Nov. 1982, pp 1099-1106.

[4.5] A. Burgueño, E. Vilar, M. Puigcerver, "Spectral analysis of 49 years of rainfall rate and relation to fade dynamic", *IEEE Trans. on Comms.,* Vol. COM-38 No 9, September 1990, pp 1359-1366.

[4.6] P.E. Wellstead and M.B. Zarrop, *Self-Tuning Systems Control and Signal Processing*, John Wiley and Sons, 1991.

[4.7] K.J. Åström, *Introduction to Stochastic Control theory,* Mathematics in science and Engineering, Vol. 71, Academic Press, 1970.

[4.8] ESA, *Second workshop of the Olympus experimenters, Volume 1, Reference book on attenuation measurement and prediction, Noordwijk, 8-10 Nov. 1994,* "Chapter 7: Characteristics of events", ESA ESTEC WPP-083, Noordwijk, The Netherlands, pp 87-123.

[4.9] T. Maseng, P.M. Bakken, "A stochastic dynamic model of rain attenuation", *IEEE Trans. on Comms.,* Vol. COM-29, May 1981, pp 660-669.

[4.10] Y. Karasawa, T. Matsudo, "Characteristics of fading on low-elevation angle Earth-space paths with concurrent rain attenuation and scintillation", *IEEE Trans. on Comms.,* Vol. COM-39, 1991, pp 657-661.

[4.11] E. Matricciani, "Physical-mathematical model of the dynamics of rain attenuation with application to power spectrum", *Electronics Letters*, Vol. 30, 1994, pp 522-524.

[4.12] E. Matricciani, "Relationship between scintillation and rain attenuation at 19.77 GHz", *Radio Science*, Vol. 31, No 2, March-April 1996, pp 273-279.

[4.13] E. Matricciani, "Scintillation and simultaneous rain attenuation at 49.5 GHz", *Proc. of Int. Conf. on Antennas and Propagation ICAP'95, 1995, Eindhoven, The Netherlands*, IEE Conf. Publ. No 407, 1995, pp 165 -168.

[4.14] G. Ortgies, "Probability density functions of amplitude scintillations", *Electronics Letters*, Vol. 21, 1985, pp 141-142.

[4.15] O.P. Banjo, E. Vilar, "Measurement and modelling of amplitude scintillations on low-elevation earth-space paths and impact on communication systems", *IEEE Trans. on Comms.,* Vol. COM-34, 1986, pp 774-786.

[4.16] M.B. Priestley, *Nonlinear and Nonstationary Time Series Analysis*, Academic Press, London, 1988.

[4.17] A. Ishimaru, *Wave propagation and scattering in random media, Vol. 1 and 2*, Academic Press, New York, Academic, 1978.

[4.18] J. Haddon, E. Vilar, "Scattering induced microwave scintillations from clear-air and rain and the influence of antenna aperture", *IEEE Trans. on Ant. and Prop., Vol. AP-34, May 1986*, pp 646-657.

[4.19] ITU, 1992- CCIR recommendations, ITU-R recommendation 838 and 839, pp 205 and 207 respectively, 1992.

[4.20] E. Vilar, M. Filip, "Measurements of 20/30 GHz amplitude scintillations. Dependence of the statistics upon the ground station measuring parameters", *Proc. Olympus Utilisation Conf., Vienna, 12-14 April 1989*, ESA SP-292, May 1989, pp 191-197.

5. Performance of a Predictive AFEC Countermeasure

5.1 Introduction

It is now possible to evaluate the statistical long term performance of different control schemes applied to practical fade countermeasures. In this chapter, the performance of an indicative low-power low-rate system using adaptive coding as a FCM is investigated. An emphasis is placed on the degradation caused by time delays due to Ka band fade dynamics. The detection/prediction scheme being non-ideal, a detection margin fixed or variable (FDM or VDM) will be introduced to compensate for channel estimation errors.

The focus will first be on the margin requirements applicable to RF domain link analysis. In such a case, the channel estimation must be performed so as to activate the appropriate level of FCM protection while minimising the FCM utilisation time. Although such an analysis is ideally suited for low fade margin systems based on, say, link power control or diversity strategies (mainly concerned with link budget type considerations), the results will also be extended to evaluate the performance of an adaptive transmission system. In such a context, the main interests are placed on bit error rate availability and average throughput.

5.2 Performance of predictive fade detection schemes

Ka band systems require a small fixed margin to account for attenuation due to oxygen, water vapour, footprint loss, pointing errors and satellite tracking. In practice, the fixed built-in power margin is chosen to cover a bit more than those collective effects i.e. a small excess security margin is included in the design process. Such systems are referred to as low fade margin systems **[5.1]**. This excess margin corresponds to the maximum acceptable level of attenuation caused by other sources not yet catered for (like rain or scintillation) for which the system can still operate with sufficient performance. Whenever the 'excess' attenuation exceeds this security margin, the system is considered as operating below grade and thus extra power margin or equivalent (i.e. FCM control effort) must be deployed by the countermeasure.

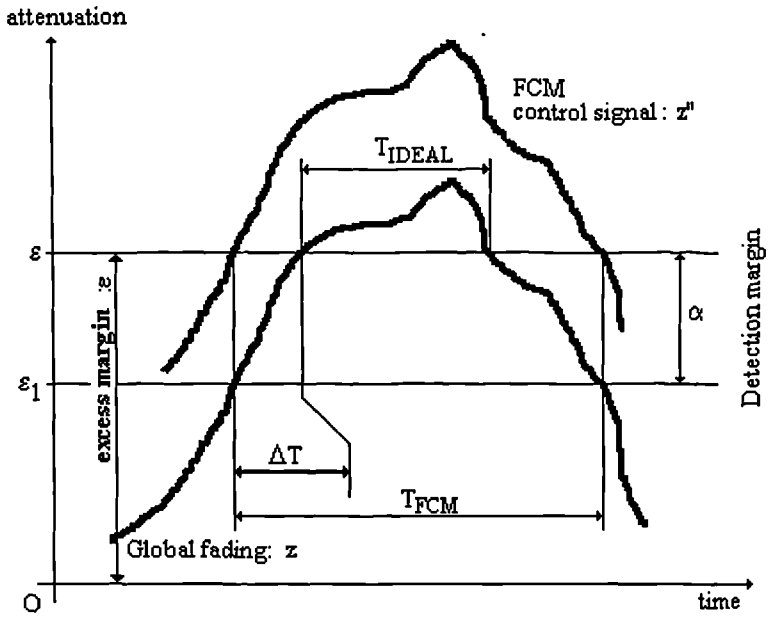

Figure 5. 1: Basic diagram and definition of the FCM switchover procedure between normal and assisted mode.

This is described graphically in Figure 5.1 where the excess fade margin ε (dB) is the maximum level in non-assisted mode for which the system still operates appropriately. If the attenuation exceeds that level then a countermeasure action is needed to compensate the fading effects. Of course the FCM will be relinquished when the threshold is crossed downwards. This corresponds to an ideal situation. One can associate an ideal duration of FCM utilisation, T_{IDEAL}, to the case where the excess fade, caused by rain and scintillation, exceeds level ε.

In practice however, the switching from non-assisted to assisted mode and vice-versa cannot be instantaneous due to the finite response time of the FCM system. Thus the initiation of a countermeasure action must be started earlier, while the relinquishment of the FCM should be made a bit later, to add security and reduce the number of switchings between assisted and non-assisted mode. This can be done by introducing a detection margin as shown in Figure 5.1. Also, a hysteresis could be added for the relinquishment but this will not be studied here **[5.2, 5.3]**.

The detection margin is introduced to cater for the stochastic variations of the Ka band fading during the estimated response time of the whole FCM system *as well as* the imperfections of the FCM estimator/predictor system.

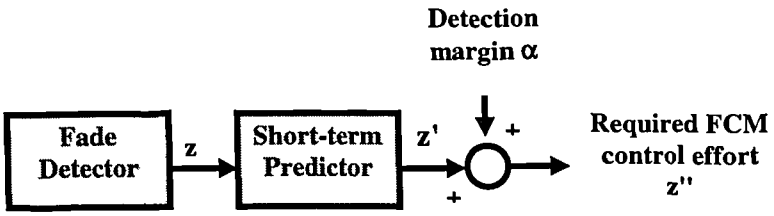

Figure 5. 2: Detection margin approach for predictive countermeasures.

Since the FDM must be implemented at any new second to yield appropriate FCM action, the simplest way is to base the FCM controller decision on the control signal FCM which is equal to the actual detected fade to which the FDM is added continuously. As seen from the controller, the estimated fades, z', will always be α dB worse than the true fade, z, thereby biasing the FCM control effort which is given by (see Figure 5.2):

$$z'' = z' + \alpha \quad \text{dB} \tag{5.1}$$

A time, T_{FCM}, can also be associated to the practical utilisation of FCM resources. Thus the utilisation factor **[5.4]** can be defined as:

$$U = \left. \frac{T_{FCM}}{T_{ideal}} \right|_{z'' \geq \varepsilon} \tag{5.2}$$

as a good indicator of the performance of predictive countermeasure systems.

It is important to attempt to minimise the FCM overall control effort and thus the FDM, so that the FCM utilisation time can be as close as the ideal (delayless) one, while still performing according to specifications. This is particularly crucial to shared-resource FCMs, since any saving in FCM utilisation time can be re-invested to protect other affected links while for adaptive transmission FCMs, this will allow a maximisation of the user data throughput.

A so-called detection outage ([**5.5**]) occurs whenever the estimated control effort z'' is less than the detected attenuation z. Such a definition is particularly crucial for the design of systems with fade countermeasures on up-links, since, ULPC systems will perform below specification during detection outages. Being interested in long-term estimates, the outage detection probability can be introduced as :

$$P_{out}^{pred} = \text{Prob}\{z'' \leq z'\} \qquad \textbf{(5.3)}$$

A large part of this chapter is dedicated to evaluating equations **(5.1)** to **(5.3)** for the Chilton-Olympus test-case example.

5.3 Fixed detection margin (FDM) approach

5.3.1 FCM control effort

If the estimator/predictor required for FCM operations was perfect (i.e. with no prediction error), there would be no need for any detection margin. However, as noted in the previous chapter, the ARMA model prediction error has a pdf consistent with scaled scintillation. Because it is based on a MMSE criterion, the predictor is unbiased, and hence the fades will effectively be under-estimated for half of the time.

If it is assumed that all detected attenuation is effectively compensated for by the countermeasure, there will be outages for half of the time, whenever the error is negative. In order to improve this situation (50% error or detection outage), a fixed fade detection margin can be introduced, to compensate for the residual error during time delays **[5. 6]**. This is written more formally as:

$$z''(t+k|t) = \hat{z}(t+k|t) + \alpha \quad \text{dB}, \quad \alpha \geq 0 \qquad \textbf{(5.4)}$$

where $\hat{z}(t+k|t)$ is the k-step ahead predicted Ka band fading, α (dB) is the fixed detection margin (FDM). As was seen in chapter 4, the implemented predictor is not capable of predicting scintillation i.e. the effective required control effort is therefore:

$$z''(t+k|t) \approx y(t+k|t)+\alpha \quad \text{dB}, \quad \alpha \geq 0 \tag{5.5}$$

where y(t+k|t) denotes the predicted rain attenuation component based on samples up to and including time t. The approximation comes from the fact that the predicted attenuation is not *strictly* equal to rain only, since for example the theoretical PSD of the ARMA model was found to capture partially some of the scintillation dynamics. The pdf associated with the control effort is :

$$f_{z''}(z'') = \Lambda_{z''-\alpha}(m,\sigma)$$

$$\Lambda_{z''-\alpha}(m,\sigma) = \begin{cases} \dfrac{1}{(z''-\alpha)\sigma\sqrt{2\pi}} \exp\left[-\dfrac{(\ln(z''-\alpha) - m)^2}{2\sigma^2}\right], & z'' > \alpha \\ = 0, & \text{elsewhere.} \end{cases} \tag{5.6}$$

5.3.2 Detection Outage Probability

Outage will occur whenever the FCM deployed power is smaller than that required, hence the outage probability can be expressed by:

$$P_{out}^{pred}(\alpha,k) = \text{Prob}\{z''(t+k|t \leq z'(t+k)\} \tag{5.7}$$

or , using **(4.9)**, and **(5.5)**,

$$P_{out}^{pred}(\alpha,k) = \text{Prob}\{e(t+k|t) \geq \alpha\} \tag{5.8}$$

The pdf associated with this term is $\text{MV}_e(\sigma_{m_{dB}}(k),\sigma_{\sigma_{np}}(k))$ and has been evaluated in **(4.7)**. Integrating this according to **(5.8)** yields the detection outage probability:

$$\begin{aligned} P_{out}^{pred}(\alpha,k) &= \int_{\alpha}^{\infty} \text{MV}_e(\sigma_m(k),\sigma_\sigma(k)) \cdot de \\ &= \frac{1}{\sigma_{\sigma_{np}}(k)} \cdot \int_{\alpha}^{\infty}\int_{0}^{\infty} \frac{1}{\sigma_{\chi_{dB}}^2} \cdot \exp\left(-\frac{e_{dB}^2}{2\sigma_{\chi_{dB}}^2} - \frac{\ln\left(\sigma_{\chi_{dB}}^2/\sigma_{m_{dB}}^2(k)\right)}{2\cdot\sigma_{\sigma_{np}}^2(k)}\right) \cdot d\sigma_{\chi_{dB}} \cdot de \end{aligned} \tag{5.9}$$

Integral (**5.9**) has been computed for different FDM and time delays and is shown in Figure 5.3. As mentioned earlier, with no FDM, the predictor will produce outages for 50% of the time. This was evaluated assuming the hypothetical back-to-back link with σ_m=0.61588 np and σ_σ=0.2674 dB (see section 3.3.2) assuming a normalised increase of the error moments as given in section 4.4.

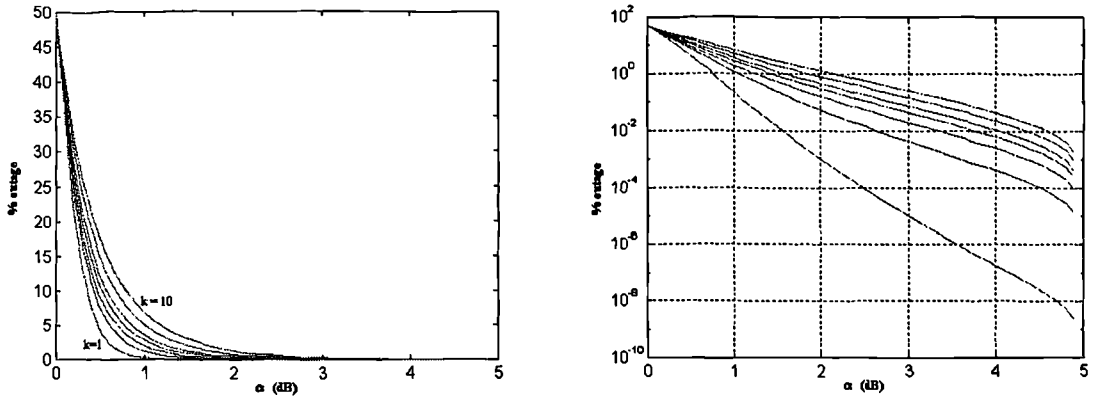

5.3(a): linear scale **5.3(b): semi-logarithmic scale**

Figure 5. 3: Outage probability as a function of the FDM (α dB) for k=1,2,3,4,5,7,10 sec. (Ka band back-to-back Chilton-Olympus link).

The linear scale plot shows similar looking results to the ones obtained via test-out procedure in **[5.7]** for frequencies of 11.6 GHz. The main difference is our larger margin requirements due to the higher frequency here (30 GHz). Multiplying $P_{out}(\alpha,k)$ by $365.25 \cdot 24 \cdot 3600$ will give the average number of outages in a normal year, and $100 \cdot (1 - P_{out}(\alpha))$ would be the estimated long-term back-to-back (RF) link availability. Some typical values were extracted from those two figures and are tabulated in Table 5.1. The results show that, for availability larger than 99.95 %, the required fixed detection margin increases dramatically with increasing time delays. The table shows a first basic trade-off that can be made. If the objective is to limit the FDM, then this may be at the constraint of a shorter time delay and/or a smaller link availability (or possibly a better predictor). This table could therefore be used to choose the value of the appropriate fixed detection margin so as to achieve a given RF link availability (in % time), for a given time delay, T=k-1 (sec.).

k (sec.)	Required FDM α (dB)				
1	0.8	0.90	1.20	1.30	1.60
2	1.10	1.30	1.80	2.10	2.70
3	1.30	1.50	2.30	2.60	3.40
4	1.50	1.80	2.60	3.00	3.80
5	1.60	2.00	2.90	3.30	4.10
7	1.90	2.30	3.30	3.60	4.40
10	2.20	2.60	3.60	4.00	4.60
P_{out}^{pred} (%)	1	0.5	0.1	0.05	0.01
% Availability	99	99.5	99.9	99.95	99.99

Table 5.1: Required Fixed Detection Margin (FDM) to achieve a given long-term availability for a given time delay, k sec. (RF analysis).

Otung et al., in **[5.8]**, estimated the required scintillation margin to 0.8 dB for a link RF availability of 99%. His study was based on an empirical study of the scintillation fades at Ka band frequencies. This value of 0.8 dB is also predicted for a similar availability for k=1 second as shown in Table 5.1. This tends to confirm the numerical validity of the Mousley-Vilar model. However, the results are extended here to account for the impact of time delays, which result in a significant increase in required 'scaled' scintillation margin.

5.3.3 FCM Utilisation factor for the FDM approach

In order to characterise the efficiency of any FCM detection scheme for low fade margin satellite systems, the ratio of practical FCM utilisation time to ideal FCM time $U = T_{FCM}/T_{ideal}$ gives good information on the quality of the FCM controller system. This performance index is also particularly useful for satellite systems based on the sharing of a back-up resource but this will not be dealt with in this thesis.

An analysis of the utilisation factor, based on simulated results has been published in **[5.4]** for 11.6 GHz link and will be used as a test to the following analysis. In this thesis, the quality of the ARMA based predictor, coupled with a fixed detection rule **(5.1)**, can be investigated using the utilisation ratio, $U(\alpha,k,\varepsilon)$, defined as the ratio between the estimated long-term FCM utilisation time and the utilisation time in an ideal case ([**5.4**]) i.e.

$$U(\alpha,k,\varepsilon)=\frac{T_{FCM}}{T_{ideal}}\bigg|_{z''\geq\varepsilon}=\frac{\text{Prob}(z''(t+k|t)\geq\varepsilon)}{\text{Prob}(z'(t+k)\geq\varepsilon)} \qquad \textbf{(5.10)}$$

where z'' and z' denote respectively the effective FCM control effort and the modified global fading variables. In the ideal control case, the deployed FCM power equals the Ka band global fading z' that is with k=1, α=0, whatever the detected attenuation level ε (dB) and therefore U is expected to equal 1. The departure from U = 1 will thus be a measure of the inefficiency of the FCM controller. Using **(5.6)**, this may be expressed as:

$$U(\alpha,k,\varepsilon)=\frac{\int_{\varepsilon}^{\infty}\Lambda_{z''-\alpha}(m,\sigma)dz''}{\int_{\varepsilon}^{\infty}MGF_{z'}(\sigma,m,\sigma_{\sigma}(k),\sigma_{m}(k))dz'} \quad \text{where } k=1. \qquad \textbf{(5.11)}$$

In expanded form this is written:

$$U(\alpha,k,\varepsilon)=\frac{\int_{\varepsilon}^{\infty}\frac{1}{(z''-\alpha)\sigma\sqrt{2\pi}}\exp\left[-\frac{(\ln(z''-\alpha)-m)^2}{2\sigma^2}\right]\cdot dz''}{\frac{1}{\sigma_{\sigma_{np}}(k)\pi}\int_{\varepsilon}^{\infty}\int_{-\infty}^{\infty}\int_{0}^{\infty}\frac{1}{\sigma_{\chi_{dB}}^2(z-e)\sigma\cdot\sqrt{2\pi}}\exp\left[-\frac{(\ln(z'-e)-m)^2}{2\sigma^2}\right]\exp\left[-\frac{e^2}{2\sigma_{\chi_{dB}}^2}-\frac{\ln\left(\sigma_{\chi_{dB}}^2/\sigma_{m_{dB}}^2(k)\right)}{2\sigma_{\sigma_{np}}^2(k)}\right]d\sigma_{\chi_{dB}}de\cdot dz'}$$

For k = 1, the utilisation factor is given in terms of the ideal delayless case, corresponding to the situation where rain and scintillation are present i.e. the global fading model. Note that by this definition, U is independent of k since it is set to 1 in the denominator. But, as seen in section 5.2, the time delay has dictated the choice of a specific value of fixed detection margin α (for a specified link availability). Thus the impact of time delays enters indirectly equation **(5.11)** via the FDM in the numerator. The use of the utilisation factor can be illustrated using a practical design example. From Table 5.1, assuming a FCM time delay of 2

seconds (k=2) on the Chilton-Olympus link, a FDM α of 1.8 dB is required to achieve a detection outage probability smaller or equal to 0.1 % (RF Link availability of 99.9%). The function **(5.11)** has been computed for different FDM parameters, (α = 0, 1, 1.8, 2, 3 dB) , k = 2 and ε as variable. It is shown in Figure 5.4.

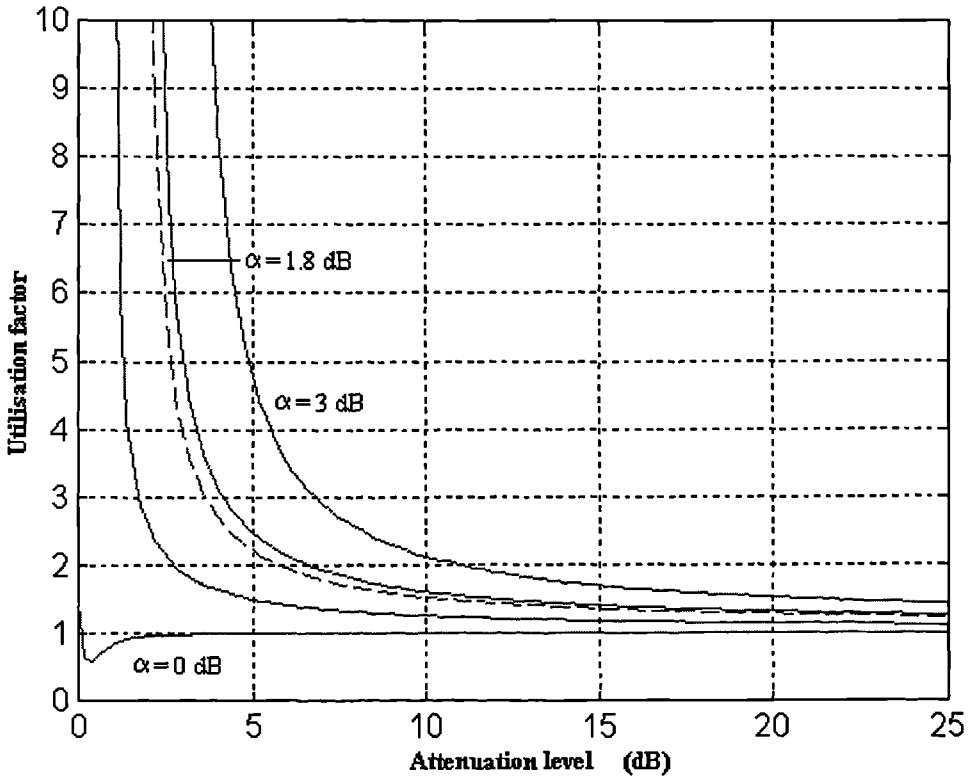

Figure 5. 4: Utilisation factor U as a function of attenuation level.

The utilisation factor can be seen as a distribution of the FCM weakness. Since the FCM power cannot be smaller than the FDM, we can see in figure 5.4 that U is a function of the FCM required equivalent power. The further U is from the ideal case U = 1, the worse the FCM detection scheme is at a particular level. If U>1, the FCM controller overestimates the actual fades and their durations. The fact that U varies with the attenuation level makes sense, since intuitively, a large FDM is not as negligible at low levels than at high levels, where we would expect U to converge towards 1. Note that it seems quite unfortunate that the utilisation

factor is particularly high for low levels of attenuation, since they are the ones that will occur the most frequently **[5.9, 5.10]**. The asymptotes occur at attenuation levels equal to α. Note that in practice the value of U at level α will *not* be infinite since practically T_{ideal} and T_{FCM} will always be finite and different from zero. These asymptotes are natural, since no deployed FCM power can be found below the FDM level α. In that sense, the FDM is equivalent to a fixed excess low fade margin. A similar design approach was used to design the ACTS rain compensation algorithm in **[5.11]** so that a 3 dB margin is always maintained.

The utilisation factor can be more usefully displayed as a function of the fixed detection margin, α, the detected attenuation level, ε, being a parameter. This is shown in Figure 5.5. To see whether these results are sensible, the reader may refer again to Figure 5.1. When $\alpha = 0$ dB, the utilisation factor should be 1. In practice, the utilisation factor is found to be close to this value, however, note that for $\varepsilon = 1$ for example, U is found to be below one. This is due to the fact that the predictor/estimator is *not* perfect and cannot capture part of scintillation. This *may* be justified in terms of scintillation enhancement effects. Now, in view of Figure 5.1, if $\varepsilon = \alpha$, we should expect U to be fairly large since this corresponds to a situation where $T_{FCM} >> T_{ideal}$. In practice U should be finite since T_{FCM} will never be infinite in the real world. From Figure 5.5, the greater the fixed power margin ε (i.e. the excess fade margin) the slower the increase in utilisation ratio. It is important to mention that the utilisation factor described here corresponds to estimated long term estimates since it is based on the pdf of detected and global fading. The larger the excess margin, ε, the less FCM action will be required (since high attenuation are statistically more scarce) and thus the impact of imperfect detection over a long period will be relatively less important.

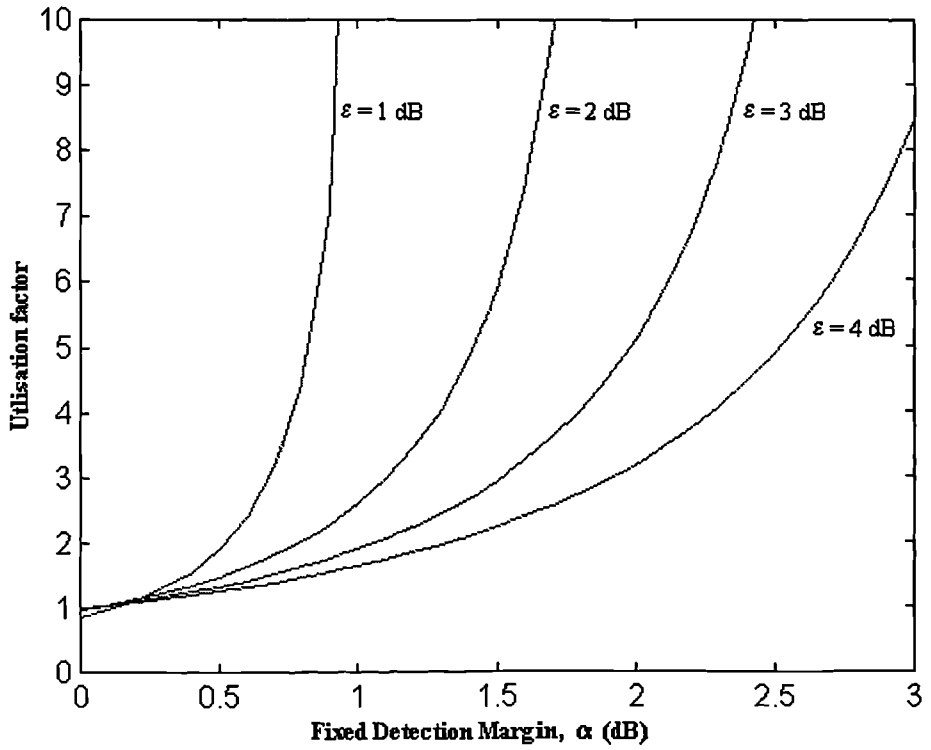

Figure 5. 5: Utilisation factor U as a function of the fade detection margin.

A conclusion, at this point, is that the combination of the results in section 5.2 and section 5.3 allows investigation of the performance and basic trade-off of predictive fade control systems. Imperfect estimation/prediction necessitates the implementation of a fixed detection margin to compensate for its residual error so that a usually *specified* RF link availability can be achieved. The larger the time delay or the worse the predictor, the larger the fixed detection margin will be. Alternatively a smaller link availability may be acceptable thereby requiring smaller FDM requirements. The value of fixed detection margin (FDM) was shown to have a definite impact on the utilisation ratio which is an index of quality of typical low fade margin systems. The larger the FDM the larger is the utilisation ratio. However this is not so clear cut, since U was also found to be dependent of the excess fixed power margin, ε, of the system and can be expected to be frequency dependent. Note in particular, that very poor utilisation factor figures are obtained for very low fade margins. In practice, due to the presence of time delays, excess margins of 4 dB or more *must* be built-in so that predictive

FCMs can perform in a channel efficient way. This is a very important and rather surprising point to consider in designing Ka band satellite systems **[5.11]**.

Although the definition of the detection problem is quite simple (Figure 5.1), the implications involve all the design parameters together. The general model described in this thesis allows qualitative and quantitative examination of the trade-off outage probability/utilisation factor including the impact of time delays. This is a new development although similar results were only published in **[5.4]**. However, they were obtained via simulation procedure and not through mathematical modelling as presented here. The proposed model thus allows a generalisation where all parameters may be chosen arbitrarily for evaluation of the performance of predictive countermeasure systems. A substantial time saving may therefore be made since the model avoids the need to run a chosen FCM estimator/predictor through empirical beacon data which may contain outliers and would be computationally more involving anyway.

5.3.4 Simulation Results and comparison with experimental data

The results of the utilisation factor are quite consistent with some published in **[5.4]**, where the utilisation factor was also found to increase monotically with the fixed detection margin. They simulated the behaviour of a predictive control strategy on Sirio data measured at 11.6 GHz and the simulation period was 3 years. Their estimate is thus reliable on a long-term basis. The authors used however a slightly different definition for the utilisation factor. They used $U'=(T_{FCM}-T_{ideal})/T_{ideal}$ which is equivalent to U'=U-1, U being the factor used in this thesis.

Transposed to our notation, they found a utilisation factor of around $U \approx 2$ for a fixed excess margin $\varepsilon = 3$ dB and a FDM of 0.7 dB. In our theoretical case (Figure 5.5), and for same FDM and excess margin, the theoretical utilisation factor is $U=1.8$. More of Dossi's points are shown in Figure 5.6 (black dots).

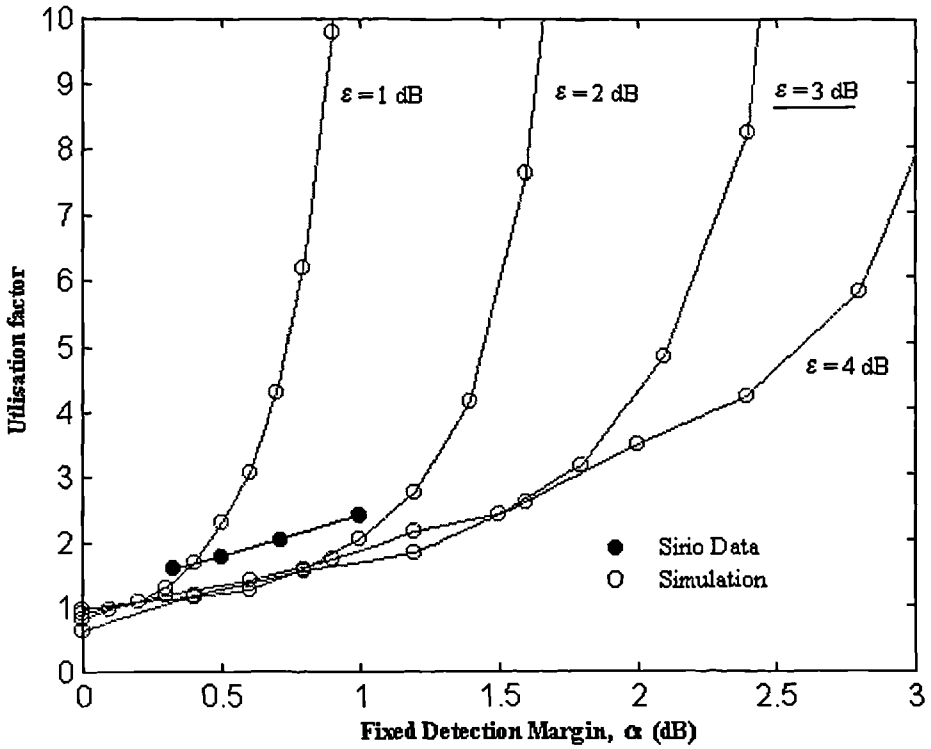

Figure 5. 6: Utilisation factor (Simulation results, 30 GHz, 600 hours).

Note in particular that the rate of change of their results is very similar to the one obtained in Figure 5.5 for $\varepsilon = 3\,\text{dB}$. There is however a 100-100*2/1.8=11% difference between their practical values and the theory. This discrepancy suggests that our theoretical analysis is based on a slightly better estimation/prediction scheme. Also, the difference may be due to the fact that they estimated the utilisation factor at a carrier frequency of 11.6 GHz, while the theoretical model was evaluated at 30 GHz. More importantly, their prediction scheme was also designed with a 1.8 dB hysteresis for delaying the time of relinquishment of the countermeasure. This is to reduce the number of FCM switchings caused by scintillation. This has the effect of increasing substantially the practical FCM utilisation time T_{FCM} and therefore the utilisation factor.

In order to test further the validity of the model in equation **(5.11)**, a simulation of a predictive control strategy has been simulated using a synthesised time-series at 30 GHz (See Appendix A4.III). The simulation period is 600 hours. The main objective was to verify that the utilisation factor with no hysteresis is indeed smaller than the one obtained by the Sirio experiment. Also, Sirio's practical results only span a small range of FDM between 0.3 and 1 dB and therefore they

do not allow us to verify the asymptotic behaviour of U when $\alpha = \varepsilon$. The simulation results are displayed in Figure 5.6. They show good agreement with the theoretical model, especially in the regions for which $\alpha << \varepsilon$. In the light of these empirical results, the proposed model is thus proven to give meaningful qualitative and quantitative results.

5.4 Variable detection margin approach

Current statistical models of scintillation describe the scintillation process as conditionally Gaussian, with its variance being itself time-varying. The short-term variance (from 1 to 10 minutes) is lognormally distributed for high elevation angles ([**5.12**]), while, for low elevation angles, the variance is better described with a gamma distribution ([**5.13**]). By taking this into account, it may therefore be possible to design fade control algorithms which are more closely matched to the dynamic characteristics of the Ka band fading process. In this section, the theoretical performance of a Variable Detection Margin (VDM) system is investigated. It attempts to evaluate scintillation fades based on the measured variance of the (scaled) scintillation process. This results in a detection scheme with increased adaptiveness, and therefore one may expect an improved overall performance.

5.4.1 Detection outage probability

There is experimental evidence that the standard deviation of the scintillation process does not vary very much on a short-term basis of the order of 1 minute [**5.14, 5-15**]. Let us assume that the real-time value of the scintillation standard deviation can be estimated on-line using a simple algorithm (see Figure 5.7) such as :

$$\hat{\sigma}_e(t) = \sqrt{\frac{1}{N-1} \cdot \sum_{i=t-N-k}^{t-k} \left[e(i) - \bar{e}\right]^2}, \qquad t \geq N + k \tag{5.12}$$

$$\text{where } \bar{e} = \frac{1}{N} \sum_{i=t-N-k}^{t-k} e(i). \tag{5.13}$$

$\bar{e}$ is the running block mean of the error made by the predictor. N denotes the size of the sliding widow used for estimating the running error standard deviation and

mean error (N=60 for the minute variance with a beacon update rate of 1 Hz) and k is the expected time delay in seconds of the FCM control system.

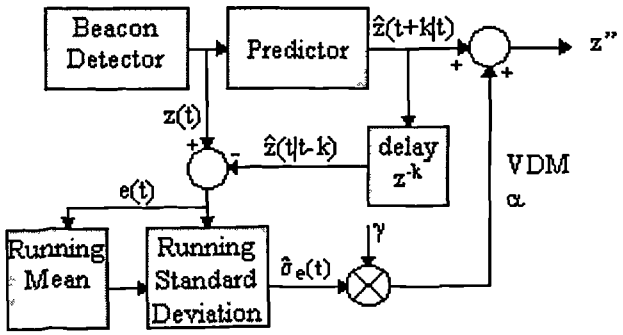

Figure 5. 7: Block diagram description of a variable detection margin scheme.

Then it is possible to devise a variable detection margin (VDM) such that the required FCM control effort becomes:

$$z'' = \hat{z}(t+k|t) + \alpha(t+k) \approx y(t+k) + \alpha(t+k) \tag{5.14}$$

where the VDM is given by (see **(4.6)**):

$$\alpha(t+k) = \gamma \cdot \hat{\sigma}_e(t) \approx \gamma \cdot \sqrt{f_2(k)} \cdot \sigma_\chi(t) \tag{5.15}$$

γ is a design parameter introduced here to control statistically the detection outage probability of the VDM detector. Detection outage probability can now be written as:

$$\begin{aligned} P_{out}^{pred}(\gamma) &= \text{Prob}\{y + \gamma \cdot \sigma_e \le y + e|\sigma_e\} \\ &= \text{Prob}\{\gamma \cdot \sigma_e \le e|\sigma_e\} \\ &= \text{Prob}\{e|\sigma_e \ge \gamma \cdot \sigma_e\} \end{aligned} \tag{5.16}$$

Based on the Mousley-Vilar model, the short-term variance of scintillation is conditionally Gaussian. From equation **(3.15)** , expressed in dB, the required value of the design parameter, γ, being given a specified detection outage probability, can be evaluated. We have:

$$P_{out}^{pred}(\gamma) = \text{Prob}\{e|\sigma_e \ge \gamma \cdot \sigma_e\} = \int_{\gamma \cdot \sigma_e}^{\infty} \frac{1}{\sigma_{e_{dB}} \cdot \sqrt{2\pi}} \exp\left(-\frac{e^2}{2\sigma_{e_{dB}}^2}\right) \cdot de \tag{5.17}$$

By making a change in variable, $u = e/\sigma_e$, **(5.17)** can be rewritten as:

$$P_{out}^{pred}(\gamma) = \frac{1}{\sqrt{2\pi}} \int_{\gamma}^{\infty} \exp(-u^2/2) \cdot du \equiv Q(\gamma) \tag{5.18}$$

Assuming that the co-error function Q(.) is invertible, the parameter, γ, is thus simply given by :

$$\gamma = Q^{-1}\left(P_{out}^{pred}\right). \tag{5.19}$$

In the range of practical interest, the control parameter γ should lie typically between 2 and 4 as shown in Figure 5.8.

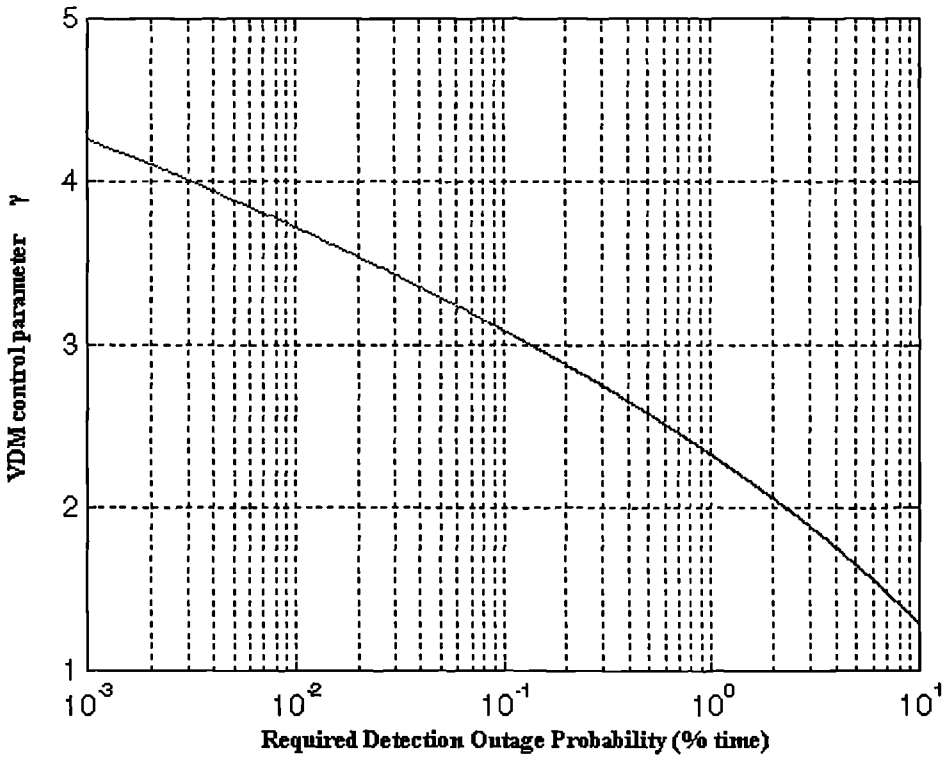

Figure 5. 8: Choice of the VDM control parameter to achieve a specified detection outage probability.

5.4.2 FCM control effort and Utilisation Factor

The variable detection margin is given by :

$$\alpha(t+k) = \gamma \cdot \hat{\sigma}_e(t) \approx \gamma \cdot \sqrt{f_2(k)} \cdot \sigma_\chi(t) \tag{5.20}$$

The pdf of the error has the characteristics of scaled variance. From equation **(3.16)** and including the impact of time delays within the context of predictive fade countermeasures, the pdf of the error variance is given by:

$$f_{\sigma^2_{e_{np}}}\left(\sigma^2_{e_{np}}\right)=\frac{1}{\sigma^2_{e_{np}}\sigma_{\sigma_{np}}(k)\sqrt{2\pi}}\exp\left(-\frac{\left(\ln\sigma^2_{e_{np}}/\sigma^2_{m_{np}}(k)\right)^2}{2\sigma^2_{\sigma_{np}}(k)}\right) \qquad \textbf{(5.21)}$$

Using the change of variables $\sigma_{e_{np}}=\sqrt{\sigma^2_{e_{np}}} \Rightarrow \frac{d\sigma_{e_{np}}}{d\sigma^2_{e_{np}}}=\frac{1}{2\sqrt{\sigma^2_{e_{np}}}}=\frac{1}{2\sigma_e}$, the pdf of the residual error standard deviation, $\sigma_{e_{np}}$, can be shown to be equal to:

$$f_{\sigma_{e_{np}}}\left(\sigma_{e_{np}}\right)=\sqrt{\frac{2}{\pi}}\cdot\frac{1}{\sigma_{e_{np}}\sigma_{\sigma_{np}}(k)}\exp\left(-\frac{\left(\ln\sigma^2_{e_{np}}/\sigma^2_{m_{np}}(k)\right)^2}{2\sigma^2_{\sigma_{np}}(k)}\right) \qquad \textbf{(5.22)}$$

Using two new changes of variables, $\sigma_{e_{dB}}=(20\cdot\log_{10}e)\cdot\sigma_{e_{np}}=8.68\sigma_{\chi_{np}}$ followed by $\sigma_{m_{dB}}=8.68\cdot\sigma_{m_{np}}$, in order to express these two quantities in dBs instead of nepers, we get the following probability density function:

$$f_{\sigma_{e_{dB}}}\left(\sigma_{e_{dB}}\right)=\sqrt{\frac{2}{\pi}}\cdot\frac{1}{\sigma_{e_{dB}}\sigma_{\sigma_{np}}(k)}\exp\left(-\frac{\left(\ln\sigma^2_{e_{dB}}/\sigma^2_{m_{dB}}(k)\right)^2}{2\sigma^2_{\sigma_{np}}(k)}\right) \qquad \textbf{(5.23)}$$

Finally, it is now easy to derive the pdf of the variable detection margin $\alpha=\gamma\cdot\sigma_{e_{dB}}$ by making a last transformation of density function. This yields the sought result:

$$f_{\alpha_{dB}}(\alpha_{dB})=\sqrt{\frac{2}{\pi}}\cdot\frac{1}{\alpha_{dB}\cdot\sigma_{\sigma_{np}}(k)}\exp\left(-\frac{\left(\ln\alpha^2_{dB}/\gamma\cdot\sigma^2_{m_{dB}}(k)\right)^2}{2\sigma^2_{\sigma_{np}}(k)}\right) \qquad \textbf{(5.24)}$$

In order to evaluate the pdf of the required control effort, z"=y+α, one must now consider whether there exist a statistical relationship between rain attenuation y and the standard deviation of the error (scintillation). It will be assumed *here* that they are statistically independent, in conformity with the global fading hypothesis. The validity of such an assumption will be discussed in the next chapter, however it simplifies greatly the analysis and it still gives a *worst-*

case scenario. In the case of statistical independence, the required FCM control effort of the VDM detection scheme is thus:

$$f_{z''}(z'') = \Lambda_y(m,\sigma) * f_\alpha(\alpha) \tag{5.25}$$

$$f_{z''}(z'') = \frac{1}{\pi\sigma \cdot \sigma_{\sigma_{np}}(k)} \int_{-\infty}^{\infty} \frac{1}{(z'-\alpha)\cdot\alpha} \cdot \exp\left[-\frac{(\ln(z'-\alpha) - m)^2}{2\sigma^2}\right] \cdot \exp\left[-\frac{\left(\ln\left(\alpha_{dB}^2/(\gamma^2 \cdot \sigma_{m_{dB}}^2(k))\right)\right)^2}{2\cdot\sigma_{\sigma_{np}}^2(k)}\right] d\alpha$$

It is now straight forward to give an expression for the utilisation factor of the VDM scheme.

$$U(\gamma,\varepsilon,k) = \frac{\int_{\varepsilon}^{\infty} f_{z''}(z'')dz''}{\int_{\varepsilon}^{\infty} GF_z(\sigma,m,\sigma_\sigma,\sigma_m)\cdot dz}, \varepsilon \geq 0 \tag{5.26}$$

In expanded form, this is written as:

$$U(\gamma,k,\varepsilon) = \frac{\frac{1}{\pi\sigma\cdot\sigma_{\sigma_{np}}(k)} \int_{\varepsilon}^{\infty}\int_{-\infty}^{\infty} \frac{1}{(z''-\alpha)\cdot\alpha} \cdot \exp\left[-\frac{(\ln(z''-\alpha) - m)^2}{2\sigma^2}\right] \cdot \exp\left[-\frac{\left(\ln\left(\alpha_{dB}^2/(\gamma^2\cdot\sigma_{m_{dB}}^2(k))\right)\right)^2}{2\cdot\sigma_{\sigma_{np}}^2(k)}\right] d\alpha \cdot dz''}{\frac{1}{\sigma_{\sigma_{np}}(l)\pi} \int_{\varepsilon}^{\infty}\int_{-\infty}^{0}\int_{-\infty}^{\infty} \frac{1}{\sigma_{\chi_{dB}}^2(z-e)\sigma\cdot\sqrt{2\pi}} \exp\left[-\frac{(\ln(z'-e)-m)^2}{2\sigma^2}\right] \exp\left[-\frac{e^2}{2\sigma_{\chi_{dB}}^2} - \frac{\ln\left(\sigma_{\chi_{dB}}^2/\sigma_{m_{dB}}^2(l)\right)}{2\sigma_{\sigma_{np}}^2(l)}\right] d\sigma_{\chi_{dB}} de \cdot dz'}$$

This function has been computed with the delay k (sec.) and the fixed excess margin, ε (dB) as parameters and the VDM control parameter γ as independent variable. This is displayed in Figure 5.9. The results are very similar to the ones obtained for the fixed detection margin system. For a fixed value of fixed excess margin, an increase of γ results in an increase of utilisation factor. The larger the value of the excess margin, the smaller is the utilisation factor.

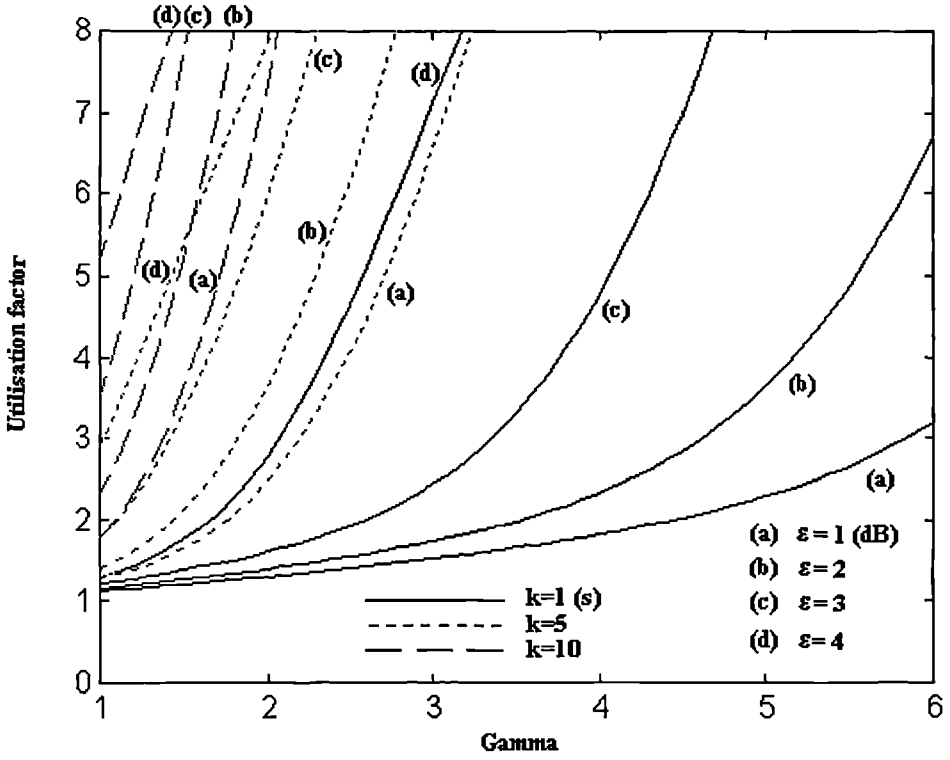

Figure 5. 9: Utilisation factor as a function of the parameter γ (VDM approach).

Two major differences with the FDM approach are that the utilisation factor does not have here any asymptotic behaviour, and, furthermore it is directly dependent upon the time delay of the FCM system (see the numerator of equation 5.26). A larger time delay results in a greater utilisation factor (i.e. FCM over-utilisation, which is particularly crucial to shared resource FCMs).

At this stage, it is worth pointing out that figures 5.8 and 5.9 allow the designer to assess the basic trade-off between detection outage probability and utilisation factor for the VDM detection scheme. Being given a fixed time delay, a larger value of γ will reduce the prediction outage probability, but this will have the consequence of increasing the FCM over-utilisation. If the latter is found to be unacceptable because too large, then the designer has then the possibility of increasing the low fixed excess margin built-in into the satellite system. This allows us to switch on a lower curve on the utilisation factor graph.

As a practical design example, notice that the utilisation factor lies between 1.2 and 2 for $\gamma \in [2 \quad 4]^*$ for a time delay of 1 second and for a fixed excess margin $\varepsilon = 4$ dB. Such a time delay is typical of ULPC countermeasure systems. This suggests that if such a system is to be designed efficiently, the designer has to provide a low fade margin of *at least* 4 dB in his/her link budget analysis. Thus, as for the FDM, the design of truly low-fade margin systems does not seem applicable to predictive Ka band systems.

5.4.3 Comparison of Fixed and variable detection margin approaches

In order to assess whether the use of the VDM is more efficient than the FDM approach, the Cumulative Distribution functions (CDFs) of both fade detection rules have been evaluated for an identical outage detection probability. The detection outage probability was chosen to be 0.001 (corresponding to 0.1% of the time). Three different time delays between 1 and 10 seconds were also considered. The comparative results are shown in Figure 5.10.

The VDM is found to be smaller then the FDM for approximately 85% of the time for a time delay of 10 seconds. A heuristic discussion is to consider the fade duration statistics of the scintillation variance and the fact that small values of scintillation variance usually last longer than larger ones **[5.16]**. As a consequence, one can expect that the VDM approach corresponds to a reduction in required FCM control effort compared to the FDM approach.

*From Fig. 5.8, this corresponds to a detection outage probability, $P_{out}^{pred}(\%) \in [0.08 \quad 2]$

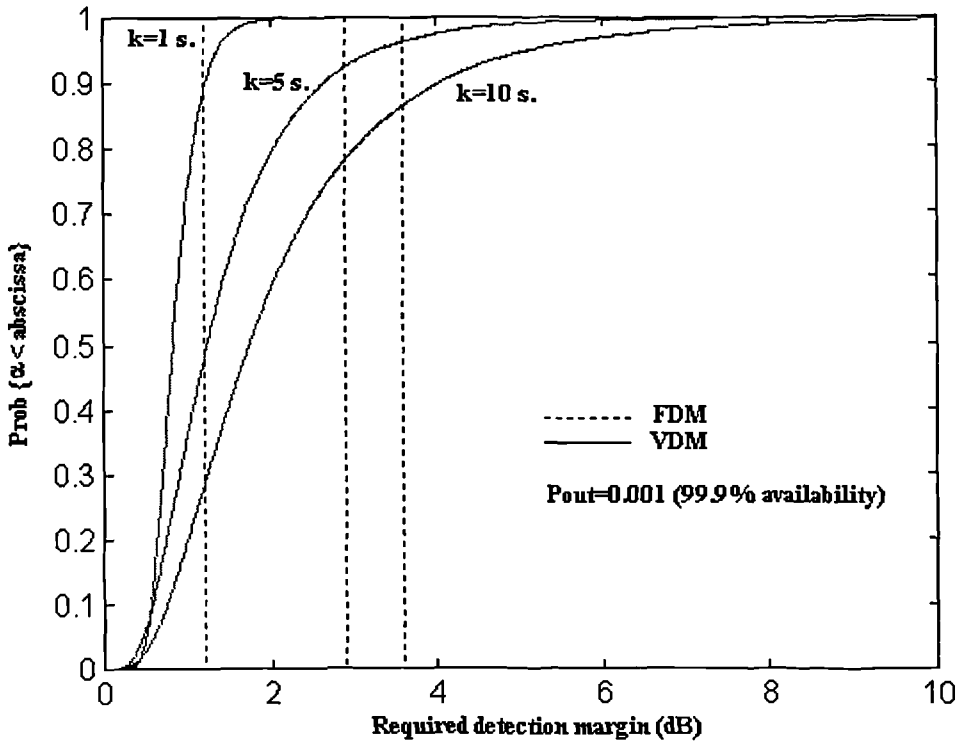

Figure 5. 10: CDF of the VDM compared to the FDM .

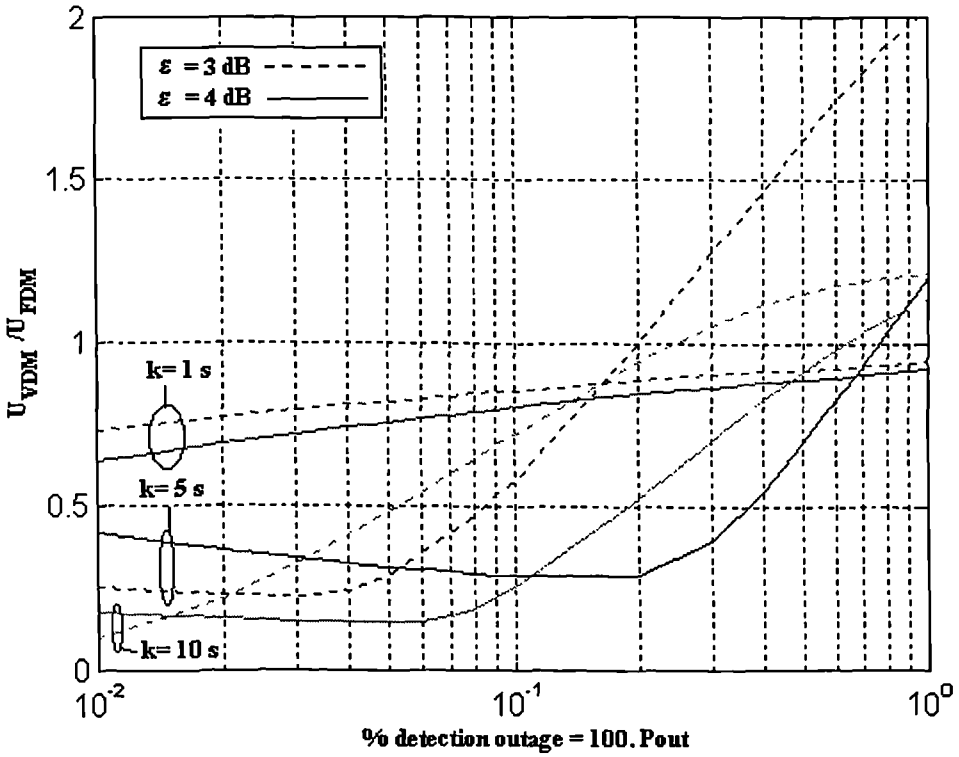

Figure 5. 11: Comparison of the utilisation factor for FDM and VDM approaches.

The FDM and VDM approaches may also be compared in terms of utilisation factor. For this, the ratio U_{VDM}/U_{FDM} has been computed from **(5.9)** and **(5.26)** for identical detection outage probabilities in the range of practical interest (Figure 5.11).

One can note that for low detection outage probability, the VDM approach yields substantially lower utilisation factors than the FDM approach. Using our example, for P_{out}=0.005 and k= 5 s, U_{VDM}/U_{FDM} is approximately 0.4. Thus the fixed excess low fade margin requirements of the VDM detection scheme will be far lower than the FDM. The VDM approach is therefore better suited to low-fade margin systems. The utilisation factor is an intermediate parameter which allows the evaluation of the likely FCM over-utilisation of the shared resource in Adaptive-TDMA (A- TDMA) or frequency diversity (FDV) **[5.5]**. More particularly, the relative value of the detection margin (fixed or variable) with respect to the in-built excess margin sets the utilisation factor. It was seen here that the detection margin has to be relatively small compared to the excess margin. Thus the FCM utilisation factor can be used to find the most appropriate excess margin, once a detection margin has been selected (depending on the expected FCM set-up delay and the specified detection outage probability).

5.5 Performance of adaptive forward error control (AFEC) countermeasure

5.5.1 Channel Capacity Utilisation [5.17]

Using the concept of control effort, it is also possible to determine the long term impact of joint rain and scintillation on the *achievable* channel capacity utilisation using a predictive FCM controller. This will essentially give the same kind of information as for the utilisation ratio. However, here the performance of the controller will be expressed in terms of channel capacity and this can find direct application whenever coding or modulation issues are of interest. From the Shannon-Hartley theorem, the channel capacity per unit bandwidth is given by:

$$\frac{C}{B} = \log_2\left(1+\frac{S}{N}\right) \qquad \text{b/s/Hz} \tag{5.27}$$

Inverting this and expressing in dB gives:

$$\frac{S}{N} = 10 \cdot \log_{10} \ (2^{C/B} - 1) \qquad \text{dB} \tag{5.28}$$

The probability that C/B does not exceed a value x may be expressed by writing:

$$\text{Prob}\{\frac{C}{B} \leq x\} = \text{Prob}\{\frac{S}{N} \leq 10 \cdot \log_{10} \ (2^{x} - 1)\}$$

Inverting this and expressing in dB gives:

$$\frac{S}{N} = 10 \cdot \log_{10} \ (2^{C/B} - 1) \qquad \text{dB} \tag{5.28}$$

The probability that C/B does not exceed a value x may be expressed by writing:

$$\text{Prob}\{\frac{C}{B} \leq x\} = \text{Prob}\{\frac{S}{N} \leq 10 \cdot \log_{10} \ (2^{x} - 1)\}$$

Using the definition of the control effort, $\frac{S}{N} = \frac{S}{N}\Big|_0 - FCM$ *, one can write the probability that the channel capacity per unit bandwidth is not exceeded:

$$\text{Prob}\{\frac{C}{B} \leq x\} = \text{Prob}\{FCM \geq \frac{S}{N}\Big|_0 - 10 \cdot \log_{10} \ (2^{x} - 1)\} \tag{5.29}$$

In the case of an ideal controller, the FCM control effort is equal to the global fading i.e. z''= z' = y+e , therefore the channel capacity utilisation can be written as:

Ideal case: $$\text{Prob}\{\frac{C}{B} \leq x\} = \int_{\tau}^{\infty} GF_{z'}(\sigma, m, \sigma_{\sigma}(1), \sigma_{m}(1)) dz' \tag{5.30}$$

In practice however, the FCM controller cannot capture the scintillation component and requires a detection margin, i.e. z''≃ y+α, and therefore the achievable channel capacity is given by (see equation 5.1):

Practical case: $$\text{Prob}\{\frac{C}{B} \leq x\} = \int_{\tau}^{\infty} f_{z''}(z'') dz'' \tag{5.31}$$

where $\tau = \frac{S}{N}\Big|_0 - 10 \cdot \log_{10} \ (2^{x} - 1)$ in both (5.30) and (5.31).

* $S/N_0 = C/N_0 - BW$, BW: bandwidth (dB.Hz)

Channel capacity utilisation for both ideal and practical control cases is plotted in Figure 5.12 for $S/N|_0$ = 18.28 dB (P_{hpa} = 0.2W, D=0.8m, see section 3.3.1) where a bandwidth corresponding to R_s =9600 symb/sec is assumed.

The vertical line (a) corresponds to the channel capacity per unit bandwidth in the non-stochastic case and was derived directly from **(5.27)**. Case (b) corresponds to the ideal control case, as described by equation **(5.30) [5.17]**. It can be seen that for approximately 25% of the time, the channel capacity in the ideal control case is greater that that of free space case due to scintillation enhancement effect. This interesting effect was first discussed in **[5.17]** and leads to the idea of efficient channel capacity utilisation whereby the choice of coding and/or modulation scheme is conditioned by the now stochastic nature of the channel capacity. This consists essentially in plotting the non-stochastic vertical C/B thresholds of different candidate modulation/coding schemes (operating at a specified same BER) and then choosing the most channel efficient in the presence of stochastic fading.

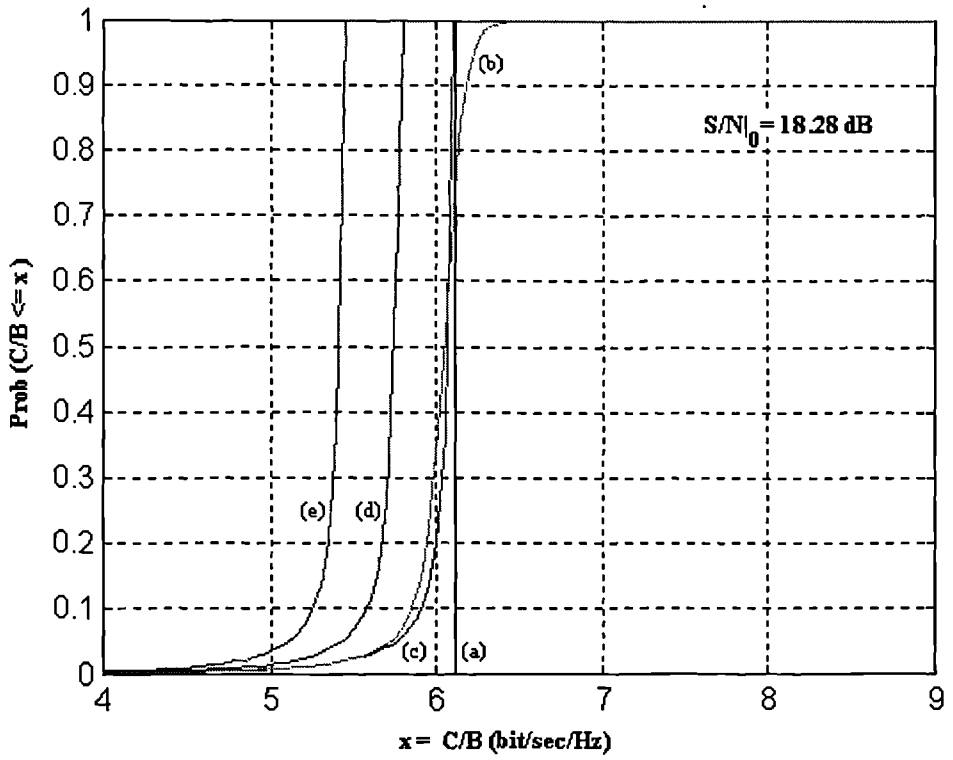

Figure 5. 12: CDF of the channel capacity per unit bandwidth: (a) non-stochastic case (b) ideal control case, (c) α =0 dB, (d) α =1 dB, (e) α =2 dB (FDM approach).

However, in the context of realistic FCM control systems, it is not possible to take advantage of the scintillation enhancements since scintillation was found not predictable as depicted by curve (c) with $\alpha = 0$ dB ([**5.18**]). The necessity to cater for predictor imperfection imposed the implementation of a fixed detection margin $\alpha > 0$. This has the effect of substantially reducing the achievable channel capacity per unit bandwidth (curves (d) and (e)), and thus the impact of time delay is found to result in a decrease of the overall throughput of the FCM system. This type of performance index is particularly interesting for adaptive transmission systems where the modulation, coding or data rate are adapted according to detected channel attenuation.

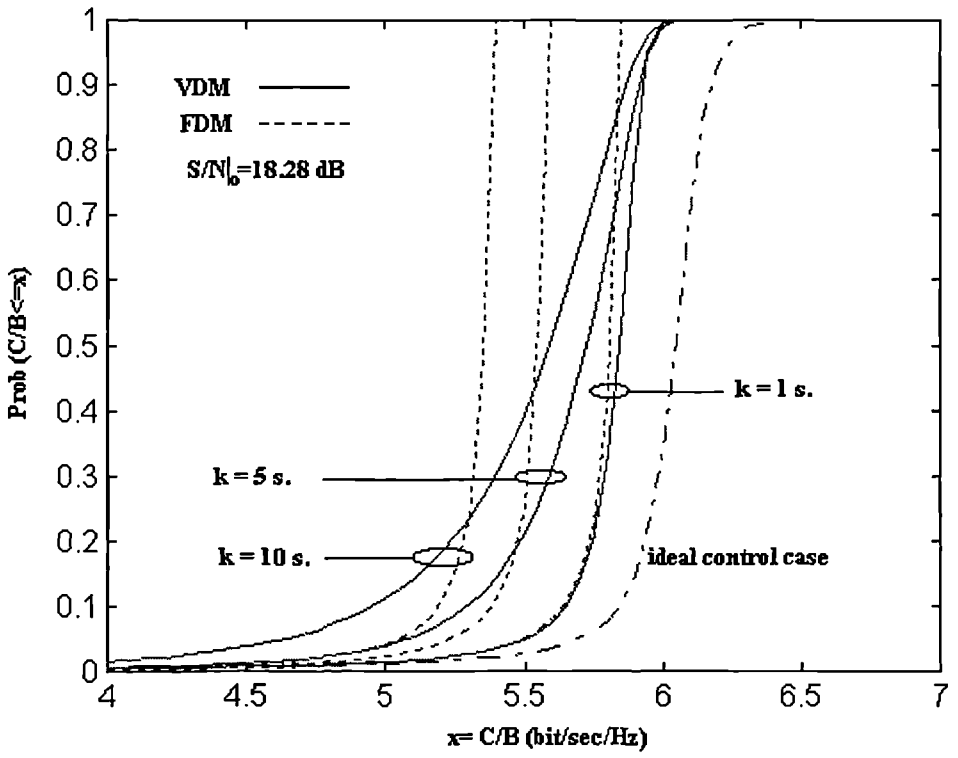

Figure 5. 13: Comparison of the channel capacity per unit bandwidth for the FDM and VDM approaches for three time delays and the same detection outage probability (0.1 % of the time).

Figure 5.13 shows the capacity per unit bandwidth for the fixed and variable detection margin schemes with respect to the ideal control case. For short time delays (k=1 s), the VDM curve is always below that of the FDM, therefore the VDM scheme is more channel efficient. Note in particular, that the VDM approach, being more adaptive (closer to being capable of predicting the scintillation enhancements) tends always to be nearer the ideal control case for relatively high values of C/B (bps/Hz). However, for long time delays, e.g. k=10 sec, the VDM scheme becomes less efficient than the FDM scheme for C/B<5.3 bps/Hz. This will occur for high values of scintillation variance, which in general occur more rarely than the small values. Therefore, one may expect that the VDM is in general more channel efficient and should result in a greater average throughput.

5.5.2 Bit error rate performance of punctured convolutional codes

Given the free distance d_{free} and the distance spectrum $\{c_d\}$ of a convolutional code with rate $\rho = b/v$, where c_d is the number of error bits in all incorrect paths at distance d from the correct path, the bit error probability P_b of Viterbi decoding is upper bounded by **[5.19]**:

$$P_b \leq \frac{1}{b} \sum_{d=d_{free}}^{\infty} c_d P_d \tag{5.32}$$

For the additive white Gaussian noise (AWGN) channel with infinite quantisation, P_d is given by:

$$P_d = Q\left(\sqrt{2 \cdot d \cdot E_s / N_0}\right) \tag{5.33}$$

where $E_s/N_0 = \rho \cdot E_b/N_0$ is the signal to noise ratio per transmitted symbol and where Q(x) is defined as:

$$Q(x) = \frac{1}{\sqrt{2\pi}} \int_x^{\infty} e^{-y^2/2}\, dy \tag{5.34}$$

The puncturing patterns and parameters d_{free} , $\{c_d\}$ of punctured convolutional codes are generally obtained via extensive computer search and are tabulated in dedicated references. For example, Yasuda et al. in **[5.20]** give the

distance spectra of codes of the family of code with rates $\rho = (N-1)/N$ by puncturing a rate 1/2, memory $\nu = 6$ code for N up to 14 and based on soft quantisation. Such adaptive coding systems have been implemented and tested in **[5.21]** and **[5.22]**. They showed excellent agreement with the theory and are easily implemented from a standard convolutional encoder/decoder chip. Hagenauer has extended in **[5.23]** the concept of punctured convolutional codes to the generation of rate-compatible punctured convolutional
(RCPC) codes. The rate compatibility restriction implies that all code bits of high code rate codes are used by lower code rates thereby allowing incremental redundancy in ARQ/FEC systems as well as continuous variation of error protection within a data frame. Another family of good RCPC codes, based on a simple search procedure, is also presented in **[5.24]**. Extended weight spectra and upper bounds on the bit error probability of the best known punctured codes with short memory ($2 \leq \nu \leq 8$) and rates between 2/3 and 7/8 are given in **[5.25]** and have been used in this study.

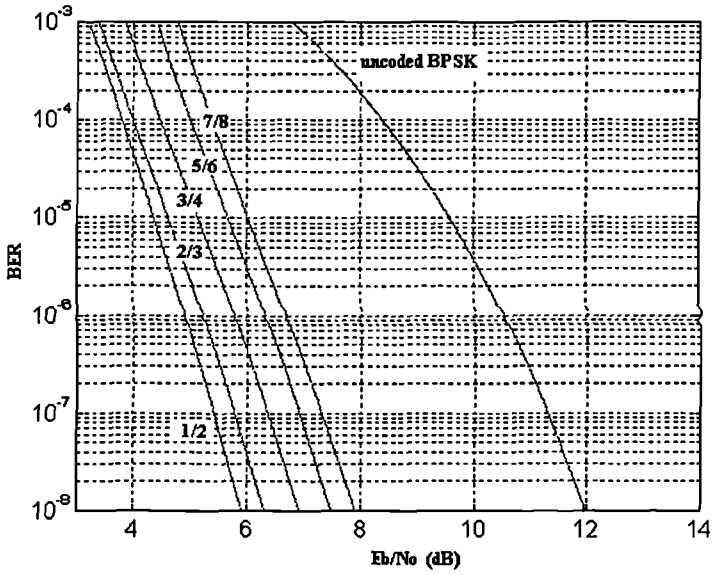

Figure 5. 14 : BER performance of punctured convolutional codes based on a half-rate mother code and Viterbi decoding (ν=6).

5.5.3 BER/throughput of a fixed FEC system and ideal AFEC countermeasure

In order to serve as a reference to the next sections, the performance of both fixed FEC and ideal AFEC FCM controllers will be calculated. Such a hypothetical controller is one that can detect and predict the global fading z as a whole. In such circumstances, there will be no detection/prediction error and therefore there is no need for a fade detection margin. In the case of adaptive FEC (AFEC) system, this will yield a maximum throughput while the BER availability will be conditioned by the specified maximum bit error rate in the presence of global fading.

The upper bound BER of a punctured convolutional code given by **(5.32)** is a function of the signal-to-noise ratio E_b/N_0 and depends on the code rate. For convenience and generality, let us rewrite **(5.32)** more compactly as:

$$P_b = g_\rho(E_b/N_0) \tag{5.35}$$

The subscript ρ denotes the rate of the code considered. Assuming that this is invertible, expressing in dB, the required E_b/N_0 at a BER $\hat{\beta}$ and code rate ρ is given by:

$$\left.\frac{E_b}{N_0}\right|_{rq@\hat{\beta},\rho} = g_\rho^{-1}(P_b = \hat{\beta}) \Leftrightarrow \left.\frac{E_b}{N_0}\right|^{dB}_{rq@\hat{\beta},\rho} = 10\log_{10}\left(g_\rho^{-1}(\hat{\beta})\right) \text{ dB} \tag{5.36}$$

From Fig. 5.14, being given a maximum BER constraint $\hat{\beta}$, we have:

$$\text{Prob}\left\{BER \geq \hat{\beta}\right\} = \text{Prob}\left\{\frac{E_b}{N_0} \leq \left.\frac{E_b}{N_0}\right|^{dB}_{rq@\hat{\beta},\rho}\right\}$$

Using $\left.\frac{C}{N_0}\right|_{0,dB} - 10\log_{10}(R_s) - z' = 10\log_{10}\left(g^{-1}(P_b)\right)$, after arrangement, the BER unavailability can be written as:

$$\text{Prob}\{BER \geq \hat{\beta}\} = \text{Prob}\left\{z' \geq \left.\frac{C}{N_0}\right|_0 - 10\log_{10}(R_s) - 10\log_{10}\left(g_\rho^{-1}(\hat{\beta})\right)\right\} \tag{5.37}$$

where $\text{Prob}(z' \geq \varepsilon) = \int_{\varepsilon}^{\infty} GF_{z'}(\sigma, m, \sigma_\sigma, \sigma_m) dz'$.

In the case of a fixed FEC scheme with code rate ρ, the user average data throughput is simply given by:

$$\overline{\eta} = \rho \cdot R_s \cdot \left(1 - \text{Prob}\left\{BER \geq \hat{\beta}\right\}\right) \tag{5.38}$$

Equation **(5.37)** and **(5.38)** have been computed for the Chilton-Olympus back-to-back link for a FCM system based on punctured convolutional codes with mother code of rate 1/2 and memory 6 (Figure 5.14). The rates that can be supported are ρ = 1/2, 2/3, 3/4, 5/6, 7/8 and 1. A fixed bandwidth corresponding to R_s=9600 symb./s is assumed.

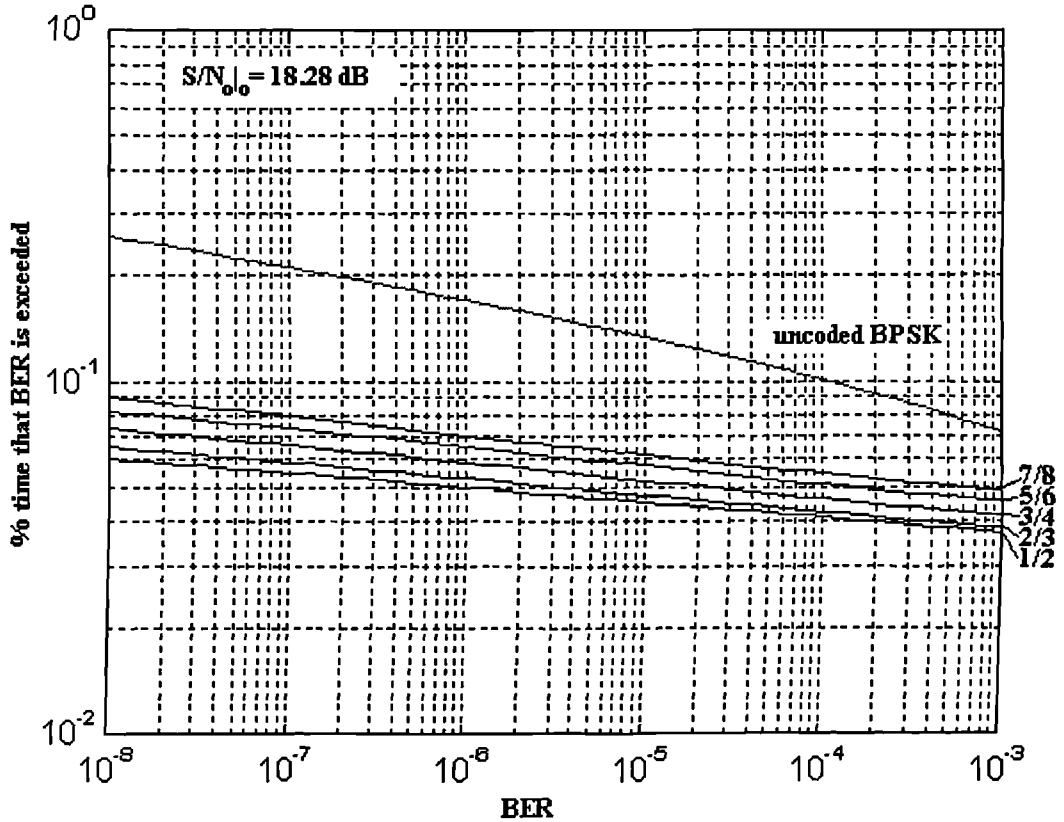

Figure 5.15: BER unavailability and average user data throughput of a fixed FEC scheme (Chilton-Olympus link, P_{hpa}=0.2W, D=0.8 m)

Fixed FEC system code rate	Rq. E_b/N_0 (dB) @ BER=10^{-7}	Excess Fade protection margin (dB)	BER availability (%)	Outage time (min)	Average user data throughput (bps)
1	11.39	6.39	99.7500	1314.9	9576.00
7/8	7.33	10.38	99.9063	492.8	8392.12
5/6	6.95	10.76	99.9113	456.0	7992.90
3/4	6.39	11.32	99.9224	408.1	7194.41
2/3	5.79	11.92	99.9307	364.5	6395.56
1/2	5.43	12.28	99.9351	341.3	4796.88

Table 5.2: Fixed FEC system performance (P_{hpa}=0.2 W, D=0.8 m, Chilton/Olympus link).

A system with fixed code rate ρ = 1/2 will have a BER availability of 99.93 % for maximum bit error rate constraint of 10^{-7} while, for example, uncoded BPSK would operate satisfactorily for approximately 99.75% of the time. These are excellent and rather surprising figures. They can be justified in terms of the *sufficient* antenna size (0.8 m), HPA power (0.2 W) and low symbol rate (9600 symb./sec) of the transmitting VSAT station, which, in this particular test case, are fairly appropriate. A lower HPA power or dish diameter or larger bit rate would decrease these availability figures. In fact, those good figures can be attributed to the fact that the fixed built-in excess margin of the FEC system is 6.39 dB, thereby allowing for efficient channel capacity utilisation and low FCM utilisation factor. Graphic output of the type of figure 5.15 is therefore ideally suited to 'tune' or dimension appropriately HPA and antenna size of the VSAT station being given a particular adaptive transmission FCM system.

Code rate in an A-FEC system	% time for which the code rate is utilised	Utilisation time (min)	Contribution to the data throughput (bps)
1	99.7500	524645.10	9576.00
7/8	0.1563	822.10	13.1292
5/6	0.0050	26.45	0.4024
3/4	0.0111	61.54	0.7970
2/3	0.0083	43.65	0.5312
1/2	0.0044	23.14	0.2112
Average user data throughput (bps)			9591.07
Availability @ BER=10^{-7}			99.9351

Table 5.3: Performance of adaptive FEC countermeasure (P_{hpa}=0.2 W, D=0.8 m, Chilton/Olympus link).

Table 5.3 shows the performance of an ideal delayless AFEC countermeasure system. While uncoded BPSK would be used for most of the time, the lower code rates (especially 7/8) allows us to increase substantially the average throughput and BER availability of the AFEC system w.r.t to uncoded BPSK.

Code rate in a fixed FEC system	BER availability w.r.t an AFEC system	Average throughput w.r.t. an AFEC system
1	0.9981	0.9984
7/8	0.99971	0.8750
5/6	0.99976	0.8333
3/4	0.99987	0.7501
2/3	0.99995	0.6668
1/2	1	0.5001

Table 5.4: Comparison of fixed and variable FEC systems.

Table 5.4 compares the estimated performance of ideal fixed and variable FEC systems and shows the great advantage of using adaptive transmission methods. The ideal AFEC countermeasure system inherits the BER availability of the most robust scheme (rate=1/2), while its throughput is slightly better than the one for a fixed uncoded BPSK system. This is the main justification to implement

adaptive transmission systems like AFEC, adaptive modulation or adaptive transmission rate as fade countermeasures.

The countermeasure system has the BER outage probability of the most robust fixed FEC system, while the user data throughput is slightly better than that of the less robust fixed system (which is the most channel efficient).

5.5.4 BER/Throughput of a FDM-AFEC system

The design of adaptive transmission systems relies on the determination of the FCM decision boundaries, so that the system satisfies a specified availability with the constraint of a maximum bit error rate denoted by $\hat{\beta}$ **[5.26, 5.27, 5.28]**. These boundaries, from which FCM switchings to a more or less robust level of protection is achieved, must be based on the predicted/corrected required FCM control effort $z''=\hat{z}+\alpha \approx y+\alpha$. α is the fixed detection margin. Its value is conditioned by the time delay, k (sec) in the FCM system and the specified detection outage probability P_{out}^{pred} (see section 5.3.2). Effectively, the adaptive coding countermeasure must switch from a code rate to the next lower rate as soon as the following inequality is satisfied:

$$\left.\frac{C}{N_0}\right|_{t,0} - 10\log_{10}\left(\frac{R_b}{\rho}\right) - (\alpha + y) - \mu_i \leq \left.\frac{E_b}{N_0}\right|_{rq@\hat{\beta},\rho} \qquad \textbf{(5.39)}$$

where the last term is the minimum E_b/N_0 required to achieve a maximum BER of $\hat{\beta}$, for a particular FEC code with rate, ρ, and a particular modulation scheme. μ_i is the margin for implementation (set to 0.75 dB). For a simple adaptive FEC countermeasure, the change in the level of coding requires a change in input bit rate so that $R_s = R_b/\rho$ remains constant **[5.2]**. In the Chilton/Olympus case studied here a low rate (CODE type) fixed symbol rate R_s = 9.6 ksymb./s has been assumed.

From **(5.33)**, the level of admissible rain fades, y (dB), for a particular BER constraint and a particular code rate, is therefore given by:

$$y \geq \left.\frac{C}{N_0}\right|_{t,0} - 10\log_{10}\left(\frac{R_b}{\rho}\right) - \alpha - \left.\frac{E_b}{N_0}\right|_{rq@\hat{\beta},\rho} \qquad \textbf{(5.40)}$$

This can be used to derive the Code Rate Change (CRC) boundaries, $\rho(y)$, of the AFEC system (Figure 5.17). The CRC boundaries is the look-up table, which is integrated within a simple FCM control algorithm **[5.29]**. The latter, based on the CRC boundaries, can choose the appropriate code rate and user data rate (so that R_b/ρ=constant), based on the detected/predicted rain attenuation y (dB).

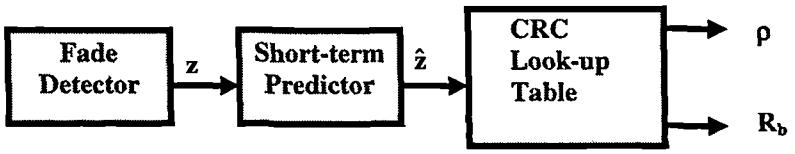

Figure 5.16: Code Rate Change (CRC) boundaries for control of FDM-FCM resources

Note that these boundaries are conditioned by the FDM required to achieve a specified detection outage probability (i.e. it depends on the desired statistical accuracy of the fade detection/prediction system). From **(5.40)**, any increase in FDM will result in a decrease in acceptable rain fades. This will subsequently translate into an increase in BER unavailability and a decrease in average data throughput. Thus the introduction of a detection margin results in a *degradation* of performance relative to the ideal delayless AFEC case (described in section 5.5.3). It is therefore important to quantify and possibly minimise this degradation.

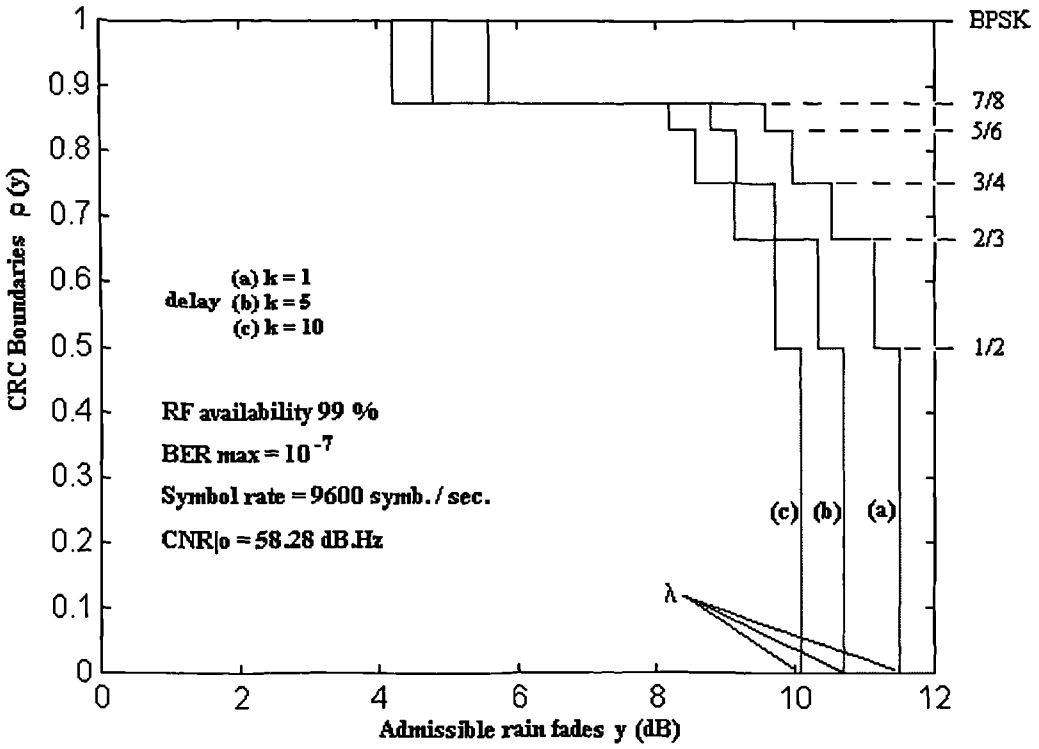

Figure 5.17: Example of CRC boundaries for an FDM-AFEC countermeasure.

The level λ (dB) in the above graph (Figure 5.17), corresponds to the highest permitted level of detected/predicted rain fade which can be compensated for with the most robust code (1/2) of the AFEC system. When y> λ, the CRC function, ρ(y) has been set to zero, to emphasise that this corresponds to a BER outage situation. As such, it is assumed here that all data is *lost* when level λ is exceeded. The BER unavailability is thus:

$$\text{Prob}\{BER \geq \hat{\beta}\} = \text{Prob}\left\{ y \geq \lambda \equiv \left.\frac{C}{N_0}\right|_0 - 10\log_{10}(R_s) - \alpha - 10\log_{10}\left(g_{1/2}^{-1}(\hat{\beta})\right)\right\} \tag{5.41}$$

where $\text{Prob}\{y \geq \lambda\} = \int_{\lambda}^{\infty} \Lambda_y(m,\sigma) \cdot dy$.

The average user data throughput can also be determined quite easily from the CRC function. It is given by:

$$\overline{\eta} = R_s \cdot \int_0^{\lambda} \rho(y) \cdot \Lambda_y(m,\sigma) \cdot dy \quad \text{bps} \tag{5.42}$$

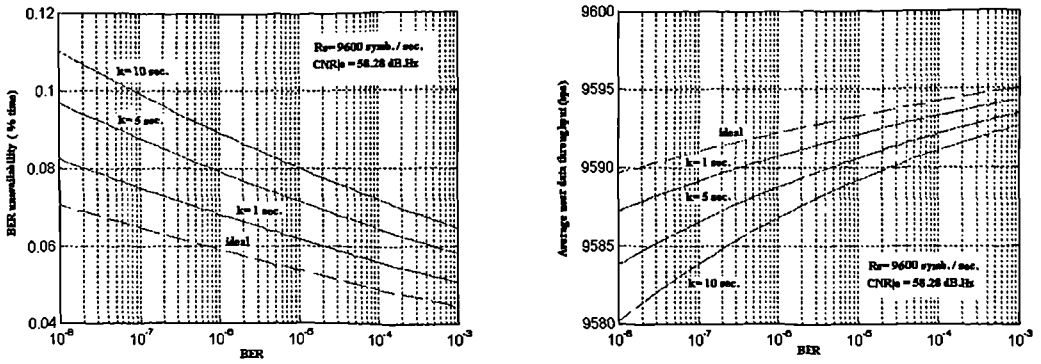

Figure 5.18: Impact of time delays on the BER unavailability and average user data throughput for the FDM-AFEC scheme. (Pout= 0.1 % of the time, Chilton-Olympus case, P_{hpa}=0.2 W, D=0.8 m).

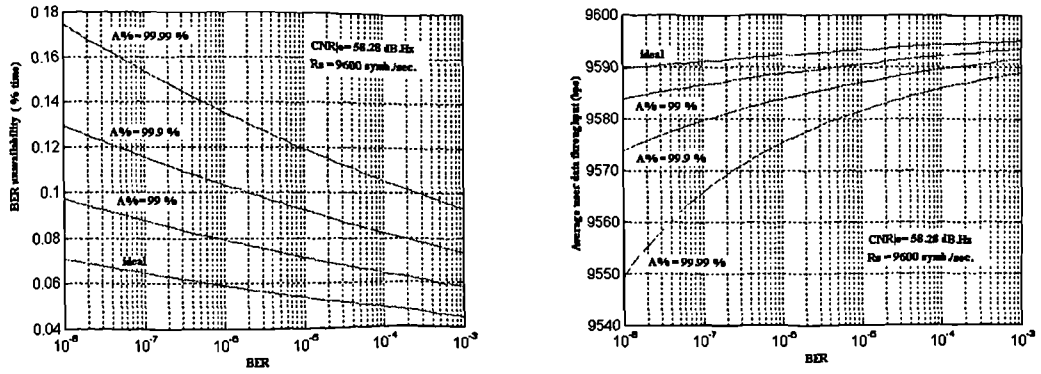

Figure 5.19: Impact of the detection outage probability on the BER unavailability and average user data throughput for the FDM-AFEC scheme (k= 5 s, Chilton-Olympus case, P_{hpa}=0.2 W, D=0.8 m).

Equations **(5.41)** and **(5.42)** have been computed for the Chilton-Olympus test-case example. All the range of interest of BER constraint was investigated. Figure 5.18 shows the impact of time delays on the BER unavailability and average user data throughput. As expected, larger delays, requiring larger FDMs, result in a degradation in performance relative to the ideal FCM case (see section 5.5.2). A similar situation occurs in Figure 5.19, which shows the impact of decreasing the detection outage probability of the fade detection/prediction

scheme. A smaller detection outage probability results in a larger FDM requirement, explaining the degradations w.r.t the ideal FCM case.

5.5.5 BER/Throughput of a VDM-AFEC system

Using a slightly different approach, it is also fairly simple to derive the performance of the variable detection margin (VDM) FEC system. In this particular case, only fixed CRC boundaries are considered, corresponding to the ideal delayless case. In this case, the VDM system must switch from a code rate ρ to the next lower code rate as soon as the following inequality is satisfied:

$$\left.\frac{C}{N_0}\right|_{t,0} - 10\log_{10}\left(\frac{R_b}{\rho}\right) - z'' - \mu_i \leq \left.\frac{E_b}{N_0}\right|_{rq@\hat{\beta},\rho} = 10\cdot\log_{10}\left(g_\rho^{-1}\left(\hat{\beta}\right)\right) \qquad \textbf{(5.43)}$$

i.e. when the predicted total control effort, z'':

$$z'' \geq \left.\frac{C}{N_0}\right|_{t,0} - 10\log_{10}\left(\frac{R_b}{\rho}\right) - \mu_i - 10\cdot\log_{10}\left(g_\rho^{-1}\left(\hat{\beta}\right)\right) \text{ dB} \qquad \textbf{(5.44)}$$

The deduced fixed CRC boundaries for the VDM approach are shown below in Figure 5.20. Note that the VDM-AFEC system has also a fixed built-in excess margin of 6.39 dB (like for the fixed or ideal AFEC systems).

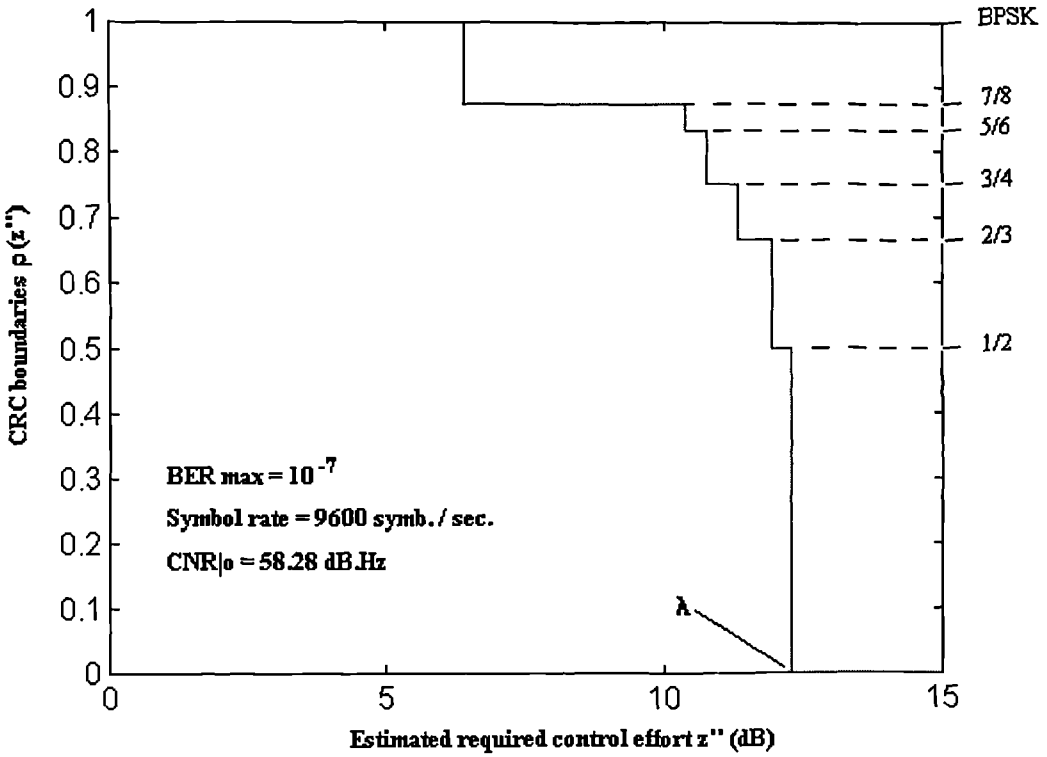

Figure 5.20: Fixed CRC boundaries for the VDM-AFEC control scheme.

Following an approach very similar to the previous two sections, the BER unavailability and average user data throughput can be calculated using respectively:

$$\text{Prob}\{BER \geq \hat{\beta}\} = \text{Prob}\left\{z'' \geq \lambda \equiv \left.\frac{C}{N_0}\right|_0 - 10\log_{10}(R_s) - 10\log_{10}\left(g_{1/2}^{-1}(\hat{\beta})\right)\right\} \quad \textbf{(5.45)}$$

where $\text{Prob}\{z'' \geq \lambda\} = \int_{\lambda}^{\infty} \Lambda_y(m,\sigma) * f_\alpha(\alpha) \cdot dz''$ (see equation **(5.19)**) and:

$$\overline{\eta} = R_s \cdot \int_0^{\lambda} \rho(z'') \cdot \Lambda_y(m,\sigma) * f_\alpha(\alpha) \cdot dz'' \quad \text{bps} \quad \textbf{(5.46)}$$

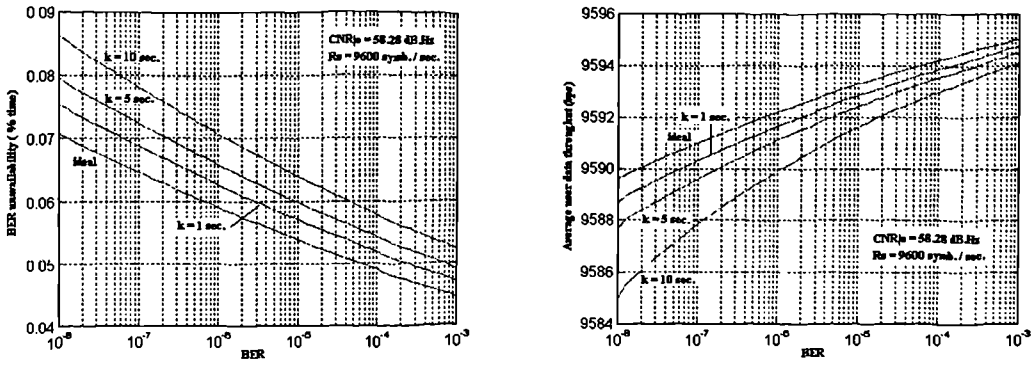

Figure 5.21: Impact of time delays on the BER unavailability and average user data throughput for the VDM-AFEC scheme (Pout=1 % of the time, Chilton-Olympus case, P_{hpa}=0.2 W, D=0.8 m).

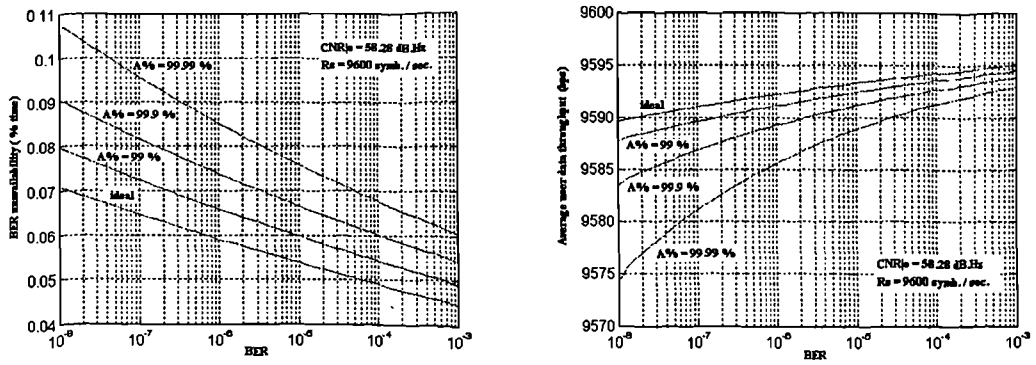

Figure 5.22: Impact of the detection outage probability on the BER unavailability and average user data throughput for the FDM-AFEC scheme (k= 5 sec., Chilton-Olympus case, P_{hpa}=0.2 W, D=0.8 m).

As for the FDM approach, Figures 5.21 and 5.22 indicate that a longer time delay and/or a lower detection outage probability, corresponding to a larger control parameter λ (i.e. a larger VDM), result both in a decrease in BER and throughput performances.

5.6 Conclusions and further work

Two different detection schemes have been analysed and compared via the mathematical definition of a novel model investigating the design implications of time delays on FCM control efficiency within the context of predictive control of countermeasure resources.
The fixed and variable detection margin approaches have been studied in detail. Theses two schemes were introduced as means to alleviate for the predictor imperfections. This has been applied to an in-bound back-to-back VSAT link using adaptive FEC as a countermeasure. However the study could be easily extended to other countermeasures.

It was found that both methods yielded small but non-negligible degradations in performance with respect to the ideal delayless control case. More particularly, the inclusion of a detection margin, *to control statistically the performance of the detection/prediction process*, has a significant impact on the achievable long term BER and data throughput of the AFEC system.

The VDM approach is better suited to adaptive transmission systems and all other systems which are expected to have short time delays of less than 5 seconds. For longer time delays the FDM approach is more economical.

The utilisation factor was used as a tool to investigate the quality of any predictive FCM controller. More work is required to see how this could be related to fade duration statistics and shared resource countermeasures like A-TDMA or frequency diversity. The utilisation factor was found to be function of the attenuation level. It is sensitive to time-delays and detection margin. Theoretical results were found to be in very good agreement with experimental ones.

Large utilisation factors were obtained (both for FDM and VDM schemes) for small excess margins. This suggests that the design of *truly* low fade margin systems is not really feasible in the context of predictive fade countermeasure systems. In order to reduce FCM over- utilisation, it seems therefore desirable to

implement systems with an in-built excess margins of at least 4 or 5 dB. For example, for the AFEC system, the in-built excess margin was of 6.39 dB (i.e. quite large). This resulted in good throughput performance relative to the ideal control case.

The VDM was found to yield smaller FCM control effort than the FDM approach for 85% of the time. The VDM scheme is therefore interesting as an attempt to reduce the interference to adjacent satellite systems. However the VDM may well drive a satellite transponder into saturation (in MCPC satellite access schemes) for large values of scintillation variance. Therefore to be better suited to ULPC systems, the maximum level of the VDM approach should be limited to a maximum value by introducing a saturation level of the VDM. This would increase the detection outage probability and should be quantified theoretically using an approach very similar to the one carried out in this chapter.

It may be possible to find a better (short-term) predictive model of the Ka band fading process. A possible way forward would be to describe, maybe only partially, the scintillation process in terms of the rain process. This involves finding a functional relationship between rain and scintillation effects. This will be addressed in the following chapter. The performance of predictive countermeasures was evaluated here assuming that rain attenuation and scintillation are statistically independent processes in compliance with the global fading hypothesis. This assumption and its validity is also assessed in chapter 6 where focus is placed on the impact of the variability of concurrent rain and scintillation effects and their scaling on the design of predictive fade countermeasure systems.

Appendix A5. 1: Comparison between FDM and VDM approaches

It is important to compare both detection rules and express the results in BER availability and average user data throughput. This was achieved by calculating the ratio between the BER unavailability of VDM or FDM with the BER unavailability obtained in the ideal case. The ratio between the average throughput of the FDM or VDM approaches over the one obtained in the ideal delayless case was also computed for identical RF detection availabilities. All the range of interest of BER constraint (the independent variable), time delays and outage detection outage probability were covered. The compound results are shown in Figures A.5.I and A.5.II.

.

BER unavailability

The BER unavailability of both FDM and VDM methods is compared with respect to the ideal control case (see section 5.5.3) in Figure A.5.I. Each of the graphs shows the results for different delays of 1, 5 and 10 seconds, each for a particular detection outage probability. Figure A.5.I(a) was obtained for $P_{out}^{pred} = 0.01$ (= 1% of the time). In this case, the VDM approach appears to yield better results than the FDM scheme irrespective of the time delay (between 1 to 10 seconds). Figure A.5.I(b) shows the situation for $P_{out}^{pred} = 0.001$ (= 0.1% of the time). In that case, the VDM approach is superior to the FDM one only for short time delays (k= 1 and 5 sec.). In Figure A.5.I(c), $P_{out}^{pred} = 0.0001$ (= 0.01% of the time), the VDM only yields smaller BER unavailabilities for k=1 sec. Therefore the VDM approach yields smaller BER outage probabilities than the FDM approach for short time delays (below 5 seconds and detection outage probabilities not smaller than 0.01%.

Average user data throughput (Figure A.5.II)

A similar discussion applies to the throughput characteristics of both FDM and VDM schemes. More particularly, for $P_{out}^{pred} = 0.01$ (= 1% of the time), the VDM always yield greater throughput than the FDM approach. When $P_{out}^{pred} = 0.001$ (= 0.1% of the time) or $P_{out}^{pred} = 0.0001$ (= 0.01% of the time), the FDM becomes more advantageous only for long time delays (10 sec.).

As a conclusion, the VDM approach should be preferred to the FDM one, only for short-time delays between 1 and 5 seconds, provided that the detection outage probability remains greater than 0.01% of the time. This results in better BER availabilities and greater user data throughput. In practice, this should be the case for systems based on adaptive transmissions which will have short time delays. Therefore the VDM approach seems to be the better scheme.

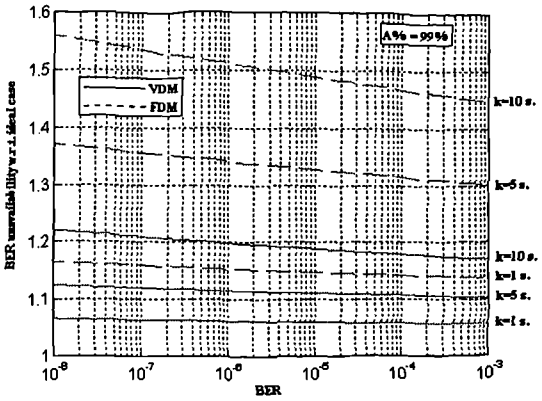

Fig A5.I(a): A%=99%

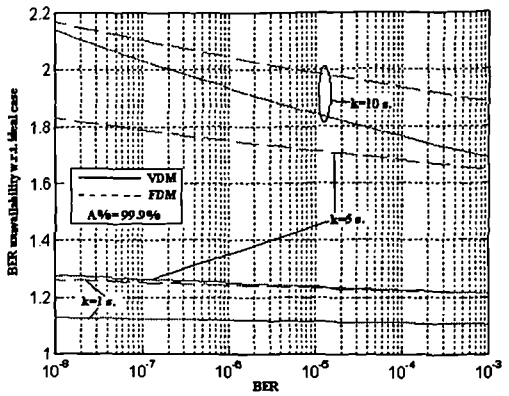

Fig A.5.I(b): A%=99.9%

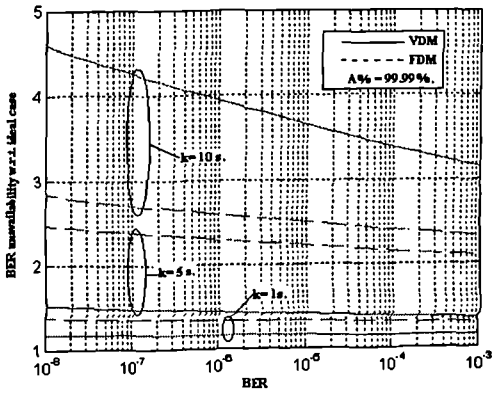

Fig A5.I(c): A%=99.99%

FigureA5.I: Comparison of BER availability for the FDM/VDM approaches.

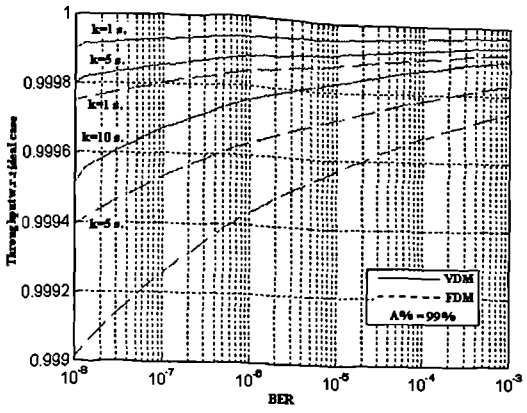

Fig A5.II.(a): A%=99%

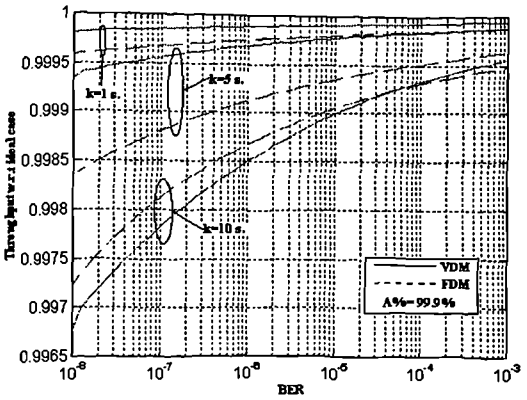

Fig A5.II(b): A%=99.9%

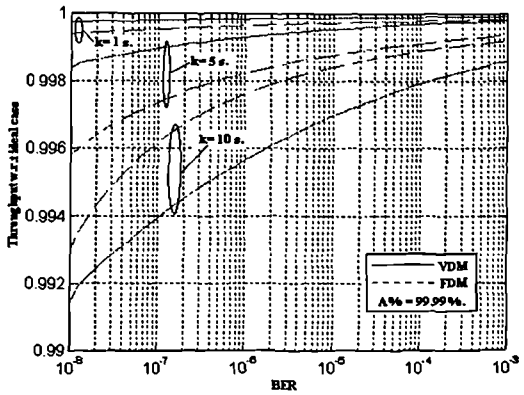

Fig A5.II(c): A%=99.99%

Figure A5.II: Comparison of Average User Throughput for the FDM/VDM approaches.

References

[5.1] E. Salonen, S. Uppala, J.P.V. Poiares Baptista at al., "Modelling and calculation of atmospheric attenuation for low-fade-margin satellite communications", *ESA Journal*, Vol. 16, 1992, pp 299-317.

[5.2] M.J. Willis, "Fade countermeasures applied to transmissions at 20/30 GHz", *Electronics & Communication engineering Journal*, 1991, pp 88-96.

[5.3] G. Tartara, "Fade countermeasures in millimetre-wave satellite communications: A survey of methods and problems", *Proc. Olympus Utilization Conf.* , April 1989, ESA SP-292, May 1989, pp 103-107.

[5.4] L. Dossi, G. Tartara, E. Matricciani, "Frequency Diversity in millimetre wave satellite communications", *IEEE Trans. on Aerospace and Electronic Systems*, Vol. AES-28, No 2, April 1992, pp 567-573.

[5..5] F. Carassa, G. Tartara, E. Matricciani, "Frequency Diversity", *Int. J. of Sat. Comms*, Vol. 6, 1988, pp 312-322.

[5.6] A. Attisani et al, "Frequency diversity as a fade countermeasure in the 20/30 GHz band: An experiment via Olympus", *Proc. Olympus Utilization Conf.* , April 1989, ESA SP-292, May 1989, pp 143-149.

[5.7] L. Dossi, "Real-time prediction of attenuation for applications to fade countermeasures in satellite communications", *Electronics Letters*, Vol. 26, No 4, Feb. 1990, pp 250-251.

[5.8] I.E. Otung, B.G. Evans, "Impact of scintillation fading on satellite EHF communications for multimedia-mobile services", *Proc. of 2nd Ka band Utilization Conf. and international workshop on SCGII, Sept. 24-26 1996, Florence, Italy,* Sept. 1996, pp 431-437.

[5.9] A. Paraboni, "A new method for the prediction of fade duration statistics in satellite links above 10 GHz", *Int. J. of Sat. Comms*, Vol. 12, 1994, pp 387-394.

[5.10] E. Vilar, E. Burgueño, et al., "Analysis of joint rainfall and duration statistics: microwave design implications", *IEEE Trans. Comms,* Vol. COM-36, No 6, June 1988, pp 650-661.

[5.11] E.H. Satorius, L.H. Tong, "Analysis of a rain compensation algorithm for K/Ka band communications", *Int. J. of Sat. Comms*, Vol. 14, 1996, pp 297-311.

[5.12] T.J. Moulsley, E. Vilar, "Experimental and theoretical statistics of microwave amplitude scintillations on satellite down-links", *IEEE Trans. Ant. and Prop.*, Vol. AP-30, No 6, 1982, pp 1099-1106.

[5.13] Y. Karasawa, et al., "Tropospheric scintillation in the 14/11 GHz bands on earth-space paths with low elevation angles", *IEEE Trans. Ant. and Prop.*, Vol. AP-36, 1988, pp 563-569.

[5.14] I.E. Otung, B.G. Evans, " Short-term distribution of amplitude scintillation", *Electronics Letters*, Vol. 31, No 16, 1995, pp 1328-1329.

[5.15] G. Orgies, "Frequency dependence of slant-path amplitude scintillations", *Electronics Letters*, Vol. 29, No 5, 1993, pp 2219-2220.

[5.16] O.P. Banjo, E. Vilar, "Dynamic characterisation of scintillation fading on low elevation earth-space paths, *URSI Symp. on wave propagation, remote sensing & Communications*, New Hampshire, July/August 1986, pp 8-7-1, 8-7-4 .

[5.17] M. Filip, E. Vilar, "Optimum Utilization of the channel capacity of a satellite link in the presence of amplitude scintillations and rain attenuation", *IEEE Trans. on Comms.*, Vol. COM-38 No 11, Nov. 1990, pp 1958-1965.

[5.18] K. Karimi, V. Aslo, H. Helmken, "A study of channel capacity utilization in the presence of rain attenuation in Florida", *Southeast con'94 creative technology transfer, a global affair*, Proc. of the 1994 IEEE south eastcon'94, 1994, pp 196-200.

[5.19] A.J. Viterbi, "Convolutional codes and their performance in communication systems", *IEEE Trans. on Comms,* Vol. COM-19, Oct. 1971, pp 751-772.

[5.20] Y. Yasuda, K. Kashiki, Y. Hirata, "High rate punctured convolutional codes for soft decision Viterbi decoding", *IEEE Trans. on Comms,* Vol. COM-32, March 1984, pp 3158-319.

[5.21] Y. Yasuda, Y. Hirata, "Development of a variable rate Viterbi decoder and its characteristics", *Proc. 6th Int. Conf. on digital satellite Comms*, phoenix Arizona, Sept. 1983, pp XII, 24-31.

[5.22] L.J.M. Smith, G.D. Burton, "Punctured coding for forward error correction in satellite communications", *Journal IERE*, vol. 58, No 3, 1988, pp 125-131.

[5.23] J. Hagenauer, "Rate-Compatible punctured convolutional codes (RCPC codes) and their applications", *IEEE Trans. on Comms.*, Vol. COM-36, No 4, Apr. 1988, pp 389-400.

[5.24] S. Kallel, D. Haccoun, "Generalized type II hybrid ARQ scheme using punctured convolutional coding", *IEEE Trans. on Comms.*, Vol. COM-38, No 11, Nov. 1990, pp 1938-1946.

[5.25] D. Haccoun, G. Begin, "High rate punctured convolutional codes for Viterbi and sequential decoding", *IEEE Trans. on Comms.*, Vol. COM-37, Nov. 1989, pp 1113-1125.

[5.26] O. Koudelka, "Adaptive transmission rate and variable redundancy systems as a fade countermeasure", *Fade Countermeasure for Satellite Communications, ESA STM-235*, May 1986, pp 11-13.

[5.27] G.R McMillen, B.A. Mazur, T. Abdel-Nabi, "Design of a selective FEC subsystem to counteract rain fading in Ku band TDMA systems", *Int. J. of Satellite Comms.*, Vol. 4, pt 2,, 1986, pp 75-82.

[5.28] M. Filip, E. Vilar, "Adaptive modulation as a fade countermeasure: An Olympus experiment", *Int. J. of Satellite Comms*, Vol. 12, 1994, pp 181-191.

[5.29] B.K. Levitt, "Rain compensation algorithm for ACTS mobile terminal", *IEEE J. on Selected Areas in Comms.*, Vol. SAC-10 No 2, Feb. 1992, pp 358-363.

6. Inclusion of Instantaneous Frequency Scaling in Predictive Ka Band Fade Detection Systems

6.1 Introduction

The performance of fade countermeasure systems depends crucially on the ability to estimate and predict in real-time the total attenuation on a particular satellite link. In the case of down-link beacon monitoring detection schemes, which represent the most complicated detection schemes, two major operations* need to be carried out (see Figure 6.1). First the down-link total attenuation needs to be short-term predicted to account for the finite response time of the FCM system (set-up time from beacon measurement to effective FCM switching). Secondly, the rain attenuation and scintillation components need to be separated and then scaled individually in frequency. To be efficient, such a detection scheme must be statistically controlled so that the probability that the total up-link estimated/predicted fade, $\hat{z}_u$, under-estimates the true up-link fade, z_u, for a certain

* *in addition to short-term prediction*

specified percentage time over a long period (typically one year). If a particular satellite link has to be designed so that a specified link availability of $A_{\%}$ is to be achieved then the overall detection outage probability, P_{out}^{d},of the fade detection scheme must satisfy the following inequality:

$$P_{out}^{d} \leq (100 - A_{\%})/100$$

where **(6.1)**

$$P_{out}^{d} = \text{Prob}\{\hat{z}_u(t + \Delta t | z_d(t)) \leq z_u(t + \Delta t)\}$$

Here Δt denotes the estimated response time of the overall FCM system (multiple of 1 second).

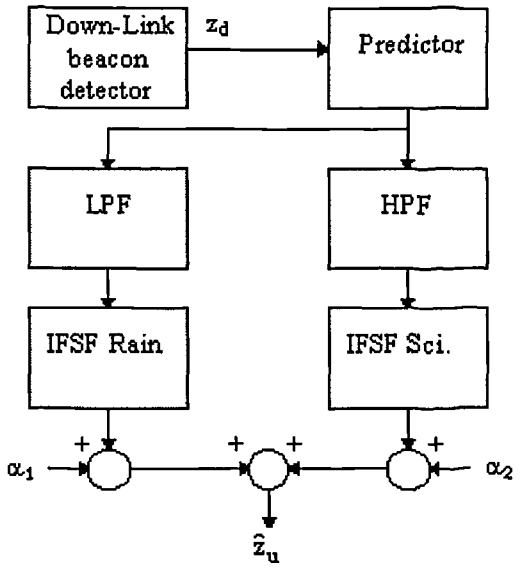

Figure 6. 1: *Principle of a down-link fade detector including instantaneous* frequency scaling of joint rain and scintillation processes*.

The numerical evaluation of equation **(6.1)** relies on the following points:

1. The time delay Δt of the FCM system.
2. The aptitude of the predictor to short-term predict the down-link attenuation and the statistical properties of joint rain and scintillation processes.
3. The statistical mean properties and variability of the Instantaneous Frequency Scaling Factor (IFSF) of rain and scintillation respectively.
4. The possible statistical relationship between rain and scintillation processes during rain events.

---

* α_1 and α_2 *are two detection margins introduced to control statistically the accuracy of the detection schemes in the presence of the stochastic scaling factors of rain and scintillaiton processes respectively.*

Chapters 4 and 5 were dedicated to the consideration of points 1 and 2 in the above list. These were the original objectives of this PhD project. However, the actual outcome, namely the variable detection margin (VDM) scheme and its statistical characterisation allow the natural inclusion of the instantaneous frequency scaling factor (IFSF) of both rain attenuation and scintillation variance. Because of the significance of such a possibility, it was therefore decided to describe how this can be performed, although this project was not initially planned to do so. To achieve this inclusion of IFSF, points 3 and 4 must first be investigated. Needless to say that each of the issues, 3 or 4 are difficult and at the forefront of current fundamental propagation research and interests. Therefore most of the work presented in this chapter should be seen as exploratory.

The objective is to obtain an overall view on how the general fade detection problem (Figure 5.1) may be solved and what propagation modelling would be necessary to reach a potential engineering solution in a coherent non ad-hoc manner. A main underlying idea is to provide sufficient feedback to propagation modellers so that the general detection problem can be solved in an integrated way. Therefore, this chapter is an attempt at addressing issues 1 to 4 altogether. This is done via the definition of a novel mathematical model of the IFSF factor and by integrating this within the context of predictive fade control FCM operations. The approach is voluntarily system-based and focuses on the performance and design of the detection system outlined in principle in Figure 5.1. A novel statistically controllable scheme, catering for instantaneous frequency scaling of rain attenuation and time delays is proposed. This model allows the determination of the variable detection margins required to cover for down-link beacon frequency scaling variations, as well as FCM set-up time delay, in the presence of both rain attenuation. No attempt was made at deriving a stochastic model for the IFSF of tropospheric scintillation. Instead, current deterministic models proposed in the literature will be used in this thesis (They are reviewed in Appendix A6.II). The last part of this chapter is dedicated to the critical analysis of the problems encountered in the building of the proposed model, giving the areas in which further work is required.

6.2 Stochastic model for the instantaneous frequency scaling factor (IFSF) of rain attenuation

This section addresses the problem of the accurate estimation of the rain attenuation level based on instantaneous frequency scaling factor (IFSF) for application to down-link beacon fade countermeasure detection systems. A new mathematical model suitable for accurately controlling the detection of Ka band rain fades is proposed. It essentially considers the impact of the temporal stochastic variations in rain drop size distribution on the mean and standard deviation of the IFSF of rain.

Accurate knowledge of the frequency scaling factor of rain attenuation is particularly useful for the design of high frequency satellite systems.
First, rain attenuation at one frequency can be extrapolated from rain attenuation statistics at another frequency using a long-term or mean estimate of the Instantaneous Frequency Scaling Factor (IFSF) of rain. Second, Fade countermeasure systems **[6.1]**, based on down-link frequency beacon monitoring, require a model for the IFSF of rain so that the attenuation can be inferred in real-time, from detected base-frequency rain attenuation **[6.2]**. If this operation is to be performed in a statistically controlled manner, any model of the IFSF should at least include a measure of the variability or spread of the IFSF around its mean.

To date, different empirical formulas have been proposed in the literature to model the mean or long-term behaviour of the IFSF of rain. They will be briefly reviewed and compared to the model proposed here in section 6.2.5. The existing models do not provide a qualitative measure of the variability of the IFSF. This is our objective. Recent propagation experiments have focused on the characterisation of the variability of the IFSF around its mean value **[6.2, 6.3, 6.4, 6.5]**. More particularly researchers used the standard deviation or equivalent to characterise the spread of the IFSF around its mean long-term value **[6.5, 6.6, 6.7, 6.8]**. Therefore their experimental results can be used to test the validity of any new proposed model of the IFSF of rain.

The variability of the IFSF is usually attributed to slow variations in rain drop size distributions **[6.9, 6.10]**. However such variations were usually assumed as deterministic in nature which is clearly unrealistic. In this thesis, the impact of temporal stochastic variations in rain drop size distribution (DSD) on the mean and standard deviation of the IFSF of rain is modelled.

6.2.1 Impact of stochastic temporal variations of rain drop size distribution on the mean and variance of the IFSF

In this section a statistical model of the IFSF of rain is developed. It takes into account the stochastic variability of the rain drop size distribution (DSD), which is believed to be the main cause for the variability of the IFSF of rain. To do so, one must first consider the specific attenuation $\alpha(R,l)$ (in dB/km) of rain given by **[6.11]**:

$$\alpha(R,l) = 4.343 \cdot 10^{-3} \int_0^{\infty} Q_t(r,\lambda,m) n(r) dr \approx aR^b \ \text{dB/km} \qquad \textbf{(6.2)}$$

R (mm/h) denotes the rain rate, L (km) is the total length of the slant path through rain, the interval $[l-dl \quad l]$, $0 \le l \le L$(km) is the small portion of slant path over which the specific attenuation is constant. $Q_t(r,\lambda,m)$ (in m^2) is the scattering cross-section of the drops having radii between r and $r+dr$ (in mm). It depends on drop radii, wavelength λ (m) and the complex refractive index m of rain . $n(r) \equiv N_0 \cdot e^{-\Lambda \cdot r}$ is the drop-size distribution (in m^3mm^{-1}). The parameters N_0 (m^3mm^{-1}) and $\Lambda \equiv cR^d$ (mm^{-1}) are empirical parameters determined from experiment.

In this thesis, only the DSDs proposed by Joss et al in **[6.12]** are considered. They found that the DSD varies considerably for different types of rain activity. The drizzle distribution (J-D) is associated with very light widespread rain composed mostly of small raindrops. The thunderstorm distribution (J-T) characterises the DSD of convective rain with high concentration of large drops. The widespread distribution (J-W) is an intermediate case and can be seen as a long-term average distribution. As the variability of the IFSF of rain is usually associated with temporal variations of DSD, only the extreme J-D and J-T distributions are selected. The

validity of the approximation in **(6.2)** has been demonstrated analytically by Olsen et al in **[6.13]** and has further been verified experimentally. Olsen et al evaluated numerically the values of the constants *a* and *b* in **(6.2)** corresponding to the J-D and J-T distributions. For convenience, the values calculated by Olsen et al. are given in Table 6.1 for a rain temperature of 0 C.

f (GHz)	J-T		J-D		Rain Tpre (C)
10	0.0169	1.076	0.0114	0.968	
11	0.0212	1.065	0.0141	0.977	
12	0.0262	1.052	0.0172	0.985	
15	0.0466	1.010	0.0282	1.003	
20	0.0983	0.946	0.0530	1.020	0
25	0.173	0.884	0.0861	1.033	
30	0.274	0.823	0.1280	1.044	
35	0.372	0.783	0.1800	1.053	
40	0.451	0.760	0.2410	1.058	
50	0.629	0.709	0.3870	1.053	
	a_{JT}	b_{JT}	a_{JD}	b_{JD}	

Table 6. 1: Parameters a and b derived by Olsen et al in [6.13] for the J-D and J-T distributions.

Note that the ITU-R (formerly CCIR) recommends the use of a logarithmic scale for extrapolating the parameter a and a linear scale for extrapolating parameter b at intermediate frequencies **[6.14]**.

In the following, the subscript or superscript *i* equals *u* or *d* depending on whether up-link frequency (e.g. 30 GHz) or down-link frequency (e.g. 20 GHz) are considered respectively.

The total attenuation $A_i(R)$ (dB) on a particular slant path of total length L is given by **[6.11]**:

$$A_i(R) = \int_0^L \alpha_i(R,l) \cdot dl \approx \overline{\alpha}_i(R) \cdot L(R, f_i) \quad \text{dB} \tag{6.3}$$

$\overline{\alpha}_i(R)$ denotes the path-averaged specific attenuation. $L(R, f_i)$ in km denotes the average path length through rain cells. It takes into account, on a long-term basis, the spatial distribution of rain cells along the satellite slant-path and the variation of the 0°C isotherm level (See Appendix A6.I). The average effective path length may in general be also dependent upon frequency **[6.15]**. However, it will be assumed here that this is not the case i.e. that the path length is only a function of R **[6.16, 3.17]**:

$$L(R) = \left[7.412 \cdot 10^{-3} \cdot R^{0.766} + \left(0.2323 - 1.806 \cdot 10^{-4} \cdot R\right) \cdot \cos\theta\right]^{-1} \tag{6.4}$$

θ (deg) is the elevation angle. Equation **(6.4)** was obtained by applying a curve fitting technique to ITU-R data. It is valid for north-western Europe and north-eastern United States for rates between 0.25 and 150 mm/h.

Based on **(6.3)** and **(6.4)**, the IFSF of rain is thus given by:

$$k(R) = \frac{A_u(R)}{A_d(R)} = \frac{\alpha_u(R) \cdot L(R)}{\alpha_d(R) \cdot L(R)} = \frac{\alpha_u(R)}{\alpha_d(R)} \tag{6.5}$$

From this definition, the IFSF, described as a function of the rain rate (i.e. the independent variable) does not depend on the average path length and it depends only on the path averaged specific attenuations. The variability of the IFSF is now described in terms of temporal random variations of the path-averaged up and down-link specific attenuations. Figure 6.2 shows the specific attenuations calculated using **(6.2)** and the appropriate values of a and b for the 30/20 GHz pair given in Table 6.1.

Let us assume that the temporal variations in drop size distribution can reasonably be well modelled as conditionally Gaussian (See Figure 6.2), i.e. the specific attenuation given a specific rain rate, R, has a normal density function with conditional mean $\overline{\alpha}_i(R)$ and standard deviation $\sigma_i(R)$ given by:

$$f(\alpha_i(R)|R) = \frac{1}{\sqrt{2\pi}\cdot\sigma_i(R)}\cdot\exp\left[-\frac{(\alpha_i(R)-\overline{\alpha}_i(R))^2}{2\cdot\sigma_i^2(R)}\right] \qquad \textbf{(6.6)}$$

Then the probability that $\alpha_i(R)$ exceeds a value $\alpha(R)$ is :

$$\text{Prob}\{\alpha_i(R)\geq\alpha(R)|R\} = Q\left(\frac{\alpha_i(R)-\overline{\alpha}_i(R)}{\sigma_i(R)}\right)\equiv\frac{P\%}{200} \qquad \textbf{(6.7)}$$

If the temporal variations of rain drop size distributions result in P% of the specific attenuations lying between the J-T and J-D distributions then it can easily be seen that from **(6.7)** and Figure 6.2 that:

$$\sigma_i(R) = \frac{|\hat{\alpha}_i(R)-\overline{\alpha}_i(R)|}{Q^{-1}(P\%/200)} \qquad \textbf{(6.8a)}$$

where

$$\hat{\alpha}_i(R) = a_{JT}^i R^{b_{JT}^i}\ , \qquad \textbf{(6.8b)}$$

$$\overline{\alpha}_i(R) = 0.5\cdot(a_{JT}^i R^{b_{JT}^i} + a_{JD}^i R^{b_{JD}^i}) \equiv a_i\cdot R^{b_i}\ , \qquad \textbf{(6.8c)}$$

Note the absolute value is introduced in **(6.8a)** as a way to ensure that $\sigma_i(R)\geq 0$. Without the absolute value, the standard deviation of the 30 GHz specific attenuation would be negative, as shown in Figure 6.2, for R>30 mm/h. This rather peculiar situation is principally due the exponents b_{JT} and b_{JD} in Table 6.1, which make the JT specific attenuation smaller than the JD specific attenuation for R>30 mm/h.

The value P% (corresponding to twice the shaded area in Figure 6.2) is a measure of the adequacy of the J-T and J-D at representing the 'extremes' in rain drop size regimes over a long-term period. The parameters a, b defined in **(6.8c)** have been evaluated numerically usually a loglinear extrapolation and the appropriate values in Table 6.1. They are given in Table 6.2 for later reference.

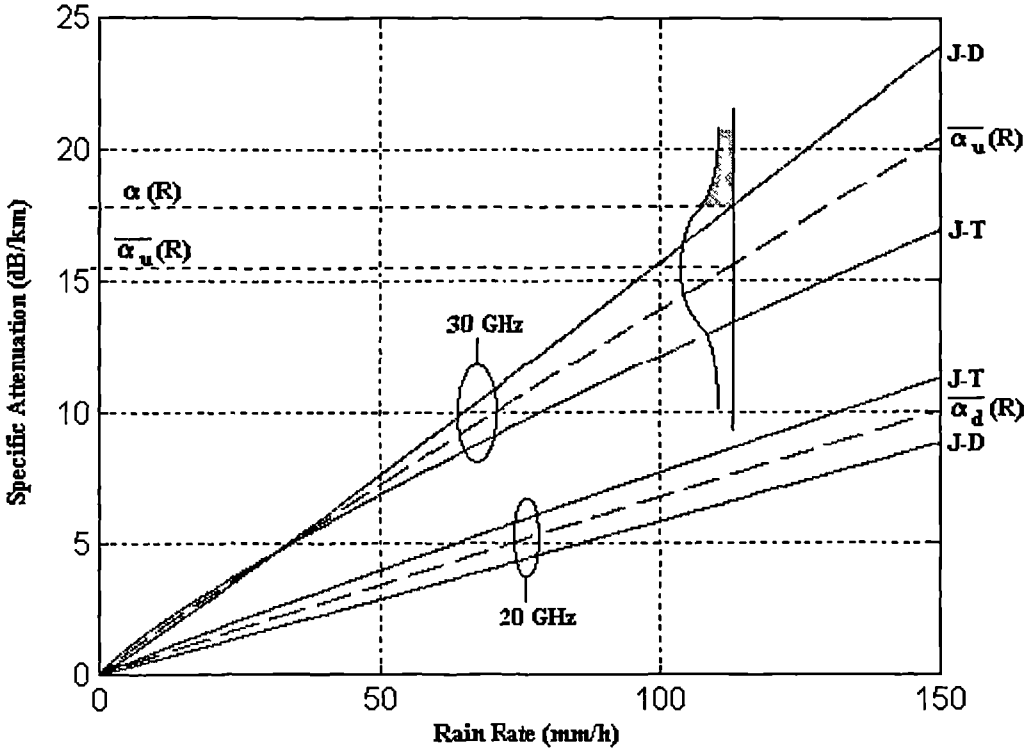

Figure 6. 2: Specific attenuations at 0°C at 20 and 30 GHz (J-T and J-D distributions).

f (GHz)	a	b
10	0.0166	1.0407
11	0.0201	1.0354
12	0.0241	1.0287
15	0.0383	1.0074
20	0.0706	0.9759
25	0.1138	0.9498
30	0.1693	0.9293
35	0.2309	0.9252
40	0.2922	0.9302
50	0.4296	0.9275

Table 6. 2: Parameters a, b identified from Table 6.1.

It can be shown **[6.18]** that the conditional mean, $\bar{k}(R)$, and variance, $\sigma_k(R)$, of the IFSF of rain attenuation, defined in **(6.5)**, can be evaluated from the means, $\bar{\alpha}_d(R)$, $\bar{\alpha}_u(R)$ and standard deviations, $\sigma_d(R)$, $\sigma_u(R)$ of up and down link specific attenuations using (The dependency on R has been omitted for clarity):

$$\bar{k}(R) \approx \frac{\bar{\alpha}_u}{\bar{\alpha}_d} + \frac{1}{2}\left[\frac{\partial^2\left(\bar{\alpha}_u/\bar{\alpha}_d\right)}{\partial\bar{\alpha}_d{}^2}\sigma_d^2 + 2r\frac{\partial^2\left(\bar{\alpha}_u/\bar{\alpha}_d\right)}{\partial\bar{\alpha}_u\partial\bar{\alpha}_d}\sigma_u\sigma_d + \frac{\partial^2\left(\bar{\alpha}_u/\bar{\alpha}_d\right)}{\partial\bar{\alpha}_u{}^2}\sigma_u^2\right]$$

$$\Rightarrow \bar{k}(R) \approx \frac{\bar{\alpha}_u}{\bar{\alpha}_d} + \frac{1}{\left[\bar{\alpha}_d\right]^2}\cdot\left[\frac{\bar{\alpha}_u\cdot\sigma_d^2}{\bar{\alpha}_d} - r\sigma_d\sigma_u\right] \qquad \textbf{(6.9a)}$$

$$\sigma_k^2(R) \approx \left[\frac{\partial\left(\bar{\alpha}_u/\bar{\alpha}_d\right)}{\partial\bar{\alpha}_d}\right]^2\sigma_d^2 + 2r\sigma_u\sigma_d\frac{\partial\left(\bar{\alpha}_u/\bar{\alpha}_d\right)}{\partial\bar{\alpha}_d}\cdot\frac{\partial\left(\bar{\alpha}_u/\bar{\alpha}_d\right)}{\partial\bar{\alpha}_u} + \frac{\partial\left(\bar{\alpha}_u/\bar{\alpha}_d\right)}{\partial\bar{\alpha}_u}\sigma_u^2$$

$$\Rightarrow \sigma_k^2(R) \approx \left(\frac{\bar{\alpha}_u}{\bar{\alpha}_d^2}\right)^2\sigma_d^2 - \frac{2r\sigma_u\sigma_d\bar{\alpha}_u}{\left(\bar{\alpha}_d\right)^3} + \frac{\sigma_u^2}{\left(\bar{\alpha}_d\right)^2} \qquad \textbf{(6.9b)}$$

σ_u, σ_d and $\bar{\alpha}_u, \bar{\alpha}_d$ can be determined from **(6.8a)** and **(6.8c)** respectively.

The parameter, r, denotes the correlation coefficient between up and down-link attenuations i.e.

$$r = \frac{\left\langle A_u(R) - \bar{A}_u(R)\right\rangle\left\langle A_d(R) - \bar{A}_d(R)\right\rangle}{\sigma_{A_u}\cdot\sigma_{A_d}} \qquad \textbf{(6.10)}$$

Typically the correlation coefficient is high and lies between 0.90 and 0.95 in experimental beacon analysis. In this thesis, a value of r=0.93 will be assumed throughout. Note that the inclusion of this parameter is physically sound, especially if one considers the scaling of rain attenuation between widely spaced sites (geographical diversity) in which case r would be substantially smaller than unity **[6.2]**.

The novel stochastic model proposed here should be contrasted with the deterministic models of the IFSF used so far in the literature, which are only based on the analysis of the first term in **(6.9a)**:

$$k(R) = \frac{\overline{\alpha}_u(R)}{\overline{\alpha}_d(R)} = \frac{a_u \cdot R^{b_u}}{a_d \cdot R^{b_d}} = \frac{a_u}{a_d} R^{b_u - b_d} \qquad \textbf{(6.11)}$$

and which give no estimate of the variability of the IFSF as in Equation **(6.9b)**.

Using the relation $A_d = a_d \cdot R^{b_d} \cdot L$, the scaling factor in **(6.11)** can be written as a function of the base frequency attenuation, A_d, the path averaged length through rain, L, being a parameter. This gives:

$$k(A_d) = \frac{a_u}{a_d}\left(\frac{A_d}{a_d \cdot L}\right)^{\frac{b_u}{b_d}-1} \qquad \textbf{(6.12)}$$

An equivalent approach, which is used in this thesis, is to plot *k(R)* and then changing the R axis into the A_d axis using the mapping $A_d = A_d(R) = a_d \cdot R^{b_d} \cdot L(R)$. This is valid provided that that *L(R)* is itself a normal (one-to-one) function, even a non-linear one as in equation **(6.4)**. A remark at this stage is that the IFSF (its mean and/or variance) depends crucially on the average length L (km) of the slant path through rain cells. More particularly, as can be seen for example in **(6.12)**, large L will decrease the value of the IFSF. Thus $k(A_d)$ can only be evaluated numerically if an accurate model for L is employed. This is discussed further in Appendix A6.I.

The sensitivity of the mean IFSF on the correlation factor r has been investigated in the range *0.90<r<1*. It was found that r does not affect the mean IFSF significantly. The parameter P%, however, has a small but noticeable impact on $\overline{k}(R)$ for levels of down-link attenuation around 10 dB as shown in Figure 6.3(a) for the 30/20 frequency pair. Note that the mean IFSF has been plotted against $\overline{\alpha}_d(R) \cdot L(R) = A_d$. Also, as *L(R)* is dependent on the elevation angle, the value of $\theta = 30^o$ was assumed in Figures 6.3(a) and 6.3(b).

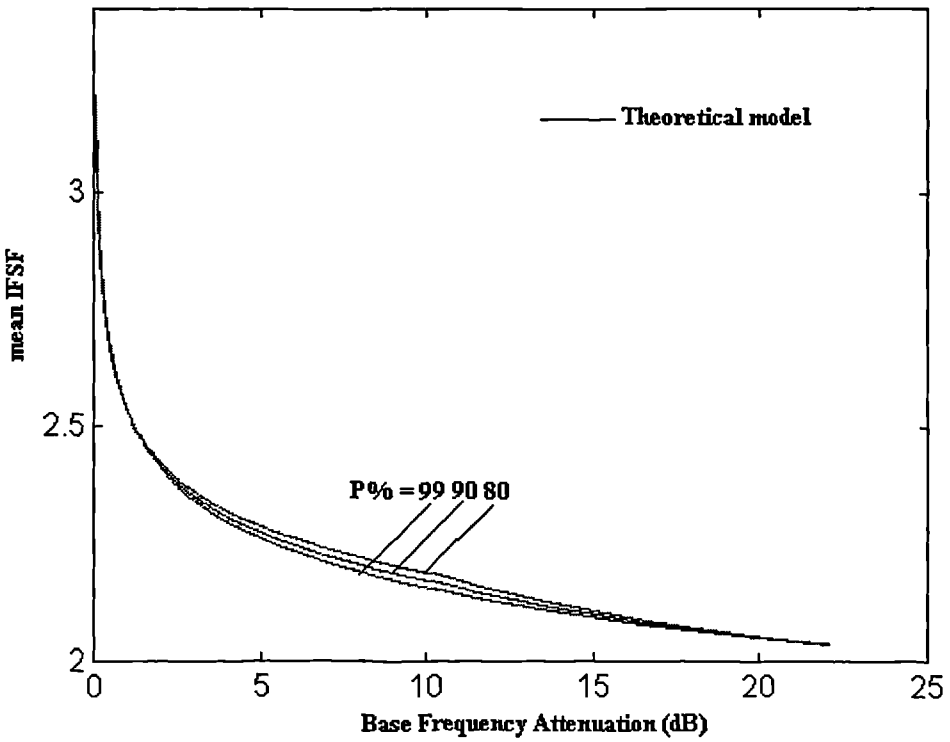

Figure 6. 3(a): Impact of the parameter P% on the mean IFSF (T=0°C,θ=30°,r=0.93, 29.65/19.77 GHz).

A similar analysis has been applied to the standard deviation of the IFSF. This is shown in Figure 6.3(b). The correlation factor was also found to have an impact (not shown here). Quite logically, lower correlation factors yielded slightly higher standard deviations. However, as expected, $\sigma_k(R)$ is more importantly affected by the value of the parameter *P%*, which thus should be evaluated accurately. Results compiled by Mauri, Paraboni and Riva in **[6.6]** are also displayed in Figure 6.3(b). The authors analysed the IFSF of rain attenuation for the 30/20 GHz pair. They only studied 14 rain events collected during the Olympus experiment at the site of Spino d'Adda. The authors provided a table of empirical values standard deviation of the IFSF for base attenuation levels between 1.5 and 22.5 dB in steps of 1 dB. These empirical values, taken directly from Table 4 of **[6.6]** are shown by circles in Figure 6.3b. The fit between the theoretical and the practical results of Spino d'Adda is good for values of down-link attenuation levels between 5 and 10 dB for P%=90%.

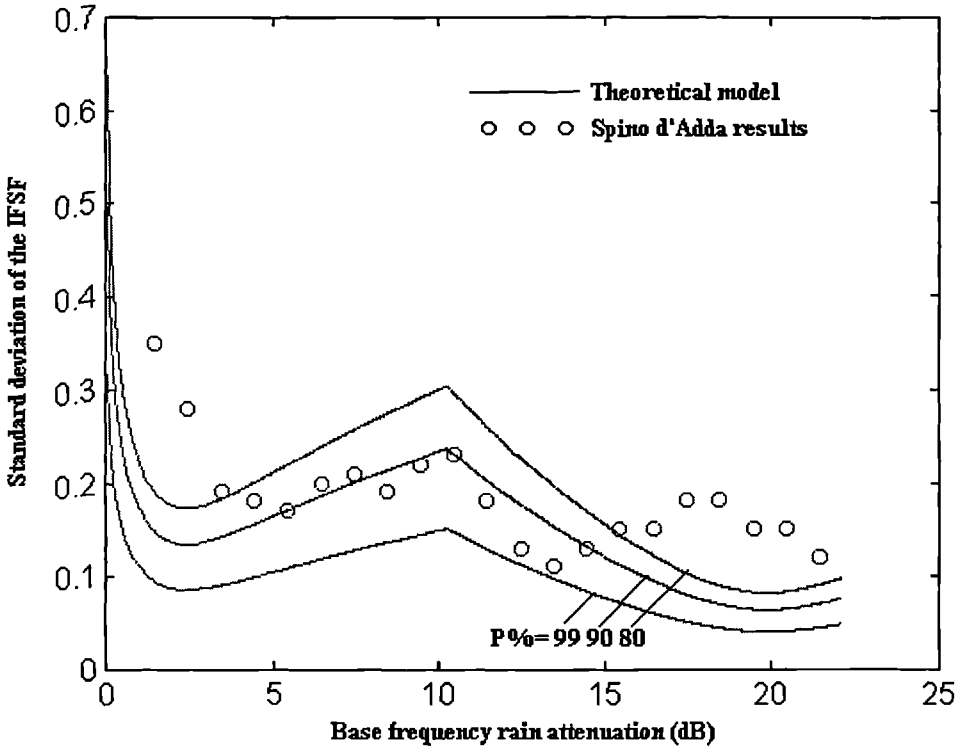

Figure 6. 3(b): Impact of the parameter P% on the standard deviation of the IFSF (T=0°C,θ=30°, r=0.93, 29.65/19.77 GHz).

For levels above 10 dB, both predict that the standard deviation should decrease, although the Spino d'Adda data shows a sharper decrease than the theory. For levels of attenuation below 5 dB, theory and practice predict similar trends although the horizontal scaling is not the same. In particular, both theory and practice show that there should be a minimum standard deviation between 1 and 5 dB. Both theory and practice also show a marked change in standard deviation for a base frequency attenuation of 10 dB. This shows that the proposed model is definitely on the right track although there are some differences. As discussed before, this change in characteristics is due to the fact that the J-D specific attenuation becomes less than the J-T specific attenuation (Figure 6.2) at 30 GHz and rain rate of 30 mm/h. This suggests that the J-T and J-D dropsize distributions, used as an input to the model, are too approximate. The evaluation of more adequate drop size distributions would require the computation of the scattering cross section of realistically distorted water rain drops as well as comparison with experimental beacon data. This is beyond the scope of this thesis.

6.2.2 Fade detection rule for Instantaneous frequency scaling of rain

In the case of down-link beacon monitoring systems, say in ULPC, the estimation of the fades at the high link frequency must be estimated in real-time based on the measured down-link attenuation via the use of instantaneous frequency scaling. In the context of fade countermeasures, it is particularly crucial that the fade detection scheme under-estimates the real up-link fades in a statistically controlled manner, so that more than appropriate FCM action can be taken for a certain percentage of time.

Whenever the frequency scaled fade is smaller than the true fade at the high frequency, there is a so-called detection outage to which can be associated an outage probability $P_{out}^{R} = (100 - A_{\%}^{R})/100$. $A_{\%}^{R}$ denotes here the required link availability (only the IFSF of rain is considered) in percent of time over a long period (typically one year). If it is assumed that the FCM technique, e.g. ULPC, can compensate perfectly for what is effectively detected (e.g. no saturation) then the detection outage probability will equal the outage probability of the ULPC link.

In general it is however preferable to set the accuracy of the detection process so that it satisfies:

$$P_{out}^{R} << P_{out}^{tot} \qquad \textbf{(6.13)}$$

where P_{out}^{tot} is the desired total outage probability of the particular satellite link. It takes into account the other source of estimation errors generated for example by the IFSF of scintillation and prediction.

Based on equation **(6.9)**, the up-link attenuation can be estimated in real-time from measured down-link attenuation using:

$$\hat{A}_{u}^{A_{\%}^{R}} = \left(\overline{k}^{R}(R) + \gamma^{R} \cdot \sigma_{k}^{R}(R)\right) \cdot A_{d}, \quad \mathrm{A_d} = \overline{\alpha}_{d}(R) \cdot L(R) \qquad \textbf{(6.14)}$$

The up-link estimate of the rain fade is chosen so as to over-estimate the true up-link fade for at least $A_{\%}^{R}$ of the time. The bracketed term in equation **(6.14)** is the fade detection rule accounting for statistically controlled IFSF variations. Note that it

is a variable detection margin scheme. The last term is the mean path and time averaged down-link attenuation $A_d = \overline{\alpha}_d(R)L(R)$.

Comprehensive results were published by Rücker in **[6.7]**. The author carried out an analysis of the IFSF of rain attenuation based on data collected during the Olympus experiment over a period of 2 years and 8 months for the 20/30 GHz pair. Rücker's experimental results showed that the conditional cumulative distribution function of the IFSF is well approximated as Gaussian for the percentiles lying between 5% and 95% and base frequency attenuation in the range 3.5 to 9.5 dB. In view of **(6.5)**, and Rücker's results, the most logical model for k is a conditionally normal model i.e.

$$f(k|R) = \frac{1}{\sigma_k(R)\sqrt{2\pi}} \exp\left[-\frac{\left(k - \bar{k}(R)\right)^2}{2\sigma_k^2(R)} \right] \qquad \textbf{(6.15a)}$$

which only requires estimates of the mean and variance of the IFSF given in equations **(6.9a)** and **(6.9b)**. Based on the Gaussian assumption, it is easy to show that the control parameter, γ^R, in **(6.14)** required to achieve an availability of $A_{\%}^R$, can be evaluated using :

$$\gamma^R = Q^{-1}\left(\frac{100 - A_{\%}^R}{100} \right) \qquad \textbf{(6.15b)}$$

and the error function is defined in **(5.34)**.

The fade detection rule **(6.14)** has been evaluated for the Chilton-Olympus in-bound VSAT link for link availabilities $A_{\%}^R$ ranging between 0.01 and 99.99%. This is shown in Figure 6.4.

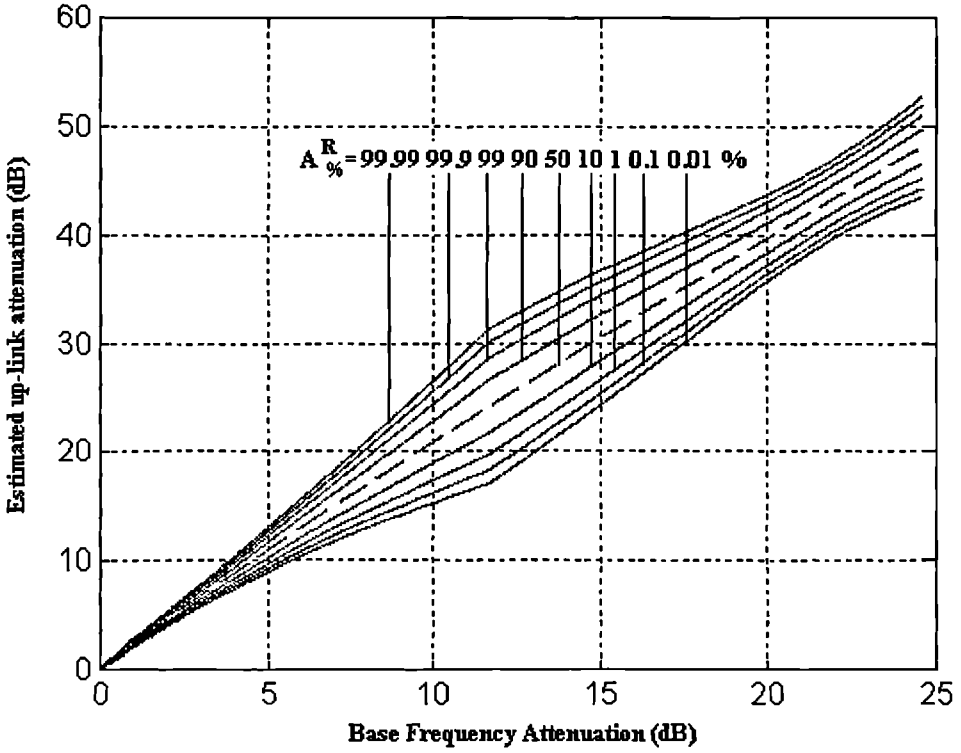

Figure 6. 4: Scaled up-link attenuation for different values of detection availability $A_{\%}$ (T=0°C, P%=97.8%, r=0.93, θ=28.56°, 28.63/19.475 GHz pair).

An advantage of the proposed model is that the detection process can be designed to achieve any arbitrary link availability $A_{\%}^{R}$. This is not the case of all the empirical models proposed in the literature which usually give only results for 50, 90, 99 % availabilities (some will be described in the following sections). The choice of the particular value, *P%=97.8%*, is justified in the next section.

Once the fade detection rule for the IFSF of rain has been evaluated using the above model, for a particular frequency pair and system set-up, it can be integrated in a fade detection scheme as a look-up table. Thus for each measured value of base-frequency detected rain attenuation, an estimate of the statistically controlled up-link rain attenuation can be read off directly and then used further in the chain to choose the appropriate level of FCM protection. Alternatively, a polynomial approximation can be fitted to the fade detection rule derived from the model proposed in this thesis, therefore for each detected level of base frequency attenuation, the up-link

attenuation can be calculated using this curve fitted detection rule. Some typical examples derived from experiment are given in the next section.

6.2.3 Model calibration based on experimental data

It is important to tune the prediction of the proposed model of the IFSF so that it can match published empirical results. More particularly, an appropriate value of the model parameter, P%, must be estimated. Although P% can be expected to be dependent upon the climatic region of each of the links considered, the data on the IFSF of rain attenuation is still too scarce to identify such a geographical dependency. Therefore only a mean value of P% will be evaluated.

Laster and Stutzman in **[6.8]** proposed three empirical laws for the IFSF at availabilities of 99% for the 20/30, 12/20 and 12/30 frequency pairs. These laws are based on a comprehensive analysis of one year of data measured during the Olympus experiment over a satellite link at 13.93° elevation angle. It is to date the most comprehensive study of the IFSF of rain attenuation. They proposed for the following detection rules for a 99% availability:

$$\hat{A}_{30}^{99\%} = 2.75 \cdot A_{20} - 0.02 \cdot (A_{20})^2 \qquad \textbf{(6.16a)}$$

$$1 \le A_{20} \le 14 \text{ dB}$$

$$\hat{A}_{20}^{99\%} = 3.94 \cdot A_{12} - 0.08 \cdot (A_{12})^2 \qquad \textbf{(6.16b)}$$

$$1 \le A_{12} \le 10 \text{ dB}$$

$$\hat{A}_{30}^{99\%} = 9.34 \cdot A_{20} - 0.39 \cdot (A_{20})^2 \qquad \textbf{(6.16c)}$$

$$1 \le A_{20} \le 4 \text{ dB}$$

Rücker also provided a curve (Figure (3b) of **[6.7]**) *for the 99% percentile.* Polynomial curve fitting to his graph yielded the following formulas:

$$\hat{A}_{30}^{99\%} = -1.4156 + 2.69 \cdot A_{20} - 0.0098 \cdot (A_{20})^2 \qquad \textbf{(6.16d)}$$

$$1 \le A_{20} \le 10 \text{ dB}$$

These detection rules were used to calibrate the proposed stochastic model of the IFSF of rain attenuation. More particularly, appropriate elevation angle, frequencies and values of P% between 80% and 99.9 % (in steps of 0.1%) were fed into the model. The best value of P% was then selected when the rms error between

each of the equations **(6.16)** and the model **(6.9)**, **(6.14)** is minimised. r=0.93, and from equation **(6.15)**, $\gamma^R = 2.33$ corresponding to 99% availability were employed. The results are given in Table 6.3.

$A^R_{\%}$	**Frequencies (GHz)**	**Elevation Angle**	**rms. error (dB)**	**Optimum P%**	**Source**
99	29.65/19.77	13.93	0.297	99.7	(6.9a)
99	29.65/12.5	13.93	0.351	96.9	(6.9b)
99	19.77/12.5	13.93	0.444	98.2	(6.9c)
90	29.65/19.77	30.00	0.141	96.4	(6.9d)
Average value of P%				97.8	

Table 6. 3: Identification of P% based on experimental results.

If we take the average of the 4 identified values of P% in Table 6.3, we get an estimate for P% of 97.8 %. Table 6.3 also shows that the individual values of P% are quite homogeneous and very close to 100%. Therefore, the J-D and J-T drop size distributions do indeed represent extreme rain activities. Using this value of *P%=97.8 %*, the theoretical and practical fade detection rule (equation **(6.16a)**) are compared and displayed in Figure 6.5 for the 30/20 GHz pair and availability of 99%. The agreement is very good.

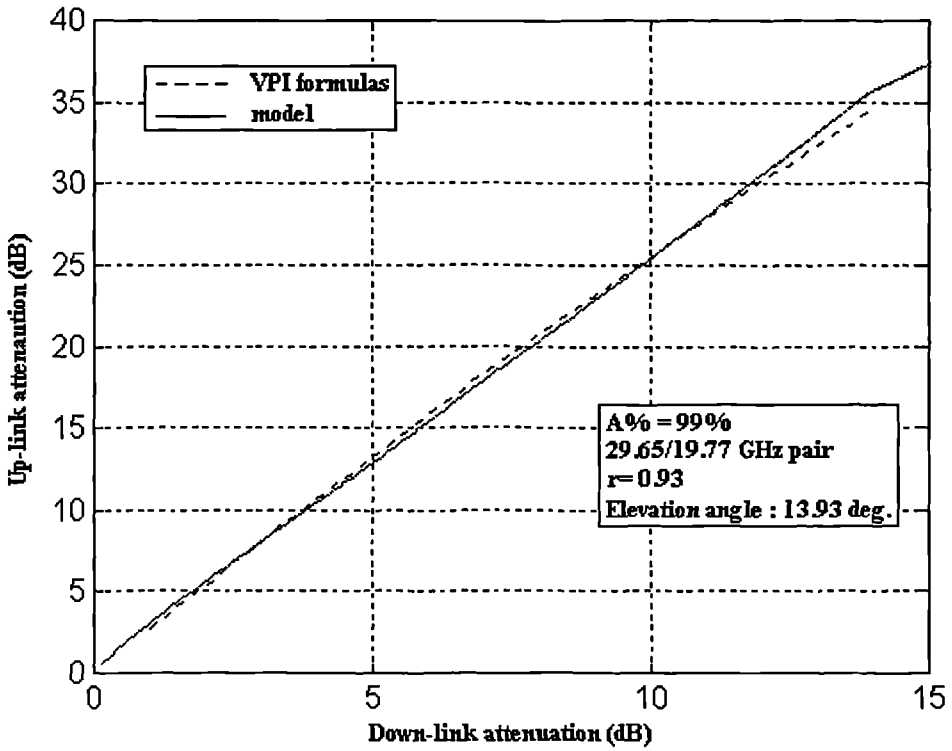

Figure 6. 5: Comparison of modelled and empirical mean instantaneous scaling of rain attenuation at 30/20 GHz for an availability of 99% (P%= 97.8%).

6.2.4 Approximate empirical models of the mean IFSF of rain attenuation

Different empirical models of the mean scaling factor of rain attenuation have been reported in the literature. For example, two common empirical models are reported by Levitt in **[6.1]** for the 30/20 GHz pair. One of them relies on a linear relationship of the form:

$$A_{30} = c_1 + c_2 A_{20} \tag{6.17}$$

Some even simpler linear models assume that the offset c_1 is zero.

Also, a log-linear model has been proposed Levitt in **[6.1]** giving:

$$\ln(A_{30}) = c_3 + c_4 \cdot \ln(A_{20}) \tag{6.18}$$

where c_i are empirical constants determined from measurements.

Taking the exponential on both sides, note that equation **(6.18)** can also be rewritten as:

$$A_{30} = e^{c_3} \cdot (A_{20})^{c_4} \equiv c_5 \cdot (A_{20})^{c_4} \tag{6.19}$$

Thus the mean IFSF can be expressed as a power law:

$$k = \frac{A_{30}}{A_{20}} = c_5 \cdot (A_{20})^{c_4 - 1} \qquad \textbf{(6.20)}$$

This last expression should be compared for example to equation **(6.12)**. It can be seen that the constants c_3 or c_5 and c_4 can also be derived from the parameters a and b of the mean rain drop size distribution and the estimated length L of the path through rain.

For example, Levitt in **[6.1]** assumed that a fixed path length L=4 km and used empirical measured values of the parameters a and b on a particular ACTS link. He estimated the values of the log-linear model to:

$$c_4 = 0.936,\ c_5 = 2.45 \qquad \textbf{(6.21)}$$

Two rough estimates of the two empirical parameters c_1 and c_2 were also evaluated from Figure 7 of **[6.1]** yielding:

$$c_1 = 1.80,\ c_2 = 1.96 \qquad \textbf{(6.22)}$$

The approximate models **(6.17)** and **(6.18)** have been fitted to the stochastic IFSF model proposed in this thesis. A 30/20 GHz link, with 30° elevation angle, r=0.93 and P%=97.8% was considered. The following parameter values were obtained:

$$c_1 = 1.554,\ c_2 = 1.9819 \qquad \textbf{(6.23)}$$

$$c_4 = 0.927,\ c_5 = 2.557 \qquad \textbf{(6.24)}$$

Clearly, the agreement between Levitt's values **(6.21)** and **(6.22)** and the ones fitted to the model **(6.23)** and **(6.24)** is quite good, especially for the log-linear approximation.

The slopes c_2 of the linear model **(6.17)** estimated in **(6.22)** and **(6.23)** are very similar and both predict a value close to 2. This value typically corresponds to the expected value of the fixed scaling factor for the 30/20 GHz pair as predicted by some empirical models of the Equiprobability Frequency Scaling Factor (EFSF) of rain attenuation (see the following section).

However the fitted values in **(6.22)** and **(6.23)** show that the offset value c_1 is not zero. Most simplified models of the mean IFSF assume so far a relation of the

type $A_{30} = k \cdot A_{20}$. The results presented in this section indicates that this is too approximate a model and that the offset should also be included if the linear modelling of the IFSF is to be retained as a viable model. This is particularly crucial for fade detection systems. If the offset is neglected, any estimate of the up-link frequency attenuation based on down-link attenuation will be biased. Since the offset is positive, this means that the up-link attenuation will be under-estimated and as a consequence, an insufficient control effort will be provided by the countermeasure. This is unsuitable. This problem may be avoided completely by using the log-linear model **(6.22)**. It has the advantage of predicting $A_{30}=0$ *dB* when $A_{20}=0$ *dB* (which is not the case of the model **(6.21)** with offset) and it matches more closely the mean IFSF curve than its linear counterpart.

6.2.5 Comparison with existing models for the EFSF of rain attenuation

The mean behaviour of the scaling factor of rain may be evaluated from long-term estimates. Different empirical model which have been proposed in the literature are briefly outlined here. Some of them yield fixed or variable mean scaling factors as function of the down-link frequency attenuation. They all attempt to describe the equiprobability frequency scaling factor (EFSF) of rain attenuation which is defined as:

$$k^R_{p\%} \equiv \frac{A_u(p_u = p)}{A_d(p_d = p)} \qquad \textbf{(6.25)}$$

where $p_u = p_d = p$ denote respectively the probability for which both the up and down-link attenuations exceed the values of A_u and A_d dB.

Fixed EFSF models

These models rely on a linear model of the IFSF without offset (see section 6.2.4). Some empirical models yields a constant mean scaling factor given by :

$$\bar{k}(A_d) \equiv \bar{k} = \phi(f_u)/\phi(f_d) \qquad \textbf{(6.26)}$$

For the ITU-R model **[6.14]**

$$\phi(f)=\frac{f^{1.72}}{1+3\cdot 10^{-7}\cdot f^{3.44}} \tag{6.27}$$

The fixed effective rain model introduced by Paraboni in **[6.2]** allows the introduction of the frequency and polarisation-dependent a and b (see Table 6.2) coefficients for the specific attenuation, in which case:

$$\phi(f)=a\cdot 66^{b} \tag{6.28}$$

Another model, proposed by Battesti in **[6.8, 6.19]**, is:

$$\begin{cases} k=\dfrac{f_u-6}{f_d-6}, & f_u, f_d \le 20\ GHz \\ k=\dfrac{f_u-10}{f_d-10}, & f_u, f_d \ge 20\ GHz \\ k=1.4\cdot\dfrac{f_u-10}{f_d-6}, & f_u>20, f_d<20\ GHz \end{cases} \tag{6.29}$$

The simple power law model also gives a fixed mean IFSF, we have:

$$\bar{k}(A_d)\equiv\bar{k}=\left(\frac{f_u}{f_d}\right)^{n} \tag{6.30}$$

with power, n, lying in the range $1.72 \le n \le 2$ as found from empirical data.

These four fixed EFSF models were compared with the one proposed here. The following procedure was used to find the EFSF:

1. Compute the up-link attenuation based on the mean IFSF curve: $\hat{A}_u^{50\%}=\bar{k}(R)\cdot\bar{\alpha}_d(R)\cdot L(R)$ using equations **(6.8)** and **(6.9)**.
2. Plot $\hat{A}_u^{50\%}(R)$ against $A_d(R)=\bar{\alpha}_d(R)\cdot L(R)$
3. Evaluate the best straight line fitting the graph obtained using a linear regression (Equation **(6.17)**, the offset being neglected). The fixed EFSF is given by the slope of that line.

The results of the comparison are shown in Table 6.4. The parameters used to estimate the EFSR were P%=99%, r= 0.93, Elevation angle of 30°. While the agreement is excellent for the 20/30 GHz pair, the differences are quite large for the other frequency pairs, although the proposed model lies in between the extreme

limits of the empirical power law model. In fact, the power n fitted to our model predictions are 1.66, 1.88, 1.78 for the 30/20, 20/12 and 30/12 frequency pairs respectively. This supports the fact that n depends on the particular frequency pair considered, and that there is no unique value of n to describe consistently the EFSR of rain over all the range of frequencies.

EFSR Model	**Frequency pair (GHz)**		
	30/20	20/12	30/12
Proposed model	1.963	2.610	5.096
ITU-R	1.956	2.390	4.674
Battesti	2.000	2.333	4.667
Paraboni	1.972	2.353	4.642
Power law n=1.72	2.008	2.407	4.836
Power law n=2	2.250	2.778	6.250

Table 6. 4: Comparison of Equiprobability Frequency Scaling Factors for the 30/20, 20/12 and 30/12 GHz frequency pairs.

Elevation Dependence of the EFSF predicted by the proposed model

The fixed EFSF model proposed here is also found to be dependent on the elevation angle. This is essentially due to the influence of the elevation-dependent effective path length (*L(R)* in equation (**6.4**)) which results in a slightly different scaling of the axes of the A_u/A_d graphs, thereby affecting the slope, *s*. More particularly, it is found that the EFSF of rain increases with elevation angle (See Table 6.5).

Elevation Angle	10	15	20	25	30	35	40
30/20	1.918	1.937	1.949	1.957	1.963	1.967	1.971
20/12	2.555	2.578	2.592	2.602	2.610	2.615	2.619
30/12	4.867	4.964	5.025	5.066	5.095	5.118	5.135
Freq. pair	**Estimated Equiprobability Scaling Factor**						

Table 6. 5: Elevation dependence of the equiprobability scaling factor.

Attenuation-dependent models of the EFSF

The variable effective rain model introduced by Paraboni in **[6.2]** introduces a base frequency attenuation dependence of the mean IFSF (see equation **(6.26)**):

$$\phi(f) = a \cdot (23 \cdot A_d^{0.39})^b \qquad \textbf{(6.31)}$$

Boithias' model **[6.20]** introduces an attenuation dependence for the mean IFSF of rain but it has no dependency of the a and b parameters of specific attenuation:

$$\bar{k}(A_d) = \left(\frac{\phi_d}{\phi_u}\right)^{1-H(\phi_1,\phi_2,A_u^d)} \qquad \textbf{(6.32)}$$

with $\phi_f = \dfrac{f}{1+10^{-4}f^2}$ where f equals f_u and f_d for up and down-link respectively, and

$$H(\phi_d,\phi_u,A_d) = 1.12 \cdot 10^{-3}\left(\frac{\phi_u}{\phi_d}\right)^{0.5}(\phi_d \cdot A_d)^{0.55} \qquad \textbf{(6.33)}$$

Fedi's model **[6.21]** assumes a constant path length of L= 4 km and relates the attenuation at up-link frequency to that at the down link frequency by the following expression:

$$A_u = 4 \cdot a_h \cdot \left(\frac{A_u}{4 \cdot a_d}\right)^{b_h/b_d} \qquad \textbf{(6.34)}$$

Dividing by A_d, we get:

$$\bar{k}^R(A_d) = \frac{4a_h}{(4 \cdot a_d)^{b_h/b_d}} \cdot (A_d)^{b_h/b_d - 1} \qquad \textbf{(6.35)}$$

Hodge model **[6.22]** considers a Gaussian rain-rate profile for rain cells. This yields:

$$\bar{k}^R(A_d) = \frac{a_h}{a_d}\sqrt{\frac{b_d}{b_h}}\left(\frac{A_d}{a_d}\left[\frac{a_d}{\pi}\right]\right)^{b_u/b_d-1} \qquad \textbf{(6.36)}$$

The parameters a and b proposed by the ITU-R model **[6.14]** are frequency and polarisation dependent only. However these values are given for a Laws and Parsons distribution. For consistency, the mean values given in Table 6.2, are used to compare the above models with the one proposed in this thesis.

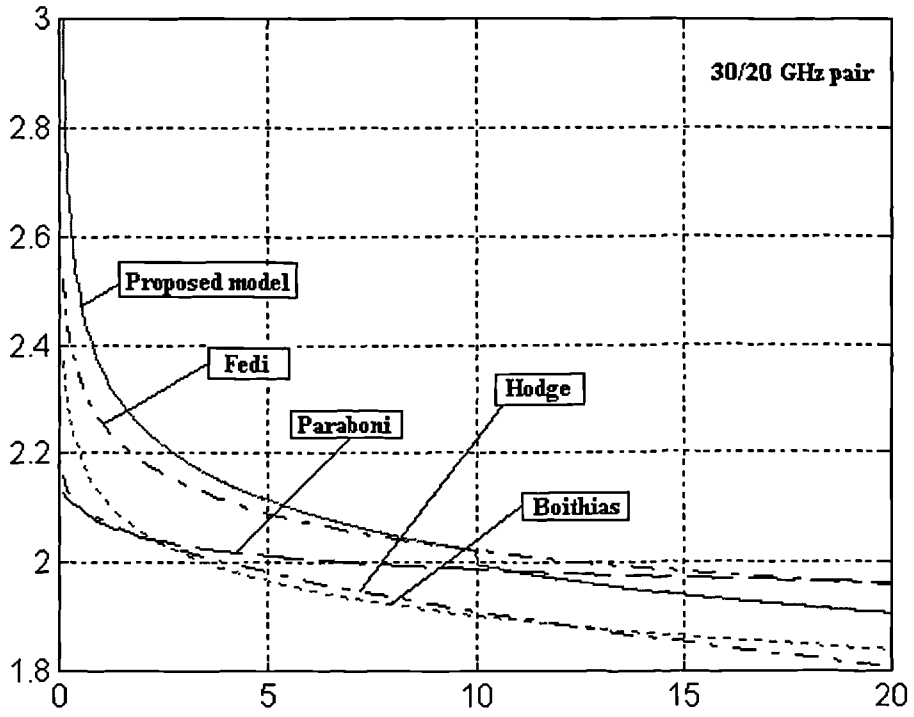

Figure 6.6: Comparison of different attenuation dependent models of the EFSF of rain attenuation.

The fixed EFSF was evaluated by fitting best line of the mean IFSF characteristics and only retaining its slope. In an identical manner, an attenuation dependent EFSR can be constructed by calculating the instantaneous slope of the mean A_u/A_d graph (shown by a dashed line in Figure 6.4) i.e. by evaluating:

$$s(A_d(R)) = \frac{dA_u(R)}{dA_d(R)} = \frac{d(\bar{k}(R)\cdot A_d(R))}{dA_d(R)},\ A_d(R) = \bar{\alpha}_d(R)\cdot L(R) \qquad \textbf{(6.37)}$$

All the attenuation-dependent models are compared in Figure 6.7. All of them, including **(6.37)**, predict that the EFSR decreases with increasing base frequency attenuation. The model proposed in this thesis is closer to Fedi's model for low attenuation level while for high attenuations it yields values of EFSR which are smaller than the one predicted by Hodge or Fedi's models. Note the abrupt change in IFSF around the base attenuation of 10 dB. Clearly further validation against empirical would be required, but this will not be attempted here.

6.3 Design of a predictive fade detection system to include IFSF

In the case of a fade detection scheme based on a variable detection margin (see Figure 5.7), the predictive fade detector can be extended to include the modelling of the IFSF of both rain and scintillation processes. This is depicted in Figure 6.7.

The short-term predictor presented in Chapter 4 is capable of predicting the slow component which corresponds to rain attenuation, i.e. $\hat{z}(t+\Delta t|t) \approx y(t+\Delta t)$. Its error, $\sigma_e(t+\Delta t|t) = \sqrt{f_2(\Delta t)} \cdot \sigma_d^x(t+1|t)$ is consistent with scaled tropospheric scintillation, where $f_2(\Delta t)$ shows explicitly the ability of a particular predictor to extrapolate the variations of the Ka band fading process during the response time Δt of the FCM system.

In such a scenario, the beacon detector (or an equivalent) measures the level of total attenuation at down-link frequency, e.g. 20 GHz. This is fed to the short-term predictor analysed in chapter 4. The predicted component, being a good estimate of rain attenuation is then scaled in frequency to evaluate the up-link rain attenuation.

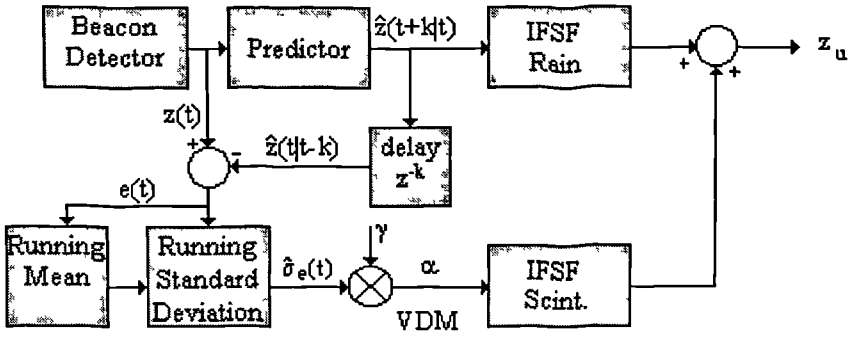

Figure 6.7: Generalised predictive fade detector including instantaneous frequency scaling of rain attenuation and scintillation standard deviation.

This is achieved in a statistically-controlled manner by using equation **(6.14)**. This assumes a stochastic model of the IFSF of rain attenuation. The standard deviation of the prediction error signal is also computed in real-time giving an estimate of the scaled scintillation intensity. It is multiplied by the parameter γ, accounting for the impact of time delays, giving the variable detection margin α. This is then scaled to up-link frequency using the deterministic ITU-R IFSF model for scintillation described in section 6.3. Thus the generalised fade detection rule for a predictive fade detector including IFSF take the form:

$$\hat{z}_u(t+\Delta t|z_d(t)) = \left[\bar{k}^R(R)+\gamma^R\cdot\sigma_k^R(R)\right]\cdot y_d(t+\Delta t|t)+\cdot k_{\sigma_x}\cdot\gamma\cdot\sqrt{f_2(\Delta t)}\cdot\sigma_d^x(t+1|t) \tag{6.38}$$

The parameter k_{σ_x} is fixed for a particular frequency pair. For example, from Table A6.1 (see Appendix A6.II), the IFSF of scintillation variance is 1.26 for the 30/20 GHz pair. Furthermore, the tuning of **(6.38)** to a particular system requires the determination of the two control parameters γ^R and γ so that an overall detection outage probability can be achieved. The partitioning between prediction-induced and IFSF induced effects needs to be considered.

More particularly, from equation **(6.1)**, the total outage probability must satisfy:

$$P_{out}^d = \Pr ob\left\{\hat{z}_u(t+\Delta t|z_d(t)) \le z_u(t+\Delta t)\right\} \le \left(100-A_{\%}\right)/100 \tag{6.1}$$

where A% is the required total detection availability. Based on **(6.38)**, the total outage detection probability will depend on the statistical relationship between rain

induced effects, associated with variable IFSF, and scintillation effects, associated with the short-term prediction error. If it is assumed that they are statistically independent, as supported by the discussion in section 6.4, then equation **(6.1)** can be written as follows (see equations **(6.13)** and **(5.16)**):

$$P_{out}^{d} = P_{out}^{pred} + P_{out}^{R} \leq (100 - A_{\%})/100 \qquad \textbf{(6.39)}$$

A particularly simple partitioning between prediction and IFSF effects can be achieved using:

$$P_{out}^{pred} = P_{out}^{R} = 0.5 \cdot P_{out}^{d} \qquad \textbf{(6.40)}$$

For example, if a total availability of 99.9% is required, then the required parameter γ (for prediction) and the parameter γ^R (for IFSF) should be chosen so as to achieve an outage probability of 0.005 (i.e. 0.05% of the time). Based on equations **(6.15b)** and **(5.19)** this gives $\gamma^R = 3.29$. From this, the detection rules for both IFSF of rain attenuation and scaled scintillation can be identified using the models described in detail in sections 6.2 and 5.4 respectively.

6.4 Model applicability and generalisation

The conditionally Gaussian model proposed in section 6.2 can be generalised and/or modified to account for effects encountered in long-term empirical studies of the IFSF. For example, some researchers have noticed the existence of an hysteresis effect on the IFSF for high level of attenuation **[6.48]**. If this is verified on long term statistical analysis of the IFSF then the Gaussian model used here could be replaced by an empirical bi-modal statistical model. For this effect to be validated, it should be associated with a repetitive physical mechanism. This hysteresis is most probably due to slow temporal changes in rain drop size representing the variability of rain storms during particular events. If repetitive, the hysteresis effect may well be associated to a typical temporal signature or profile from which a better model of the IFSF can be drawn.

The design of fade countermeasure control systems requires an accurate investigation on the relationship between rain and scintillation processes. Such a study relies on the dynamic analysis and separation of the propagation effects encountered at Ka band frequencies.

This thesis considered that the temporal variations in drop size distribution give a good estimate of the variability of the IFSF of rain attenuation. However (see Appendix A6.III) Otung argues that those variations are the source of rain-induced scintillation. This is also very plausible. Clearly, Otung's model refers to fast variations in DSD while the one proposed here refers to slow temporal variations. Also Matricciani's model (see Appendix A6.III), considering extra-turbulent cloud activity during rain events cannot be discarded. The crucial difficulty is the dynamic separation of rain and scintillation and other effects like gaseous attenuation and it would require further research.

For example, particular studies may focus on :

- the efficient extraction of gases attenuation from co-polar attenuation time-series,
- the characterisation of scintillation w.r.t cloud coverage: this is to identify the link between scintillation and cloud turbulence during rain and dry conditions. This would provide a test of Matricciani's hypothesis,
- the study of the temporal variability of DSD during rain storms conditioned on rain rate. In particular, the characterisation of the slow and fast components of this variability would give a good indication on the partitioning between the variable IFSF of rain attenuation (proposed model) and rain induced scintillation (Otung's model).

6.5 Conclusions

A novel model of the instantaneous frequency scaling factor of rain attenuation was presented in this chapter. This model has then been included in a generalised fade detection scheme, where the impact of time delays and variable instantaneous frequency scaling are considered simultaneously. It is applicable to predictive detection systems which are based on measurements of the link attenuation at a base-frequency. Its great advantage over a more empirical model is that it can be used to design a system with an arbitrary link availability.

The proposed model considers the impact of slow temporal stochastic variations in drop size distribution on the mean and standard deviation of the scaling factor. This model assumes a conditionally Gaussian model of the specific attenuation conditioned on rain rate. It was assumed that most temporal variations lie between the J-T and J-D distributions, which were used as reference or extremes to the model. The model was then calibrated using recent results published in the literature. It was also compared to other proposed empirical models and it was found to yield similar results.

The design of fade detection schemes relies on the functional or statistical relationship between rain and scintillation processes. Based on a literature survey, it appears that the scaling factor of dry scintillation can be assumed to be constant and that it is well modelled by the current ITU-R model. In the case of wet scintillation, three different physical mechanisms relating rain and scintillation variance are in contention. Non-coherent scattering in Ka band satellite systems has been proven negligible by Haddon and Vilar. Matricciani's model considers the increase in cloud turbulence during rain storms while Otung's model assumes that rain-induced scintillation is due to fast variations of drop size distribution around their mean value.

Clearly, the latter hypothesis along with the proposed model in this chapter, overlap in some way and would require a detailed analysis of the temporal variability of rain drop size distribution which should be split into slow and fast components. However current statistical model obtained by Salonen et al tend to show that the correlation between rain and scintillation is negligible in practical cases. Therefore the global fading hypothesis, which assumes statistical independence between rain and scintillation still seems appropriate for the modelling and design of fade countermeasures.

Appendix A6.I: Modelling of the effective path length on satellite links

The modelling of the effective path length on satellite to Earth paths is a difficult well-known problem. It essentially consists in estimating the total attenuation on an extended satellite link based on point rainfall rate. It has always been at the forefront of fundamental propagation modelling and research.

A first very crude approach is to consider that specific attenuation is homogeneous i.e. $\overline{\alpha}_d(R)$, $\overline{\alpha}_u(R)$ along the path length L through the rain layer which is given by:

$$L = \frac{H_R - H_s}{\sin\theta}, \theta \geq 10^o \qquad \textbf{(A6.I.1)}$$

where H_R and H_s are the estimated height above sea level of the 0°C isotherm and the earth station altitude respectively. θ is the link elevation angle. H_R depends itself on the latitude, φ, of the earth-station. In the northern hemisphere **[6.49]**:

$$H_R = \begin{cases} 5 - 0.075 \cdot (\varphi - 23) & \text{for } \varphi > 23 \\ 5 & \text{for } 0 \leq \varphi \leq 23 \end{cases} \qquad \textbf{(A6.I.2)}$$

As melting particles have different specific attenuation than rain particles, a better model can also consider the impact of the melting layer (≈ 0.4 km below H_R) on the total specific attenuation on a satellite link. In particular, Klassen showed in **[6.50]** that the total attenuation is smaller at one carrier frequency when there is a larger melting layer. This has also the interesting effect of lowering the scaling factor of rain attenuation.

More realistic models also attempt to include the spatial structure of rain cells. More particularly, there is experimental evidence that the rain rate differential between two points horizontally separated by x km are connected via a correlation function of the form $c(x)=e^{-kx}$. Thus at any given time, if it rains at rate R at a point x, then all the point rainfall rates along the path L are statistically connected to each other, thereby affecting the overall specific attenuation of the link (so that the attenuation on the link is itself lognormal given that R at one point is also

lognormal). Such complex models are presented for example in **[6.51]** and **[6.52]**. The latter is a two-layer model which also considers the impact of the melting layer. However the accuracy of such models, when compared to experimental results is quite poor and hence it may appear more appropriate to recourse to more empirical models. A related feature is that intense rainfall rate rain cells are usually more limited in geographical extent than low rainrate cells **[6.53]**. This suggests that the path length can be seen as dependent on rain-rate and that L(R) is decreasing monotically with R. Thus, instead of attempting to calculate the overall specific attenuation on an satellite link by considering the statistical impact of the spatial structure of raincells on the overall specific attenuation statistics as in **[6.51]** and **[6.52]**, an equivalent method is to assume that the specific attenuation over a link is fixed (and equal to a chosen arbitrary mean value) but the total length of the link through rain is dependent on the rain rate, as measured on the ground. This is achieved based on the following principle:

$$A_i = \left(\overline{\alpha}_i(R) \cdot f(R)\right) \cdot L = \overline{\alpha}_i(R) \cdot L(R) \quad \text{where L(R)} \equiv f(R) \cdot L \qquad \textbf{(A.6.I.3)}$$

Here $\overline{\alpha}_i(R) = \overline{a}_i \cdot R^{\overline{b}_i}$ denotes the assumed mean specific attenuation along the satellite path of physical length *L*. *f(R)* is an empirical function embodying the spatial structure of the rain cells. L(R) is called the effective path length of the satellite to earth link. Note that in general, *f(R)* will be a stochastic variable with a specific (but unknown) pdf. It could be evaluated by solving the problem: given that A_i and R are well approximated as lognormal variables, what should be the pdf of *f(R)* so that the equality in **(A6.I.3)** is statistically valid. An estimate of the mean of *f(R)* can however be identified from the CDFs of joint rainfall rate, $R_{p\%}$, and rain attenuation, $A_{p\%}$, exceeded for p% of the time using:

$$f(R_{p\%}) \approx \frac{A^i_{p\%}}{\overline{a}_i \cdot \left[R_{p\%}\right]^{\overline{b}_i} \cdot L} \equiv r_{p\%} \qquad \textbf{(A.6.I.4)}$$

Note that $f(R_{p\%})$ is dependent upon frequency since each of the parameters a and b of the mean specific attenuation are themselves dependent on frequency. This approach has been used widely, in which case $f(R_{p\%}) = r_{p\%}$ is referred to as the path reduction factor.

In the case of the current ITU-R model **[6.54]**, the path reduction factor is constant and given by:

$$r_p = r_{0.01} = \frac{1}{1 + L \cdot \cos\theta / 35 \cdot \exp(-0.015 \cdot R_{0.01})} \qquad \textbf{(A.6.1.5)}$$

where $R_{0.01}$ denotes the rain rate exceeded for p%=0.01% of the time.

A very recent paper by Goddard and Thurai in **[6.55]** pointed out that the ITU-R model did not fit their radar data obtained on a 1.5° elevation angle. They proposed a path reduction factor for terrestrial microwave links which is dependent on rain rate and physical horizontal path length. It is given by (after a normalisation to links with arbitrary elevation):

$$r_p = 1.35 + 2 \cdot \left[\left(L \cdot \frac{\cos\theta}{\cos 1.5} \right)^{-0.053} - 2.25 \right] \cdot \log_{10} R_p \qquad \textbf{(A.6.I.6)}$$

This equation is monotically decreasing with rain rate, which is more satisfactory than the ITU-R model, however Goddard and Thurai do not provide a relation which depends on frequency as can clearly be expected from equation **(A.6.I.4)**.

Appendix A6.II: Model for the instantaneous frequency scaling factor (IFSF) of dry scintillation variance

Tropospheric scintillation occurs due to variations of the atmospheric refractive index denoted by n. These variations are of the order of 10^{-4} around the value of 1. Therefore it is common to use the refractivity index defined by $N \equiv (n-1)\cdot 10^6$. N is given by **[6.24]**:

$$N = \frac{77.6 \cdot P}{T} + 3.73256 \cdot 10^5 \cdot \frac{e}{T^2} \qquad \textbf{(A6.II.1)}$$

P denotes the atmospheric pressure (mb), T is temperature (K), e is water vapour pressure (mb). The first term is referred to as the dry term, N_{dry}, of the refractivity while the second is called the wet term, N_{wet}. e depends on the relative humidity U in % and the temperature, t in Celsius. It is given by:

$$e = \frac{H}{100} \cdot 6.1121 \cdot \exp\left(\frac{17.502 \cdot t}{t + 240.97}\right) \qquad \textbf{(A6.II.2)}$$

Although these two equations were based on monthly variations of each of its meteorological parameters, clearly, the short-term temporal variations of the N_{wet} term can be associated to random variations of temperature and humidity within a layer of atmospheric turbulence.

Karasawa, and al were the first to identify a causal relationship between the scintillation variance and the N_{wet} term of refractivity **[6.25, 6.26]**. Their results were slightly modified (in particular the elevation dependence was changed from Karasawa's original exponent of 1.3 to 1.2) and they now constitute the current ITU-R model for scintillation. The monthly mean value of the short-term standard deviation of the received signal's log amplitude predicted by the ITU-R model **[6.27]** is :

$$\sigma_\chi^i = \frac{\sigma_{ref} \cdot f_i^{7/12} \cdot g(f_i, D_i, \theta_i)}{\sin^{1.2}\theta_i} \text{ dB} \qquad \textbf{(A6.II.3)}$$

where

$$\sigma_{ref}^{ITU-R} = 3.6 \cdot 10^{-3} + 1.03 \cdot 10^{-4} N_{wet} \text{ dB} \qquad \textbf{(A6.II.4)}$$

The aperture averaging of an antenna with finite dimension is **[6.28]**:

$$g(f_i, D, L) = \sqrt{3.8637(x^2+1)^{11/12}\sin\left(\frac{11}{6}\tan^{-1}\left(\frac{1}{x}\right)\right) - 7.0835x^{5/6}} \qquad \textbf{(A6.II.5)}$$

$$x = 0.0584 \cdot k \cdot (\eta D_i)^2 / L \qquad \textbf{(A6.II.6)}$$

$k=2\pi/\lambda$ is the wave number, D is the physical diameter of the antenna with efficiency, η.

The effective path length, L, through the turbulent layer is:

$$L = 2h / \left[\left(\sin^2\theta_i + (2h/r_e)\right)^{1/2} + \sin\theta_i\right] \text{ m} \qquad \textbf{(A6.II.7)}$$

The ITU-R recommends h=1000 m for the height of the turbulent layer. r_e denotes the effective radius of the earth ($=8.5\cdot10^6$ m).

The deterministic model of the IFSF of scintillation variance is usually based on the ratio:

$$k_{\sigma_\chi} = \frac{\sigma_\chi^u}{\sigma_\chi^d} = \left(\frac{f_u}{f_d}\right)^{7/12} \cdot \frac{g(f_u, D_u, \theta_u)}{g(f_d, D_d, \theta_d)} \cdot \left(\frac{\sin\theta_u}{\sin\theta_d}\right)^{1.2} \qquad \textbf{(A6.II.8)}$$

An alternative to this model of the IFSF derived from the ITU-R is also often used for the modelling of scintillation (see for example **[6.29]**). It is based on the theoretical work of Tartaskii **[6.30]** and it assumes that the elevation dependence is given by an exponent of 11/12 (= 0.916) instead of 1.2 in (6.45).

Based on the analysis of 100 station-months of monthly data, Ortgies in **[6.31]** verified the validity of the $f^{7/12}$ dependency of the IFSF of scintillation. He also found that this occurs for a turbulent height of 1 km as recommended by the ITU-R model.

In the case of two co-located links with same elevation angle and a same antenna, the deterministic scaling factor of scintillation standard deviations simplifies to:

$$k_{\sigma_\chi} = \frac{\sigma_\chi^u}{\sigma_\chi^d} = \left(\frac{f_u}{f_d}\right)^{7/12} \cdot \frac{g(f_u, D, \theta)}{g(f_d, D, \theta)} \qquad \textbf{(A6.II.9)}$$

It has always been assumed that the above model is only applicable for meteorological parameters average over periods of one month. However, important recent results obtained by Van De Kamp and al in **[6.32, 6.33]** showed that the dependency of σ_χ on the N_{wet} term is also valid over much shorter time spans of the order of three days. Van de Kamp found that the dependency of the scintillation standard deviation on the N_{wet} term is well approximated by the empirical formula:

$$\sigma_\chi^{19.8} = 0.057 + 2.79 \cdot 10^{-3} \text{ dB} \qquad \textbf{(A6.II.10)}$$

By considering their particular experimental set-up, namely D=1.8 m, η=0.63, θ=12.7°, f =19.8 GHz (vertical polarisation) and feeding these into (6.40) to estimate σ_{ref}, it is found that:

$$\sigma_{ref}^{Kamp} = 2.11 \cdot 10^{-3} + 0.774 \cdot 10^{-4} \cdot N_{wet} \text{ dB} \qquad \textbf{(A6.II.11)}$$

In view of equation **(A6.II.4)**, Van de Kamp et al found that the current ITU-R model over-estimates the N_{wet} contribution to the scintillation variance, however this has no impact on the deterministic scaling of scintillation variance. Similar results have been published in **[6.34]**. Glover et al also found that the ITU-R model overpredicts the monthly mean scintillation intensity for dry scintillation, while for wet scintillation, the ITU-R model only overpredicts for spring and winter months.

An important question at this stage is to decide whether it is worth investigating the possibility of deriving a stochastic model of the IFSF of scintillation standard deviation, as was done in the previous section for rain attenuation. Such a decision must be based on measured cross-correlation factors between co-located dual frequency standard deviation time-series.

Karasawa et al studied in **[6.26]** the scaling of scintillation standard deviation for the 14/11 GHz frequency pair. They found correlation factors of the order 0.996 for hourly measured ratios of standard deviations. For the ratio of amplitude scintillation, the correlation factor dropped down to values around 0.91. This

suggests that the deterministic scaling of scintillation standard deviation is more reliable that the deterministic scaling of scintillation amplitudes, the latter probably requiring a stochastic model. However, the scaling of scintillation amplitudes or variances, depends crucially on the set-up of the experiment. Virginia Polytechnic studied in **[6.35]** the important impact of the separation distance between receiving antennas on the correlation factor. They found median correlation factors of the order of 0.65 for co-located links at 30 and 20 GHz pairs, which is much smaller than Karasawa's values. This large difference may be due to the fact that their study was based on one-minute data, while Karasawa's was based on monthly measurements. It may also be due to the different filtering methods used to extract the scintillation component from the raw beacon time-series.

Ortgies evaluated in **[6.36]** the equiprobability ratio of scintillation amplitudes for the 30/20, 30/12.5 and 20/12.5 GHz pairs. He found that the scaling factor agrees well with the ITU-R model **(A6.II.9)** for the IFSF of standard deviations. He found that the IFSF is constant except for scintillation variances close to zero (in which case the IFSF of amplitudes is indeterminate corresponding to a 0/0 situation). Thus there is no experimental evidence showing that the IFSF of scintillation standard deviations is level-dependent. Tervonen in **[6.37]** evaluated the equiprobability ration of scintillation variance found that the scintillation amplitude ratio has a level dependence, however the author estimated that this was due to a non-optimum separation of rain and scintillation effects. In **[6.38]**, Otung, Norbury and Mahmoud proposed a new empirical model of the scintillation standard deviation. This model is normalised in such a way that it implicitly assume a constant IFSF ratio equal to the ITU-R model given in **(A6.II.9)**.

Based on this discussion, and due to lack of experimental evidence of the contrary, it is reasonable to assume that the IFSF of scintillation standard deviation is sufficiently well modelled by the current ITU-R model. This model will thus be retained in later sections. In particular, the IFSF of turbulent scintillation has been evaluated in Table A6.1 for three test case frequency pairs using **(A6.II.9)** with an elevation of 30°, an effective antenna diameter of 0.5 metre.

Frequency pair (GHz)	IFSF of scintillation standard deviation
30/20	1.259
20/12	1.339
30/12	1.685

Table 6.6: IFSF of dry scintillation standard deviation based on the ITU-R model.

Appendix A6.III: Relationship between rain and scintillation

The ITU-R model for the IFSF of scintillation variance reviewed above is mainly valid for dry scintillation, corresponding to non-rainy conditions. Current propagation theory is trying to consider the possible relationship between rain and scintillation processes. This is crucial to fade countermeasure systems, which have to operate during clear-sky as well as wet conditions.
The search of a functional relationship between rain attenuation and scintillation is significant for the following three reasons.

- The modelling of the IFSF of scintillation variance can be expected to vary from dry to wet conditions if there is a correlation between rain and scintillation. This is particularly important for base-frequency detection schemes for which real-time IFSF has to be performed.
- As we saw in chapter 4, the rain attenuation component is well short-term predicted using the ARMA based predictor. If there is a relationship between rain and scintillation, it should be possible, at least partially, to infer the level of scintillation activity based on detected/predicted rain attenuation.
- The global fading model used and modified in this thesis relies on the assumption that rain and scintillation are statistically independent.

The rationale of a link between rain and scintillation processes must be probed from a physical perspective. Dry scintillation is associated with coherent scattering of electromagnetic waves due to the temporal variations in temperature and humidity which affect the air refractive index. This phenomenon occurs sporadically but all the time. This is usually referred to as turbulent attenuation. Particular intense fast dry scintillation events, surimposed on the small slow attenuation caused by absorption by cloud particles, have been noticed during the passage of heavy cumulus clouds through the radio path **[6.39]**. These occur more often in summer and around noon.

Two other mechanisms have also been identified as potential sources of scintillation events. They belong to the class of wet scintillation and only occur when it rains. There is first the incoherent scattering caused by raindrops. This incoherent component also results in fast fluctuations around the mean coherent average field converting into random amplitude and phase scintillation **[6.40]**. However Haddon and Vilar showed in **[6.28]** that this effect is negligible in finite aperture receive antennas. These only intercept a tiny fraction of the incoherently scattered power due to large aperture smoothing. Another mechanism considers the impact of *short-term* temporal variations of the drop size distribution (DSD) on the *short-term* variation of the coherent scattered field by raindrops. The analysis of such a phenomenon is difficult since it requires the separation of the slow changes in DSD (resulting in slow variations of rain attenuation and its IFSF as studied in section 6.2) from the fast changes in DSD source of scintillation.

Otung et al studied those effects in **[6.41]**. Based on simulation results, they found that the standard deviation of rain-induced scintillation follows a power rule given by:

$$\begin{cases} \sigma_{\chi}^{20\ \mathrm{GHz}} = 0.01053 \cdot R^{1.06122}\ \mathrm{dB} \\ \sigma_{\chi}^{30\ \mathrm{GHz}} = 0.02319 \cdot R^{1.03345}\ \mathrm{dB} \end{cases} \qquad \textbf{(A6.III.1)}$$

where R is the rainrate in mm/h. For heavy rain (150mm/h), this gives rain-induced scintillation of 2 and 4 dB at 20 and 30 GHz respectively which are rather large. They also found a quasi-linear relationship between rain-induced scintillation and rain specific attenuation. As the latter is polarisation dependent, rain-induced scintillation is larger on horizontal polarisation. In **[6.42]**, Otung studied the variations in drop size distribution using a distrometer. He found that rain-induced scintillation is of the same order of magnitude as turbulent scintillation. He also mentioned that his simulation results may over-estimate due to the difficulty of identifying the fast variation in drop size distribution around its slowly time-varying mean. Such a separation, if carried out efficiently and consistently, should allow to devise a stochastic model of the IFSF of wet scintillation variance. This would require a study of the variability of the fast variations in DSD around the mean result in **(A6.III.1)**.

The two mechanisms, just described, generate wet scintillation and they assume the presence of rain in the strict sense (i.e. the rain rate is not zero). Another

line of approach considers the relationship between scintillation and rain attenuation, the latter corresponding to situations where the co-polar mean attenuation is above a certain low level (e.g. 1 to 3 dB) but there may or may not be rain on the path. Although such a viewpoint is less satisfactory on a purely physical basis, it can however yield the required answer needed for the efficient design of countermeasure control systems.

Vanhoenacker and Vander Vorst in **[6.43]** found some correlation at 11.4 and 35 GHz between the variance of the scintillation process and the measured sky noise temperature representative of absorptive effect like gases, cloud and rain attenuation. Matricciani et al in **[6.44]** and **[6.45]** analysed rain attenuation co-polar data at 19.77 and 49.5 GHz respectively. They found a good correlation between the mean scintillation standard deviation, σ_χ^i and rain attenuation, A_i, at a carrier frequency f_i. Their curve fit is given by:

$$\sigma_\chi^i = C \cdot A_i^{5/12} \text{ dB} \qquad \textbf{(A6.III.2)}$$

with C=0.0391 at 19.77 GHz for A>1.5 dB while C=0.075 for A<3 dB and C=0.056 for A>3dB.

This empirical relationship was justified using the thin layer model proposed by Matricciani in **[6.44]** whose underlying physical mechanism is that rain attenuation induced scintillation is generated by larger cloud turbulence during rain conditions (in a loose sense). Here the separation problem translates to the difficulty of separating wet from dry scintillation since turbulence is associated with clouds in the presence or not of true rain events. Matricciani's model assumes that the effective path length L through rain is equal to the maximum possible length through the turbulent layer. It considers the average rain attenuation on a link with the physical length of the path through rain ($L=H_R/\sin\theta$, H_R=rain height, θ =elevation angle):

$$A_i = \overline{\alpha}_i \cdot L \qquad \textbf{(A6.III.3)}$$

The scintillation standard deviation, including the aperture averaging effect is given by **[6.44]**:

$$\sigma_\chi^i = g(f_i, D, L) \cdot 6.5 \cdot \sqrt{D} \cdot C_n \cdot k^{7/12} \cdot L^{5/12} \text{ dB} \qquad \textbf{(A6.III.4)}$$

where D (m) is the actual turbulent tract located aloft between L-D and L, with D<<L.

Feeding (6.50) into (6.51) yields:

$$\sigma_{\chi}^{i} = \left\{6.5 \cdot C_n \cdot \sqrt{D} \cdot k^{7/12} \cdot g(f_i, D, L) \cdot [\overline{\alpha}_i]^{-5/12}\right\} \cdot A_i^{5/12} \equiv C_i \cdot A_i^{5/12} \text{ dB} \qquad \textbf{(A6.III.5)}$$

The bracketed term corresponds to the constant C in **(A6.III.2)**. The constant C is dependent upon frequency i.e. $C=C_i$ (i equals u or d for up and down link frequency) as found empirically by Matricciani et al. This model presents some difficulties. For example, in view of **(A6.III.4)**, the model relies on the joint determination of C_n, D via remote-sensing of the atmosphere. This may prove very difficult and it is simpler to employ empirical curve fitting to evaluate C as provided in **[6.44]** and **[6.45]**. Therefore this model could be used directly to evaluate the variability of the IFSF of scintillation standard deviations. Furthermore, from **(A6.III.2)**, the IFSF of scintillation standard deviations can be expressed in terms of the IFSF of rain attenuation (see section 6.2). For the 30/20 GHz pair this gives :

$$k_{\sigma_x} = \frac{0.5 \cdot [0.075 + 0.056]]}{0.0391} \cdot \left(\frac{A_u}{A_d}\right)^{5/12} = 1.675 \cdot k(R)^{5/12} \qquad \textbf{(A6.III.6)}$$

This suggests that the IFSF of scintillation intensity is also stochastic. This fits also with the fact that rain-induced scintillation, like rain, is also polarisation dependent. Such characteristics have also been mentioned in **[6.32]**. As a test case example, an estimate of the IFSF of rain is 1.963 (see Table 6.3) for the 30/20 GHz pair. Using equation **(A6.III.6)**, the mean IFSF of scintillation is estimated to 2.218. This is very different from the expected IFSF of dry scintillation which should be 1.259.

Although, so far, the evidence shows that there is a link between rain and scintillation, some other authors believe that this relationship can be neglected in practical cases. Essentially, this is the point of view which is chosen in this thesis.

This is backed up, for example, by Karasawa and Matsudo who studied in **[6.46]** the power spectrum of scintillation during rain events. They found the two processes are slightly correlated but it should be insignificant on statistical basis and they asserted that rain and scintillation can be treated as independent. Similar conclusions were reached by Salonen et al in **[6.47]** who studied different ways of combining mathematically the statistics of rain and scintillation to match the empirical CDF of

the total attenuation on particular satellite links. They also found that statistical independence yielded the best results. In **[6.33]**, Salonen et al further extended the statistical analysis and they found a clear dependence between rain attenuation and scintillation standard deviation. They then compared two methods of combining rain and scintillation statistics. One considered a dependent summing while the other assumed independence. They found that the difference between the two is negligible and thus independence is good enough for practical cases.

As a conclusion, although there is a very probably a relationship between rain attenuation and scintillation variance, further investigations are required. In particular, the physical nature of this link has yet to be established and quantified in a clear and precise manner. The mechanisms proposed in the literature are definitely on the right track but they seem to over-estimate the long-term statistical contribution of wet scintillation on the total fade statistics. As the design of FCM control systems must rely on a accurate long-term statistical model for joint rain and scintillation and based on current evidence, statistical independence can still be assumed to hold. The identification of a link between rain and scintillation relies on the efficient extraction of scintillation of the two processes and separation methods should therefore be apprehended in a very critical manner. A possible linking with rain rate, instead of total absorptive attenuation (clouds, rain and gases) may appear more appropriate. This would however require the extraction of the short-term temporal variations in dropsize distribution from the slower ones, source of variable IFSF of rain attenuation (studied in section 6.2). This is also difficult and it can directly be paralleled to the problem of extracting rain effects from wet scintillation.

References

[6.1] M.G. Willis, "Fade countermeasures applied to transmissions at 20/30 GHz", *Electronics & Communication Engineering Journal*, April 1991, pp 88-96.

[6.2] "Project COST 205:Frequency and polarisation scaling of rain attenuation", *Alta Frequenza*, Vol. LIV, No 3, May-June 1985, pp 157-181.

[6.3] ESA, *OPEX 2nd Workshop of the Olympus Experimenters, Vol. 1: Reference book on attenuation measurement and prediction*, ESA WPP-083, Noordjwick, 8-10 Nov. 1994.

[6.4] BT Technology J., Satellite propagation measurements, BT Laboratories, Vol. 10, No 4, October 1992.

[6.5] D.C. Cox, H.W. Arnold, "Results from the 19- and 28-GHz COMSTAR satellite propagation experiments at Crawford Hill", *Proc. IEEE*, Vol. 70, No 5, May 1982, pp 458- 488.

[6.6] M. Mauri, A. Paraboni, C. Riva, "Instantaneous Frequency Scaling", *OPEX 2nd Workshop of the Olympus Experimenters, Vol. 6: Proceedings*, ESA WPP-083, Noordjwick, 8-10 Nov. 1994.

[6.7] F. Rücker, "The impact of the variation of instantaneous frequency scaling factors on up-link power control", *AEÜ*, Vol. 48, No2, 1994, pp 119-121.

[6.8] J.D. Laster, W.L. Stutzman, "Frequency scaling of rain attenuation for satellite Communications links", *IEEE Trans. on Ant. and Prop.*, Vol. AP-43, No. 11, Nov. 1995, pp 1207-1215.

[6.9] D.G. Sweeney, T. Pratt, C.W. Bostian, "Hysteresis effect in instantaneous frequency scaling of attenuation on 20 GHz and 30 GHz satellite links", *Electronics Letters*, Vol. 28 No 1, January 1992, pp 76-78.

[6.10] A.R. Holt, "Frequency scaling propagation parameters using dual-polarization radar results", *Radio Science*, Vol. 19, No 1, Jan-Feb. 1984, pp 222-230.

[6.11] L.J. Ippolito, *Radiowave propagation in satellite communications*, Van Nostrand Reinhold, 1986.

[6.12] J. Joss, J.C. Thams, A. Waldvogel, "The variation of rain drop-size distributions at Locarno", *Proc. Int. Conf. Cloud Physics*, 1968, pp 369-373.

[6.13] R. Olsen, D.V. Rogers, D.B. Hodge, "The aR^b relation in the calculation of rain attenuation", *IEEE Trans. on Ant. and Prop.*, Vol. AP-26, No 2, March 1978, pp 318-329.

[6.14] CCIR, Report 721-3, "Attenuation by hydrometeors in particular precipitation, and other atmospheric particles", *Reports of the CCIR, Annex to Volume V, Propagation in non-ionized media*, ITU-R, Geneva, 1990, pp 226-245.

[6.15] H.N Kheirallah, J.P. Knight, R. L. Olsen et al, "Frequency dependence of effective path length in prediction of rain attenuation statistics", *Electronics Letters*, Vol. 16, No 12, June 1980, pp 448-450.

[6.16] I.P. Shkarofski, "Dependence of rain attenuation and cross-polarization on drop size distribution", *IEEE Trans. on Ant. and Prop.*, Vol. AP-27, No 4, July 1979, pp 538-542.

[6.17] V.K. Bhargava, D. Haccoun, R. Matyas, P.P. Nuspl, *Digital communications by satellite: Modulation, Multiple Access and Coding*, Wiley-Interscience, John Wiley and sons, 1981.

[6.18] A. Papoulis, *Probability, Random Variables, and Stochastic Processes*, Third edition, McGraw-Hill international editions, 1991.

[6.19] J. Battesti, "Au sujet de la dépendance en fréquence de l'affaiblissement dû á la pluie", *Ann. Télécommun.*, Vol. 36, No 3-4, 1981, pp 274-275.

[6.20] L. Boithias, "Similitude en fréquence pour l'affaiblissement par la pluie", *Ann. Télécommun.*, Vol. 44, No 3-4, 1989, pp 186-191.

[6.21] J.E. Allnut, *Satellite-to-ground radiowave propagation*, IEE, Peter Peregrinus Ltd, London, UK, 1989, pp 219.

[6.22] D.B. Hodge, "Frequency scaling of rain attenuation", *IEEE Trans. Ant. Prop.*, May 1977, pp 446-447.

[6.23] M.R. Spiegel, *Theory and problems of advanced calculus*, Schaum's outline series, Mc Graw Hill, international editions, 1974.

[6.24] ITU-R Rec. PN.453-4, "The radio refractive index: its formula and refractivity data", *ITU-R recommendations, Propagation in non-ionized media, PN-series Volume*, ITU-R, 1994, pp 206-213.

[6.25] Y. Karasawa, M. Yamada, J.E. Allnutt, "A new prediction method for tropospheric scintillation on Earth-Space paths", *IEEE Trans. on Ant. and Prop.*, Vol. AP-36, No 11, Nov. 1988, pp 1608-1614.

[6.26] Y. Karasawa, K. Yasukawa, M. Yamada, "Tropospheric scintillation in the 14/11 GHz bands on Earth-Space paths with low elevation angles", *IEEE Trans. on Ant. and Prop.*, Vol. AP-36, No 4, Nov. 1988, pp 563-569.

[6.27] ITU-R Rec. PN.618-3, "Propagation data and prediction methods required for the design of Earth-space telecommunications systems", *ITU-R recommendations, Propagation in non-ionized media, PN-series Volume*, ITU-R, 1994, pp 329-343.

[6.28] J. Haddon, E. Vilar, "Scattering induced microwave scintillations from clear-air and rain on Earth-Space paths and the influence of antenna aperture", *IEEE Trans. on Ant. and Prop.*, Vol. AP-34, pp 646-657, May 1986.

[6.29] I.E. Otung, M.S. Mahmoud, B.G. Evans, "Dual frequency measurement for remote sensing", *Electronics Letters*, Vol. 31, No 23, Nov. 1997, pp 1972-1973.

[6.30] V.I. Tartaskii, *The effects of the turbulent atmosphere on wave propagation*, Israel programme for scientific translations, Jerusalem, 1971.

[6.31] G. Ortgies, "Frequency dependence of slant-path amplitude scintillations", *Electronics Letters*, Vol. 29 No 25,Dec. 1993, pp2119-2220.

[6.32] M.M.J.L Van De Kamp, J.K. Tervonen, E.T. Salonen, J.P.V. Poiares Baptista, " Scintillation prediction models compared to measurements based on a time base of several days", *Electronics Letters*, Vol. 32 No 12, June 1996, pp 1074-1075.

[6.33] M.M.J.L Van De Kamp, J.K. Tervonen, E.T. Salonen, "Tropospheric scintillation measurements and modelling in Finland", *Proc. 10th Int. Conf. on Ant. and Prop., IEE Conf. publ. No 436, 14-17 April. 1997, Edinburgh,* 1997, pp 2.141-2.144.

[6.34] M.M.B Yusoff, I.A. Glover, P.A. Watson et al, "Evidence for the presence of turbulent attenuation on low-elevation angle earth-space paths- Part I: Comparison of CCIR recommendations and scintillation observations on a 3.3° path", *IEEE Trans. on Ant. and Prop.*, Vol. AP-45, No 1, Jan. 1997, pp 79-84.

[6.35] T. Pratt, D. Sweeney, F. Haidara, "Olympus propagation experiment at Virginia Tech: recent results for frequency scaling and scintillation", *Proc. of the 16th meeting of Olympus propagation experimenters, OPEX XVI*, Aveiro, Portugal, Oct. 1991, pp 99-131.

[6.36] G. Ortgies, "Slant path frequency scaling of amplitude scintillations during clear-sky conditions and rain", *AEÜ*, Vol. 47, No 4, 1993, pp 203- 208.

[6.37] J. Tervonen, "Scintillation results on a 12.7° Elevation path", *Proc. of the 21st meeting of Olympus propagation experimenters, OPEX XXI*, Louvain la Neuve, Belgium, May 1994, pp 173-181.

[6.38] I.E. Otung, M.S Mahmoud, J.R. Norbury, "Radiowave amplitude scintillation intensity: Olympus satellite measurements and empirical model", *Electronics Letters,* Vol. 31 No 21, Oct. 1995, pp 1873-1875.

[6.39] D.C. Cox, H.W. Arnold, H.H. Hoffman, "Observations of cloud produced scintillation on 19 and 28 GHz earth-space paths", *Radio Science*, Vol. 16, 1981, pp 885-907.

[6.40] C. Capsoni, M. Mauri, A. Paraboni, "Incoherent effects in electromagnetic propagation through rain", *Ann. Telecommunications*, Vol. 32, 1977, pp 409-414.

[6.41] I.E. Otung, M.S. Mahmoud, B.G. Evans, "Dependence of rain-induced amplitude scintillation in Ka band satellite links on drop size distribution", *Proc. Conf. Microwaves 94: The application of RF microwave and millimetre wave technologies*, 1994, pp 345-349.

[6.42] I.E. Otung, M.S. Mahmoud, "Rain-induced scintillation on satellite downlinks, *Electronics letters*, Vol. 32, No 1, Jan. 1996, pp 65-66.

[6.43] D. Vanhoenacker, A, Vander Vorst, "Experimental evidence of a correlation between scintillation and radiometry at centimeter and millimiter wavelengths", *IEEE Trans. on Ant. and Prop.*, Vol. AP-33, No 1, Jan 1985, pp 40-47.

[6.44] E. Matricciani, M. Mauri, C. Riva, "Relationship between scintillation and rain attenuation at 19.77 GHz", *Radio Science*, Vol. 31, No 2, March-April 1996, pp 279-279.

[6.45] E. Matricciani, M. Mauri, C. Riva, "Scintillation and simultaneous rain attenuation at 49.5 GHz", *Proc. of the Int. Conf. on Ant. and Prop., ICAP'95,Eindhoven, The Netherlands,* IEE Publ. No 407, Vol. 2, 1995, pp 165-168.

[6.46] Y. Karasawa, T. Matsudo, "Characteristics of fading on low-elevation angle earth-space paths with concurrent rain attenuation and scintillation", *IEEE Trans. on Ant. and Prop.*, Vol. AP-39, No 5, May 1991, pp 657-661.

[6.47] E.T. Salonen, J.K. Tervonen, W.J. Vogel, "Scintillation effects on total fade distributions for Earth-Satellite links", *IEEE Trans. on Ant. and Prop.*, Vol. AP-44, No 1, Jan 1996, pp 23-27.

[6.48] D.G. Sweeney, T. Pratt, C.W. Bostian, "Hysteresis effects in instantaneous frequency scaling of attenuation on 20 and 30 GHz satellite links", *Electronics Letters,* Jan. 1992, Vol. 28 No 1, pp 76-77.

[6.49] CCIR, Rec. 839, "Rain height model for prediction methods", *ITU-R recommendations, Propagation in non-ionized media, PN-series Volume*, ITU-R, 1994, pp 244.

[6.50] W. Klassen, "Attenuation and reflection of radiowaves by a melting layer of precipitation", *IEE Proc.,* Vol. 137, Pt. H, No 1, February 1990, pp 39-44.

[6.51] R.M. Manning, "A unified statistical rain-attenuation model for communication link fade model", *Int. J. of Satellite Communications*, Vol. 8, 1990, pp 11-30.

[6.52] E. Matricciani, "Rain attenuation predicted with a two-layer rain model", *Europ. Trans. on Telecommunications and related technologies*, Vol. 2, No 6, 1991, pp 715-727.

[6.53] C. Capsoni, F. Fedi, A. Paraboni, A. Pawlina, C. Magistroni, "Data and theory for a new model of the horizontal structure of rain cells for propagation applications", *Radio Science*, Vol. 22, No 3, May-June 1987, pp 395-404.

[6.54] Rec. ITU-R PN.618-3, "Aspects relative to space telecommunication systems", *ITU-R recommendations, Propagation in non-ionized media, PN-series Volume*, ITU-R, 1994, pp 329-343.

[6.55] J.W.F. Goddard, M. Thurai, "Radar-derived path reduction factor for terrestrial systems", *Proc. of the Int. Conf. on Ant. and Prop., ICAP'97, Edinburgh, UK,* IEE Publ. No 436, Vol. 2, 1997, pp 218-221.

7. Conclusions and further work

7.1 Predictive fade countermeasures

The performance of a satellite communication system operating at Ka (20/30 GHz) band can be seriously affected during poor propagation conditions. As these only occur on relatively rare occasions, it is inadequate to compensate for atmospheric effects on a permanent basis. The implementation of adaptive systems aimed at restoring/maintaining or maximising in real-time the grade of service during severe conditions are broadly known as fade countermeasure (FCM) systems.

Different techniques have been proposed in the literature and adaptive forward error control (AFEC) is just one particular FCM strategy. To be deployed efficiently, any countermeasure must be driven by a control system which is closely tailored to the statistical and dynamic characteristics of the Ka band fading process. In particular, it is important that the level of attenuation be not under-estimated unreasonably so that bit error rate (BER) performance can be maintained below a pre-set level, which depends on the service(s) to be supported by the communication

system. The practical limit of FCM systems is thus the inability to achieve a sufficiently high long-term BER availability. Within this limitation, a constraint imposed on the design of any FCM system is that it is desirable to maximise the user data throughput.

This implies that the FCM control system should over-estimate the actual fades in a statistically controlled manner, so that just more than appropriate FCM action can be taken. The over-estimation should be as small as possible to meet the desirable constraint of maximising the channel capacity utilisation. The performance of any FCM system is thus crucially conditioned by the accuracy of the detection scheme. It will depend on how the actual measurement is carried out, and, in particular, how measurement/prediction/estimation errors are compensated for in any practical system.

In this thesis, the focal point is the impact of the dynamics of the Ka band fading process on the design and performance of otherwise ideal FCM systems. Although this is important, no specific attention is placed on how the level of actual attenuation is being measured on any particular satellite link, or how the inherent measurement errors are being compensated for. It is therefore assumed that perfect detection is being performed. For most applications, this implies that a suitable FCM control protocol has been implemented between transmitter and receiver through the satellite transponder.

The emphasis is placed on the impact of time delays on FCM system performance and design, within the context of predictive fade countermeasures and in the presence of dynamic Ka band fading. The impact of the variability of the instantaneous frequency scaling factor (IFSF) of rain attenuation has also been analysed. A stochastic IFSF will infer on the accurate determination of up-link attenuation, based on ideally detected down-link attenuation.
These two problems, time delays and IFSF, share a same viewpoint. They refer to the ability of FCM control systems at integrating realistically the random and dynamic nature of the Ka band fading process. As such the analysis is system-based, although

it lies at the interface with the more fundamental physical and statistical modelling of the propagation medium.

7.2 Thesis overview

By definition, FCM schemes are adaptive control systems, which need to be matched closely to the characteristics of the global fading, to the type of services to be supported and the particular FCM scheme to be employed. The problem was therefore constrained very early to the analysis of a well-documented typical in-bound back-to-back VSAT link between the site of Chilton and the Olympus satellite. Based on geographical link diversity models, this particular configuration corresponds to a worst-case design analysis. Therefore it should yield somewhat conservative results.

Adaptive user rate transmission countermeasures, to which adaptive forward error control (AFEC) coding belong, were also chosen in this thesis. Due to their large built-in margin, such techniques were particularly suitable to low-rate low-power in-bound VSAT links.

At frequencies, like 20 or 30 GHz, rain attenuation and tropospheric amplitude scintillation are the major source of dynamic impairment. The global fading (GF) model, proposed originally by Filip and Vilar, considers the association or combination of these two propagation processes. Although recent radiowave propagation experiments have now permitted the verification and extension of current statistical propagation models, like the global fading model, little is still known on the dynamic impact of the fading process on overall Ka band system performance and design. This is crucial to the design engineer. To draw any long-term performance, the solution must be of statistical nature and it should account for the performance of realistic systems in the presence of realistic Ka band fading.

Any FCM control system must cater for the finite response time of practical FCM systems. As a consequence, fade countermeasures must be short-term predictive, so that the level of Ka band fading can be inferred in advance and

appropriate countermeasure action can be taken for most of the time. With a similar argument, the variability of the IFSF of rain attenuation needs to be considered since its inherent randomness will also result in channel sounding errors.

In this thesis, the development and characterisation of a predictive FCM controller is described. It is subsequently found that the instantaneous scaling of rain attenuation and tropospheric scintillation can be naturally included in the proposed predictive system. To be carried out efficiently, this integration requires consideration of the possible statistical/functional relationship between rain and scintillation processes, as well as the definition of novel stochastic models, quantifying the variability of the IFSF of rain attenuation and/or scintillation around their mean values.

7.2.1 Short-term prediction of the Ka band fading process

In order to analyse the impact of time delays on FCM operation and design, it is first necessary to associate a dynamic structure to the Ka band fading process. Since the approach of this project is essentially system-based, a discrete model based on the ARMA structure was chosen. This type of linear discrete stochastic model is ideally suited for computer-based FCM controllers. It comes from the field of so-called self-tuning systems. It also corresponds to an attempt to comply with the global fading hypothesis, which assumes that rain and scintillation are additive and statistically independent.

The applicability of self-tuning algorithms to real satellite situation is very attractive for efficient on-line control of FCM resources. Their main advantage is that they can naturally track the non-stationarity of the Ka band fading process. Such algorithms may be considered as 'universal'. They can be applied to any particular geographical satellite link whatever the particular FCM technique being used (Short-term prediction being necessary in most practical cases). Due to the good convergence properties of self-tuning systems, bearing in mind that the best ARMA structure (matched to the dynamics of the Ka band fading process) has been identified in Chapter 4, it can be assumed that the detector/predictor will capture

appropriately the fading dynamics irrespective of the geographical locations of transmitting and receiving stations.

The short-term predictability of the Ka band fading process has been investigated using time-series analysis tools applied to an empirical time-series. The minimum mean square error (MMSE) approach was used as an attempt to minimise in some statistical sense the error of an ARMA/Minimum Variance predictor. It was found that an ARMA (3,3) model is the most appropriate and that it can capture almost optimally the dynamics of the Ka band fading process.

An on-line predictive algorithm for model parameter estimation has also been implemented with the Recursive Extended Least Square (RELS) algorithm. The proposed self-tuning predictor is readily useable in real computer-based applications. Simulation results have been provided. The self-tuning predictor has also been compared to other schemes proposed in the literature and was found to give unbiased and smaller errors than its competitors.

The short-term predictor is capable of capturing well the slow component due to rain attenuation while the error is essentially consistent with a scaled tropospheric scintillation process. As the performance and design of communication systems must in general be based on long term performance, a statistical model whereby the performance of the predictive FCM system can be drawn, has been developed. In essence, the model of the global fading has been *modified* to include the imperfections of the self-tuning predictor in the presence of rain attenuation and tropospheric scintillation within the context of predictive FCM control operations. This extension of the GF model was performed via a moment analysis on the error made by the predictor.

The modified global fading model (MGF), derived at a frequency of 30 GHz, has then been generalised to other carrier frequencies using a heuristic discussion on the normalised power spectrum of the Ka band fading process. Although this is based on an approximation, the generalised MGF can reasonably be expected to be valid in most practical cases.

7.2.2 Performance of predictive fade countermeasures

Although most of the work presented in this thesis is applicable to any countermeasure strategy, the choice of adaptive coding technique can find direct application for VSAT in-bound networks relying on a FDM(A)-SCPC access to the satellite transponder resource. Other techniques, like adaptive bit rate or adaptive modulation, are also good contenders for such network configurations. These techniques, along with the ones based on re-route and shared resource strategies have been reviewed in Chapter 2.

Clearly, adaptive transmission techniques are applicable to the type of services which can tolerate an occasional reduction in effective user data during severe atmospheric conditions. The design objective is to achieve successful transmission of information between transmitter and receiver. Depending on the type of services (e.g. data or voice) to be supported, this has to be achieved being given a certain bit error rate (BER) inequality constraint, that is, a strict maximum BER threshold, which should only be exceeded for a certain time percentage over a long period. In this thesis only yearly statistics are considered but worst-month statistics may also be of interest to system designers. Therefore the objective is to achieve a maximum BER availability being given a certain BER threshold. If this availability is found to be too low, then the FCM system is inadequate and it would require for example a higher HPA power, a larger dish diameter or possibly the transmission rate over the satellite channel could be lowered. In parallel to this basic objective, it is also desirable to maximise the user data throughput to work as close as possible to channel capacity.

Due to the steepness of the Eb/No versus carrier-to-noise ratio curve, any under-estimation of the actual level of attenuation encountered on any satellite link will cause large variations of the real-time bit error rate, which may well exceed its specified maximum level. To avoid this, and therefore to maximise the BER availability of the adaptive system, the FCM controller has to give 'wrong' information to the countermeasure by assuming that the fade is worse than what it effectively is. This is achieved by adding a small detection margin on top of the total

detected level of atmospheric attenuation. The smaller that margin will be, the better will be the throughput of the adaptive transmission countermeasure.

This extra margin, which may be fixed or variable, will depend on the ability of the FCM controller at predicting and/or estimating the level of dynamic fading, bearing in mind, that FCM operations must be short-term predictive and should (if applicable) cater for the random nature of the scaling factor of the Ka band fading process.

7.2.2.1 Advantages and limitations of fade countermeasure systems over non-adaptive systems

As demonstrated in Chapter 5, the main advantage of FCM (i.e. adaptive) techniques over conventional fixed transmission systems is that they result in an increased user data throughput and reduced BER unavailability. In particular, an ideal AFEC system, based on punctured convolutional codes and BPSK, supporting code rates ranging from 1 (i.e. uncoded) down to 1/2, has a greater throughput than a fixed system with unity code rate, while it has a BER availability slightly greater than the one with the most robust fixed FEC system (i.e. with rate 1/2).

On the other hand, the adaptiveness of FCM systems is introduced at the detriment of a greater system complexity. For example, a suitable FCM control protocol must be provided so that accurate synchronisation between receiver and transmitter, through the satellite, can be achieved. This also implies that the FCM system will have a finite response time, which will depend on the particular control protocol. Therefore a suitable detection margin has to be introduced and is one of the central specification of practical FCM systems. If this margin is minimised, the degradations relative to the ideal AFEC case will remain small.

7.2.2.2 Fixed Detection Margin (FDM) approach

Once a particular predictor of the Ka band fading process, like the self-tuning predictor proposed in chapter 4, has been characterised statistically, it is important to try and compensate for its prediction error. More particularly, the FCM controller has to over-estimate the detected fades in a statistically controlled way. One simple way to achieve this, is simply to bias the error of the predictor by adding a constant offset to the detected level of fades. It is found in Chapter 5 that this fixed detection margin depends on the ability of the predictor to infer the likely changes in attenuation, the overall response time of the FCM system and the required detection outage probability. The latter is simply the desired probability that the FCM controller under-estimates the actual fades. The model in Chapter 5 showed qualitatively that higher fixed margins are needed for large time delays in the FCM system, and/or, smaller detection outage probabilities.

The performance of the fixed detection margin approach is then analysed in terms of the FCM utilisation factor. This factor essentially gives a qualitative measure of the over-utilisation of countermeasure resources of practical systems relative to the one that would be achieved by a delayless ideal system. The theoretical model of the utilisation factor, proposed in this thesis, has also been tested against simulated and empirical data obtained during the Sirio experiment. It was found to be in very good agreement.

The utilisation factor is useful to evaluate the performance of low excess margin predictive fade countermeasure systems. In particular, it can help to evaluate numerically the excess margin required for the design of practical low-fade margin satellite links. Although useful in its own right, to check upon the effectiveness of the fixed detection margin approach, the utilisation factor may therefore prove essential for dimensioning appropriately the shared common resource in adaptive TDMA or frequency diversity countermeasures. Such an analysis is however beyond the scope of this thesis* . The underlying idea would be that large FCM over-utilisation would

---

* *This would require considering joint link diversity statistics (which by assumption were discarded here) and also fade duration statistics*

limit the total number of stations that can access simultaneously the back-up resource.

A main result of this study is that truly low fixed fade margin systems are particularly inefficient because they result in large FCM over utilisation. This is rather surprising and therefore it is very important. Countermeasure systems should therefore be designed with fixed excess margins of at least 4 or 5 dB. In the case of the AFEC system Chilton-Olympus back-to-back link, the built-in excess margin at a BER threshold of 10^{-7} is 6.39 dB, which is substantially greater than the prescribed 4 or 5 dB. This explains why the test-case AFEC system has a good overall throughput performance with respect to the ideal delayless case. On the other hand, its good BER availability can mainly be attributed to the sufficiently large dish diameter (0.8 m) , HPA power (0.2W) and low maximum bit rate (up to 9600 bps).

Instead of adding the fixed detection margin (FDM) to the detected/predicted total attenuation, an alternative method consists in shifting to the left the positions of the code rate change (CRC) boundaries of the A-FEC system by an amount equal to the FDM. The CRC boundaries constitute the effective control rule from which the switching to a more or less robust level of FCM protection is actually performed. In a practical system, this would be implemented as a look-up table. This alternative approach was employed to estimate the BER availability/throughput performance of the FDM-AFEC test case system. In particular, it was found that longer time delays and/or lower detection outage probabilities result in a quantifiable and non-negligible degradation in availability/throughput performance. Therefore, the degradation caused by practical predictive FCM controller, in the presence of time delays, should be considered in system planning.

7.2.2.3 Variable detection margin approach

The variable detection margin approach (VDM) as a means of compensation for predictor imperfections has also been analysed. It is an attempt at exploiting the fact that the variance of the scintillation process is constant on a short-term basis. As the prediction error is merely a scaled scintillation process, the variance of the error will also be constant over short periods of time. The self-tuning predictor can predict well the slow rain attenuation component because it is based on a minimum mean square error criterion. In that sense, it can perform an almost optimal separation of rain and scintillation. This only requires the on-line estimation of the running block variance and mean of the a posteriori error made by the predictor.

Although it is different from the fixed detection margin approach, the analysis of the VDM approach requires almost the same type of procedure. The only great difference is in determining the overall FCM control effort which depends on a scaling parameter used to control the statistical accuracy i.e. the detection outage probability of the fade detector/predictor.

Like for the FDM approach, long time delays and low detection outage probabilities result in a large values of VDM. This has in turn a quantifiable non-negligible impact on the utilisation factor, the BER availability and throughput of the AFEC test-case system.

7.2.2.4 Comparison of fixed and variable detection margin

The VDM approach results in lower FCM control effort for approximately 85% (this is for a delay of 10 seconds) of the time when compared to its fixed counterpart. This figure is even higher for shorter time delays.

When expressed in terms of utilisation factor and channel capacity utilisation the VDM is found to be more economical than the FDM approach, in particular for countermeasure systems with short response times (below 5 seconds). The variable

detection margin is therefore better suited to low fade margin systems. Similar results were found by comparing the throughput/BER performance of fixed and variable detection margins.

7.2.3 Stochastic modelling of the instantaneous frequency scaling factor (IFSF) of rain attenuation

A new stochastic model of the IFSF of rain attenuation is proposed in Chapter 6. The novelty lies in that the model gives a measure of the spread of the IFSF. It considers the impact of the *slow* stochastic temporal variations in drop size distribution (DSD) on the mean and standard deviation of the IFSF. It is based on a Gaussian density function conditional on rain rate and it assumes that the temporal variation in rain activity lies between the Joss-Drizzle (J-D) and Joss-Thunderstorm (J-T) DSDs. Model calibration was performed from experimental results collected by other researchers during the Olympus propagation experiment.

The model has been validated against empirical data. It has also been compared to other empirical models of the equi-probability scaling factor. It was found to yield sensible results, although more work would be required to refine the model and make it more realistic. Clearly, a good model of the IFSF of rain attenuation can only be obtained if one has first a good model of rain attenuation itself. This prompts to a verification and/or comparison of current models proposed in the literature. In particular, the estimation of the attenuation on a slant path based on point rainfall intensity needs a critical re-assessment. Within this general problem, the modelling of the effective path length on satellite to earth link (or equivalently the path reduction factor) would definitely be useful. In this thesis, a published empirical model of the effective path length was used. This model assumes a monotically decreasing dependence on rain-rate but it is independent of carrier frequency. This is likely to be too unrealistic. A precise calculation of the specific attenuation for the J-T and J-D distributions with realistically distorted rain drops would also permit the inclusion of polarisation effects in the modelling process.

7.2.4 Design issues in generalised predictive fade detection systems

A great advantage of the VDM predictive fade detector, apart of its better performance over the FDM scheme, is that it allows a natural integration of IFSF. This is because, the self-tuning predictor performs a quasi-optimal separation of rain and scintillation effects and that an estimate of the scintillation standard deviation is also evaluated on-line. This fits well with current models of the IFSF of scintillation, which usually refer to the variance or standard deviation of the process rather than its amplitude itself.

The performance of FCM systems depends crucially on the ability to estimate and predict the total attenuation suffered on any satellite link. In the case where total attenuation is measured at a base frequency, typically 20 GHz, the fade controller must estimate the up-link fade via the use of instantaneous frequency scaling. In this thesis, only a stochastic model of the IFSF of rain attenuation has been considered, the scaling of the scintillation variance being assumed as deterministic and equal to the values predicted by the current ITU-R model for dry scintillation.

The design and modelling of such a system relies on the functional or statistical relationship between rain attenuation and tropospheric scintillation. The global fading hypothesis, used throughout in this thesis, assumes that both processes are statistically independent. There is experimental evidence that this is not the case. However, empirical results have also shown that this statistical dependence is *weak* and thus that it can be neglected in practical cases.

Current fundamental propagation research has identified two main processes which may explain the physical nature of the relationship between rain and scintillation rocesses. One mechanism, proposed by Matricciani, considers the increase in cloud turbulence during rain events. Otung asserts that rain-induced scintillation is produced by the fast variations in rain drop size distribution. These two explanations are entirely plausible and they are likely to co-exist in the real world. Clearly further empirical and theoretical studies are needed to quantify their relative contributions.

7.3 Original aspects of this research

In summary, the novel aspects of this research presented in this thesis are considered to be:

1. Identification, statistical characterisation and software implementation of an on-line short-term predictor matched to the spectral dynamics of the Ka band fading process.
2. Extension and generalisation of the global fading model by inclusion of the statistical impact of time delays due to the finite response time of a practical predictive countermeasure system in the presence of rain and scintillation processes.
3. Analysis and comparison of two fade detection schemes, namely the fixed and variable detection margin approaches, as means of controlling statistically the estimation error made by the proposed predictor. Analytical modelling of the FCM utilisation factor. Quantification of the impact of time delays on the throughput and bit error rate availability of a test-case AFEC system.
4. Introduction of a new model of the instantaneous frequency scaling of rain attenuation for inclusion in predictive controllers relying on base frequency detection strategies.

7.4 Further work

7.4.1 Fade countermeasure systems

This thesis further confirms that countermeasure systems are technologically viable. In particular, it was shown that a FCM technique, based on readily available punctured convolutional codes, with their relatively modest coding gain, is sufficient to provide high link availability and user data throughput on a low-power low-rate in-bound VSAT link.

This research has demonstrated that the consideration of more specific design problems does not change the overall validity of the above general statements. However the design and performance of practical countermeasure systems are conditioned greatly by the estimation errors made by practical FCM controllers.

These inaccuracies in determining signal strengths are of two natures:

- there is the basic measurement error made by any particular fade detector. This has not been studied here. Ways of quantifying and then compensating for these measurement errors should be considered in the design stages of *practical* Ka band systems;
- a second class of error is caused by the stochastic and dynamic nature of the Ka band fading process which makes it difficult to estimate or predict the likely variations of propagation effects. These are more general in nature and are common to all fade countermeasure systems, irrespective of the engineering choice made by the designer. In this thesis, the impact of time delays and frequency scaling have been considered within the context of predictive control of fade countermeasure resources.

The implementation of practical fade countermeasure systems also relies on the design of a suitable FCM control protocol so that appropriate FCM service information can be passed safely from transmitter to receiver through the satellite transponder. Due to its importance, this information should be heavily protected via coding and/or redundancy. This is to ensure initiation, maintenance, relinquishment and recovery of the flow of useful information even during heavy atmospheric impairment. Such an FCM control protocol will depend on the way fade detection is performed and on which particular countermeasures (on in-bound and out-bounds links) are employed. As such, it is system specific and it will also be conditioned by engineering constraints and choices.

A related but more fundamental issue is the integration of fade countermeasure within otherwise classical communication satellite systems. FCM systems must comply with general architectures like for example the OSI framework. A particular topic is the association or co-ordination of fade countermeasure with

Automatic Repeat reQuest (ARQ) strategies, so that data packets can be delivered safely and efficiently over the satellite channel at the data link layer.

Two basic approaches can so far be envisaged :

- the ARQ scheme and the fade countermeasure are operated independently, in which case the satellite channel and its associated FCM are seen as a Super Binary Symmetric Channel (SBSC) by the ARQ strategy. Such a design philosophy allows for predictive control of FCM resources as studied in this thesis and necessitates the on-line monitoring of channel conditions;
- a hybrid ARQ (HARQ) strategy is employed, in which case the changes in FCM protection (such as FEC code rate in an AFEC system) are solely conditioned by the repetition of faulty frames as detected by the ARQ subsystem. This solution can be very attractive and simple because it may not even need the real-time monitoring of the channel conditions, thereby postponing the use of predictive FCM control. Many different HARQ schemes have already been proposed in the relevant specialised literature. Most of them refer to adaptive system based on punctured convolutional codes. Further development would be needed for HARQ system based on adaptive modulation (APSK, AQAM). Being given a particular adaptive technique, like AFEC, it would be interesting to find out which HARQ is the best suited to the Ka band fading channel. Once identified, it can then be compared to the SBSC approach.

Such a comparison must be based on a theoretical analysis of the BER/throughput performance of each candidate schemes at a packet-by-packet level in the presence of Ka band fading.

The current trend indicates that high rate applications on in-bound VSAT links are also of practical interest. The adaptive coding technique based on punctured convolutional codes considered in this thesis is only applicable to low-power low-rate VSAT applications. The move to higher data rates on in-bound links implies the use of more powerful adaptive codecs. One possible solution is to recourse to concatenated codes with the inner code being an adaptive one based on punctured CV codes.

Current work on adaptive modulation as a FCM only refers to uncoded transmissions. Adaptive modulation is also a possible contender for such services although it has comparatively higher power requirements than AFEC systems. This can be remedied by the combination of adaptive modulation and coding techniques. This leads naturally to the field of adaptive treillis coded modulation (A-TCM) as a countermeasure. This may prove particularly powerful.

7.4.2 Theoretical modelling and simulation of FCM systems

The design of countermeasure system must rely on both theoretical and simulation results so that fundamental system parameters can be evaluated prior to the effective design of real Ka band systems.

In this thesis, the concept of global fading has been used and then extended to cater for the impact of time delays modelling on the design and performance of predictive Ka band satellite link suffering dynamic fading.

The global fading hypothesis considers the statistical impact of rain attenuation and tropospheric scintillation on a back-to-back satellite to Earth link. This avoids the need to include the modelling of site diversity between two different slant-paths.

This simplification is particularly attractive and it can be expected to yield conservative results, since it assumes that the attenuation on up- and down-link are perfectly correlated. Obviously this will not be the case in practical systems. Therefore, if a system operates satisfactorily on a back-to-back link, it should perform even better in the practical case.

A non back-to-back assumption would however add more realism. In particular it would allow:

- the design systems more tightly matched to their expected environment;
- the decoupling of up- and down-links. This would open the way, for example, to combined countermeasure systems based on ULPC/A-TDMA for out-bound links;

- the evaluation of the accurate dimensioning and performance of shared common resource systems by inclusion of geographical diversity in the modelling process.

The simulation of FCM systems is crucial to FCM design. The main objective is to develop a program that can give indicative results close to reality with the constraint of remaining not too computationally heavy. A bit-by-bit type of simulation (including satellite tranponder and up and down-links) seems quite unsuitable if one wishes to obtain long-term (e.g. one year) average results. It is required however to test the integrity of possible FCM control algorithms. They must be tested on a long-term basis in the presence of dynamic fading. This may be based on experimental or synthesised Ka band time-series. As indicated in this thesis, a significant problem with employing countermeasure techniques is the consequence of inaccuracies in determining signal strengths and commanding changes. A computer simulation program should therefore consider the practical inaccuracies introduced by the basic signal processing operations performed by practical FCM controllers and detectors as well as the limitations of practical fade detection schemes in the presence of dynamic Ka band fading.

7.4.3 Propagation research

The design of fade countermeasure systems requires a fundamental departure from the classical approach which was essentially based on link budget analysis and cumulative distribution functions and/or empirical (curve-fitted) models.

As indicated in this thesis, the modelling of FCM systems in the presence of Ka band fading relies upon the integration of the probability density functions and power spectrum densities of rain and scintillation. The underlying feature is the greater understanding on their functional, physical or statistical relationship. The central issue is the efficient separation of rain and wet scintillation.

In this thesis, it is asserted that the slow temporal variations in drop size distribution (DSD), caused by changes in rain activity and/or type, is the source of variable rain attenuation thereby affecting its scaling factor. Otung considers that the fast variations in DSD generates rain-induced scintillation. Turbulence-induced

scintillation may be quantified by a comparative analysis of scintillation and cloud coverage during rain and dry conditions.

The numerous and detailed work accumulated in the field of fade countermeasure prompts now to the effective design of real or laboratory-based Ka band systems in order to prove their technical feasibility. Fade countermeasures as a field of research are mature enough to enter this practical phase, thereby giving to engineers and scientists the chance to test their ideas and build the technical expertise necessary to exploit the soon profitable Ka band.

This research focused on the modelling of the impact of time delays and instantaneous frequency scaling on the design and performance of practical fade countermeasures. The theoretical analysis presented in this thesis could provide the basis for the development of practical FCM systems, which are driven by a predictive control algorithm closely matched to the dynamic and stochastic properties of the Ka band fading channel.

B.C Gremont, A.P. Gallois, S.D. Bate, "Self-tuning prediction of Ka band hydrometeor attenuation and applications to fade countermeasures", Proc. 3rd Int. Spymp. on communication theory and applications, pp 417-421, 1995. [*]

TK.P. Chung, B.C Gremont, A.P. Gallois, "Frequency scaling of rain attenuation: results from Olympus satellite", Proc. Int. Conf. On antennas and propagation, Eindhoven, The Netherlands, IEE, Vol. 2, pp 178-181, 1996. [*, #]

B.C Gremont, A.P. Gallois, S.D. Bate, "Efficient fade compensation for Ka band VSAT systems", Proc. 2nd Ka band utilization Conf. and workshop on SCGII, Florence, Italy, pp 439-443, 1996. [*,#]

B.C Gremont, A.P. Gallois, S.D. Bate, "Fade countermeasure development at Coventry University", presented at COST 255 meeting, Athens, Greece, Nov. 1996. [*]

B.C Gremont, A.P. Gallois, S.D. Bate" Predictive fade countermeasures for Ka band satellite systems", Proc. Int. Conf. On antennas and propagation, Edinburgh, Scotland, IEE, Vol. 2, pp 109-114, 1997. [*, #]

B.C Gremont, A.P. Gallois, S.D. Bate, "Predictive fade control for Ka band communications", Proc. 4th Int. Symp. on communication theory and applications, pp 417-421, 1995. [*]

B.C Gremont, A.P. Gallois, S.D. Bate, "Fade countermeasure development at Coventry University: final report to COST 255", presented at COST 255 meeting, Brussels, Belgium, Oct. 1997 [*, #]

N.B: # presented by the author, * written by the author

Self-Tuning Prediction of Ka band hydrometeor Attenuation and Application to Fade Countermeasures.

B.C. Gremont, A.P. Gallois, S.D. Bate

Coventry University, School of Engineering
Priory Street, Coventry, CV1 5FB, UK

ABSTRACT

The next operational frequency band allocated to communication satellite services is the Ka band. Although the shift up in the radio frequency window presents some undeniable advantages, such as the possibility to respond to the increasing demand in transfer and format of information, a major technical modification of satellite link architecture is required to meet such requirements. The proposed solution is called fade countermeasures (FCM) which have been the source of intensive research materialised for example in the COST 205 [1] or the Olympus propagation programmes [2].

INTRODUCTION

Operations of geostationary satellite systems at frequencies of 20 and 30 GHz or more requires the investigation of meteorological effects which were not of great concern for C or even Ku band systems, where generally a large fixed power margin was used to overcome them. At these high frequencies it is necessary to use so-called Fade CounterMeasures to compensate in real-time for the signal fades by maintaining the carrier-to-noise ratio within the discrimination capability of the receiver and achieve a given long-term availability of a satellite link.
All FCM techniques available today have however a main drawback. Although they are capable of providing the necessary extra power to compensate for the attenuation due mainly to rain and clouds, such low-fixed margin controlled systems require some kind of predicting scheme in order to at least switch on or off the FCM at the right instants and avoid unwanted outages resulting in short transmission blackouts at the receiving end.
The specification of a control system capable of driving existing FCM schemes are very much design specific and these issues are not treated in depth in this paper where focus is placed on the real-time compensation of hydrometeor attenuation and more particularly its short-term prediction. At the present moment, this work can only give partial results.

THE NEED FOR PREDICTION

As pointed out earlier by Willis [3] considerations of the response time of an overall FCM controlled link require the prediction of the attenuation with a lead time of the order of 10 seconds. This time allows for the round-trip delays between earth-station and a satellite, the decision-making algorithm, the FCM actuator response time etc.
In order to achieve a given long-term availability, depending mainly on the fixed power margin included in the FCM controlled link and the receiver quality ratio G/T, the FCM will have to be activated at precise instants to avoid unwanted outages.
There are two broad classes of FCM techniques [4]. Using control engineering terminology they could be divided as follows:
- 'Bang-bang' FCM schemes such as site diversity or frequency diversity. In such systems the FCM is applied in a on/off manner. These methods are very efficient however they seem to be intended primarily for up-link monitoring because they require the use of either two earth stations or two frequency bands.
- Adaptive FCM techniques (AFCM) such as adaptive modulation, Up-Link or Down-link Power Control (ULPC, DLPC) or adaptive coding schemes [5]. These techniques (except ULPC) although technically more involved are potential candidates for the monitoring of down-links.

These methods imply that the receiving earth-station needs to communicate in real-time to the satellite or transmitting earth-station the predicted required FCM extra power and its identity.
In both classes there is a common need to predict the instants at which the attenuation will effectively cross a link-budget design-specific power level. In the case of AFCM systems, the monitoring must also be entertained while the fade is occurring to determine what amount of FCM equivalent power is effectively required. However it can be noticed that even for diversity systems, this operation can possibly be carried out to determine in advance the FCM switch-off instants. In both configurations the above description is based on the assumption that it is feasible to have an absolute or independent measurement of the fade occurring on the link. This is feasible for up-link or down-link control using a beacon signal monitoring and instantaneous frequency scaling however this is not really satisfactory and some alternative ways can be found.

DYNAMIC CHARACTERISTICS OF ATTENUATION

The main problem in the prediction of fade is that the attenuation signal, on a short-term basis, is a non-stationary process [1] that is usually decomposed in two different components. One of high amplitude in the low-frequency region

is the attenuation due to rain and clouds, while scintillation is of low amplitude at high frequencies typically above 0.01 Hz as shown in Figure 1.
Although the separation of such effects is of physical reality **[6]** this appears to be a great problem when considering the possible implementation of an effective prediction scheme, due to the subjective choice of an appropriate cut-off frequency which may cause loss of information for rain fade prediction.
It has been usual to separate hydrometeor and scintillation using different linear digital filters based on the implicit assumption that both effects are orthogonal. This is unsatisfactory under rainy conditions because some correlation between amplitude of scintillation and slope of rain attenuation can be noticed as shown in Figure 2 (the slope was calculated as S=z(t)z(t-1) and a discrete low-pass moving average filter of order 10 was used). This tends to confirm that tends to confirm that prediction of hydrometeor attenuation cannot optimally be achieved without loss of information if one attempts to separate ran and scintillation due to their non-linear relationship.
In this paper, it was therefore decided to look for a suitable discrete linear stochastic model with no pre-processing. It will be shown later that such an approach is sufficient to derive a possible predictor of hydrometeor attenuation. However due to the slow sampling rate used in this study (1Hz), the fast scintillation which is uncorrelated with the hydrometeor component will be seen as a non-measurable quasi Gaussian noise and will be the source of prediction error.

DYNAMIC MODEL ESTIMATION AND PREDICTION OF ATTENUATION

The following model estimation is based on an experimental discrete time series measured by the Rutherford Appleton Laboratory (RAL) at their site at Chilton (UK) using the Olympus satellite at a sampling frequency of 1 Hz. From this data, 17 ran events at 30 GHz of different amplitudes and durations were selected for study and fitted into fixed observation windows of 4000 seconds for easy comparison and averaging of autocorrelation functions and power spectrum densities.
Parametric identification methods **[7]** were used to fit an ARIMA model to the Olympus time-series. This involved the identification of the fixed orders and coefficients of the general non-stationary AutoRegressive Integrated Moving Average difference equation of order (p,d,q) described in detail by Box and Jenkins **[8]**:

$$A(q^{-1}).w(t)=C(q^{-1}).e(t) \qquad \text{where } w(t)= \nabla^d z(t)$$

$$\Leftrightarrow w_t = -a_1 w(t-1) - a_2 w(t-2) - \ldots a_p w(t-p)+e(t)+ c_1 e(t-1)+\ldots +c_q e(t-q)$$

where
q^{-1} is the backward shift operator i.e. $q^{-1}.z(t)=z(t-1)$
$A(q^{-1})$ is the autoregressive monic polynomial (AR) of order p
$C(q^{-1})$ is the moving average monic polynomial or order r
$\nabla^d z(t)$ is the dth difference of z_t e.g. $\nabla^1 z(t) = z(t) - z(t-1)$
e(t) is a white noise component forming an independent identically distributed sequence having zero mean and a variance assumed fixed

This type of model is particularly well suited for series having non-stationary behaviour such as a non-fixed mean value which is the case for rain fades when observed on short-term time intervals. the model assumes that the dth difference of the hydrometeor attenuation is a stationary process and is perturbed by a stationary coloured noise that can be modelled by passing a white Gaussian sequence into a discrete linear filter having transfer function $C(q^{-1})$. It tries to model the scintillation component which is known to be almost normal **[9]**. The other filter $A(q^{-1})$ states that the hydrometeor component derivative w(t) which is a one-step ahead prediction is obtained as a finite weighted function of past values of w(t) over an horizon between t-p and t-1. This can easily be extended to a k-step ahead predictor.
This model is linear time-invariant which at first sight is not good enough to adapt to changes from dry to wet conditions and reversely. The approach is first to find a suitable model structure using off-line methods i.e. essentially to find the order (p,d,q) of the ARIMA model.
From this, on-line recursive methods will be applied to model parameters estimation (polynomial coefficients) giving a linear time-variant predictor trying to adapt to changing conditions on the satellite link.
Two different approaches were chosen to determine suitable estimates which were then assessed in terms of their prediction error performance which is the primary objective. A validity check of the predictors was applied by testing the whiteness of their residuals via autocorrelation method.
This methodology is intended to give a way to check if any averaging assumption can be made and whether a self-tuning FCM predictor can yield better results from either a strictly event-based analysis or for a more general approach.

The results of the off-line estimation showed that the whiteness of the residuals was generally for a model ARIMA (3,0,3) for the event-based analysis whilst the model derived from the autocorrelation of the 17 events was a model (1,0,0) corresponding to a Markov process.

Figures 1,3,4 show typical results for a batch estimation for the model ARIMA (3,0,3) with a parametric evaluation based on the extended least squares method. The estimated power spectrum densities derived from both the real signal and the model (driven by stationary white noise) show a good agreement. Some partial results on the prediction capabilities based on an identified model ARIMA (3,0,3) are shown in Figure 2. They also show good agreement which is function as expected of the prediction lead time which is here of 10 seconds. The prediction error being almost Gaussian can be characterised by its mean and variance.
It is worth noting that such a model driven by white noise will not yield a lognormal characteristic. This can be overcome by transforming the attenuation using a memoriless non-linear function which can transform the signal into on having a normal density **[10]**. This was also implemented but it did not yield any better performance in terms of prediction error. Therefore the simplest option of using a purely linear model was chosen for the present study.

SELF-TUNING PREDICTION OF HYDROMETEOR ATTENUATION

A basic representation of a self-tuning FCM predictor is shown in Figure 5. At the present stage, this type of filter is being under consideration at Coventry University. A preliminary feasibility study test shows that self-tuning prediction gives interesting performance in terms of prediction error and adaptability to the changing conditions on the link. The adaptation scheme used as based on the recursive estimation of the model parameters using the extended least squares (ELS) algorithm with a minimum variance cost function of the residuals **[11]**. Figure 6 is a typical plot of the instantaneous prediction error using the mentioned recursive estimation for a model structure ARIMA (3,0,3). Approximately the same value of prediction error variance was obtained showing that minimum variance self-tuning prediction yields as good results as for the optimal batch estimation.
The system as described in Figure 5 is a simplistic representation of a FCM link in which the actuator has an ideal linear characteristic at all frequencies and is simply modelled as a pure time delay of k samples. Further study is required to include in the control loop realistic dynamic features of FCM actuators.

CONCLUSION

Minimum variance self-tuning prediction is introduced as a means to minimise the short-term prediction error necessary for good adaptive FCM operations of controlled satellite links at Ka band frequencies. This was motivated by the variability of the hydrometeor attenuation and the correlation between scintillation and rain fades during events. It was noted that on-line methods yield similar prediction performance as off-line ones. As the adaptivity of the self-tuning filter can track changes in atmospheric conditions this represents a great advantage for having optimal linear prediction at all times. The only limitation of such an approach is the choice of a fixed linear ARIMA structure based on an event-based analysis narrowing the modelling scope. the residuals are almost uncorrelated and have an almost Gaussian probability density function for a model (3,0,3) and show good agreement in the frequency domain. It is believed that predictive control scheme can be devised for application to FCMs. The present synopsis gives only partial results of an on-going research at Coventry and more comprehensive and comparative results are expected for the time of the symposium.

REFERENCES

[1] " Project COST 255: Dynamic characteristics of rain attenuation", Alta Frequenza, Vol. LIV No 3, 1985
[2] " OPEX 2nd Workshop of the Olympus Propagation Experimenters Vol. 1", ESA WPP-083, Nov. 1994.
[3] " Fade countermeasures applied to transmissions at 20/30 GHz", M.J. Willis, Elect. & Comm. Eng. Jour., pp 88-96, April 1991.
[4] " Application of fade countermeasures applied to transmissions at 20/30 GHz, A.P. Gallois, this symposium.
[5] " Adaptive coding as a satellite channel fade countermeasure", S.D. Bate, this symposium.
[6] " Radiowave propagation for space communications systems", L.J. Ippolito, Proc. IEEE, Vol. 69 No 6, pp 697-727, June 1981.
[7] " System identification : theory for the user", L. Ljung, Prentice Hall, 1987.
[8] " Time-series analysis and forecasting : revised edition", G.E.P. Box & G.M. Jenkins, Holden-day, 1976.
[9] " Probability density function of amplitude scintillation", G. Ortgies, Elect. Letters, Vol. 21 No 4, pp 141-142, 1985.
[10] " Probability, Random variables and stochastic processes", A. Papoulis, Mc-Graw-Hill, 1991.
[11] " Self-tuning systems, Control and signal processing", P.E. Wellstead & M.B. Zarrop, Wiley, 1991.

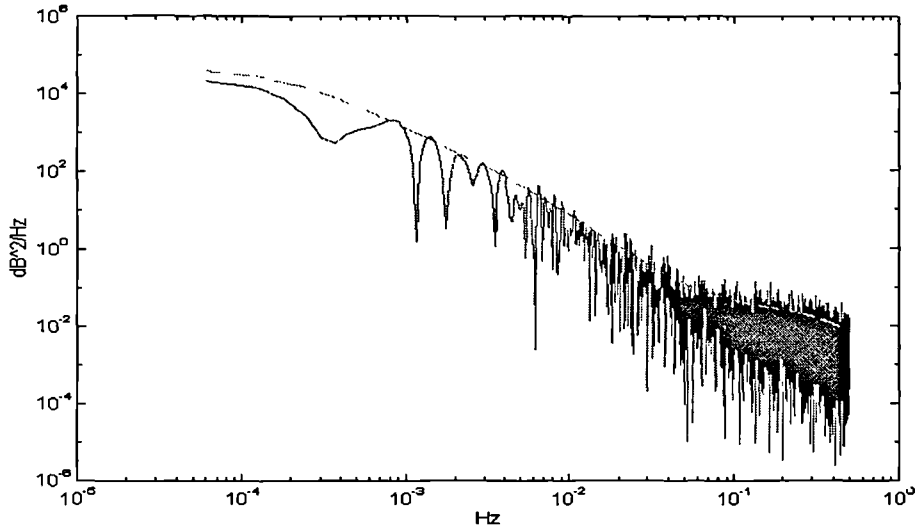

Fig. 1 *Power spectrum density of a rain event at 30 GHz.The dashed line is the theoretical PSD.*

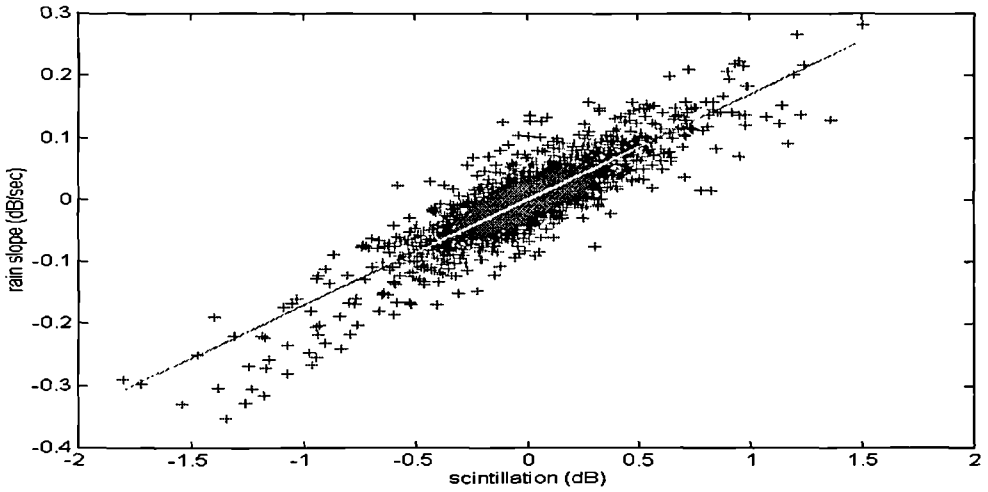

Fig. 2 *Correlation between rain slope and amplitude scintillations.Least squares fit:y=0.17*x*

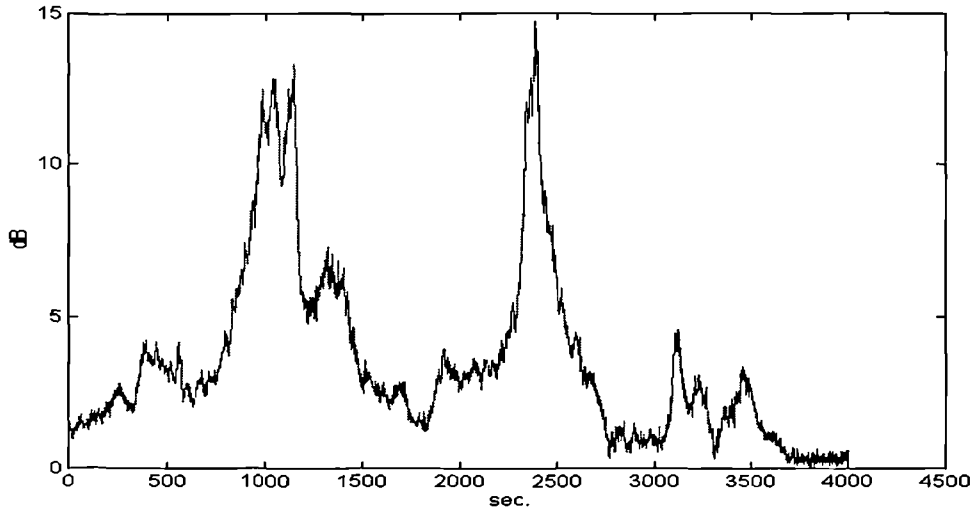

Fig. 3 *A typical rain event at 30 GHz with tropospheric scintillations obtained from the Olympus satellite.*

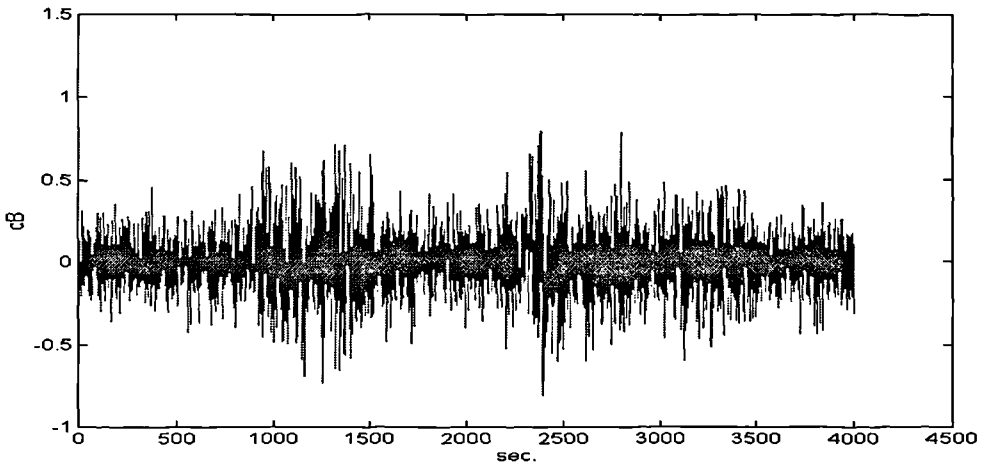

Fig. 4 *Instantaneous prediction error obtained from the model ARMA (3,3) with a lead time of 1 second. The error variance is 0.03 dB²*

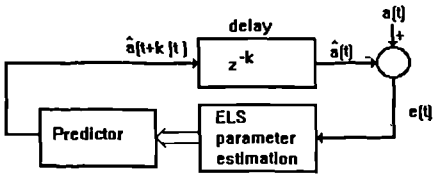

Fig. 5 *Self-tuning predictor*

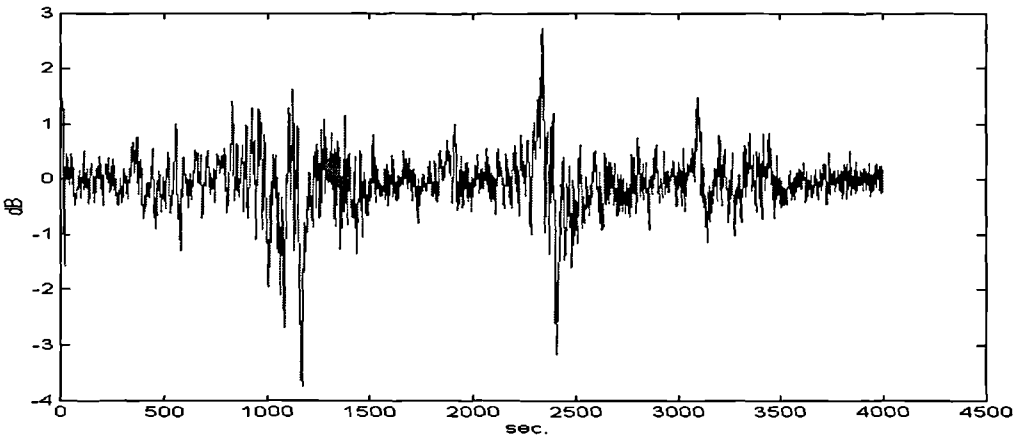

Fig. 6 *Instantaneous prediction obtained by the self-tuning controller with a lead time of 10 seconds. The predicted event is the one shown in Fig 3. The error variance is here 0.254 dB²*

FREQUENCY SCALING OF RAIN ATTENUATION: RESULTS FROM OLYMPUS SATELLITE

T K P Chung, A P Gallois, B C Gremont

Coventry University, United Kingdom

1. INTRODUCTION

Due to the increasing demand in capacity of satellite communication and the present congestion of both C and Ku bands, the use of the Ka band will become a fully operational reality in a very near future. To design an effective and reliable satellite system at such frequencies, it is essential to consider the statistics of different propagation aspects on both a long term and short term basis. This is particularly true for high frequency systems where water absorption is predominant and can not be counteracted permanently using a fixed power margin.

Although extensive measurements have been made in recent years for reliability and diversity, long term frequency scaling of attenuation allows extension of long term statistics measured at one frequency to a different frequency.

Fade Countermeasure (FCM) techniques are widely accepted as a solution to reduce the large fixed fade margins required for Ka band satellite systems. Up-link Power Control (ULPC) has been investigated as a means of FCM on the up-link signal by adaptively controlling the up-link transmitted power to compensate in real-time for rain attenuation [1]. It is ineffective to measure the up-link 30 GHz received signal on-board the satellite and then transmit the information simultaneously back to earth. The more practical approach is to monitor a 20 GHz down-link signal on the same slant-path and use instantaneous frequency scaling to evaluate the attenuation on the up-link [2].

In this paper, results of frequency scaling were deduced at Coventry University. These are based on Olympus data measured by the Rutherford Appleton Laboratory (RAL) at their site at Chilton (UK) [3]. These results are compared with the CCIR models and show a good agreement.

2. LONG TERM FREQUENCY SCALING

The CCIR recommends the following model to be used for single frequency scaling on the same slant path in a range between 8 to 80 GHz [4][5]:

$$\frac{A_1}{A_2} = \frac{g(f_1)}{g(f_2)} \tag{1}$$

where

$$g(f) = \frac{f^{1.72}}{1 + 3*10^{-7}*(f^{1.72})^2} \tag{2}$$

A_1 and A_2 being the hydrometeor attenuation dB at frequencies f_1 and f_2 in GHz respectively. This model does not consider microstructure or intensity profile of rain, which implies a constant ratio of the attenuation, whereas the actual ratio appears to vary with rainfall intensity.

This study of long term frequency scaling is based on data measured at Chilton and processed by the European Space Agency's DAPPER software. It spans a period of 11 months from September 1991 to July 1992.

Figures 1, 2 and 3 show the obtained plots B2/B1V, B2/B0 and B1V/B0 (B2=30 GHz, B1V=20 GHz vertical polarisation, B0=12.5 GHz) for the period between 9/91 and 7/92. From these graphs, nominal scaling factors were deduced using a linear regression giving the scaling factors shown in Table 1. It can be seen that they are in close agreement with the values obtained from the CCIR model.

Figures 4, 5 and 6 show the B2/B1V versus B1V, B2/B0 versus B0 and B1V/B0 versus B0 graphs. All of them high fluctuations of the ratios in the low attenuation regions. while the ratios seem to stabilise for higher values of attenuation, and tend toward the CCIR scaling factors. The fluctuations of attenuation ratio at very low attenuations are probably due to the domination of gaseous absorption. When considering the ratios for high attenuation, more stable values are obtained, se Figures 4, 5 and 6. These values give over-estimates compared with those of the CCIR model.

The corresponding percentage study gave the following ratios for the period September 1991 to July 1992 (Figure 7).

		0.01%	0.1%	1.0%
B2/B0		5.8	5.0	4.3
B2/B1V	1.9	1.6	1.4	
B1V/B0		3.0	2.9	3.0
B1V/B1H		1.0	1.0	1.0

All the scaling factors obtained in this study are generally larger than the CCIR models except for the B2/B1V data.

3. INSTANTANEOUS FREQUENCY SCALING

This study was based on data from September 1991 to May 1992. It was decided to examine only rain events larger than 8 dB at 20 GHz with vertical polarisation.

Figure 9 shows a typical scatter plot of the instantaneous attenuation for all channel combinations. The estimation of the slope allowed determination of the corresponding instantaneous scaling factors and are summarised in Table 2. The B2/B1 attenuation ratios appear to be relatively close to those of the CCIR model for long term scaling. The B2/B0 and B1/B0 attenuation ratios appear to be higher than those of the long term CCIR model.

It was also found that the instantaneous scaling factor was not constant during certain events (see Table 2) exhibiting hysteresis. This may be due to variations of the drop size distribution on the slant path [6].

For some other events the scatter plot showed a poor correlation between the different channels resulting in approximate estimate.

4. CONCLUSION

This paper gives the results obtained at Coventry University on long term and short term frequency scaling. These results are based on data measured by RAL at their site at Chilton (UK) and spans a period of 11 months and 8 months respectively.

It was found that the long term scaling factors show a close agreement with the factors derived from the CCIR model with an overall tendency to over estimate except for B2/B1V.

the instantaneous scaling factors for each pair of frequencies showed a high variability, indicating that the short term scaling factor is not constant. Also a hysteresis was noticed during certain events.

Acknowledgements

The authors would like to thank the Rutherford Appleton Laboratory (UK) for providing the propagation data and also the European Space Agency for all the information. Also the Radiocommunication agency of DTI and SERC for jointly funding the research. In the long term frequency scaling study, the attenuation statistics are the collaborative efforts of the Olympus Propagation Experimenters Group (OPEG) of UK.

References

[1] Hörle J, 1989, 'Up-link power control of earth statioms as a fade countermeasure of 20/30 GHz satellite communications experiment', Proc. Olympus Utilisation Conference, ESA SP-292, 109-115.

[2] Cacopardi S, Martinino F, Reali G, 'Power control techniques performance evaluation in the SCPC/DAMA access scheme', Proc. 3th European Conf. on Satellite Communications, IEE-381, p294-300, 1993.

[3] Norbury JR, Davies PG, 'Cooperationin Olympus propagation studies in the UK and status of the facility at the Rutherford Appleton Laboratory', Proc. The 13th Meeting of Olympus Propagation Experimenters, p99-104, 1990.

[4] CCIR, Recomendations and reports of the CCIR, 1986: Propagation in Non-ionized Media, Vol. 5, Rep.564.3, p389-431, 1986.

[5] CCIR, Recomendations and reports of the CCIR, 1986: Propagation in Non-ionized Media, Vol. 5, Rep.721-2, p199-214, 1986.

[6] Seeney DG, Pratt T, Bostian CW, 'Hysteresis effects in instantaneous frequency scaling of attenuation on 20 and 30 Ghz satellite links', Electronics Letters, Vol. 28, No 1, p76-78, 1992.

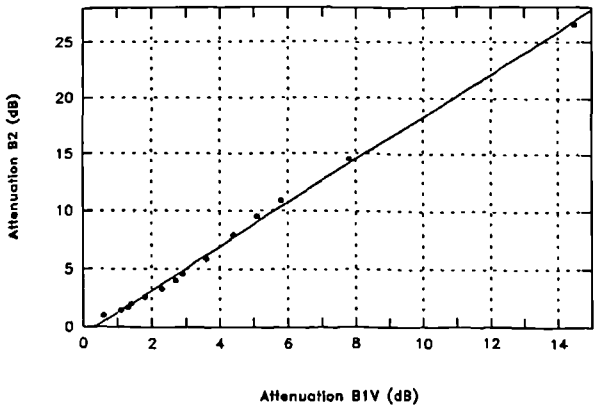

Figure 1: Attenuation of B2 against B1V (9/91-7/92)

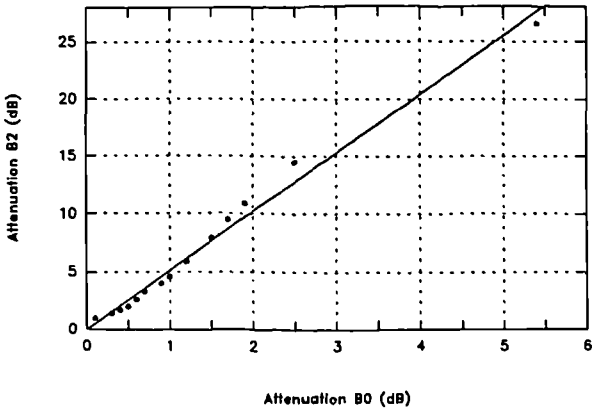

Figure 2: Attenuation of B2 against B0 (9/91-7/92)

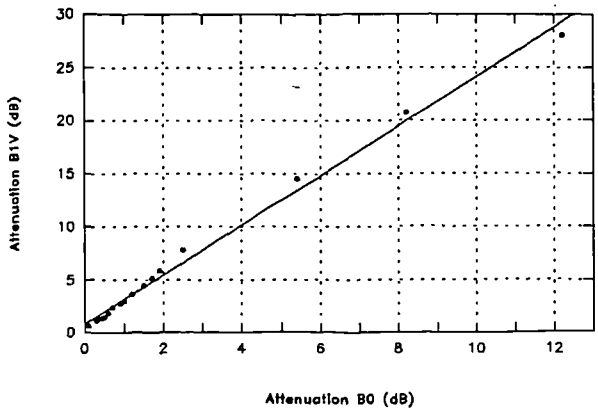

Figure 3: Attenuation of B1V against B0 (9/91-7/92)

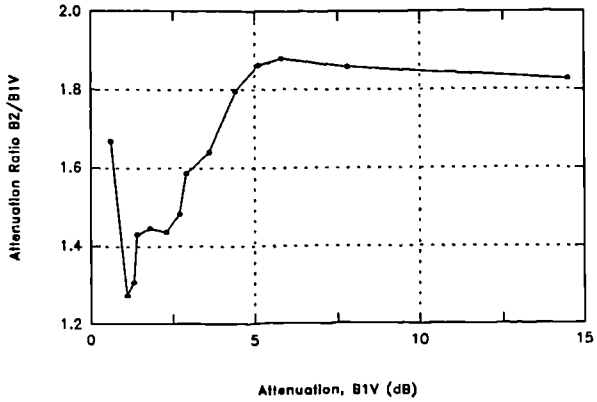

Figure 4: Attenuation Ratio of B2/B1V against B1V (9/91-7/92)

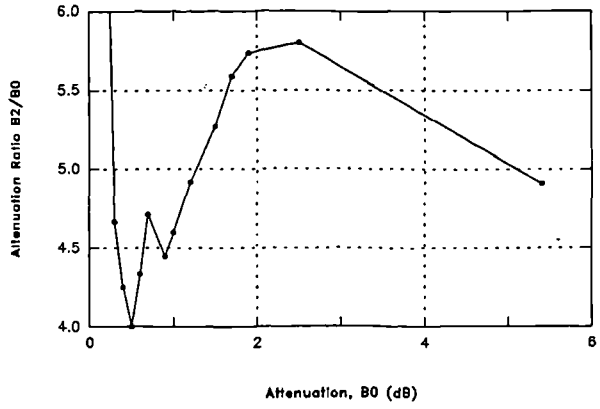

Figure 5: Attenuation Ratio of B2/B0 against B0 (9/91-7/92)

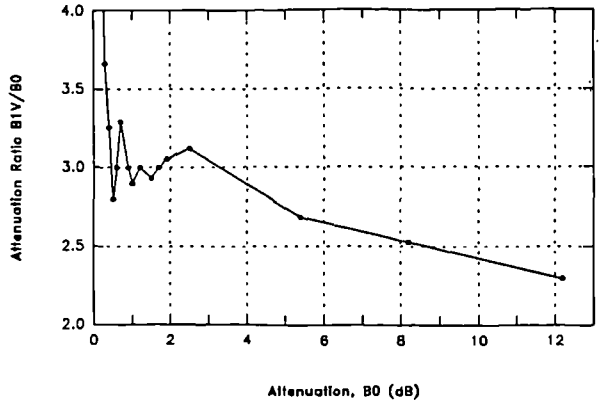

Figure 6: Attenuation Ratio of B1V/B0 against B0 (9/91-7/92)

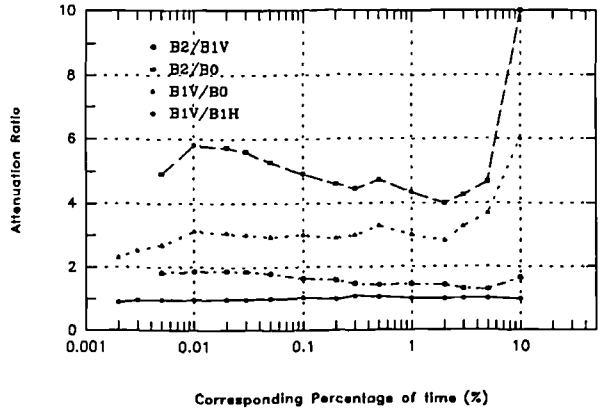

Figure 7: Attenuation Ratios against corresponding time (9/91-7/92)

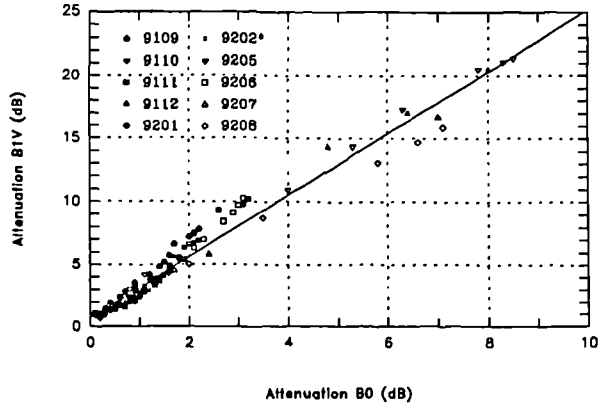

Figure 8: Monthly Attenuation of B1V against B0

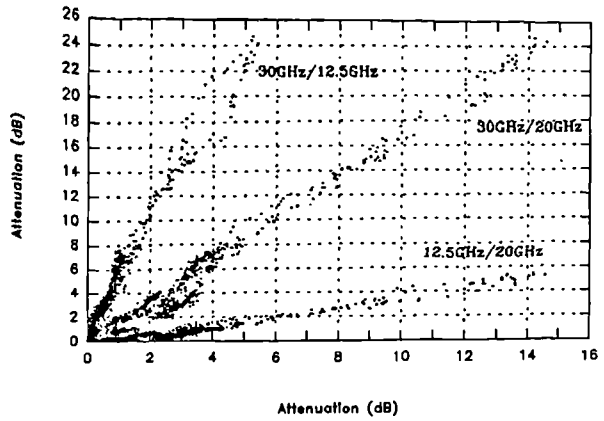

Figure 9: Scatter plot of Instantaneous attenuations (92050913)

Beacons		A_1/A_2		Maximum Deviation (dB)	
f_1	f_2	CCIR	Nominal	f_1	f_2
B2	B1V	1.96	1.9	1.0	0.2
B2	B0	4.28	5.2	1.6	0.4
B1V	B0	2.18	2.3	1.5	0.6
B1V	B1H	--	0.9	1.0	1.5

Table 1: Nominal scaling factors

Case (yymmddhh)	Median Instantaneous Attenuation Ratio		
	B2V / B1V	B1V / B0V	B2V / B0V
CCIR	1.96	2.18	4.28
91092816	2.0	3.0	6.0
91110300	1.7 *	1.6*	3.7 *
91110301	**	**	**
91111217	1.8	3.0	5.0
91121722	1.65 or 2.7 **	2.1	4.0 or 7.5 **
92050913	1.7	2.5	4.3
92050916	1.8*	2.8*	5.3*
92052413	1.9	2.5	4.5

* by approximation, not very conclusive
** unable to determine

Table 2: Median Instantaneous Attenuation Ratios

Efficient fade compensation for Ka band VSAT systems

B.C. Gremont, A.P. Gallois, S.D. Bate,
Communication Systems Group,
Coventry University, School of Engineering,
Priory street, Coventry, CV1 5FB, UK.
Tel:(+44) 1203 838848
Fax:(+44) 1203 838949

Abstract: The performance of a typical adaptive coding countermeasure applied to an in-bound VSAT link is evaluated. The objective is to provide a simple statistical model allowing the quantification of the impact of joint rain and scintillation processes in the presence of time delays within the context of predictive fade control operations. This involves the determination of the appropriate fixed detection margin and code rate change boundaries in response to detected fading. It is found that rain attenuation is quite predictable while scintillation is the major source of errors and thus cannot be neglected. The model is derived from an event-based analysis of the short-term predictability of the Ka band fading using time-series analysis tools.

I. INTRODUCTION

The Ka band is very attractive for supporting new services like VSAT networks, which can take full advantage of smaller antenna size and low interference levels. The major problem at frequencies above 10 GHz is the high level of dynamic fading, dominated by rain and tropospheric scintillation effects. Fade countermeasure (FCM) techniques were proposed as a way to counteract these adverse atmospheric effects more efficiently [1]. They should be opposed to the more classical fixed power margin approach, which is clearly unsuitable at Ka band for high link availability specifications. Instead, the FCM strategy is based on a 'compensation when required' strategy which leads to a better channel capacity utilisation [2]. FCM control refers to the real-time algorithm required to deploy the FCM technique appropriately based on detected channel conditions. A major issue is the inherent time delay encountered in satellite systems. A consequence is that FCM operations must be based on a short-term predictive scheme accounting for the effects of joint rain and scintillation processes during those time delays. This issue is addressed in this paper where the global fading model for rain and scintillation (see section II or [2]) is modified to include the limitations of a short-term predictor of the Ka band fading. This model is then used to evaluate quantitatively the impact of time delays on the choice of appropriate FCM control rule and system performance for a typical in-bound back-to-back link using an adaptive coding countermeasure. Although this is the object of current propagation research, it has been assumed here that rain and scintillation processes are statistically independent and additive [3]. This, with the assumption of a back-to-back link configuration, yields a well-tractable model from which a worst-case design analysis can be drawn without the need to include geographical link diversity.

II. IMPACT OF PROPAGATION EFFECTS ON SATELLITE COMMUNICATIONS

A typical link budget analysis of a low power VSAT system has been evaluated for a back-to-back link system between Chilton (UK) and the Olympus satellite. The main parameters are: an elevation angle of 28.6°, ITU-R rain-zone F, a slant path distance of 38792 km. Up and down link frequencies are 19.1 and 28.1 GHz respectively. For a VSAT station with P_{hpa}=0.2W and dish diameter D=0.8m, the overall clear-sky carrier-to-noise ratio is $C/No|_{t,0}$=58.28 dBHz corresponding to $C/No|_{d,0}$=68.47 dBHz and $C/No|_{u,0}$=58.72 dBHz.

The equivalent impact of up and down link rain attenuation, y in dB, (i.e. the total drop in overall CNR $C/No|_t$ caused by rain) has been evaluated from the ITU-R model assuming the back-to-back link hypothesis. The equivalent rain fade was found to be lognormal with two-parameter pdf given by:

$$\Lambda_y(m,\sigma) = f_y(y) = \frac{1}{y\sigma\cdot\sqrt{2\pi}}\cdot\exp\left[-\frac{(\ln y - m)^2}{2\sigma^2}\right],\ y>0$$

$$f_y(y) = 0\ ,\ \text{elsewhere} \qquad (1)$$

with m=-2.5583 and σ=1.5751(obtained by curve fitting). This is depicted in Figure 1 showing also that the link is rather up-link limited.

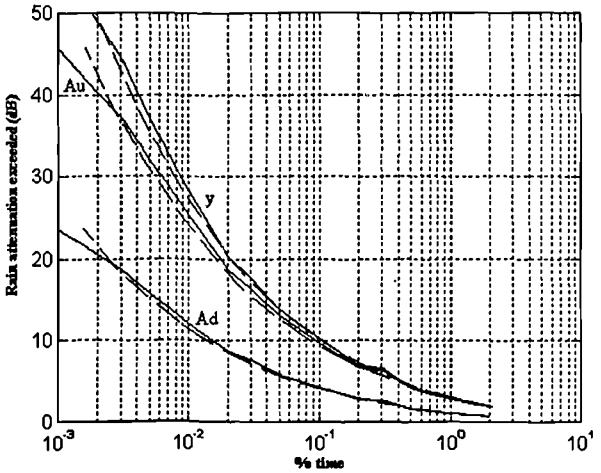

Fig. 1 *Up/down-link and equivalent rain fading for a Ka band Chilton/Olympus link (dashed lines are fitted lognormal model).*

Similarly, the long term statistical impact of scintillation on $C/No|_t$ can be estimated using the two-parameter Mousley-Vilar (hereafter denoted by MV) model [4] defined by:

$$MV_\chi(\sigma_m,\sigma_\sigma) \equiv f_{\chi_{dB}}(\chi_{dB})$$

$$= \frac{1}{\sigma_{\sigma_{np}}\cdot\pi}\cdot\int_0^\infty \frac{1}{\sigma^2_{\chi_{dB}}}\cdot\exp\left[-\frac{\chi^2_{dB}}{2\sigma^2_{\chi_{dB}}} - \frac{\ln\left(\sigma^2_{\chi_{dB}}/\sigma^2_{m_{dB}}\right)}{2\cdot\sigma^2_{\sigma_{np}}}\right]\cdot d\sigma_{\chi_{dB}} \qquad (2)$$

where χ denotes the equivalent scintillation random variable (in dB) and results in fades and enhancements of the overall CNR, C/No|$_t$. The parameters σ_m (dB) and σ_σ (np), are frequency and elevation dependent and are obtained from empirical formulas given in [2]. For the Chilton/Olympus link we have $\sigma_\sigma = 0.64588$ (np) and $\sigma_m = 0.2764$ (dB).

Assuming statistical independence and that rain and scintillation are additive then the global fading process $z = y-\chi$ (dB) has pdf given by [2]:

$$GF_z(m,\sigma,\sigma_\sigma,\sigma_m) \equiv f_z(z) = \Lambda_y(m,\sigma) * MV_\chi(\sigma_m,\sigma_\sigma) \qquad (3)$$

where * denotes the convolution operator.

III. PREDICTIVE FADE CONTROL

In order to consider the possible impact of time delays on FCM systems in the presence of global fading, a short-term predictor of the Ka band fading is required. Its prediction ability will depend on how this model can capture the essential dynamics of joint hydrometeor and scintillation processes.

The following parametric model identification is based on an experimental discrete beacon time series. It was measured by the Rutherford Appleton Laboratory (RAL) at their site at Chilton (UK) during the ESA's Olympus experiment. The sampling frequency was 1 Hz. From this data, 17 rain events at 30 GHz of different amplitude and duration were selected for preliminary study. They were fitted into fixed observation windows of 4000 seconds, for easy comparison and averaging of autocorrelation functions and power spectral densities (PSD).

The objective was to derive the best discrete linear model of the ARMA* (na,nc) class [5] defined by:

$$z(t) = -\sum_{n=1}^{na} a_n \cdot z(t-n) + e(t) + \sum_{n=1}^{nc} c_n \cdot e(t-n) \qquad (4)$$

where z and e are the global fading variable (dB) and the residual sequence (dB) respectively. The optimum orders na and nc of the ARMA model were determined using the AIC (Akaike's) criterion coupled with a Gauss-Newton algorithm for iterative MMSE estimation of the corresponding parameters a_n and c_n [5]. All the possible combinations (na,nc) for na and nc = 0 to 5 were evaluated. This represents 35 models per event. The best model was then identified by studying the average results for the selected events. Model validation was performed by testing the whiteness of the residual sequences {e} of the candidate models with autocorrelation methods. Upon application of this procedure, it was found that the raw beacon time-series is best approximated by a model ARMA(3,3) whose theoretical PSD has the form [5]:

$$S_{zz}\left(e^{i\omega}\right) = \frac{\sigma_e^2}{2\pi}\left|\left(1+\sum_{n=1}^{nc=3} c_n.e^{-n\,i\,\omega}\right)\Big/\left(1+\sum_{n=1}^{na=3} a_n.e^{-n\,i\,\omega}\right)\right|^2 \qquad (5)$$

where σ_e^2 is the variance of the residuals. A typical PSD fitted to one 30 GHz event is shown in Figure 2 showing the appropriateness of the ARMA(3,3) model in the spectral domain.

* Auto Regressive Moving Average

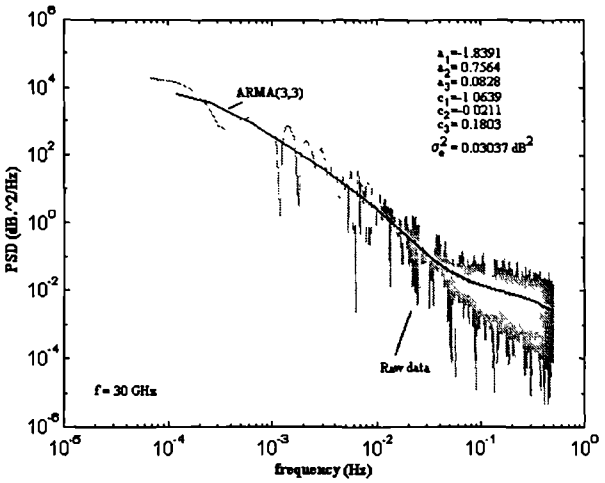

Fig. 2. *Experimental and modelled PSD for one event at 30 GHz.*

The ARMA(3,3) model in (4) is already predictive, with the global fading process inferred from three previous samples of z. Similar results are quoted in [6]. This can easily be extended to a k-step ahead predictor by using the minimum variance approach (see Appendix I) based on the minimisation of the predicted error variance given samples up to time t. For k=1, the ARMA model simply gives a MMSE estimate of z denoted $\hat{z}$. A close inspection of the data revealed that the residuals {e} conformed to a MV pdf i.e. (see Figure 3 for k=1) the error is $e(t+1|t) \approx \chi(t)$**. Full statistical characterisation of {e} has therefore been performed via a moment analysis described below where the sample second and fourth moments $m_2(k)$ and $m_4(k)$ were studied as a function of the lead time. For k=1 (no prediction), we can already state that $m_2(1) \approx m_2$ and $m_4(1) \approx m_4$, i.e., they are the long term MV parameters corresponding to (σ_σ,σ_m) in (2). Although they may be related to the spectral characteristic of the Ka band fading (Appendix I), the average sample second and fourth moments were computed for the 17 Ka band events as a function of the prediction time k. Least square fitting yielded:

$$m2(k)=m_2.(0.0337+0.487k+0.5251k^2) \qquad (6a)$$

$$m4(k)=m_4.(0.046+0.368k+0.319k^2+0.3499k^3-0.0312k^4 +0.0022k^5) \qquad (6b)$$

The increase in moments (bracketed term) may be assumed as invariant at one particular frequency (see Appendix II). The sample pdf of the error signal e(t+k|t) can now be evaluated for different k. The theoretical pdf shown by dashed lines in Figure 3 was obtained by computing (see equation (2)):

$$f_e(e) = MV_e(\sigma_m(k),\sigma_\sigma(k)) \qquad (7)$$

where the two parameters of this pdf have been evaluated from the second and fourth moments of the theoretical MV model given by [4]:

$$\sigma_\sigma^2(k) = \ln\left(\frac{m_4(k)}{3.[m_2(k)]^2}\right) \ (np) \qquad (8a)$$

** In fact, the residuals correspond to that part of scintillation which is white and unpredictable but make most of the scintillation variance (see [6]).

$$\sigma_m^2(k) = \sqrt{3}[m_2(k)]^2 / \sqrt{m_4(k)} \quad \text{(dB)} \qquad \textbf{(8b)}$$

The sample pdf of {e} has been computed for all selected events at 30 GHz and is shown in Figure 3 along with the model (6)-(8). The model is particularly good for scintillation amplitude below 0.3 dB. For k=1, the statistical model reduces to the MV model while when the model attempts to predict (k>1), the error pdf kurtosis diminishes with increasing lead times according to (8a).

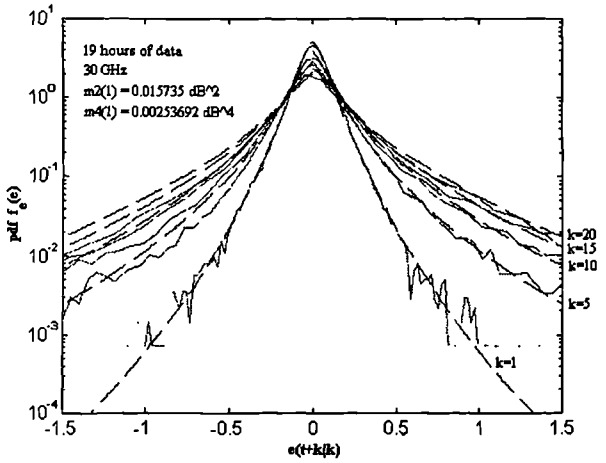

Fig. 3. *Modelled and measured pdf of the prediction error for different prediction times.*

This shows the greater spread of errors around the zero mean, proving that the predictor is unbiased. The ARMA(3,3) based predictor seems therefore capable of predicting the dynamics of the hydrometeor process, i.e. $\hat{z} \approx y$, while its error corresponds to that unpredictable part of the scintillation process. The ARMA predictor may therefore be assumed as quasi-optimal since its error has been reduced to a white process. Further improvement *may* be achieved, by considering possible functional relationships between rain and scintillation processes.

Outage Probability

The objective of FCM control is to compensate in the RF domain on a dB-dB basis for the detected fades. As the ARMA based predictor is unbiased, there will be under-estimation of the real fade for 50% of the time (outages). To avoid this, a fixed detection margin (FDM), α (dB), is usually introduced so that the FCM deployed equivalent power, FCM (dBW),becomes $FCM = \hat{z} + \alpha \approx y + \alpha$. Outage will therefore occur whenever $FCM \le y - e$ which yields the RF outage probability:

$$P_{out}(\alpha,k) = \text{Prob}(e \ge \alpha) = \int_{\alpha}^{\infty} MV_e(\sigma_m(k), \sigma_\sigma(k))de \qquad \textbf{(11)}$$

This function has been computed and is shown in Figure 4 for a typical Ka band link. If plotted on a linear scale, one

would obtain similar looking results to those obtained in [6] via simulation procedure at frequencies of 11.6 GHz. The main difference is our larger margin requirements due to the higher frequency (30 GHz). Multiplying $P_{out}(\alpha,)$ by $365.25 \times 24 \times 3600$ will give the average number of outages in a normal year, and $A\% = 100 \times (1 - P_{out}(\alpha))$ would be the estimated long-term back-to-back link availability.

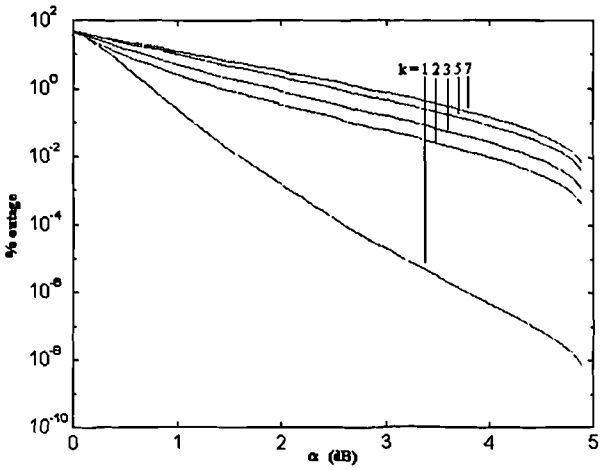

Fig. 4. *Percentage of outage, 100* $P_{out}(\alpha)$ as a function of the fixed detection margin, α, for different time delays.*

IV. Performance of an Adaptive-FEC (AFEC) Countermeasure

An important issue for the design of adaptive code rate systems is the determination of the Code Rate Change (CRC) boundaries [7], so that the FCM satisfies a specified availability with the constraint of a maximum bit error rate (BER) denoted $\hat{\beta}$. The CRC boundaries to a more or less robust level of FCM protection must be based on the estimated required FCM control effort $FCM = \hat{z} + \alpha \approx y + \alpha$. It can easily be shown that this yields the condition:

$$\hat{z} \approx y = \left.\frac{C}{N_0}\right|_{t,0} - 10\log_{10}\left(\frac{R_b}{\rho}\right) - \left.\frac{E_b}{N_0}\right|_{rq@\hat{\beta},\rho} - \alpha - \mu_i \quad \text{(dB)} \qquad \textbf{(12)}$$

where the third term is the minimum E_b/N_0 required to achieve a maximum BER of $\hat{\beta}$, for a particular FEC with code rate, ρ and a particular modulation scheme (BPSK). The adaptive FEC countermeasure must be deployed so that the symbol rate R_b/ρ=constant [1]. In the Chilton/Olympus case a fixed bandwidth BW=9.6kHz has been assumed. the margin for implementation μ_i was set to 0.75 dB and α is the margin due to imperfect FCM detection/prediction. It depends on the time delay and the chosen RF availability and can be determined from Figure 4. The CRC boundaries for an adaptive FEC system based on a (N-1)/N punctured convolutional code with ρ=1/2,v=6 mother code and Viterbi decoding have been evaluated using (12). The thresholds are tabulated in Table 1 for different time delays (k in sec.). For example, with k=1, RF availability of A%=99.9%, we have ρ=7/8 if $y \le 9.19$ dB,.... ρ=1/2, if $10.74 < y \le 11.10$ dB, y being the predicted rain attenuation.

code rate r	$E_b/N_0\|_{rq}$	delay (k) 1	5	10
7/8	7.32	9.19	7.50	6.80
5/6	6.94	9.58	7.88	7.18
3/4	6.38	10.14	8.44	7.74
2/3	5.78	10.74	9.04	8.34
1/2	5.42	11.10	9.40	8.70
v=6	$\hat{\beta}=10^{-7}$	CRC thresholds (P_{out}=0.1%)		

Table 1. example of CRC boundaries for an adaptive FEC system on the Chilton/Olympus link using punctured CV codes and BPSK.

BER availability and average throughput

The BER availability may be defined as the percentage of time that $\hat{\beta}$ is exceeded when the most robust code rate is used. Based on the knowledge of the CRC boundaries the BER outage probability is simply:

$$P_{out,\hat{\beta}} = \text{Prob}(y \geq \lambda) = \int_{\lambda}^{\infty} \Lambda_y(m,\sigma)dy \qquad (13)$$

where λ is the CRC level for which $\hat{\beta}$ is exceeded with the most robust transmission scheme (ρ=1/2 here) and is found at the bottom line of Table 1. Given the CRC thresholds, it is also quite straight forward to estimate the average throughput, $\overline{R}$, of the AFEC system. Assuming that the codec stays at rate 1/2 when it is in outage, the throughput is given by:

$$\overline{R} = BW \cdot \int_{0}^{\infty} \rho(y)\Lambda_y(m,\sigma)dy \quad b/s \qquad (14)$$

Equations (13) and (14) have been computed for different availabilities (A%) and time delays for BER constraints ranging from 10^{-8} to 10^{-3}.

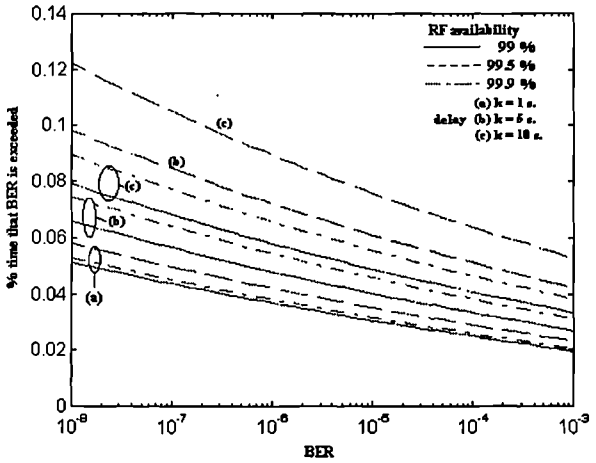

Fig. 5. BER unavailability of the AFEC system for different RF availability and time delays.

As can be seen in Figures 5 and 6, the estimated performance of the test case AFEC system, expressed in terms of BER availability and average throughput, is quite reasonable. This is primarily due to the fact that the VSAT station HPA power and dish diameter are sufficiently large. Decreasing any of those two parameters would degrade both BER and average throughput. The degradations brought by time delays albeit small are not negligible. For example, for an RF availability of A%= 99.9%, $\hat{\beta}=10^{-8}$, the BER availability (dashed lines labelled (a) and (c)) is reduced by 0.1223-0.0582= 0.0641% (i.e. 337 min. in a year) while the average throughput drops by 8398.6-8395.3=3.3 bps (i.e. 104×10^6 less bits in an average year). This emphasises that catering for scintillation effects with a fixed detection margin matched to the expected delay in the system has an impact on long term performance and it should be considered in system planning.

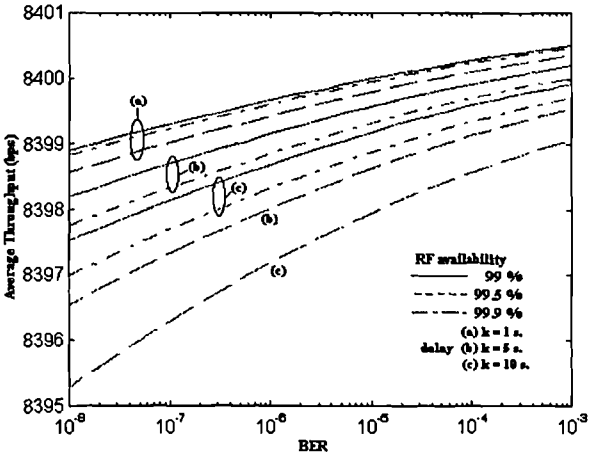

Fig. 6 Average throughput for different RF availabilities and different time delays.

V. CONCLUSION

A model allowing the evaluation of an adaptive coding countermeasure in the presence of Ka band fading and time delays has been presented. The discrete model is ideally suited for computer-based predictive FCM control system provided a recursive estimation of the ARMA model parameters is developed (typically recursive extended least squares or Kalman filter).

The back-to-back link hypothesis allows a tractable worst-case statistical analysis to be performed without including the site diversity problem. It is based on the concept of global fading for joint rain attenuation and tropospheric scintillation and has been extended to include the limitations of a predictive FCM controller. In this paper, a fixed detection margin was considered.

While rain attenuation seems fairly predictable, the error of a minimum variance predictor of the Ka band fading was found to be consistent with scintillation. The impact of time delays was thus characterised in terms of the moments of the Mousley-Vilar model, found to agree with our experimental data. This was then used to determine the required detection margin in the RF domain so as to ensure a specified RF availability. For adaptive transmission schemes, the impact of time delays was found to affect the positions of the CRC boundaries, resulting in a quantifiable decrease in average throughput and BER availability when time delays are increased. The calculated results show, however, that an adaptive convolutional coding technique is quite suitable for a low power in-bound VSAT application provided that HPA power and dish diameter of the VSAT station are large enough.

APPENDIX 1

The ARMA model defined by (2) can be rewritten in polynomial form using the delay operator q^{-1}. $y(t) = y(t-1)$. This yields two polynomials, $C(q^{-1})$ and $A(q^{-1})$, of order (na,nc)=(3,3). This is written:

$z(t)=C(q^{-1})/A(q^{-1}).e(t) \Rightarrow z(t+k)=C(q^{-1})/A(q^{-1}).e(t+k)$ **(A1)**

k being the prediction interval ($k \geq 1$) where the implication is true if z is ergodic.

Aström ([8]) introduced two polynomials $F(q^{-1})$ and $G(q^{-1})$ such as to satisfy the Diophantine equation:

$$C(q^{-1}) = A(q^{-1})F(q^{-1}) + q^{-k}G(q^{-1}) \quad \textbf{(A2)}$$

where F and G and are polynomials of order (k-1) and max(na-1,nc-1) respectively. Feeding (A2) into (A1) yields:

$$z(t+k) = F(q^{-1})e(t+k) + G(q^{-1})/C(q^{-1})y(t) \quad \textbf{(A3)}$$

In order to find the MMSE estimate, we wish to minimise

$$V_k = E\{ (z(t+k) - \hat{z})^2 \} \quad \textbf{(A4)}$$

where $\hat{z}$ denotes the best estimate of z at time (t+k) given data up to and including t. Feeding (A3) in (A4) gives:

$$V_k = E\{F^2(q^{-1})e^2(t+k)\} + E\{(\hat{z} - G(q^{-1})/C(q^{-1})y(t))^2\} \quad \textbf{(A5)}$$

This is minimised by letting the MMSE predicted value be $\hat{z} = G(q^{-1})/C(q^{-1})z(t)$ and provided that the sequence $\{e(t)\}$ (with variance σ_e^2) is uncorrelated the predicted error variance can be shown to be:

$$V_k = \left(1 + \sum_{i=1}^{k-1} f_i^2 \right)^2 \sigma_e^2 \quad \textbf{(A6)}$$

The solution of the MMSE prediction problem involves solving the Diophantine equation (A2) for $F(q^{-1})$ and $G(q^{-1})$ given $A(q^{-1})$ and $C(q^{-1})$. In its original work, Aström derived a set of general recursive equations for doing so. Aström's solution applied to the ARMA(3,3) model are:

$$V_1 = \sigma_e^2 \text{ and} \quad \textbf{(A7)}$$

$f_1 = c_1 - a_1$ $\qquad$ $f_3 = c_3 - a_1 f_2 - a_2 f_1$

$f_2 = c_2 - a_1 f_1 - a_2$ $\qquad$ $f_i = - a_1 f_{i-1} - a_2 f_{i-2} - a_3 f_{i-3}$, $i > 3$

Similar relationships can be found in [8] for determining $G(q^{-1})$.

APPENDIX II

An important work on the power spectrum density (PSD) of rain was published in [9]. The authors showed that the normalised PSD of the rain process can be assumed on a long term basis as invariant in shape on a loglog scale, but it is merely shifted up or down depending on the intensity of rain activity. A major difference with [9] is that the ARMA model also captures part of the scintillation process as displayed in Figure 2 for frequencies above 4×10^{-2} Hz. It was found however that the experimental normalised spectrum of the Ka band fading (i.e. rain+scintillation) also displays this invariance in shape (Figure 7) even on a short term basis. Translated to this paper, this means that the normalised PSD of the ARMA model in (5) also displays this feature i.e. $h_{zz}(e^{iw}) = S_{zz}(e^{iw}) / S_{zz}(e^{i0})$ is also invariant.

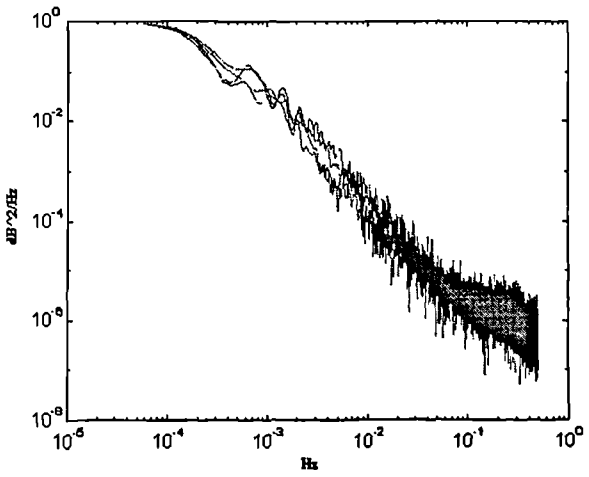

Fig. 7 *Monthly Average normalised spectra for a small selection of rain events at 30 GHz during 4 different months (91/09,91/10,91/11,91/12).*

It can easily be seen from (5) that the normalised spectrum is only a function of $\omega = 2\pi f$ and the 6 parameters a_i, c_i , i=1,2,3 and consequently the normalised increase in error variance (the bracketed term in (A6)) is also invariant at one frequency (here 30 GHz).

REFERENCES

[1] M.J. Willis, "Fade Countermeasures applied to transmissions at 20/30 GHz", *Electronics and Communications Journal*, April 1989, pp. 88-96.

[2] M. Filip, E. Vilar, "Optimum utilization of the channel capacity of a satellite link in the presence of amplitude scintillations and rain attenuation", *IEEE Trans. Commun.*, Vol. COM-38, no. 11, November 1990, pp. 1958-1965.

[3] E.T. Salonen, J.K. Tervonen, W.J. Vogel, "Scintillation Effects on total fade distributions for Earth-Satellite links", *IEEE Trans. Antenn. Propag.*, Vol. AP-44, no. 1, January 1995, pp 23-27.

[4] T.J. Mousley, E. Vilar, "Experimental and theoretical statistics of microwave amplitude scintillations on satellite down-links", *IEEE Trans. Antenn. Propag.*, Vol. AP-30, no. 6, November 1982, pp. 1099-1106.

[5] L. Ljung, *System identification: theory for the user*, Prentice-Hall information and system sciences series, Thomas Kailath editor, 1987.

[6] L. Dossi, "Real-time prediction of attenuation for applications to fade countermeasures in satellite communications", *Electron. Lett.*, Vol. 26, no. 4, February 1990, pp. 250-251.

[7] B.K. Levitt, " Rain compensation algorithm for ACTS mobile terminal", *IEEE Journ. on Select. Areas in Comms.*, Vol. SAC-10, No 2, Feb. 1992, pp 358-363.

[8] K.J. Aström, *Introduction to stochastic control theory*, Mathematics and science engineering, Vol. 70, Academic Press, 1970.

[9] A. Burgueño, E. Vilar, M. Puigcerver, "Spectral analysis of 49 years rainfall rate and relation to fade dynamics", *IEEE Trans. Commun.*, Vol. COM-38, no. 9, Sept. 1990, pp 1359-1366.

Fade countermeasure development at Coventry University–Final report to COST255

CP 43001

Boris Gremont[1] , Paul Gallois[2] and Steve Bate[2]

[1] Formerly with Coventry University. Now with University of Portsmouth, Anglesea building, Anglesea Rd, Portsmouth PO1 3DJ, UK

[2] Coventry University, School of Engineering, Priory Street, Coventry CV1 5FB, UK

1. Introduction

The fade countermeasure (FCM) development described in this report gives an overview of the project undertaken by B. Gremont for the award of a PhD at Coventry University. This three year project entitled "Fade Countermeasure modelling for Ka band digital satellite links" is almost completed, having been initiated as a direct result of the participation of Coventry University in ESA/ESTEC's OPEX project. The likely contribution of this work is a greater understanding of the links between propagation effects and FCM design. This paper is non–mathematical and focuses on the main results and practical solutions relevant to the design and performance of predictive fade countermeasures.

FCMs are by definition adaptive control low excess (fade) margin systems whose objective is to compensate in real–time for the *detected* level of fades on a satellite link. The management and performance of Ka band FCM systems is thus conditioned greatly by the ability of practical FCM controllers at detecting/predicting the actual level of the total attenuation on a satellite link.

This has been the main focus of the research work. The outcome is both practical (i.e. it provides algorithms which could be used in practical FCM controllers) and theoretical (the proposed algorithms have been tested and characterised statistically). The model allows a quantitative and qualitative analysis of predictive fade countermeasure systems. The results also prompt a critical re–assessment or extension of some fundamental propagation models which do not give all the answers needed for the design of efficient FCM systems closely tailored to the Ka band fading satellite channel.

2. Performance criteria and design issues

2.1 Performance criteria

A critical design parameter specified for any satellite link is its availability. This is the percentage of time that the information can be transmitted and received with an acceptable quality. For digital signals, the quality is objectively described in terms of the bit–error–rate (BER) or equivalently, carrier–to–noise–ratio (CNR), or E_b/N_0. In view of equation **(1)**, where R_s is the channel symbol rate, this does not present any great difficulty:

$$E_b/N_0 = C/N_0|_{overall} - 10\log_{10} R_s \ dB \qquad (1)$$

According to CCIR/CCITT recommendations, an outage event is said to occur in a digital receiver if its BER exceeds a specified threshold (typically between 10^{-8} and 10^{-3}, depending on the service) for not more than 10 consecutive seconds [1].

Outage time is the accumulated seconds for all outage events in a given long period, say a year or a worst month. If an outage event lasts more than 10 seconds, the system is said to be unavailable (**Figure1**). This distinction between outage time and unavailability comes from the fact that digital trunks often lose framing when high BERs persist over a long period. In the real world however, outage and unavailability are often used interchangeably. In the strict sense, radio unavailabilty would be associated with long–lasting events like for example rain storms, while outages are associated with brief events like the ones generated by amplitude scintillation **[2]**. As the most stringent requirement is to design a system with a good BER *outage* availability (rather than ten seconds availability), scintillation cannot be neglected in the context of digital Ka band radio communications.

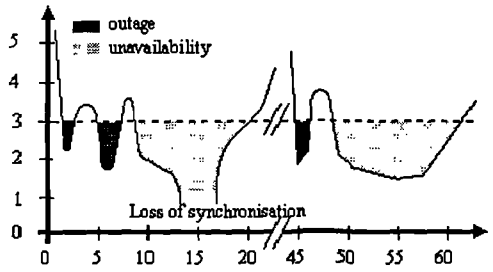

Figure 1: *BER history for a particular link, showing outage and unavailability times. The BER threshold is 10^{-3} (ordinate is $-\log_{10}$ BER).*

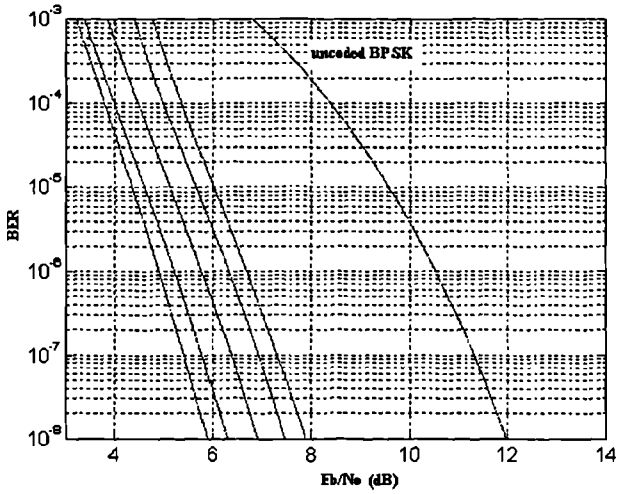

Figure 2: *BER vs Eb/N_0 for uncoded BPSK and punctured convolutional codes with Viterbi decoding. The BER threshold is 10^{-7}.*

This is particularly relevant if we consider the steepness of the BER versus CNR curve of any practical coding/modulation scheme (see **Figure 2** for example). Typically one dB variation in CNR produces a change of one order of magnitude in error probability. In the context of FCMs, any channel estimation error, especially any *under–estimation* of the real total fade, means that the system may well operate below its specified BER threshold. If this effect is not controlled, the overall long–term BER availability of the system may be very poor. Clearly the engineering solution must be formulated in terms of a statistical model.

2.2 Design issues relevant to fade detection schemes

The inaccuracies in determining signal strengths can be due to one of three reasons:

1. There are the measurement errors made by the particular fade detector **[3]** and associated signal pre–processing operations required to estimate the effective CNR (or equivalent). Any measurement device, signal processing operations (e.g. decimation, sampling, quantisation, filtering etc) will bury the true CNR component in a noise component which will affect the estimation accuracy. These errors should be quantified (once a fade detector has been implemented) and possibly they should be compensated for via a small dedicated power margin **[4]**.

2. A second class of error depends on the way the effective total fade over a satellite link is measured and/or calculated in real–time.

   (a) In a single FCM system, the total CNR drop can be monitored at the receiver which is then transmitted via a suitable FCM protocol to the receiver for appropriate counteraction. In that case, the FCM controller knows the total impact of the fades on the overall CNR, therefore FCM control action can be taken in a simple and direct manner.

   (b) If UL and DL fades are measured independently via two separate beacons (or equivalent), the FCM controller must rely on a model of the satellite link (i.e. UL, DL and satellite transponder **[5]**) in order to determine the required single FCM action level based on the computed drop in overall CNR (**[6]**, **[7]**).

3. A third class of error is caused the random and dynamic nature of the Ka band fading process which makes it difficult for systems to estimate or predict the likely variations of the fades. Essentially, these errors refer to the ability of systems at integrating practically the dynamics and stochasticity of the Ka band fading process. Two major problems need to be considered here:

   (a) The finite response time of practical countermeasures is a source of performance degradation which can be minimised by the implementation of predictive control strategies. The implementation of a short–term predictor must be justified in terms of the dynamics of the Ka band fading process, and any proposed practical predictor must be characterised statistically so that the long–term performance of practical predictive FCM systems can be drawn. This has been the main objective of this research work **[9]**.

   (b) In the case where fade detection is carried at a low carrier frequency (typically 20 GHz), the FCM controller must estimate the up–link attenuation (e.g. at 30 GHz). This requires a new model of the instantaneous frequency scaling factor of rain and scintillation (both during rainy and dry conditions) **[10]**.

The randomness of these two effects also forces the designer to add a small detection margin to the measured level of total attenuation (**Figure 3**). Predictive control strategies are introduced to minimise this extra margin (called hereafter a detection margin).

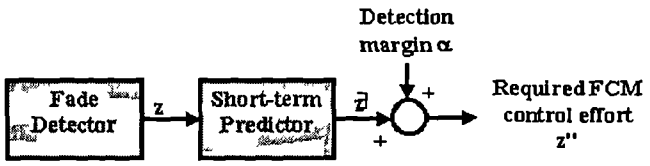

Figure 3 : *Detection margin (α) introduced to control the under–estimation of the true fades made by the FCM controller.*

Points 1. and 2. in the above list are dependent on the architecture and practical solutions used by the engineers. They are very system–dependent. The work presented here treats only the analysis and modelling of point 3. This is in nature a more general problem and it is common to all FCM systems. Furthermore, it lies at the interface between propagation modelling and FCM systems and is susceptible of providing some feedback to propagation researchers.

2.3 Optimisation for efficient design of FCM control systems

The design of efficient FCM systems and their associated controllers should be seen as an optimisation problem. The objective is to design an adaptive system which can achieve a possibly high BER availability while the FCM resources have to be used as economically as possible.

In order to achieve a certain BER (outage) availability, the designer is constrained to add a small detection margin, α, (**Figure 3**) to the detected level of attenuation, so that the underestimation of fades can be controlled statistically and matched to desired specifications. However, any over–estimation of the real fade will lead to an over–utilisation of the FCM resources.

Within the context of predictive FCMs, an attempt is made to minimise this fade detection margin. Such a minimisation will yield, in the case of FCMs like adaptive FEC a maximisation of the user data throughput while providing the required grade of service. More significantly, an economical use of FCM resources allows a maximisation of the number of stations that can be supported simultaneously by a shared common resource FCM system (e.g. ATDMA or frequency diversity) **[11]**. FCM over–utilisation is well measured by a quantity called the FCM utilisation factor defined by (see **Figure 4**) :

$$U(\epsilon, \Delta t) = \frac{T_{FCM}}{T_{ideal}} \qquad (2)$$

where Δt (sec.) denotes the expected response time of the FCM system and ϵ (dB) is the small built–in excess margin. T_{ideal} is the FCM utilisation time in the case where there are no time delays, i.e. the response of the whole FCM system is instantaneous. The fixed excess power margin corresponds to the maximum level of fades above clear–sky levels for which the system can operate without needing countermeasure action. When this excess margin is exceeded, FCM control effort must be deployed. A crucial design question which will be answered here is: How small should that excess margin be to ensure a good utilisation of FCM resources?

3. Short–term prediction of the Ka band fading process

The detection of Ka band fades is usually performed at a sampling frequency of 1 Hz, which is enough to characterise the dynamics of the 10 to 30 GHz satellite channels. The short–term predictability of the Ka band fading process has been investigated using time–series analysis tools applied to empirical beacon collected by the Rutherford Appleton Laboratories at 30 GHz during ESA's Olympus experiment. The identification of the best one–step (i.e. one second) ahead predictor yielded the following ARMA–type difference equation **[12]**:

$$y(t) = \sum_{n=1}^{3} a_n \cdot y(t-n) + e(t) \sum_{n=1}^{3} c_n \cdot e(t-n) \qquad (3)$$

$y(t)$ denotes the predicted rain attenuation component at time t, e(t) is the prediction error made by the ARMA predictor given in (3). The 6 model parameters are determined on–line using the standard RELS/Minimum Variance algorithm giving a k–step ahead (k=1,2,3,.... sec.) minimum mean square error (MMSE) estimate of the Ka band fading process (see **Figure 5**).

Such a MMSE criterion makes sense since the main objective of FCMs is to compensate for rain attenuation. MMSE is thus used as a means of tracking the slow rain attenuation compo-

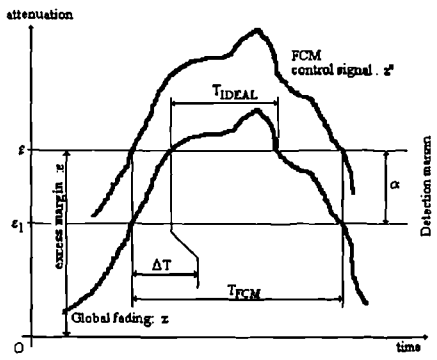

Figure 4: *Definition of the FCM utilisation factor.*

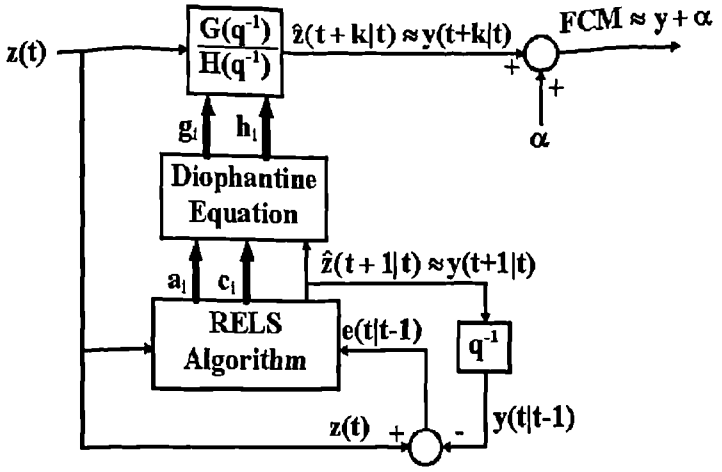

Figure 5: *On–line predictor of the Ka band fading process based on an ARMA structure and the minimum variance approach.*

nent while minimising the spread of the error around that mean slow–dynamics path. Statistical characterisation of this short–term predictor revealed that;

1. The ARMA–based predictor can track and predict the slow component of the Ka band fading process, namely rain attenuation, i.e. the predicted attenuation is modelled by the two–parameter lognormal pdf $\Lambda_y(m,\sigma)$ of rain attenuation (This parameters can easily be evaluated from empirical data of from the ITU–R model).
2. The error made by the predictor has the characteristics of a scaled scintillation process and agrees to a two–parameter Moulsley–Vilar distribution denoted by $MV_e(\sigma_m(k),\sigma_\sigma(k))$ (**see Figure 6**). For k = 1 (sec.) the model reduces to the classical model of amplitude scintillation as originally described in **[14]** and **[15]** from propagation experiment. The longer the time delay the larger are scintillation amplitudes. However the statistical model $MV_e(\sigma_m(k),\sigma_\sigma(k))$ has now been extended to include the practical performance of a short–term predictor. This scaling of scintillation statistics depends on three factors: the choice of a dynamic structure used for prediction (here it is ARMA), the expected time delay k of the FCM system, and the scintillation statistics as described originally by Moulsley and Vilar (they depend on the carrier frequency and the elevation angle). The dependency of the predictor's ability at predicting the Ka band process is introduced in the model via two fitted empirical functions $f_2(k)$ and $f_4(k)$ which describe respectively the increase of the second and fourth order normalised moments of the error with time delay. Other predictors would have different empirical functions $f_2(k)$ and $f_4(k)$. Effectively, these two functions can be shown to relate to the normalised spectrum of the Ka band fading process (i.e. rain+scintillation). The latter being invariant in shape, $f_2(k)$ and $f_4(k)$ can be assumed invariant with time and/or carrier frequency **[16]**.

4. Predictive Control of FCM resources

In order to control the accuracy of the predictive fade detection scheme, it is important to evaluate the required 'scaled scintillation margin' so that the fade detector will under–esti-

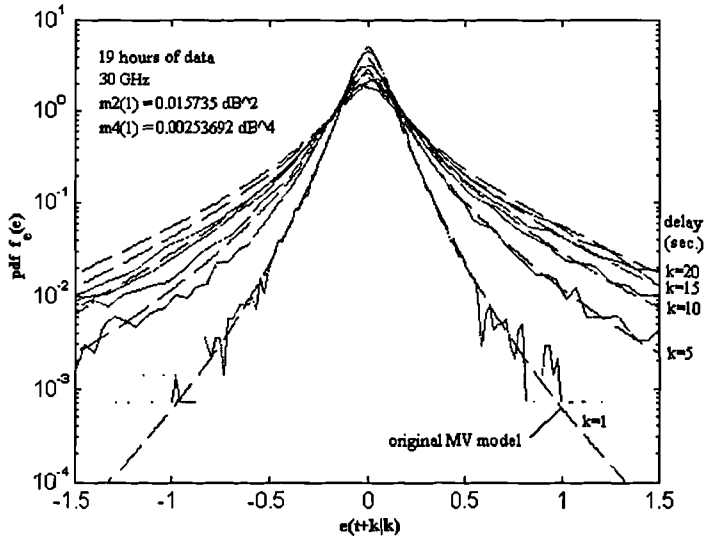

Figure 6: *Transformation of scintillation statistics within the context of predcitive fade countermeasures.*

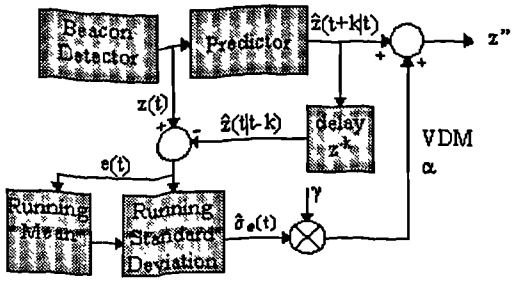

Figure 7: *Block diagram description of the variable detection margin (VDM) scheme.*

mate the actual fades for a specified percentage of time. Two different strategies are presented in section 4.1. They are compared in section 4.2 in terms of FCM utilisation factor which is useful to evaluate the required excess margin of FCM systems. In section 4.3, BER availability and average user data throughput are evaluated for a typical predictive Ka band FCM system.

4.1 Required fade detection margin

The objective is to evaluate the required detection margin (fixed or variable) so that a certain arbitrary detection outage probability (i.e. the probability that the FCM controller under–estimates the real fade) can be achieved.

1. Fixed Detection Margin (FDM) approach (see **Figure 3**): In this case a fixed offset is added to the predicted rain attenuation so as to bias the prediction error and control statistically the probability of under–estimating the real fade. The required FDM, a (dB), is obtained by integrating the pdf of the error (scaled scintillation from a to infinity). The results are shown in **Figure 8**. For example, for a time delay of $k = 10$ s, a FDM a of 1.2 dB is required to achieve a detection outage %time of 5% (i.e. the predictive FCM controller will over–estimate the true fades for 95 % of the time).
2. Variable Detection Margin (VDM) approach: In order to bring even more adaptiveness to the FCM controller, an attempt was made at implementing a variable detection margin scaled scintillation margin. It is based on the well–known fact that the scintillation variance is constant over short–term periods of times (up to one minute) **[19]**. As the ARMA/minimum variance can predict rain, it can be seen as a quasi–optimum on–line separator of rain and scintillation components. Thus an on–line a–posteriori estimate of the scaled scintillation variance can be estimated in real–time using a simple algorithm shown in **Figure 7**. As the variance does not change over intervals of the order of 10 seconds (The expected maximum response time of FCM systems), the analysis is still valid and remains very tractable. In this case the control parameter γ sets the amplitude of the VDM.

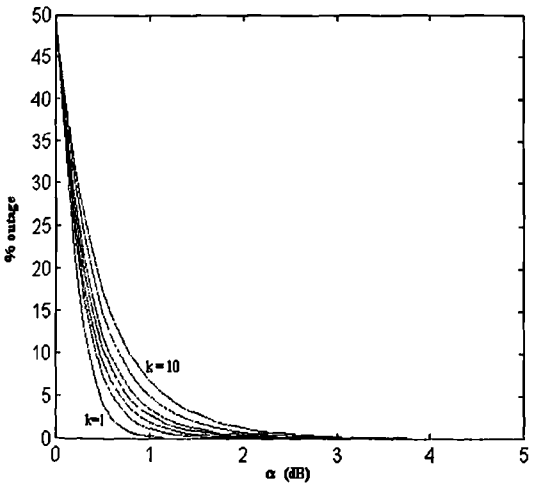

Figure 8: *% time detection outage versus required fixed detection margin (α) for different time delays.*

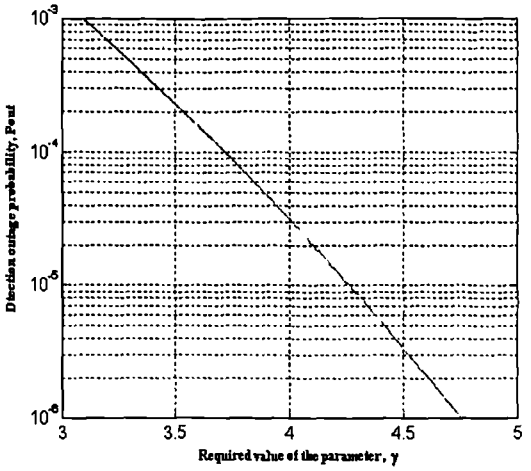

Figure 9: *Choice of the VDM control parameter to achieve a desired detection outage probability.*

4.2 Required fixed excess margin

Both FDM and VDM have been compared by calculating the theoretical FCM utilisation factor (U–factor) for each of the proposed schemes. The analysis is quite complex but it is particularly relevant to determining the performance of shared common resource systems like adaptive TDMA or frequency diversity. **Figure 10** shows the theoretical U–factor and practical one for the FDM approach . The agreement is excellent and it is also backed–up by practical results collected during the Sirio experiment at 11 GHz **[11]**.

The following comments are important to the design of low–excess margin system in the carrier–to–noise (i.e. link budget) domain:

1. The utilisation factor depends on the detection margin *and* the fixed excess margin. For example (see **Figure 10**), a system with a built–in fixed excess margin of $\epsilon = 4\ dB$ and a FDM of $a = 2dB$ would have a FCM utilisation factor of $U \approx 3.4$. This is a rather bad figure (ideally we would like U=1) and thus a FCM system can be expected to utilise its resource quite inefficiently.
2. Graphs like the ones in **Figure 10** can be employed to choose the required excess margin for a FCM system. First, being given a time delay, one can choose the required detection margin a so that a specified detection outage probability can be achieved (section 3.1). Using this value of a, the excess margin, ϵ, can be chosen from graphs 10 so as to set the utilisation factor to a desired value.

The main result of this analysis is that long time delays and/or bad short–term predictor of the Ka band fading process necessitate large detection margins (on the right of **Figure 10**). Thus the designer is constrained to provide a large fixed excess margin so that FCM channel capacity can be utilised efficiently.

For example, based on **Figure 10**, a fixed excess margin of at least 4 or 5 dB should be built in into the system if one wants to get U–factor of reasonable values. This is an important re-

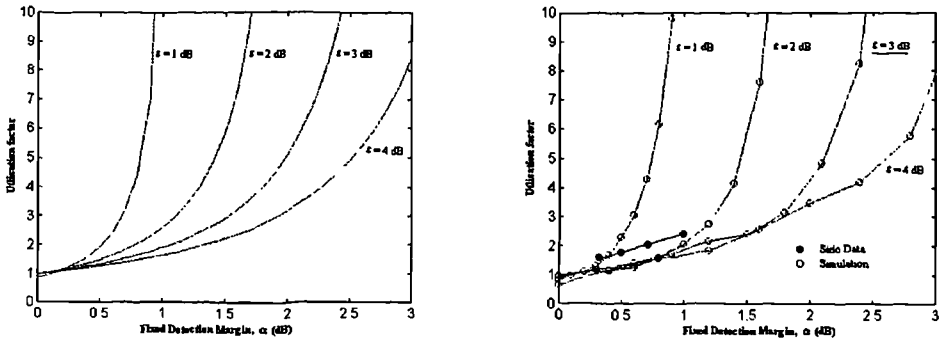

Figure 10: *Comparison of theoretical (left) and simulated/experimental (right) FCM utilisation factor (FDM approach).*

sult since fade countermeasure systems were seen as low–fade margin systems. The results presented here indicate however that this is cannot really be the case.

As we shall see in the next sub–section, an adaptive FEC (AFEC) countermeasure has a built–in excess margin of 6.9 dB for a BER threshold of 10^{-7}, which is quite larger than the 4 or 5 dB prescribed above. As a consequence the throughput performance of the AFEC system is quite good.

Although not described in detail here, the FCM utilisation factor for the VDM approach has also been evaluated and compared (for the same detection outage probabilities) to the one obtained for the FDM approach. The U–factor for the VDM was found to be less than 0.8 times the U–factor of the FDM. Due to its improved adaptiveness, the VDM is generally more channel efficient than its fixed counterpart, especially for FCM systems with time delays of less than 5 seconds and relatively low outage detection probabilities. For longer time delays the FDM approach may be preferred (in fact it also depends on the detection outage probability). This will not be discussed here any more, however the VDM approach can be assumed as superior to the FDM for most practical FCM applications, since most of them will have in practice short–time delays. Therefore the VDM predictive controller will be retained in the rest of this document.

4.3 BER availability/throughput of an AFEC countermeasure

The analysis has also been applied to the calculation of the BER availability and user data throughput of a typical low–power low–rate AFEC countermeasure. This type of system is particularly applicable to in–bound Ka band VSAT links based on a star architecture and FDM(A)–SCPC access to the satellite transponders. It can accommodate user services which can tolerate an occasional reduction in user data rate during severe atmospheric conditions. A system based on punctured convolutional codes (rates 1, 7/8, 5/6, 3/4, 2/3, 1/2), with Viterbi soft–decision decoding and BPSK was assumed (**Figure 2**). The rate adaptiveness is introduced to maximise the long–term data throughput. The symbol rate is 9.6 ksymb/sec. When the FEC code rate, ρ, is varied, the user data rate is also changed so that (see equation (**1**)) $R = R_b/\rho$=9600 symb/s. The HPA power is assumed to be 0.2 W and the antenna diameter is 0.8 m. Link budget calculations were performed for a typical 30/20 GHz link between the site of Chilton and ESA's Olympus satellite. A back–to–back application was considered

(worst–case design): this allows the exclusion of site diversity in the modelling process by having two perfectly correlated up and down link faded segments.

4.3.1 Code Rate Change (CRC) Boundaries

The CRC boundaries is the look–up table in the FCM controller from which the switchings to a more or less level of FCM protection will be initiated based on detected/corrected total attenuation on the overall clear–sky CNR (or equivalent). Given a certain BER threshold, the overall clear–sky CNR of the in–bound VSAT link and using **Figure 1**, it is easy to estimate the level of admissible fades at which the FEC code rate need be changed to maintain the BER below the threshold. These are given in **Table 1**.

FEC code rate, ρ	Rq E_b/N_0@BER=10^{-7} (dB)	Built–in excess margin (dB)
1	11.39	6.89
7/8	7.33	10.95
5/6	6.95	11.33
3/4	6.39	11.89
2/3	5.79	12.49
1/2	5.43	12.85

Table 1: *CRC boundaries for an AFEC countermeasure based on punctured convolutional codes (BPSK, Clear–Sky Overall CNR = 58.28 dBHz, Rs=9.6 ksymb/sec).*

4.3.2 Impact of delays on BER availability and average user data throughput

The BER availability is the probability that the BER exceeds its specified threshold (**Figure 1**). It depends on the position of the required E_b/N_0 at the BER threshold and also on the statistics of the predicted/corrected required FCM control effort, $y + a$, (a is the VDM). As the VDM is simply a scaled version of the scintillation variance, one has first to consider the possible statistical relationship between rain and scintillation. As a worst–case design assumption, it was assumed here, that rain and scintillation are statistically independent.

The BER availability and average user data throughput has been compared to the ones that would be obtained in the ideal delayless case. This is shown in **Figure 11** where the overall clear–sky CNR level of the back–to–back link was 58.28 dBHz. The abscissa spans all the BER thresholds of practical interest. From section 4.2, the VDM was set so that the detection outage probability is 0.01 (i.e. under–estimation of true fades for 1% of the time). As can be expected the smaller the BER threshold the larger is the BER unavailability. More importantly the availability of the AFEC system is affected by its expected response time. This should be taken into account at the design stages. Note however that the low–power low–rate system discussed here can achieve link BER availabilities of the order 99.9% which is quite satisfactory (8.8 hours of BER outage per year). The existence of time delays results in a degradation of throughput performance in reference to the ideal delayless case.

The examples in **Figure 11** show that overall the AFEC countermeasure is quite sufficient to achieve good performance on the Ka band fading channel. These figures can be justified in terms of the sufficient antenna diameter (0.8 m), HPA power (0.2 W) and low channel sym-

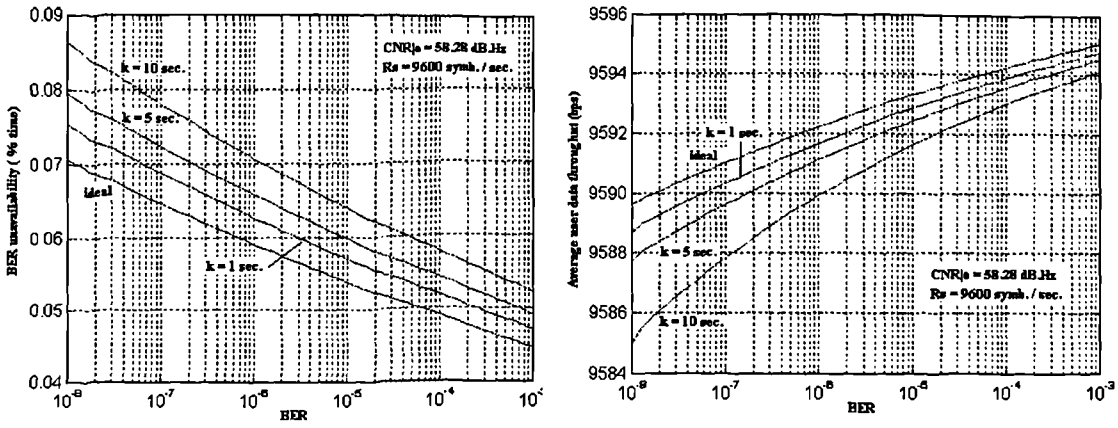

Figure 11: *BER availability and average user data throughput of a predictive AFEC countermeasure.*

bol rate (9.6 ksymb/sec) yielding a large built–in excess margin of 6.9 dB. Therefore this system is quite efficient at utilising the available channel capacity. A smaller HPA power/dish diameter or a larger symbol rate would substantially reduce the BER/throughput performance of the FCM system and the designer may then be forced to use a more robust FEC scheme (e.g. concatenated codes).

5. Inclusion of Instantaneous Frequency Scaling Factor (IFSF)

In the cases where the real–time sounding of the satellite channel is carried out at a base frequency (typically 20 GHz at Ka band), the FCM controller must also integrate a model of the instantaneous frequency scaling factor (IFSF) of joint rain and scintillation processes so that the attenuation at 30 GHz can be inferred from the (ideally) measured down–link total attenuation on the overall CNR (or equivalent). To be useful to FCM design, not only an estimate of the mean IFSF must be known but more importantly the designer must also have an estimate of the variability of the scaling factor around its mean value **[18]**.

5.1 Construction of a stochastic model of the IFSF rain attenuation

A new model of the IFSF of rain attenuation has been developed for application to predictive FCM control operations. Only output results will be presented here. The model considers the impact of the slow temporal stochastic variations in rain drop size distribution on the mean and standard deviation of the IFSF of rain.

A typical example of the estimated standard deviation of the IFSF of rain is shown in **Figure 12**. It is also compared to some results obtained at Spino d'Adda for the 29.77/19.77 GHz pair **[20]**. Although the results are different, the proposed model seems to be on the right track. Further work is required. Based on the Gaussian assumption, once the standard deviation of the IFSF is known, it is straight forward to determine how many standard deviations (σ) need to be added to the mean IFSF to encompass any desired percentile. A typical output is shown in **Figure 13** for percentiles ranging from 0.01 to 99.99%.

The stochastic model was derived from simple physical assumption. It considers that the specific rain attenuation at one carrier frequency can be modelled as conditionally Gaussian on rain–rate and varies randomly between the Joss–Drizzle (J_D) and Joss–Thunderstorm (J_T)

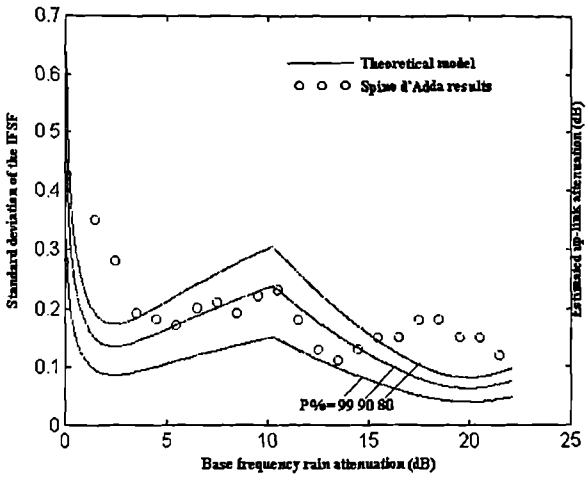

Figure 12: *Theoretical and empirical standard deviation of the IFSF of rain as a function of the down–link (19.77 GHz) rain attenuation level.*

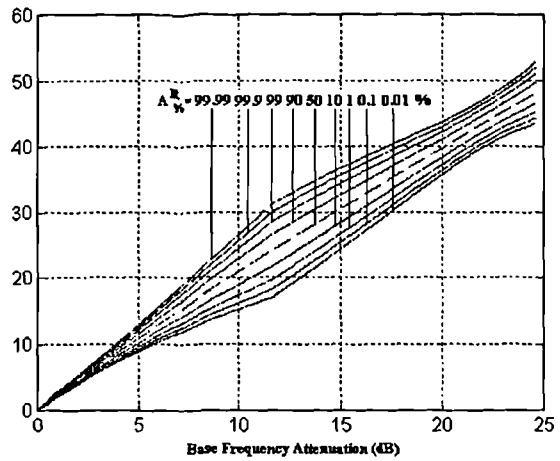

Figure 13: *Theoretical fade detection rule used for statistically controlled estimation of the IFSF of rain based on detected down–link attenuation.*

distributions. So far only the case of spherical rain drops has been considered. The model was normalised using recently published experimental results on the rain attenuation scaling. The model is slightly elevation and carrier–frequency dependent. It also considers the correlation coefficient between high and low frequency links (which will be very high for co–located links, low for divergent satellite–to–earth paths) and the meteorological variability in rainstorm activity between the J–D and J–T extremes via a fitted empirical parameter.

5.1 Generalised predictive FCM controller

The short–term predictive controller and its associated variable detection margin allows a natural inclusion of the IFSF of both rain attenuation and amplitude scintillation. This extension is shown in **Figure 14**.

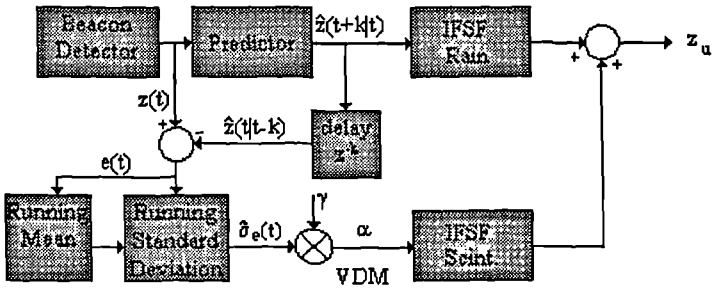

Figure 14: *Inclusion of IFSF of rain attenuation and tropospheric scintillation in the predictive VDM controller*

This relies once again on the fact that the ARMA–based predictor can be seen as a quasi–optimal on–line separator of rain and scintillation due to its MMSE criterion. Furthermore, the system in **Figure 14** knows the actual variance of the 'scaled' scintillation process, which is

the usual quantity used for scaling the scintillation process in frequency. In this work, it has only be assumed that the IFSF of rain is a random quantity, Thus the up–link attenuation can be estimated from the detected /predicted down–link attenuation using a generalised detection rule of the form:

$$\hat{z}_u(t + \Delta t | z_d(t)) = \left[\bar{k}(R) + \gamma_R \cdot \sigma_k^R(R)\right] \cdot y_d(t + \Delta t | t) + k_{\sigma_d} \cdot \gamma \cdot \sigma_e(t + \Delta t | t) \quad (4)$$

Subscripts u and d stands for up and down link respectively. $\bar{k}(R)$ and $\sigma_R(R)$ denotes the mean and standard deviation of the IFSF (It depends on rain rate or equivalently on down–link attenuation). k_{σ_d} is the deterministic scaling factor of scintillation standard deviation from the current ITU–R model. γ is the parameter used for controlling the outage detection probability of predictive FCMs as described in section 4.1. The square bracketed term in **(4)** is a detection rule which considers the mean scaling of rain attenuation to which is added a variable detection margin, $\gamma_R \cdot \sigma_k^R(R) \cdot y_d(t + \Delta t | t)$ dB. This new VDM depends on the value of the parameter γ_R introduced here to control the probability of under–estimating the IFSF of rain attenuation. In a practical system, the square–bracketed term would be approximated by a curve fitted curve. For example, based on a comprehensive empirical study of the IFSF of rain, the authors in **[21]** suggested that a second–order polynomial function is appropriate.

6. Further work

Different areas have been identified as of interest to the development of Ka band countermeasure systems and associated models in the presence of Ka band dynamic fading.

1. The FCM utilisation factor is a parameter which is particularly useful to the design and/or dimensioning of shared resource Ka band systems. The analysis presented here could therefore be applied to investigate the impact of time delays on the performance of ATDMA or frequency diversity systems.
2. A back–to–back link was analysed in this work. This can be expected to yield conservative results. A non back–to–back application, including geographical (dual) link diversity would add more realism to the model. It would permit to design systems more tightly to their expected environment, to decouple up and down links (opening the way to dual countermeasure systems each with possible different time delays). This could also be a starting point to the analysis and dimensioning of shared common resource FCMs based on a model of site diversity over a distributed coverage area in which FCM response time can be included).
3. An important issue is the definition of a statistical model for joint rain and scintillation. Both were assumed here as statistically independent. This is currently a controversial issue in the field of propagation.
4. Inclusion of level–dependent fade duration statistics in the model could allow for a separation between outage and unavailability periods as defined by the CCITT/CCIR guidelines.
5. A good model of the IFSF of rain requires first a good model of rain attenuation. Particular the modelling of the effective path length (or equivalently the path reduction factor) should be re–assessed to identify its dependency on *both* rain rate and carrier frequency.

6. The potential variability of the IFSF of scintillation variance should be investigated.

6. Conclusions

This research work confirms that countermeasure systems are technically viable. In particular, it is indicated that a FCM technique based on readily available punctured convolutional codes, with its modest coding gains is sufficient to provide good BER availability and user data throughput for a low–power low–rate VSAT terminal.

This research has demonstrated that the consideration of more specific problems, like the impact of time delays and instantaneous frequency scaling, does not change the validity of the above general statements. However, further work at the interface between FCM system design/modelling and fundamental propagation research is required.

7. Acknowledgements

Boris Gremont would like to thank his director of studies, Mr Paul Gallois, and his second PhD supervisor, Dr Steve Bate for their guidance and help throughout this project. The constructive comments made by Dr Thompson, chairman of Working Group 3 of COST 255, were most useful at the MPhil/PhD transfer stage of this work and helped putting this research on a different and more useful footing.

The authors would like to acknowledge Coventry University for funding this research. Thank you to COST 255 for inviting and funding Boris to make this presentation.

8. References

[1] L.J. Greenstein, M. Shafi, "Outage calculation methods for microwave digital radio", IEEE Comm. Mag.,Vol. 25, No 2, pp 30–39, 1978.

[2] A. Paraboni, C. Riva, "A new method for the prediction of fade duration statistics in satellite links above 10 GHz", Int. J. Sat. Comm., Vol. 12, pp 387–394, 1994.

[3] F.J. Pegal, "A review of fade detection techniques", Proc. of the 14th NASA propagation experimenters meeting (NAPEX XIV) and the Advanced Communications Technology Satellite (ACTS), Propagation studies miniworkshop, Austin Texas, pp 240252, May 1990.

[4] L. Dossi, "Real–time prediction of attenuation for applications to fade countermeasures", Elect. Lett., Vol. 26, No 4, pp 250–251, 1990.

[5] R.G. Lyons, "Combined effects of up– and down–link fading through a power–limiting satellite repeater", IEEE Trans. Comms, pp 350–352, March 1977.

[6] E.H. Satorius, L.H. Tong, "Analysis of a rain compensation algorithm for K/Ka band communications", Int. J. Sat. Comm., Vol. 14, pp 297–311, 1996.

[7] B.K. Levitt, "Rain compensation algorithm for ACTS Mobile terminal", IEEE J. Sel. Areas in Comm., Vol. SAC–10, pp 358–363, 1992.

[8] L. Dossi, "Real–time prediction of attenuation for applications to fade countermeasures", Elect. Lett., Vol. 26, No 4, pp 250–251, 1990.

[9] G. Tartara, "Fade countermeasures in millimitre–wave satellite communications: a survey of methods and problems", Proc. Olympus Utilisation Conf., Vienna April 1989, ESA SP–292, May 1989, pp 107–107.

[10] F. Rucker, "The impact of instantaneous frequency scaling factors on up–link power control", AEU, Vol. 48, No 2, pp 119–121, 1994.

[11] L. Dossi, G. Tartara, E. Matricciani, "Frequency diversity in millimetre wave satellite communications", IEEE Trans. Aero. and Elect. Syst., Vol. AES–28, No 2, pp 567–573, 1992.

[12] L. Ljung, "System identification, theory for the user", Prentice–Hall, Information and systems science series, Thomas Keilath editor, 1987.

[13] K.J. Astrom, "Introduction to stochastic control theory", Mathematics in science and engineering, Vol. 71, Academic Press, 1970.

[14] T.J. Moulsley, E., Vilar, "Experimental and theoretical statistics of microwave amplitude scintillations on low elevation Earth–Space paths", IEEE Trans. Ant. Prop., Vol. AP–30, No 6, pp 1099–1106, 1982.

[15] E. Vilar, J.R. Larsen, "Elevation dependence of amplitude scintillations on low–elevation earth–space paths", Proc. 6th Int. Conf. Ant. Prop., ICAP'89, University of Warwick, 1989.

[16] B.C. Gremont, A.P. Gallois, S.D. Bate, "Efficient fade compensation for Ka band VSAT systems", Proc. 2nd Ka band utilisation conference and international workshop on SCGII, Florence (Italy), Sept. 24–26 1996, pp 439–443, 1996.

[17] B.C. Gremont, A.P. Gallois, S.D. Bate, "Predictive Fade countermeasure for Ka band satellite systems", Proc. 10th Int. Conf. Ant. Prop ICAP'97, Edinburgh (UK), April 14–17 1997, Vol. 2, pp 2.109–2.114, 1997.

[18] T.K.P. Chung, A.P. Gallois, B.C. Gremont, "Frequency scaling of rain attenuation: results from Olympus", Proc. 9th Int. Conf. Ant. Prop ICAP'95, Eindhoven (The Netherlands, Vol. 2, pp 2.178–2.181, 1995.

[19] I.E. Otung, B.G. Evans, "Short–term distribution of amplitude scintillation on a satellite link", Elect. Lett., Vol. 31, No 16, pp 1328–1329, 1995.

[20] M. Mauri, A. Paraboni, C. Riva, "Instantaneous frequency scaling", OPEX 2nd Workshop of the Olympus experimeters, Vol. 6:Proceedings, ESA WPP–083, Noordwijck, 8–10 Nov. 1994.

[21] J.D. Laster, W.L. Stutzman, "Frequency Scalling of rain attenaution for satellite communication links", IEEE Trans. Ant. Prop, Vol. AP–43, No 11, pp 1207–1216, 1995.

PREDICTIVE FADE COUNTERMEASURES FOR Ka BAND SATELLITE SYSTEMS

B.C. Gremont, A.P. Gallois, S.D. Bate

COVENTRY UNIVERSITY, UK

***Abstract:** This paper investigates the performance of a predictive fade control strategy based on a minimum variance approach for application to low fade margin Ka band satellite systems. Ideal beacon detection is assumed. A statistical model based on a modified concept of global fading process is developed. This is used to evaluate the performance of the fixed detection margin approach to account for scintillation-induced effects. This is expressed in terms of FCM utilisation ratio. The impact of time delays on the design and performance of an adaptive transmission rate countermeasure is also evaluated.*

I. INTRODUCTION

The real-time control of fade countermeasure (FCM) resources based on beacon detection presents three problems. *First*, in the case of a down-link (DL) beacon detector, the estimation of the impact of joint rain and scintillation necessitates an efficient real-time separation/recombination and instantaneous scaling of each atmospheric effect (1), so as to evaluate the up-link (UL) attenuation. This is a very difficult problem which is not considered here. *Secondly*, the deployment of single FCM techniques must be based on the *total* degradation on both UL and DL through the satellite transponder. This mainly implies the definition of a FCM control protocol, whereby FCM service information, can be passed in both the forward and return directions, so that the required total FCM control effort can be accurately evaluated (2). The integration of such FCM protocols within ARQ systems, to achieve very low error rates, also needs consideration. The total attenuation may be inferred either using a two-dimensional model for UL and DL (especially if geographical link diversity must be included and/or hybrid FCMs are used), or, alternatively, the total atmospheric degradation can be approximated to a one-dimensional problem (refer to Levitt (3) for more information). In this paper, it is assumed that we have knowledge of the total degradation caused by joint rain and scintillation on the *overall* clear-sky carrier-to-noise ratio (CNR), at a rate of 1 Hz. This is achieved by considering a well-tractable back-to-back in-bound VSAT link. This assumption avoids the inclusion of diversity in the modelling process and it yields a worst-case design analysis. This model was originally introduced by Filip and Vilar in (4). *Thirdly*, FCM control operations must be short-term predictive. This is to account for the likely variations of the Ka band fading process, during the response time of the FCM system. This delay will be dominated by the propagation time delay to and from the satellite, as well as the FCM service communication protocol, and, whether on-demand assignment of FCM protection is employed. In a previous analysis published in (5), it was found that, while rain is fairly predictable, scintillation is not. The latter is the source of channel estimation errors, which need to be catered for via the implementation of a fixed detection margin (FDM). This yielded a new model, based on a *modified* concept of global fading, and is reviewed in section II. In section III, the performance of the FDM approach as a predictive fade control strategy is expressed in terms of FCM utilisation ratio. This is particularly useful for the analysis of low fade margin systems and can be applied to the design of channel-efficient shared-common resource FCMs (see (6)). It is emphasised here that the FDM approach results in a degradation in utilisation factor, prompting the search for a functional relationship between rain and scintillation processes (7). This may pave the way to very efficient *variable* detection margin systems. In section IV, the analysis focuses on the choice of Data Rate Change (DRC) boundaries (3) and on the long-term performance of an adaptive transmission rate countermeasure. Finally the opportunity to maximise user throughput by selection of FEC code rate is described for an hybrid fixed FEC/adaptive transmission rate FCM system .

II. PREDICTIVE FADE CONTROL

In (5), it was found that the best one-step ahead predicted (k=1 sec.) estimate of the global fading, $\hat{z}$ [dB], with a residual error, e [dB], is given by the following linear difference equation:

$$\hat{z}(t) = y(t) - e(t) = -\sum_{n=1}^{3} a_n \cdot y(t-n) + \sum_{n=1}^{3} c_n \cdot e(t-n)$$

Here y [dB] denotes the rain attenuation random variable. Rearranging, we obtain the definition of the ARMA** (3,3) model (see (8)) given by :

$$\hat{z}(t) = y(t) = -\sum_{n=1}^{3} a_n \cdot y(t-n) + e(t) + \sum_{n=1}^{3} c_n \cdot e(t-n) \quad [1]$$

(rain comp. | scintillation)

This simple dynamic model assumes simply that rain and scintillation are *additive* processes. In a self-tuning context (8), the parameters, a_n and c_n , are time-varying

** *Auto Regressive Moving Average.*

and are determined *on-line* solely so as to minimise the error variance σ_e^2 [dB^2]. The ARMA model can easily be extended to a k-step ahead predictor by using the minimum variance approach (see (5) or (8)) which consists in minimising:

$$\sigma_e^2(k)=E\{(z(t+k)-\hat{z})^2\} \quad dB^2 \qquad [2]$$

given information up to and including time step (t-1).

Statistical characterisation of the prediction ability of the ARMA model revealed that the sample error sequence {e(t)}, conforms to a Mousley-Vilar (9) pdf hereafter denoted by MV (see Fig.1):

$$MV_e(\sigma_m(k),\sigma_\sigma(k)) \equiv f_{e_{dB}}(e_{dB}) \qquad [3]$$

$$=\frac{1}{\sigma_{\sigma_{np}}(k)\cdot\pi}\cdot\int_0^\infty \frac{1}{\sigma^2_{e_{dB}}}\cdot\exp\left[-\frac{e^2_{dB}}{2\sigma^2_{e_{dB}}}-\frac{\ln\left(\sigma^2_{e_{dB}}/\sigma^2_{m_{dB}}(k)\right)}{2\cdot\sigma^2_{\sigma_{np}}(k)}\right]\cdot d\sigma_{e_{dB}}$$

Therefore, for k=1, we may assume that $e\approx\chi^*$, i.e. scintillation is not predicted. χ [dB] denotes the scintillation random variable and has parameter $(\sigma_m(1),\sigma_\sigma(1))$ as derived with the original MV model (5) (see Figure 1). A consequence is that $\hat{z}\approx y$, i.e. rain is predicted justifying the definition in eq. [1].

The dependence on time delays of the two MV model parameters $(\sigma_m(k),\sigma_\sigma(k))$ with the ARMA-based predictor was determined empirically from experimental copolar data via a moment analysis. Least square fitting yielded:

$$m_2(k)=\sigma_e^2(k)=m_2.(0.0337+0.487k+0.5251k^2) \qquad [4a]$$

$$m_4(k)=m_4.(0.046+0.368k+0.319k^2+0.3499k^3-0.0312k^4+0.0022k^5) \qquad [4b]$$

where m_2 and m_4 are the second and fourth order moments corresponding to the MV original parameters $(\sigma_m(1),\sigma_\sigma(1))$. The moments and MV parameters are related by (see (9)):

$$\sigma^2_\sigma(k)=\ln\left(\frac{m_4(k)}{3.[m_2(k)]^2}\right) \quad (np) \qquad [5a]$$

$$\sigma^2_m(k)=\sqrt{3}[m_2(k)]^2/\sqrt{m_4(k)} \quad (dB) \qquad [5b]$$

The normalised increase in moments (bracketed terms in eqs [4a] and [4b]) can be related to the normalised spectral characteristics of the Ka band global fading, and thus it may be assumed as invariant at one particular frequency (see (5)).

Modified Global Fading (MGF) model

Assuming statistical independence (in practice they were just merely uncorrelated) between what is predicted, namely y, and the error, e, the modified global fading (MGF) model for z= y-e may be defined as:

$$MGF_z(\sigma,m,\sigma_\sigma(k),\sigma_m(k))=f_z(z)$$
$$=\Lambda_y(m,\sigma)*MV_e(\sigma_\sigma(k),\sigma_m(k)) \qquad [6]$$

where * denotes the convolution operator and $\Lambda_y(m,\sigma)$ is the two-parameter lognormal model for rain attenuation (see eq. [9] and set $\alpha\approx 0$).

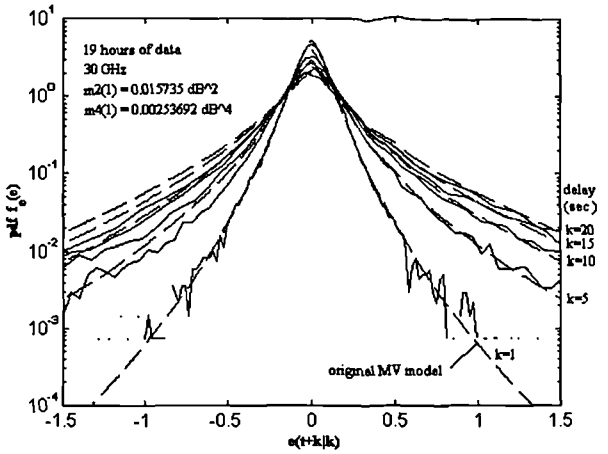

Figure 1: Sample and fitted pdf of the prediction error.

The MGF model in eq. [6], shown in Figure 2, reduces to the global fading model originally introduced by Filip and Vilar in (4) for k=1 second. However, the model has been extended to cater for the imperfections of the ARMA-based predictor which results in a transformation of the scintillation pdf.

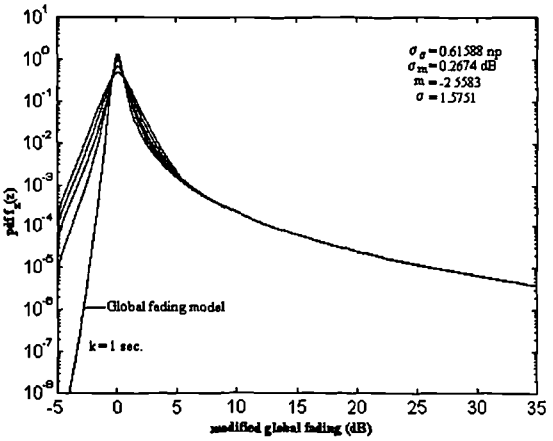

Figure 2: Modified Global Fading model.

Required fade detection margin (FDM)

As the error made by the ARMA model is unbiased, the FCM controller will underestimate the fades for 50 % of the time (50 % outage). It is necessary to introduce a fixed detection margin, α [dB] so that the effective control effort becomes FCM(t)= y(t)+α. This is to compensate (via straight biasing) for 'scaled' scintillation-induced fades. Outage will therefore occur whenever $FCM\le y-e$, i.e. whenever the FCM control effort is less than required. This yields the RF outage probability:

$$P_{out}(\alpha,k)=Prob(e\ge\alpha)=\int_\alpha^\infty MV_e(\sigma_m(k),\sigma_\sigma(k))de \qquad [7]$$

---

* *In fact, e is merely a MMSE estimate of the scintillation process. This normalisation yields however conservative results.*

This function has been computed and is shown in Figure 3 in linear scale for a typical Ka band link.

For example, for k=10 sec., a FDM $\alpha \approx 1.2$ dB is required to achieve an RF outage percentage of 5 % (availability 95 %). Thus, given an RF availability constraint, the required FDM for predictive fade control, in the presence of time delays, can be determined using the MGF model.

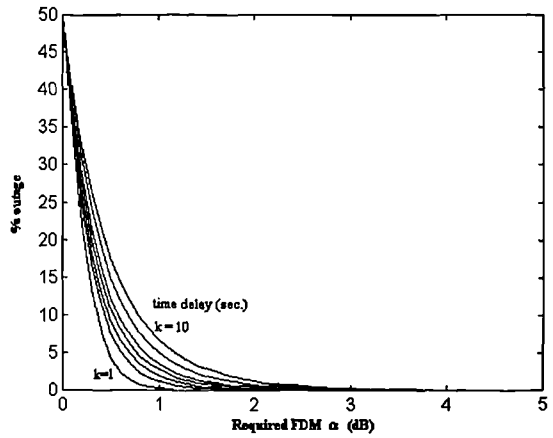

Figure 3: Required FDM.

III. FCM UTILISATION FACTOR

The introduction of a FDM to cover for fast variations of the Ka band fading is equivalent to telling the FCM that the fade is effectively α dB worse than its true value. In the case of adaptive transmission systems (e.g. A-FEC or APSK), this will result in a reduced channel capacity utilisation (4) ,while , for common-resource systems, this will translate into an over-utilisation/over-dimensioning of the required back-up resource. A good indicator (see Figure 4) of the performance of predictive FCM control strategies is the utilisation factor, U, defined by :

$$U(\alpha,\varepsilon) = \frac{T_{FCM}}{T_{ideal}}\bigg|_{z\geq\varepsilon} = \frac{Prob(FCM(t+k|t) \geq \varepsilon)}{Prob(z(t+k) \geq \varepsilon)} \qquad [8]$$

In the graph, only the rain component is shown. The scintillation part should be added, α being chosen so that $FCM \leq z$ occur only for a specified percentage of time. The level ε is the excess low fade margin for which the system can still operate satisfactorily without needing FCM action. A time period, T_{IDEAL} , can therefore be associated with the case where the global fading, $z = y+\chi$, is *perfectly* predictable* . However the detected/predicted fade does not include scintillation thereby requiring biasing via the FDM. Since this operation must be carried out at all times, this defines a practical time period, T_{FCM}, for which FCM action will be deployed. The departure of U from the value 1 will thus be an indication of the poor performance of predictive FCM using the FDM approach.

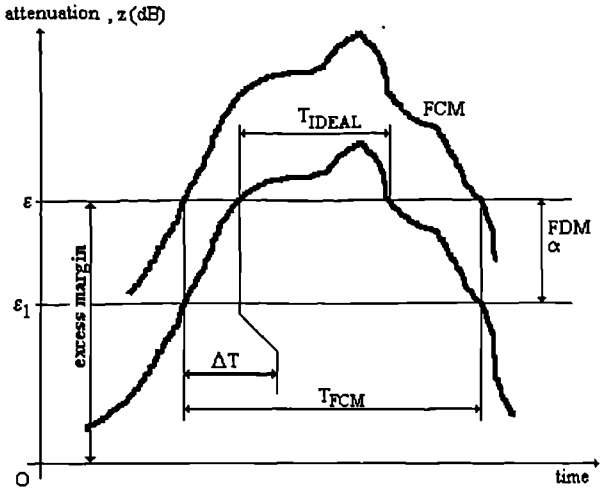

Figure 4: Definition of the utilisation factor for predictive low-fade margin systems.

The biased FCM control effort, $y+\alpha$, can be shown to have a pdf given by:

$$\Lambda_{y-\alpha}(m,\sigma) = f_y(y-\alpha) = \frac{1}{(y-\alpha)\sigma\sqrt{2\pi}}\exp\left[-\frac{(\ln(y-\alpha) - m)^2}{2\sigma^2}\right], \; y>\alpha \qquad [9]$$
$$= 0 \;, y \leq \alpha$$

The utilisation factor defined in eq. [8] can now be expanded as:

$$U(\alpha,\varepsilon) = \frac{\int_{\varepsilon}^{\infty} \Lambda_{y-\alpha}(m,\sigma)dy}{\int_{\varepsilon}^{\infty} MGF_z(\sigma, m, \sigma_\sigma(1), \sigma_m(1))dz} \;, \varepsilon \geq 0 \,. \; [10]$$

The integrand in the denominator corresponds to the (ideal) global fading model, $z = y+\chi \approx y+e(t+1|t)$, i.e., the MGF with k=1. Note that the time dependence is included indirectly (in the numerator of eq. [10]) via the FDM α.

The utilisation factor can be more usefully displayed as a function of the fixed detection margin, α, the excess fade margin, ε, being a parameter. This is shown in Figure 5.

The results are quite consistent with some published work by Dossi et al (3), where the utilisation factor was also found to increase monotically with the fade detection margin. The authors used however a slightly different definition of utilisation factor (they used $U' = (T_{FCM} - T_{ideal})/T_{ideal}$ which is equivalent to $U' = U-1$, U being the factor used here).

* *i.e. rain but also scintillation fades and enhancements.*

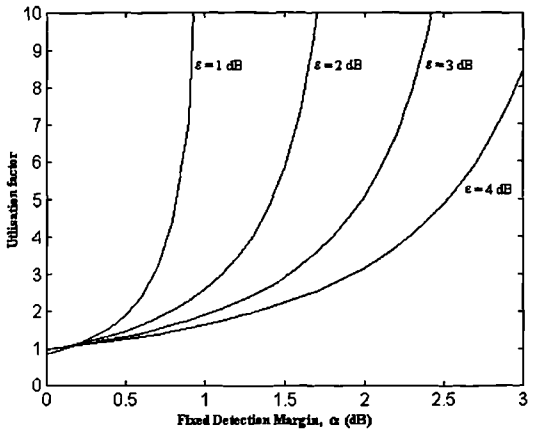

Figure 5: Utilisation factor as a function of the FDM.

Transposed to our notation, they found a utilisation factor of $U \approx 2$ for a fixed detection margin of $\alpha = 0.7$ dB assuming a fixed excess power margin of $\varepsilon = 3$ dB. In our case (Figure 5) the utilisation factor is U = 1.8 for a similar situation. The discrepancy may be explained by the fact that they also implemented an hysteresis cycle to lower the number of switchings caused be the scintillation component. Also their work was performed for a frequency of 11.6 GHz, while here the results describe a Ka band satellite link.

So far, it has been assumed that the effective control effort was not constrained by the inclusion of a limited FCM dynamic range (e.g. saturation in ULPC) or a hysteresis cycle. Such non-linearities would affect the pdf of the FCM control effort and thus the utilisation factor.

IV. Impact of delays on the FCM control rule and performance of an adaptive rate FCM

We now investigate the design and performance of an adaptive transmission rate FCM, whereby the user data rate, R_b bps, is varied according to detected/predicted channel conditions. The detection process is assumed to be based on beacon monitoring, with perfect instantaneous scaling (if applicable) and that the total drop of the overall clear-sky CNR, $CNR|_{t,0}$, has been determined accurately using a two-dimensional UL/DL plane (3).

FCM Control Rule

With such assumptions, we can now determine the Data Rate Change (DRC) boundaries (3) at which the FCM will have to switch to a more or less robust level of FCM protection, based on detected/predicted rain fades. This must be done so that a maximum BER constraint, $\bar{\beta}$, is satisfied. BPSK, and convolutional coding/Viterbi decoding with mother code with rate k/n=1/2 are assumed. For a punctured code with rate $\rho = N-1/N, N \geq 2$, over an AWGN channel, $\bar{\beta}$ is upper bounded by:

$$\bar{\beta} \equiv g\left(\frac{E_b}{N_0}\right) \leq \frac{1}{k} \sum_{d=d_{free}}^{\infty} c_d \cdot Q\left(\sqrt{2d \cdot \rho \cdot \frac{E_b}{N_0}}\right) \qquad [11]$$

where d_{free} and the distance spectrum $\{c_d\}$ can be found in (10), and, $Q(x) = \int_x^{\infty} e^{-s^2/2}\, ds$.

From [11], assuming that g(.) is invertible, we can write:

$$\left.\frac{E_b}{N_0}\right|_{rq} = 10 \cdot \log_{10}\left(g^{-1}(\bar{\beta})\right) \quad \text{dB} \qquad [12]$$

The DRC boundaries based on detected/predicted attenuation, y, that is, the total drop in overall CNR due to rain, can be located using the condition:

$$\left.\frac{E_b}{N_0}\right|_{rq} \equiv \left.\frac{C}{N_0}\right|_{t,0} - (y+\alpha) - 10 \cdot \log_{10} R_b - \mu_i$$

Combining with [12] and rearranging gives the admissible rain fades (in dB):

$$y = \left.\frac{C}{N_0}\right|_{t,0} - 10 \cdot \log_{10} R_b - \alpha - \mu_i - 10 \cdot \log_{10}\left(g^{-1}(\bar{\beta})\right) \quad [13]$$

In this paper, a low-power VSAT to hub back-to-back link with P_{hpa}=0.2W and dish diameter D=0.8m is considered. From link budget analysis, the overall clear-sky carrier-to-noise ratio is $C/No|_{t,0}$=58.28 dBHz . The FCM is adaptive transmission rate with allowable user data rates of 38400, 19200, 9600 and 4800 bps. The margin for implementation μ_i was set to 1.50 dB. The code rate was chosen to be ρ=7/8 while the BER inequality constraint was set to $\bar{\beta} = 10^{-6}$.

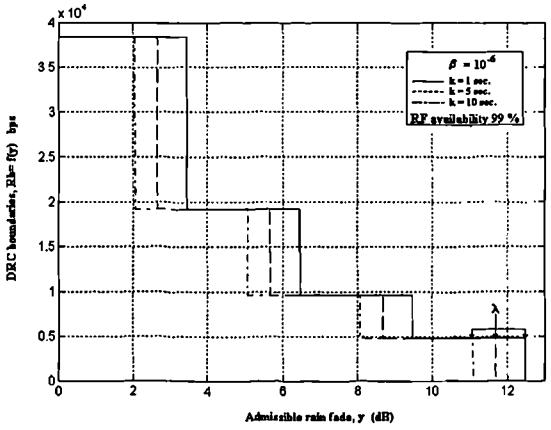

Figure 6: Typical DRC boundaries for an adaptive rate FCM.

Using equation [13], the DRC function $R_b = f(y) \Leftrightarrow y = f^{-1}(R_b)$ has been computed and is shown in Figure 6, for different delays, and, one particular RF availability. Whenever $\bar{\beta}$ is exceeded with the most robust data rate (9600 bps), the user rate is set to zero from a level $y \geq \lambda$ (see Fig. 6). This is to emphasise that this corresponds to a BER outage

situation. In a *practical* FCM controller, the data rate would however remain at 9600 bps. It is therefore considered here that user data is lost when the BER constraint is exceeded.

BER availability and average throughput

The BER outage probability may be defined as the probability that the BER constraint is exceeded with the most robust transmission. It can easily be found from the DRC function. We have:

$$P_{out,\hat{\beta}} = \Pr ob\left(\beta \geq \hat{\beta}\right) = \Pr ob(y \geq \lambda) = \int_{\lambda}^{\infty} \Lambda_y(m,\sigma)\cdot dy$$

$$\text{where } \lambda = \min\left\{f^{-1}(R_b = 0)\right\}. \qquad [14]$$

The BER outage characteristic (Fig. 7) shows trends very similar to the ones obtained in (5). Smaller BER outage probabilities can be obtained either by increasing the BER constraint and/or reducing either the specified RF availability or the time delay.

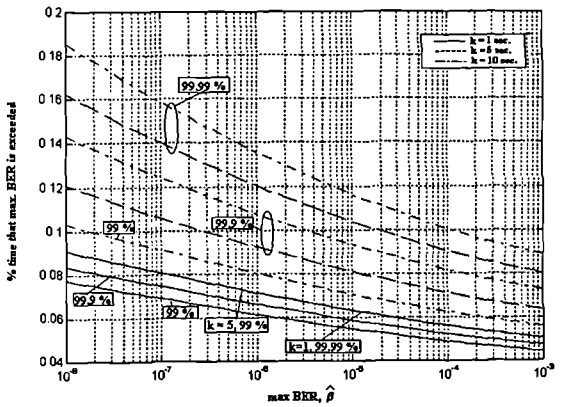

Figure 7: BER outage percentage time ($100\cdot P_{out,\hat{\beta}}$).

Similarly, the average user data throughput can be evaluated directly from the DRC function with:

$$\overline{R}_b = \rho\cdot\int_0^{\lambda} f(y)\cdot\Lambda_y(m,\sigma)dy \quad b/s \qquad [15]$$

where ρ=7/8 in our particular case.

The average user data throughput shows great dependence on both time delay and RF availability constraint. More particularly, for delay of 5 or 10 seconds (Fig. 8), the user throughput decreases with decreasing BER constraint up to a certain threshold beyond which, the throughput remains approximately constant. This may be explained by recalling that the smaller the BER constraint, the smaller the admissible rain fades, thereby shifting the DRC thresholds (see Fig. 6) to the left. As a consequence, the higher user rate, R_b=38400 bps, is sometimes never used by the FCM for high BER constraints. The throughput is thus limited to $\rho\cdot 19200 = 7/8\cdot 19200 = 16800$ bps approximately.

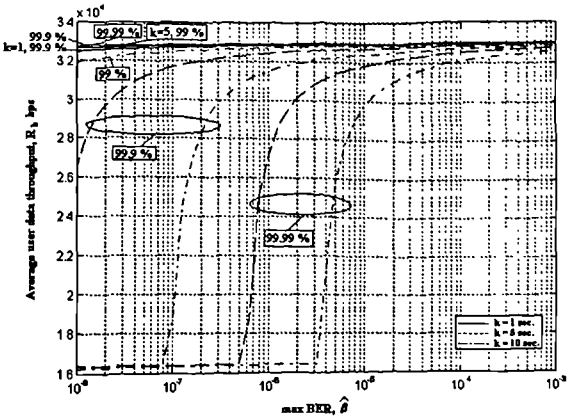

Figure 8: Average user data throughput.

Selection of the fixed FEC code rate

While the FDM was chosen to satisfy a certain RF availability given a time delay, we have no real control on the BER/throughput characteristics shown in Figures 7 and 8. However, the selection of the code rate ρ of the FEC scheme can give the designer an extra degree of freedom, allowing a trade-off between BER availability and user throughput. This comes from the fact that FEC and adaptive rate transmission can be seen a hybrid countermeasure system, the FEC being a non-adaptive one. Clearly, a lower FEC code rate would result in a decrease in BER outage probability (greater BER availability) but also in a decrease in average user throughput. To assess this trade-off, the BER availability, $100\cdot(1-P_{out,\hat{\beta}})$ has been plotted against average user throughput (see eqs [15] and [16]). This is achieved over a continuous range of BER constraints given by 10^x (x being the exponent shown next to the curves in Figure 9) for FEC code rates of ρ=1, 7/8, 5/6, 3/4 ,2/3 and 1/2. The specified RF availability was chosen to be 99 % and the time delay was chosen to be 5 seconds.

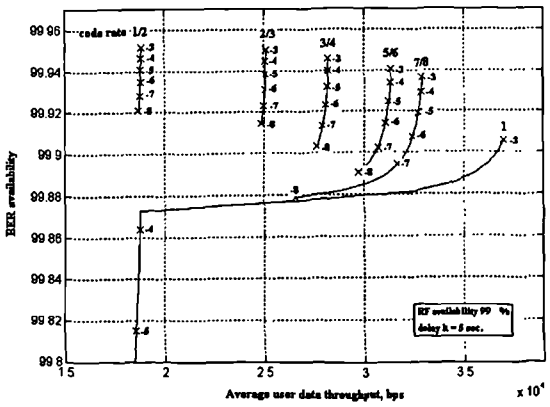

Figure 9: BER availability/user throughput trade-off.

As expected, for any particular fixed FEC code rate, the larger the BER constraint the larger is the BER availability and also the larger the user data throughput.

As an example, we will consider the points where the BER constraint is $\widehat{\beta} = 10^{-6}$. We can notice that while the BER availability is approximately constant for code rates from 2/3 to 7/8, it drops quite substantially for uncoded BPSK. Bearing in mind that it is always interesting to maximise the user throughput, uncoded BPSK appears also quite unsuitable. Since the code rate $\rho = 7/8$ is the one with the largest throughput and yields availability of the same order as the other more robust codes, this code rate represents the best engineering choice for this BER constraint.

V. Conclusion

The global fading model, introduced originally in (4), has been modified to cater for imperfect predictions within the context of predictive fade control strategies. The prediction error of a minimum variance predictor of the Ka band fading was found to have a MV characteristic, 'scaled' by time delays. This was used to develop a model, whereby the required fixed detection margin can be determined to compensate for the 'scaled' scintillation fades. This is achieved being given a time delay and a RF availability specification. The performance of such a predictive control strategy has been analysed in the RF domain by calculating the FCM utilisation ratio. The latter was found to be dependent on the fixed detection margin and the built-in low excess margin. A possible improvement of the channel capacity utilisation could be achieved by considering hypothetical functional relationships between rain and scintillation processes. This would yield a variable detection margin detection scheme allowing to minimise the utilisation factor to a value closer to one. This would be useful for both shared resource and classical FCMs. Finally the impact of time delays on the design and performance of an adaptive transmission countermeasure has been evaluated. Increasing time delays and/or RF availability constraints were found to affect the positions of the DRC boundaries of the countermeasure systems. These boundaries constitutes the control rule (table look-up) used by the FCM controller to effectively switch to a more or less robust level protection

This time-delay dependence resulted in a quantifiable decrease in BER availability and average user data throughput. However, the combination of a fixed FEC scheme with the adaptive transmission rate technique allows designers to operate directly on the trade-off user-throughput/BER availability, offering a possible optimisation.

The global fading hypothesis assumes that the total degradations of atmospheric effects on the overall clear-sky CNR is known. This corresponds to an *ideal* detection case. A possible decoupling of UL and DL fades through the satellite transponder (3) could allow inclusion of instantaneous frequency scaling (if applicable). This would also allow to consider geographical link diversity as well as hybrid FCMs (e.g. ULPC/A-TDMA) based on separate detection schemes. The outcome of such an approach could be the determination of the required margin to cover for time delays *and* instantaneous frequency scaling errors. Also, this could be used for dimensioning the back-up resource in distributed satellite systems.

VI. References

1. J.D. Laster, W.L. Stutzman, " Frequency scaling of rain attenuation for satellite communication links", 1995, IEEE Trans. on ant. and prop., Vol. 43, No 11, pp. 1207-1216.
2. N. Lay, K. Dessouky, " A communication protocol for mobile satellite systems affected by rain attenuation", IEEE J. on Sel. Areas in Comms., 1992, Vol. 10, No 6, pp. 1037- 1047.
3. B.K. Levitt, " Rain compensation algorithm for ACTS mobile terminal", 1992, IEEE J. on Select. Areas in Comms., Vol. SAC-10, No 2, pp 358-363.
4. M. Filip, E. Vilar, "Optimum utilization of the channel capacity of a satellite link in the presence of amplitude scintillations and rain attenuation", 1990, IEEE Trans. Commun., Vol. COM-38, no. 11, pp. 1958-1965.
5. B.C. Gremont, A.P. Gallois, S.D. Bate, " Efficient fade compensation for Ka band VSAT systems", 1996, Proc. 2nd Ka band utilization Conf. and international workshop on SCGII, Sept. 24-26 1996, Florence, Italy, pp 439-443.
6. L. Dossi, G. Tartara, E. Matricciani, " Frequency Diversity in millimiter wave satellite communications", 1992, IEEE Trans. on aerospace and electronic systems, Vol. AES-28, No 2, pp. 567-573.
7. E. Matricciani, M. Mauri, C. Riva, " Relationship between scintillation and rain attenuation", 1996, Radio Science, Vol. 31, No 2, pp 279-279.
8. P.E. Wellstead, M.B. Zarrop, 1991, "Self-Tuning systems, Control and signal processing", John Wiley and Sons
9. T.J. Mousley, E. Vilar, "Experimental and theoretical statistics of microwave amplitude scintillations on satellite down-links", 1982, IEEE Trans. Antenn. Propag., Vol. AP-30, No. 6, pp. 1099-1106.
10. D. Haccoun, G. Begin, " High rate punctured convolutional codes for Viterbi and sequential decoding", 1989, IEEE Trans. on Comms., Vol. COM-37, pp 1113-1125.

Predictive Fade Control for Ka Band Communications

B.C. Gremont, A.P. Gallois, S.D. Bate,
Communication Systems Group,
Coventry University, School of Engineering,
Priory street, Coventry, CV1 5FB, UK.
Email: gremont@coventry.ac.uk
Tel:(+44) 1203 838848
Fax:(+44) 1203 838949

***Abstract:** A predictive fade control algorithm for Ka band satellite systems is analysed. The goal is to control, via table-look-up, the transmission data rate over a satellite link according to short-term predicted total attenuation. It is shown that system performance and design are affected by the time delays due to the non-instantaneous response of fade countermeasure systems.*

I. INTRODUCTION

In satellite communications above 10 GHz, rain attenuation and scintillation fading, caused by irregularities of the refractive index in the troposphere, must be compensated in a real-time manner by deploying a fade countermeasure (FCM) [1]. Due to the complex nature of both rain and scintillation processes, the control of FCM resources will have to be computer-based and support the main functions outlined in Fig. 1. FCM control is essentially an algorithm, which must be justified in terms of the properties of Ka fading process and the particular FCM being used.

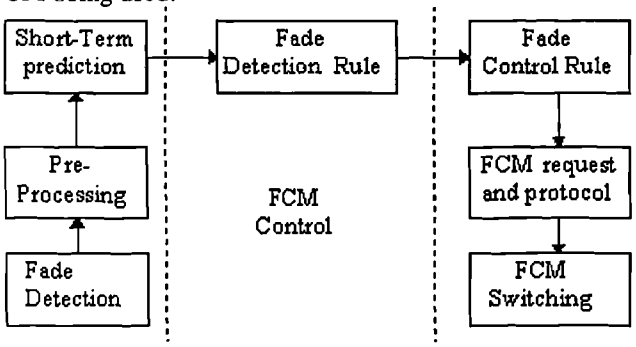

Fig. 1: Basic operations required for FCM control.

An important issue relevant to all fade countermeasures, is that the FCM controller must account for the total response time from fade detection to effective FCM switching [2]. As a consequence FCM control must be short-term predictive and account for the variations of the Ka band fading during this total time delay. To be at all efficient, the FCM controller must avoid detection outages, which correspond to an under-estimation of the level of attenuation. This is important in the context of low fade margin systems, like VSAT systems (see Fig. 2). At any time t, the FCM controller must predict the variations of the Ka band fading in order to deploy the FCM appropriately at time t+Δt . Since this operation must be carried out every seconds, a simple way is simply to add to the detected attenuation a fixed detection margin (FDM) of α dB. As we shall see shortly, it is important to minimise the value of the FDM. This can be done by implementing a short-term predictor of the Ka band process. The FDM therefore depends on the prediction ability of the FCM controller, the time delay and the dynamic/stochastic properties of the Ka band fading.

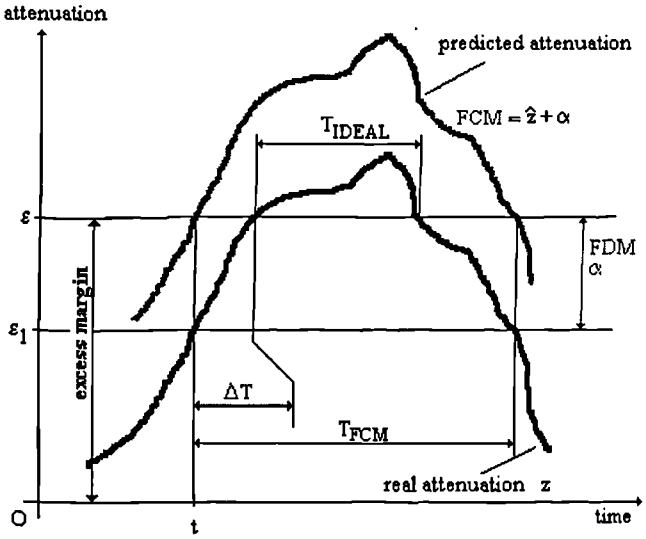

Fig. 2. *FCM utilisation factor for low fade margin systems.*

In the context of low fade margin systems, FCM action is only required when the detected/predicted attenuation exceeds a certain threshold or excess margin denoted ε. Clearly the use of the FDM approach as a fade detection rule introduces an over-utilisation of the FCM resources. This is measured by the FCM utilisation factor defined by [3]:

$$U(\alpha,\varepsilon) = \left.\frac{T_{FCM}}{T_{ideal}}\right|_{z\geq\varepsilon} \qquad (1)$$

Clearly, the FDM should be minimised as much as possible.

II. PREDICTION OF THE KA BAND FADING PROCESS

Upon application of parametric identification methods on Olympus co-polar data at 30 GHz, it was found in [4] that the Ka band attenuation time-series is well one-step ahead predicted by a model ARMA(3,3) defined by:

$$\hat{z}(t) = y(t) = -\sum_{n=1}^{3} a_n \cdot y(t-n) + e(t) + \sum_{n=1}^{3} c_n \cdot e(t-n) \quad (2)$$

This model assumes that rain attenuation, y, and scintillation* e are additive processes, i.e. the total fade is $\hat{z}(t) = y(t) - e(t)$. However, being given samples up to (t-1), it was found that the scintillation-induced error e(t) is not predicted, while the rain component is well estimated. In a self-tuning context, the six parameters of the ARMA model are time-varying. In our study, they were computed on-line using the Recursive Extended Least squares (RELS) algorithm [5], whose sole objective is to minimise at each time step t the variance of the error signal e. The model was then extended to a k-step ahead predictor by using the minimum variance approach introduced by Astrom in [6].

As any FCM controller must avoid under-estimating the total fade on a satellite link, the sample error probability function of the error signal was evaluated for different time delays (Fig. 3). It was found that the error made by the ARMA/Minimum variance prediction algorithm agrees to a Mousley-Vilar (MV) model whose two parameters are scaled by the time delays (k=1,2,3... sec).

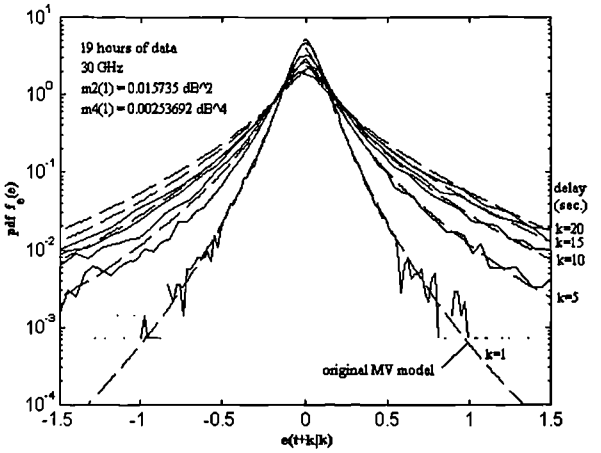

Fig.3. Sample and fitted pdfs for different time delays

As the Mousley-Vilar model was introduced to model on a long-term basis the pdf of tropospheric scintillation [7, 8], we can assume effectively that the residual error of the predictor is consistent with scintillation. The transformation of scintillation statistics with time delay, k, is modelled as follows:

$$MV_e(\sigma_m(k), \sigma_\sigma(k)) \equiv f_{e_{dB}}(e_{dB}) \quad (3)$$

$$= \frac{1}{\sigma_{\sigma_{np}}(k)\cdot\pi} \int_0^\infty \frac{1}{\sigma^2_{e_{dB}}} \cdot \exp\left[-\frac{e^2_{dB}}{2\sigma^2_{e_{dB}}} - \frac{\ln\left(\sigma^2_{e_{dB}}/\sigma^2_{m_{dB}}(k)\right)}{2\cdot\sigma^2_{\sigma_{np}}(k)} \right] \cdot d\sigma_{e_{dB}}$$

where the two delay-dependent parameters $\sigma_\sigma(k)$ and $\sigma_m(k)$ of the MV model are given by:

$$\sigma^2_\sigma(k) = \ln\left(\frac{m_4(k)}{3.[m_2(k)]^2} \right) \text{ (np)} \quad (4a)$$

$$\sigma^2_m(k) = \sqrt{3}[m_2(k)]^2 / \sqrt{m_4(k)} \text{ (dB)} \quad (4b)$$

and the second and fourth order moments are given by the following empirical formulas:

$$m_2(k) = \sigma_e^2(k) = m_2.(0.0337+0.487k+0.5251k^2) \quad (5a)$$

$$m_4(k) = m_4.(0.046+0.368k+0.319k^2+0.3499k^3-0.0312k^4 +0.0022k^5) \quad (5b)$$

The parameters m_2 and m_4 are the moments corresponding to the original parameters σ_σ and σ_m of the Mousley-Vilar model in [8] and by inverting equations 4a and 4b.

Using the model (3),(4),(5), we can now evaluate the required fixed detection margin, α. The detected/predicted control signal FCM=y+α must be greater than the total attenuation on the link, z = y+e(t+|t) (i.e. rain+scintillation), this yields:

$$P_{out}(\alpha,k) = \text{Prob}(e \geq \alpha) = \int_\alpha^\infty MV_e(\sigma_m(k), \sigma_\sigma(k))de \quad (6)$$

where P_{out} is the probability of having detection outages (see section I). This is plotted in semilog scale in Fig. 4.

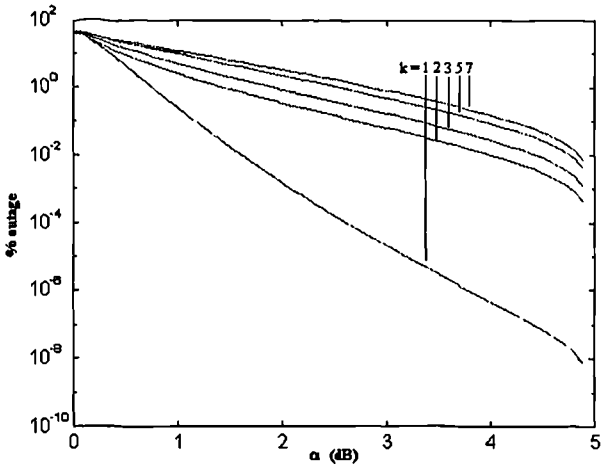

Fig. 4. *Percentage of outage, 100* $P_{out}(\alpha,k)$ as a function of the fixed detection margin, α, for different time delays (k in sec.).*

The graph in Fig. 4 is a tool for determining the required FDM margin given a time delay and a desired detection outage probability which is a design parameter. It is conditioned by the properties of scintillation and takes into account the prediction ability of the ARMA/Minimum Variance predictor.

III. Design and Performance of an Adaptive Data Rate Countermeasure

The fade control rule (see Fig. 1) refers to the look-up table, or data rate change (DRC) boundaries [9], from which the symbol rates of the adaptive rate FCM will be selected based on detected/predicted level of attenuation. For example, a reduction of the symbol rate by 2 would result in a gain of 3dB. Such a gain against fading is introduced at the expense of a variable user data throughput and is conditioned by a maximum acceptable

* *e is merely a MMSE estimate of the scintillation process.*

BER, $\hat{\beta}$. Thus if $\hat{\beta}$ is exceeded due to fading with one user data rate R_b, the FCM controller will switch to a smaller data rate. The BER outage probability is defined as the probability of having $\hat{\beta}$ exceeded with the smallest data rate available to the FCM controller. The use of a fixed detection margin was introduced so as to limit the probability of underestimating the total fade over a satellite link. This is effectively equivalent to saying to the fade controller that the fade is α dB deeper than reality and therefore the time-delay dependent FDM will limit the admissible levels of fades which can be accommodated by the adaptive rate countermeasure.

It can easily be shown that the DRC boundaries must satisfy the following conditions:

$$y = \left.\frac{C}{N_0}\right|_{t,0} - 10\cdot\log_{10} R_b - \alpha - \mu_i - \left.\frac{E_b}{N_o}\right|_{rq@\hat{\beta},\rho} \quad \text{dB} \qquad (8)$$

where R_b (bps) is the user data rate, α is the fixed detection margin, μ_i=1.5 dB is a margin for implementation. The overall clear-sky carrier to noise ratio, $C/N_o|_{t,o}$. From a link budget analysis of a typical in-bound VSAT link, a low-power VSAT amplifier (P_{hpa}=0.2W and dish diameter D=0.8m) the CNR was found to be $C/No|_{t,0}$=58.28 dBHz . The last term in (8) corresponds to the required E_b/N_o given a maximum BER constraint, $\hat{\beta}$. BPSK, and punctured convolutional coding/Viterbi decoding with code rate ρ was assumed (puncturing from a rate 1/2 mother code, v=6). The allowable user data rates of 38400, 19200, 9600 and 4800 bps were assumed. Using equation (8), the DRC function has been computed and is shown in Figure 6, for different delays, and, When $\hat{\beta}$ is exceeded with the most robust data rate (9600 bps), the user rate is set to zero from a level $y \geq \lambda$ (see Fig. 5). This is to emphasise that this corresponds to a BER outage situation.

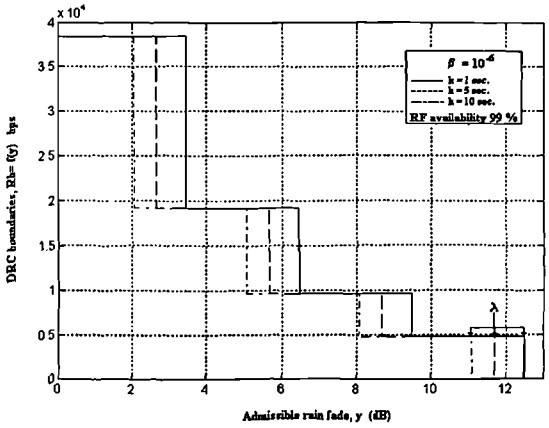

Fig. 5. Typical DRC boundaries for an adaptive rate FCM.

In a *practical* FCM controller, the data rate would however remain at 9600 bps. It is therefore considered here that user data is lost when the BER constraint is exceeded. Based on the DRC function, expressions for the BER availability and average user data throughput can easily be found to be:

$$P_{out,\hat{\beta}} = \text{Prob}\left(\beta \geq \hat{\beta}\right) = \text{Prob}(y \geq \lambda) = \int_{\lambda}^{\infty} \Lambda_y(m,\sigma)\cdot dy \qquad (9)$$

and

$$\overline{R}_b = \rho \cdot \int_0^{\lambda} f(y)\cdot \Lambda_y(m,\sigma)dy \quad b/s \qquad (10)$$

respectively.

In order to assess the BER availability/average throughput trade-off and choose the most appropriate FEC code rate ρ, equations (9) and (10) have been computed and plotted one against the other. This was achieved over a continuous range of BER constraints $\hat{\beta}$ given by 10^x (x being the exponent shown next to the curves in Figure 7) for FEC code rates of ρ=1, 7/8, 5/6, 3/4 ,2/3 and 1/2. The specified detection availability was chosen to be 99 % (i.e. P_{out}= 0.01) and the time delay was chosen to be 5 seconds. As expected, for any particular fixed FEC code rate, the larger the BER constraint the larger is the BER availability and also the larger the user data throughput. As an example, we will consider the points where the BER constraint is $\hat{\beta}$ = 10^{-6}. We can notice that while the BER availability is approximately constant for code rates from 2/3 to 7/8, it drops quite substantially for uncoded BPSK. Bearing in mind that it is always interesting to maximise the user throughput, uncoded BPSK appears also quite unsuitable. Since the code rate ρ = 7/8 is the one with the largest throughput and yields availability of the same order as the other more robust codes, this code rate represents the best engineering choice for this BER constraint.

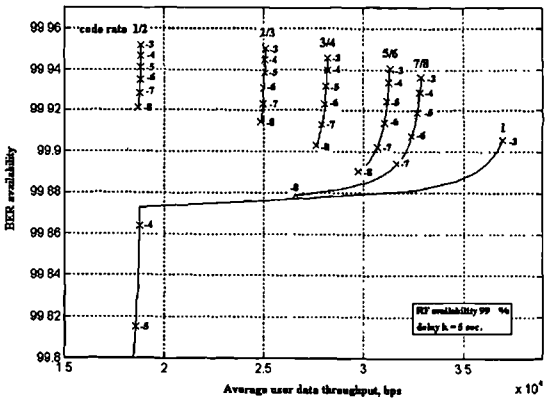

Fig. 6. BER availability/user throughput trade-off.

IV. CONCLUSION

The implementation and system design implications of predictive fade control for fade countermeasure systems has been analysed. The application of a time-varying predictor based on a MMSE criterion to experimental beacon data revealed that its residual error agrees to a Mousley-Vilar (MV) pdf. The time delays result in a

transformation of the original MV model. It was identified by studying the second and fourth order moments of the error sequence, after application of the ARMA-based predictor to real data. The error was found to be consistent with tropospheric scintillation, while the slower trend due to rain attenuation is well predicted. In order to avoid outage situations (i.e. under-estimation of the total fade), the fixed detection margin (FDM) was introduced as an easy way to set the accuracy of the detection/prediction scheme. The detection outage probability is thus a design parameter which needs to be specified by the user. Clearly. the longer the total delay, or the smaller the detection outage probability, the larger is the FDM. The introduction of the FDM as a way to combat 'scaled' scintillation effects was also shown to have an impact on the position of the Data Rate Change (DRC) boundaries of an adaptive transmission rate countermeasure. These boundaries depend on the maximum BER constraint (this is also a specified parameter), the value of the FDM, the rain fade statistics and the particular modulation/code and data rates of the system considered. The levels of admissible detected/predicted rain fades at which the switching to higher or lower transmission rate depend on the value of the FDM. Large FDMs were then shown to result in a degradation in long-term BER availability and user throughput. By plotting these two one against the other, the most appropriate level of FEC coding can then be selected.

REFERENCES

[1] M.J. Willis, "Fade Countermeasures applied to transmissions at 20/30 GHz", *Electronics and Communications Journal*, April 1989, pp. 88-96.

[2] G. Tartara, "Fade countermeasures in millimetre-wave satellite communications: A survey of methods and problems", *Proc. of the Olympus Utilisation Conf, Vienna, April 1989*, ESA SP-292, Apr. 1989, pp103-107.

[3] L. Dossi, "Real-time prediction of attenuation for applications to fade countermeasures in satellite communications", *Electron. Lett.*, Vol. 26, no. 4, February 1990, pp. 250-251.

[4] B.C. Gremont, A.P. Gallois, S.D. Bate, "Efficient fade compensation for Ka band VSAT systems", *Proc. 2nd Ka band Utilization Conf. and Int. workshop on SCGII, Florence (Italy)*, Sept 24-26 1996, pp 439-443.

[5] P.E. Wellstead, M.B. Zarrop, *"Self-Tuning systems, Control and signal processing"*, John Wiley and Sons, 1991.

[6] K.J. Aström, *"Introduction to stochastic control theory"*, Mathematics and science engineering, Vol. 70, Academic Press, 1970.

[7] T.J. Mousley, E. Vilar, "Experimental and theoretical statistics of microwave amplitude scintillations on satellite down-links", *IEEE Trans. Antenn. Propag.*, Vol. AP-30, no. 6, November 1982, pp. 1099-1106.

[8] E. Vilar, J.R. Larsen, " Elevation dependence of amplitude scintillations on low-elevation Earth-Space paths", *Proc. 6th Int. Conf. on Antennas and Propagation ICAP'89, University of Warwick*, April 1989.

[9] B.K. Levitt, " Rain compensation algorithm for ACTS mobile terminal", *IEEE Journ. on Select. Areas in Comms.*, Vol. SAC-10, No 2, Feb. 1992, pp 358-363.

APPENDIX: RELS ALGORITHM [5]

The algorithm used for on-line estimation of the 6 ARMA model parameters was the Recursive Extended Least Squares (RELS) algorithm. It can accommodate in a simple manner the coloured noise corresponding to the moving average terms in the ARMA model definition. A directional forgetting factor was also implemented in order to avoid covariance wind-up and also add extra parameter tracking capabilities to the algorithm.

Defining

$$\hat{\theta}(t) = [-a_1 \quad -a_2 \quad -a_3 \quad c_1 \quad c_2 \quad c_3]$$

$$\phi^T(t) = [y(t-1) \quad y(t-2) \quad y(t-3) \quad \varepsilon(t-1) \quad \varepsilon(t-2) \quad \varepsilon(t-3)]$$

where $\varepsilon(t) = y(t) - \phi^T(t)\theta(t-1)$

is the prediction error using output prediction based on information up to (t-1). The RELS algorithm is then at time t:

(i) Form $\phi^T(t)$

using y(t) and $\varepsilon(t) = y(t) - \phi^T(t)\theta(t-1)$

(ii) Evaluate the directional forgetting factor

$$r(t-1) = \lambda' - \frac{1-\lambda'}{1+\phi^T(t)\mathbf{P}(t-1)\phi(t)}$$

(iii) Compute the covariance matrix using :

$$\mathbf{P}(t) = \mathbf{P}(t-1)\left[\mathbf{I}_6 - \frac{\phi(t)\phi^T(t)\mathbf{P}(t-1)}{r^{-1}(t-1) + \phi^T(t)\mathbf{P}(t-1)\phi(t)}\right]$$

(iii) Evaluate the updated model parameters at time t

$$\hat{\theta}(t) = \hat{\theta}(t-1) + \mathbf{P}(t)\phi(t)\left[y(t) - \phi^T(t)\hat{\theta}(t-1)\right]$$

The initial covariance matrix was set to $\mathbf{P}(t) = 100\mathbf{I}_6$ and the forgetting factor parameter was set to $\lambda' = 0.97$.

Minimum Variance Prediction

This algorithm is described in [4] or the detailed demonstration can be found in Aström's original work in [6].